Cannat, M., Karson, J.A., Miller, D.J., et al., 1995
Proceedings of the Ocean Drilling Program, Initial Reports, Vol. 153

3. SITE 920[1]

Shipboard Scientific Party[2]

HOLE 920A

Date occupied: 3 December 1993

Date departed: 4 December 1993

Time on hole: 1 day, 11 hr, 03 min

Position: 23°20.310′N, 45°1.038′W

Bottom felt (drill-pipe measurement from rig floor, m): 3339.00

Distance between rig floor and sea level (m): 10.50

Water depth (drill-pipe measurement from sea level, m): 3328.50

Total depth (from rig floor, m): 3353.00

Penetration (m): 14.00

Number of cores (including cores with no recovery): 1

Total length of cored section (m): 28.00

Total core recovered (m): 1.68

Core recovery (%): 6

Oldest sediment cored: Unknown

Hard rock:
Depth (mbsf): 14.00
Nature: Polygenic gravel

Comments: Predominantly serpentinized peridotite

HOLE 920B

Date occupied: 4 December 1993

Date departed: 9 December 1993

Time on hole: 4 days, 17 hr, 15 min

Position: 23°20.310′N, 45°1.038′W

Bottom felt (drill-pipe measurement from rig floor, m): 3339.00

Distance between rig floor and sea level (m): 11.10

Water depth (drill-pipe measurement from sea level, m): 3327.90

Total depth (from rig floor, m): 3465.40

Penetration (m): 126.40

Number of cores (including cores with no recovery): 13

Total length of cored section (m): 126.40

Total core recovered (m): 47.78

Core recovery (%): 39.7

Oldest sediment cored: None

Hard rock:
Depth (mbsf): 126.40
Nature: Serpentinized harzburgite, diabase oxide gabbro, gneissic amphibolite
Measured velocity (km/s): 3.65–5.76

HOLE 920C

Date occupied: 9 December 1993

Date departed: 13 December 1993

Time on hole: 3 days, 18 hr, 10 min

Position: 23°20.304′N, 45°1.032′W

Bottom felt (drill-pipe measurement from rig floor, m): 3343.0

Distance between rig floor and sea level (m): 10.80

Water depth (drill-pipe measurement from sea level, m): 3332.2

Total depth (from rig floor, m): 3359

Penetration (m): 16.0

Number of cores (including cores having no recovery): 0

Total length of cored section (m): 0.00

Total core recovered (m): 0.00

Core recovery (%): 0

Oldest sediment cored: None

Hard rock: None

Comments: Hard-rock guide base (HRGB) shifted too much to continue drilling

HOLE 920D

Date occupied: 13 December 1993

Date departed: 19 December 1993

Time on hole: 6 days, 12 hr, 10 min

Position: 23°20.322′N, 45°1.044′W

Bottom felt (drill-pipe measurement from rig floor, m): 3338.00

Distance between rig floor and sea level (m): 10.50

Water depth (drill-pipe measurement from sea level, m): 3327.50

Total depth (from rig floor, m): 3538.80

Penetration (m): 200.80

Number of cores (including cores with no recovery): 22

Total length of cored section (m): 200.80

Total core recovered (m): 95.08

Core recovery (%): 47

Oldest sediment cored: None

Hard rock:
Depth (mbsf): 200.80
Nature: Serpentinized harzburgite, diabase, metagabbro, oxide gabbro
Measured velocity (km/s): 3.90–5.21

Principal results: Site 920 is located on the western median valley wall of the Mid-Atlantic Ridge (MAR) at 23°20.32′N, 45°01.00′W, about 35 km south of the Kane Transform (Fig. 5, "Introduction," this volume). The site is set in an extensive body of serpentinized peridotite that is exposed in a 2-km-wide belt that extends parallel to the MAR axis at least 20 km (Fig. 3, "Introduction," this volume). These rocks are interpreted as exposures

[1] Cannat, M., Karson, J.A., Miller, D.J., et al., 1995. *Proc. ODP, Init. Repts.,* 153: College Station, TX (Ocean Drilling Program).
[2] Shipboard Scientific Party is given in the list of participants preceding the contents.

of highly altered upper mantle material that have been unroofed by extensional tectonics, probably during a period of spreading with very limited magmatic construction. Drilling at Site 920 achieved the best total penetration and recovery of any hard-rock drilling efforts in massive serpentinized peridotite, and it has provided a glimpse of processes that operate beneath slow-spreading mid-ocean ridges.

Hot, weak asthenospheric upper mantle is believed to rise and undergo decompression melting to yield basaltic melts beneath mid-ocean ridge spreading centers. Geological, geophysical, and geochemical studies support the conclusion that the oceanic upper mantle comprises anhydrous peridotite. As the upper mantle cools its strength increases rapidly and it is added to the lithosphere. In most models of seafloor spreading, the lithosphere is very thin at spreading centers and thickens rapidly off axis. On slow-spreading ridges, however, the axial lithosphere may be thicker, allowing faults to penetrate into the subaxial upper mantle. In addition, cool or infertile upper mantle may locally generate thin or discontinuous magmatic crust. Faults that penetrate into the subaxial lithosphere may provide permeable pathways for hydrothermal circulation causing widespread hydrothermal alteration and serpentinization. Displacement on such major faults may also expose serpentinized peridotites on the seafloor.

Serpentinized peridotites have been recovered from the seafloor including the MARK area for years (Miyashiro et al., 1969). Most samples have been collected by dredging tectonic escarpments of the median valley walls where the geologic context of any given sample is unconstrained and likely to have been derived from talus ramps. Submersibles have permitted the collection of samples directly from serpentinite outcrops produced by recent tectonics in the MARK area. Samples have been collected from a variety of outcrop settings and structural domains, and the spacing of samples is typically tens to hundreds of meters. Rotary drilling in serpentinite permits the collection of more continuous sections of serpentinized peridotite that are limited by the depth of penetration and total recovery. Moreover, drilling avoids weathered or tectonized surfaces of major escarpments, invalidating the perennial question of how representative samples from tectonic escarpments may be of larger scale crustal volumes.

Holes 920A, 920B, 920C, and 920D were drilled on a gently sloping terrace situated at the top of a steep cliff exposing massive to schistose serpentinized peridotite. The terrace lies at a depth of 3340 mbsl and is covered with a smooth blanket of pelagic ooze and an unknown thickness of poorly consolidated rubble.

Hole 920A was spudded unsupported and drilled to a depth of 14 mbsf (Table 1). Circulation in the hole was lost, probably resulting from sand- to pebble-size clasts of serpentinite in a gray clayey matrix obstructing the flow of fluids through the jets of the drill bit. Core 153-920A-1W contained 0.84 m of poorly consolidated serpentinite-clast sandstone and polygenic gravel.

Hole 920B was spudded while attempting reentry into Hole 920A. It achieved a total penetration of 126.4 mbsf, with a total recovery of 47.8 m of serpentinized harzburgite (37.8%). Penetration rates were approximately 60 m per day, and recovery increased downward (54% cumulative recovery below 70 mbsf). Hole 920B was abandoned after an unsuccessful attempt to set a free-fall funnel in order to make it a multiple reentry hole.

After the unsuccessful reentry attempt at Hole 920B, the HRGB was deployed on a 10° slope, less than 15 m away from Hole 920B. Hole 920C was drilled with a 17-1/2 in. bit, to approximately 19 mbsf, a penetration that was judged sufficient to ensure stability of the casing. During subsequent hole cleaning and pulling-out operations the HRGB tilted to an angle of >15°, too great an inclination for drilling. The HRGB was retrieved without further drilling.

Hole 920D was spudded about 18 m north of Hole 920B (Table 1). Drilling proceeded at a rate of 2 to 3 m/hr and reached a depth of 200.8 m, recovering 95.08 m of serpentinized harzburgite (47.4% cumulative recovery). During an attempt to pull out of the hole for logging, the drill string jammed in the hole and had to be severed. The hole was abandoned and *JOIDES Resolution* transitted to Site 921.

Although Holes 920B and 920D reached penetrations sufficient for logging, neither hole proved to be stable enough. Hole 920B was drilled with a non-releasable bit, but the hole was too unstable and could not be re-entered. Hole 920D was drilled with a releasable bit to allow for logging, but the BHA jammed in the hole before logging operations could be performed.

Drilling in the four holes at Site 920 met with different degrees of success. Only 1.68 m of rubble and serpentinized peridotite were recovered from Hole 920A; Hole 920C had no recovery. Holes 920B and 920D reached depths in excess of 126 m and 200 m, respectively, and recovered a total of 150 m of serpentinized peridotite and lesser variably deformed and metamorphosed mafic rocks. Seven rock units in Hole 920B and 13 in Hole 920D have been identified. Preliminary results of igneous, metamorphic, structural, paleomagnetic, and physical properties studies of cores from Holes 920B and 920D are presented below.

Most of the material recovered is serpentinized harzburgite. Despite the typically intense alteration of the rock to serpentinite, primary mineralogy and textures can be inferred from distinctive pseudomorphs and local patches of relatively fresh material. Ultramafic rock units sampled at Site 920 include dominantly massive harzburgite with locally interlayered pyroxene-rich (up to 35% orthopyroxene) and pyroxene-poor harzburgite to dunite. Layer thicknesses range from a few meters to a few centimeters. Medium- to coarse-grained porphyroclastic textures are nearly ubiquitous with large (4–25 mm) orthopyroxene porphyroclasts surrounded by finer grained (submicroscopic to 3 mm) polygonal aggregates of orthopyroxene and olivine neoblasts. Clinopyroxene (<5%) and chrome spinel (~1%) are also present.

Of special interest are numerous elongated segregations or veins of spinel, clinopyroxene, plagioclase, or a combination of these phases may have crystallized along former melt channels in the peridotite. These range from linked, cuspate aggregates of spinel or clinopyroxene that are to be distributed along grain boundaries and at multiple grain contact points of the peridotite, to gabbroic layers up to a few centimeters wide. Both concordant and discordant examples of these types of veins occur in the foliated serpentinized harzburgite host. These veins are occasionally bounded by symmetrical, parallel bands of pyroxene-poor harzburgite to dunite.

The primary igneous mineralogy of the rocks is pervasively altered, typically to >80% secondary phases. These include mainly serpentine with lesser tremolite-actinolite, talc, chlorite, magnetite, and carbonate minerals, reflecting pervasive metamorphism at greenschist facies to low-temperature conditions. Multiple generations of serpentine veins in these ultramafic rocks record a history of progressive alteration and volumetric expansion. Locally preserved cummingtonite and talc suggest that a higher-temperature paragenesis may also have affected these units, at least locally. Pyroxene- and/or plagioclase-bearing melt channels range from fresh to highly altered with extensive replacement by tremolite-actinolite, chlorite, secondary plagioclase, prehnite, carbonate minerals, and magnetite.

Deformation features bear witness to a complex strain history over progressively decreasing temperatures. With the exception of a few high-temperature shear zones, typically 10 to 20 cm wide, a high-temperature foliation and subordinate lineation defined by moderately elongated orthopyroxene porphyroclasts and aggregates is remarkably constant through the cores. These early, high-temperature features are overprinted in most samples by an anastomosing foliation, highlighted by thin, white, serpentine veins. This foliation appears to result from the preferred orientation of fine, discontinuous veins of serpentine, and serpentine and iron oxide minerals cutting the background serpentine network. The anastomosing serpentine fabric is cut by later generations of serpentine-bearing extensional and sheared veins. The relative intensity and dip of the high-temperature pyroxene foliation, anastomosing serpentine foliation, and the densities of discrete vein arrays vary considerably along the lengths of the cores. These characteristics integrate to define several distinct structural domains.

Gabbroic intervals a few centimeters to a few tens of centimeters thick are interspersed within the serpentinized harzburgite. They are pegmatitic to medium-grained metagabbros rich in iron oxide minerals that display various degrees of deformation and metamorphism. Some of these gabbroic units have been pervasively deformed at granulite to amphibolite facies conditions. These deformed units contain pervasively recrystallized brown amphibole, calcic plagioclase, clinopyroxene, and olivine, and they have strong tectonite fabrics. One iron oxide mineral-rich gabbro appears to have been highly deformed to produce a porphyroclastic mylonite.

Lower temperature greenschist facies mineral assemblages partially replace the high-temperature mineralogy and one sample is partially rodingitized. Prehnite and zeolite veins are common in these lithologies. At present it is not clear if the deformation and metamorphism that has affected some of these gabbroic units is related to that of the surrounding serpentinized harzburgite, or if these two rock types have been tectonically juxtaposed after experiencing distinct tectonic and thermal histories.

A diabase dike with partially preserved chilled margins cuts the serpentinized harzburgite in both Holes 920B and 920D. In addition to this diabase, several other distinctive mafic and ultramafic units have been tentatively correlated between the two holes.

Paleomagnetic studies on half-core and mini-core samples have been used to document the magnetic properties of the rock types recovered. The serpentinized harzburgite has very high natural remanence (mean 11.8 ± 4.9 A/m) and susceptibility (0.01–0.1 SI). Strong susceptibility anisotropy appears to be the result of magnetite concentrations that commonly parallel the anastomosing serpentine foliation. The measured inclination is similar to that of the present field for this location and therefore the orientations of various structures in the core may be at least partially corrected. Assuming that the paleomagnetic declination matches the present day magnetic dipole, it appears that the anastomosing serpentine foliation in Holes 920B and 920D dips dominantly to the east (i.e., toward the Mid-Atlantic Ridge axis).

Density, porosity, ambient pressure compressional-wave velocity, electrical resistivity, and thermal conductivity have been documented for the major rock units recovered. The preliminary results of these studies show correlations between these physical properties, lithologies, and degrees of alteration.

OPERATIONS

St. John's Port Call

Leg 153 began at 0830 hrs, 22 November 1993, with the first mooring line at Seabase Docks, St. John's, Newfoundland. *JOIDES Resolution* arrived in St. John's two days ahead of schedule because of deteriorating weather in the Leg 152 operating area; the ship set sail with all Leg 153 personnel with the last mooring line at 1530 hrs, 27 November 1993.

Transit to Site 920 (MK-2)

The transit from St. John's to Site 920 (MK-2) covered 1500 nmi in 138.5 hr (5.8 days) at an average speed of 10.8 kts. During the transit a hard-rock guide base was moved into the moonpool area and partially assembled in anticipation of deployment at Site 920.

Site 920 (MK-2) Mid-Atlantic Ridge

No seismic profiling was done on approach to Site 920. The vessel navigated to the geographic coordinates for MK-2 where thrusters and hydrophones were lowered; final positioning was achieved in dynamic positioning (DP) mode. A positioning beacon was launched at 1212 hr, 3 December, initiating Site 920.

Once in DP mode a standard nine-drill collar RCB bottom hole assembly (BHA) was made up and tripped to the seafloor. The vibration isolated television (VIT) equipped with a releasable beacon was lowered down the drill string for the seafloor survey. After approximately 8 hr of seafloor survey a backup beacon was dropped from the VIT at 0700 hr, 4 December.

Hole 920A

After retrieving the VIT, Hole 920A was spudded at 0912 hr, 4 December. Seafloor depth was determined by drill-pipe measurement to be 3339 meters below rig floor (mbrf) or 3328.3 mbsl. Hole 920A was cored to 3354 mbrf or 14 mbsf recovering 0.84 m of core (Table 1) when the drill bit became plugged and prevented fluid circulation in the hole. The core barrel was retrieved, fluid circulation reestablished, and another core barrel was dropped. Upon landing of the second core barrel we determined the drill bit was still plugged and preventing fluid circulation.

Table 1. Coring summary, Holes 920A, 920B, and 920D.

Core	Date (Dec. 1993)	Time (UTC)	Depth (mbsf)	Cored (m)	Recovered (m)	Recovery (%)
153-920A-						
1W	04	2300	0.0–14.0	14.0	0.84	
2M	05	1130	0.0–14.0	14.0	0.84	6.0
Coring totals				14.0	0.84	6.0
Washing totals				14.0	0.84	
Combined totals				28.0	1.68	
153-920B-						
1W	06	0445	0.0–14.0	14.0	3.21	
2R	06	0830	14.0–23.5	9.5	0.89	9.4
3R	06	1345	23.5–33.2	9.7	2.47	25.4
4R	06	1650	33.2–42.7	9.5	1.15	12.1
5R	06	2040	42.7–51.9	9.2	3.61	39.2
6R	06	2355	51.9–61.0	9.1	3.03	33.3
7R	07	0340	61.0–70.4	9.4	3.54	37.6
8R	07	0700	70.4–79.7	9.3	5.62	60.4
9R	07	1055	79.7–89.1	9.4	4.38	46.6
10R	07	1510	89.1–98.5	9.4	5.75	61.2
11R	07	1900	98.5–107.7	9.2	2.40	26.1
12R	07	2350	107.7–117.2	9.5	7.11	74.8
13R	08	0425	117.2–126.4	9.2	4.62	50.2
Coring totals				112.4	44.57	39.7
Washing totals				14.0	3.21	
Combined totals				126.4	47.78	
153-920D-						
1R	14	1050	0.0–8.0	8.0	0.00	0.0
2R	14	1630	8.0–17.5	9.5	1.84	19.3
3R	14	2220	17.5–27.3	9.8	1.90	19.4
4R	15	0325	27.3–36.9	9.6	2.82	29.4
5R	15	0820	36.9–46.5	9.6	4.88	50.8
6R	15	1145	46.5–56.2	9.7	3.14	32.4
7R	15	1540	56.2–65.9	9.7	2.37	24.4
8R	15	1950	65.9–75.6	9.7	3.42	35.2
9R	15	2345	75.6–78.1	2.5	2.43	97.2
10R	16	0435	78.1–85.3	7.2	5.09	70.7
11R	16	0915	85.3–95.0	9.7	3.82	39.4
12R	16	1415	95.0–104.6	9.6	6.41	66.8
13R	16	1900	104.6–114.3	9.7	4.35	44.8
14R	17	0100	114.3–123.9	9.6	6.78	70.6
15R	17	0620	123.9–133.4	9.5	7.14	75.1
16R	17	1125	133.4–143.0	9.6	7.75	80.7
17R	17	1530	143.0–152.6	9.6	4.58	47.7
18R	17	2030	152.6–162.3	9.7	4.57	47.1
19R	18	0120	162.3–171.9	9.6	2.83	29.5
20R	18	0620	171.9–181.5	9.6	6.03	62.8
21R	18	2240	181.5–191.2	9.7	5.37	55.3
22R	19	0400	191.2–200.8	9.6	7.56	78.7
Coring totals				200.8	95.08	47.4

The wireline became stuck in an attempt to unseat the core barrel to reestablish hole circulation. Repeated attempts to shear release the wireline running tool were unsuccessful. The Kinley Cutter was deployed and the wireline severed just above the wireline sinker bar. The wireline and drill pipe were retrieved, ending Hole 920A at 2315 hr, 4 December.

Hole 920B

A nine-drill collar BHA was assembled and run in the hole. The VIT was deployed for an attempt at reentering Hole 920A. The BHA was landed on the seafloor and believed to be setting on the edge of Hole 920A. The VIT was recovered to allow the drill string to be rotated in an effort to "walk" the bit into Hole 920A.

Rotating the drill string did not result in entering Hole 920A and thus Hole 920B was spudded at 2015 hr, 5 December. Hole 920B was initially drilled to 3353 mbrf (14 mbsf) to allow a pipe connection to be made without pulling the bit above the seafloor. 3.21 m of core was recovered from this interval and designated a wash core. Hole 920B was then cored 112.4 m to a total depth (TD) of 3465.5 mbrf (126.5 mbsf). 13 RCB cores were cut, recovering 44.57 m of core for a recovery rate of 39.7%.

With 42.75 total rotating hr on the drill bit a pipe trip was made for a bit change. A modified free fall funnel (FFF) was deployed before pulling out of the hole.

The bit cleared the FFF at 1328 hr, 8 December, and the ship was offset 10 m to the south for a jet test to determine the sediment thickness. The bit was jetted in 1.2 m with a flow rate of 250 gallons per minute (gpm) and 10,000 lb weight on bit (WOB). The drill string was then retrieved.

A new 12 drill collar BHA including a Hydrolex jar and 7-1/4 in. drill collar was made up and deployed. The FFF at Hole 920B was reentered at 0800 hr, 9 December. The hole was reamed down 26 mbsf without fully entering the borehole.

The decision was made to trip out and deploy the HRGB. Hole 920B ended when the bit cleared the seafloor at 1623 hr, 9 December.

Hole 920C

The HRGB was picked up and run in the hole, landing first on a 16° slope. Sonar indicated the possibility of more level terrain to the east so the HRGB was picked up and moved 5 m east. The tilt beacon, bull's-eyes, and gravity indicators all indicated a 10° slope to the east-southeast. The HRGB was positioned approximately 35 m east and 12 m north of Holes 920A and 920B. The seafloor depth was determined by drill-pipe measurement to be 3343 mbrf (3332.2 mbsl). The drill string was released from the HRGB and recovered.

A new BHA was made of a 17-1/2 in. bit and 12 drill collars. By the time the BHA was lowered to the seafloor the HRGB had settled, tilting an additional 2.6°. The HRGB was reentered at 0325 hr, 11 December, and drilling commenced.

While drilling a 16-m-deep hole the HRGB tilted an additional 1.3°. As the hole was being prepared for casing, the HRGB tilted another 1.9°, achieving an angle of 15.8°. Since the HRGB was equipped with a gimbal lock-out feature that stops movement of the reentry cone assembly once the HRGB is landed, the reentry cone/hanger assembly was rotated 5.8° off vertical with settling of the HRGB. Increased torque indicated the reentry cone assembly was binding on the BHA. With the HRGB effectively leaning on the BHA, the bit could not be worked back to the bottom of the hole. The decision was made to pull out of the hole and move the HRGB. When the BHA was pulled out, the HRGB tilted an additional 2.7°.

The 17-1/2 in. drilling BHA was recovered and replaced with the Dril Quip 20 in. CADA running tool. The CADA running tool was tripped to the seafloor and the HRGB reentered at 1431 hr, 12 December. As the running tool was being latched into the HRGB the reentry cone assembly toppled over. An attempt was made to straighten the reentry cone assembly and reenter it. However, since the landing point of the running tool was above the gimbal point and there was no stabilization of the running tool below the gimbal point, the reentry cone assembly toppled over again. Since the running tool could not be latched into the HRGB reentry cone assembly, the drill string was tripped out.

A 6-ft-long 17-1/2 in. stabilizer was fabricated from a 10 ft drill-collar pup and 1-in.-thick steel plate. The stabilizer was made up below the CADA running tool and three drill collars were added above. The assembly was tripped to the seafloor and reentry attempted. On the third attempt the reentry cone assembly was righted and reentered. With the stabilizer in place the reentry cone assembly stayed upright enabling the running tool to be latched in. The HRGB was then recovered.

Hole 920D

A standard 12 collar RCB BHA was made up and run in the hole. Hole 920D was spudded at 0545 hr, 14 December, 10 m east of Hole 920B. Seafloor depth was determined by drill-pipe measurement to be 3338 mbrf or 3327 mbsl.

Hole 920D was cored through RCB #20 to a depth of 3519.6 mbrf (181.6 mbsf) with only minor hole problems. However, while dropping RCB #21 the drill string became stuck. The drill string was eventually freed and RCB #21 and #22 were cut to a depth of 3538.8 mbrf (200.8 mbsf), where the drill string became stuck again. Once free, the drill string was worked to 3487 mbrf (149 mbsf), where all drill-string motion was lost.

After working the stuck pipe for 12 hr a severing charge was lowered to 3342 mbrf (4 mbsf) and detonated. The severed drill string was pulled clear of the seafloor at 2012 hr, 19 December, ending Hole 920D.

Camera Survey

Site 920 was selected during a VIT survey of the western MARK area rift valley wall, as a potential site for deep drilling in ultramafic rocks exposed at the ocean floor, using the HRGB as a reentry template. This survey was conducted in an area previously explored during *Nautile* dive HS 13 (Mével et al., 1991; Fig. 5, "Introduction," this volume).

A positioning beacon was dropped at 23°20.33′N, 45°00.78′W, 3635 mbsl. The survey was started from this location and progressed upslope in a westerly direction (Fig. 1). Total time spent on bottom was 7 hr, 30 min.

The first outcrop was encountered less than 50 m from the beacon. It does not form massive scarps, but slabby, often schistose dip-slope surfaces, covered by a thin mud blanket. Similar outcrops, sampled during the *Nautile* dive, and during *Alvin* (Karson et al., 1987) and other *Nautile* dives in this region of the Mid-Atlantic Ridge, were found to be composed of serpentinized peridotites.

Moving upslope, more outcrops similar to the first one were encountered, extending laterally over a few tens to 100 m and interspersed with muddy and/or rubbly areas. Local slope, estimated by determining lateral offsets by navigational methods and depths by repeatedly tagging the seafloor with the end of the drill string, appears to be on the order of 30° (Fig. 1B), an estimate consistent with submersible observations (Mével et al., 1991). The few flatter benches coincide with rubbly areas with no outcropping rock faces.

This topographic pattern changes abruptly at about 3380 mbsl, about 450 m west of the positioning beacon (Fig. 1A), where a 40 m high steep cliff is exposed, facing east-southeast, and comprising massive outcrops of slabby and schistose ultramafic rocks. A flat terrace covered by a smooth blanket of pelagic ooze is on top of that cliff, at a depth of 3340 mbsl. This terrace was surveyed in detail, and repeated tags suggested a local slope to the east of less than 15°. A second beacon was dropped at 23°20.32′N, 45°01.04′W, and Hole 920A was spudded as a pilot hole.

Lithologic Units

Drilling at Site 920, mainly in Holes 920B and 920D, provided the first substantial cores of oceanic serpentinites from a slow-spreading ridge (Fig. 2; Tables 2 and 3). These penetrated to depths greater than 126 and 200 m, respectively, with cumulative recoveries of 47.78 m (37%) in Hole 920B and 95.08 m (47.4%) in Hole 920D. The two holes are only 20 m apart and several units are present in both cores. Yet subtle to obvious differences between the cores document the scale of heterogeneity over a short lateral distance (18 m) and give a sense of the compositional and textural variations that are present in this crustal volume.

The predominant rock types recovered at Site 920 are serpentinized harzburgite, with lesser amounts of lherzolite, dunite, clinopyroxenite, and websterite along with variably altered olivine gabbro, gabbro, oxide-rich metagabbro, oxide-rich gabbronorite, oxide-rich clinopyroxenite, amphibolitized microgabbro, gneissic amphibolite, hornblendite, rodingitized gabbro, and plagioclase-olivine phyric diabase. Partially serpentinized harzburgite is the dominant rock type sampled and forms the bulk of the sections cored ("Igneous Petrology," this chapter).

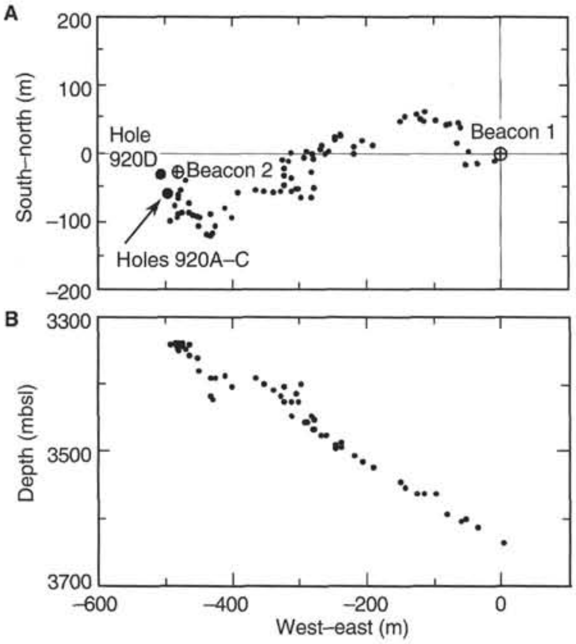

Figure 1. **A.** Map view of traverse from original Site 920 positioning Beacon 1 to Beacon 2 dropped from the VIT to locate Holes 920A–D. Holes 920 A–C: 23°20.312′N, 45°01.04′W; Hole 920D: 23°20.322′N, 45°01.044′W. Dots represent positions where bottom depth was estimated by "tagging" the seafloor with the bit and determining drill pipe length. **B.** Same tag positions as plotted in A (cross-section view, no vertical exaggeration). Average slope along traverse is ~30°.

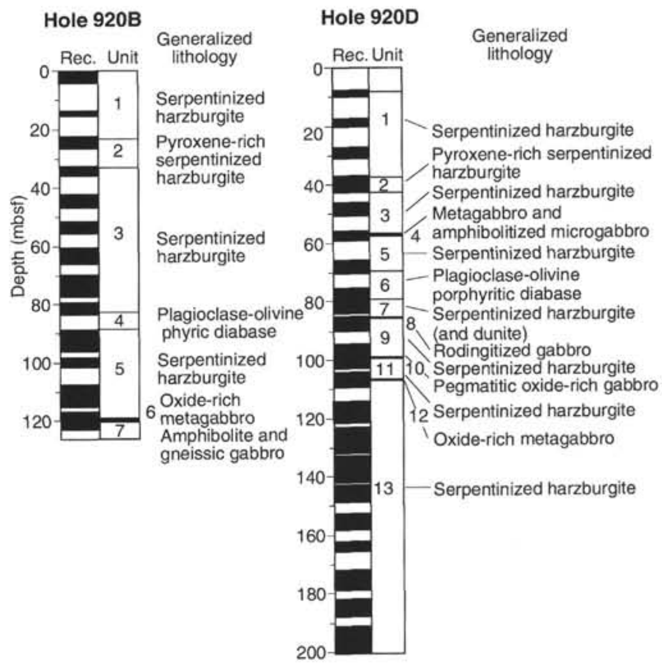

Figure 2. Core recovery (in black), plotted as the cumulative section lengths projected to the top of each core, and distribution of lithologic units, Holes 920B and 920D.

Cores were subdivided into units based on changes in the macroscopic characteristics, texture and/or composition ("Igneous Petrology" section of "Explanatory Notes," this volume). Within the ultramafic rocks, the degree of variability in texture and composition was typically subtle but generally expressed on a relatively large scale. Apart from fine-scale modal layering (centimeter scale) with sharp contacts, larger-scale modal variation occurs over distances of several meters or tens of meters and tends to be gradational. This aspect made it difficult to define significant unit boundaries on the scale of the core.

In contrast, discrete compositional changes from ultramafic to gabbroic rocks or diabase were easily recognizable during core section descriptions. New units were defined where a "significant" and "obvious" change in composition or texture was accompanied by recovery of more than 10 cm of the new lithology. This size designation is completely arbitrary. This dimension represents the general size of individual pieces of core and is generally greater than that of minor compositional bands whose contacts are both contained in a single piece and larger bands that span multiple pieces. For the latter, only minimum dimensions are known. Individual units of gabbroic and metagabbroic material recovered in the cores are all less than 0.8 m in length and therefore their actual volume tends to be over-represented in terms of numbers of units. In contrast, the larger scale, more subtle and gradational variations within peridotites are under-represented in unit designations, but well resolved by modal data gathered during visual and thin-section description of the core (see "Igneous Petrology," this chapter). Smaller magmatic veins less than 10 cm also are under-represented at the unit scale, despite their relative abundance in some intervals of the core. In some cases, their small size could be attributed to poor recovery; in others, where both vein contacts are preserved, the scale of the veins or bands is well displayed and varies in width from 1 mm to several centimeters. Despite these statistical problems, the essential character and distribution of the various serpentinized peridotite types and altered magmatic veins or other intrusives are preserved within the detailed shipboard macroscopic and thin-section descriptions. A brief overview of these data is presented in the following summary.

Hole 920A

Approximately 50 cm of polygenetic gravel was recovered from Hole 920A, consisting of angular clasts of serpentinized peridotite, serpentinite breccia, metagabbro, and minor amounts of fresh mafic volcanic glass. Serpentinite and serpentinite breccia are extensively altered and veined with serpentine, chlorite, and carbonate and iron oxide minerals. Foraminifers were also recovered from the muddy matrix. Fragments of serpentinized peridotite were recovered from below this gravel to a depth of 0.84 mbsf. These clasts comprise light green to black serpentinized harzburgite to lherzolite with reconstructed modes between 70%–93% olivine, 7%–23% orthopyroxene, 6%–10% clinopyroxene, and traces of chrome spinel. The rocks are dominantly porphyroclastic in texture, defined by orthopyroxene porphyroclasts ranging from less than 1 to 18 mm and show a weak tectonic alignment. Clinopyroxene generally forms small anhedral grains associated with orthopyroxene, whereas the olivine is highly altered and serpentinized. Disseminated yellow-brown spinel is also present in most samples. The degree of serpentinization and other alteration is 95%–100%. The recovery of cream-colored pelagic clay within the lower interval and the drilling problems suggest that this material was derived from unconsolidated talus.

Hole 920B

Drilling penetrated to 126.4 mbsf with a final cumulative core recovery of 47.78 m (39.7%). This includes 3.21 m of core recovered in the first core barrel, which was overdrilled and designated a wash core. Total recovery in cores designated as "R" cores was 44.57 m (39.7%). Rock core recovered in Hole 920B consisted of serpentinized, dominantly porphyroclastic harzburgite, lherzolite, and dunite along with variably altered pyroxenite, diabase, gabbro, metagabbro, and gneissic amphibolite. Of the material recovered, 96% is serpentinized peridotite, with protoliths ranging from dunite to lherzolite, but serpentinized harzburgite is the predominant lithology, forming 85% of the total

Table 2. Summary of lithologic units defined for Hole 920B.

Unit	Name	Cored interval From	Cored interval To	Curatorial depth to top (mbsf)	Recovered (m)
1	Pyroxene-poor serpentinized harzburgite	1R-1, 0 cm	2R-1, 100 cm	0	4.20
2	Pyroxene-rich serpentinized harzburgite	3R-1, 0 cm	3R-2, 122 cm	23.50	2.45
3	Pyroxene-poor serpentinized harzburgite	4R-1, 0 cm	9R-3, 43 cm	33.20	20.15
4	Plagioclase-olivine phyric diabase	9R-3, 51 cm	10R-1, 0 cm	83.16	1.39
5	Serpentinized harzburgite	10R-1, 7 cm	13R-3, 95 cm	89.17	18.83
6	Oxide-rich metagabbro	13R-3, 105 cm	13R-3, 134 cm	120.94	0.31
7	Amphibolite and gneissic gabbro	13R-4, 0 cm	13R-4, 72 cm	121.28	0.74

Table 3. Lithologic units, Hole 920D.

Unit	Rock type	Cored interval From	Cored interval To	Curatorial depth to top (mbsf)	Recovered (m)
1	Serpentinized harzburgite	1R-1, 0 cm	2R-1, 100 cm	8.00	7.54
2	Pyroxene-rich serpentinized harzburgite	5R-1, 82 cm	5R-4, 115 cm	37.72	3.69
3	Serpentinized harzburgite	5R-4, 115 cm	R-1, 122 cm	41.88	4.61
4	Metagabbro and amphibolitized microgabbro	7R-1, 140 cm	7R-2, 10 cm	57.60	0.37
5	Serpentinized harzburgite	7R-2, 37 cm	8R-3, 36 cm	58.04	3.86
6	Plagioclase-oliviene porphyritic diabase	8R-3, 47 cm	10R-1, 82 cm	69.27	3.27
7	Serpentinized harzburgite with dunite	10R-1, 85 cm	11R-1, 39 cm	78.95	4.86
8	Rodingitized gabbro	11R-1, 39 cm	11R-1, 72 cm	85.74	0.24
9	Serpentinized harzburgite	11R-1, 74 cm	12R-3, 74 cm	86.04	6.66
10	Pegmatitic oxide-rich gabbro	12R-3, 93 cm	12R-3, 106 cm	98.66	0.35
11	Serpentinized harzburgite	12R-4, 0 cm	13R-2, 118 cm	99.03	4.60
12	Oxide-rich metagabbro	13R-2, 126 cm		106.75	0.17
13	Serpentinized harzburgite	13R-3, 0 cm	22R-8, 0 cm	106.93	54.46

core. The remaining 4% of the rocks recovered consists of variably deformed and/or metamorphosed plagioclase- and clinopyroxene-bearing plutonic and hypabyssal rocks. The lithology and core recovery intervals are summarized in Tables 1 and 2 and shown in Figure 2.

Seven units were described in Hole 920B (Table 2). These include a pyroxene-poor serpentinized harzburgite section (Unit 1), a pyroxene-rich serpentinized harzburgite (Unit 2; Fig. 3), a second pyroxene-poor serpentinized harzburgite (Unit 3), a slightly altered diabase intrusion (Unit 4) with a chilled contact zone (Fig. 4), another unit of serpentinized harzburgite (Unit 5), a thin and relatively undeformed oxide-rich metagabbro unit with well preserved igneous textures that was marked at its base by a porphyroclastic mylonite (Unit 6), and a strongly deformed and recrystallized unit consisting of two rock types in subvertical contact, a fine-grained amphibolite and a coarser-grained gneissic gabbro (Unit 7). Although the amphibolite and gneissic gabbro of Unit 7 lithologies share a near-vertical tectonic contact that runs along the length of the core (Fig. 5), they were designated as part of the same unit because they appear to share the same high-temperature tectonite fabrics.

Contacts were not recovered between any of the units described above. The diabase (Unit 4), however, is assumed to have intruded the harzburgite because a chilled margin (Fig. 4) was recovered adjacent to the overlying serpentinized harzburgite of Unit 3. The contact between the igneous-textured metagabbro of Unit 6 and the gneissic rocks of Unit 7 is tectonic because a porphyroclastic mylonite (see "Metamorphic Petrology" section) with a high-temperature foliation was recovered at the base of Unit 6. Rocks from each of these units have experienced somewhat different structural and metamorphic histories and may therefore have been tectonically juxtaposed along the mylonitic shear zone or by later faulting.

Hole 920D

Drilling penetrated to a depth of 200.8 mbsf in Hole 920D with a total cumulative core recovery of 95.08 m (47.4%). The core consists of the following lithologies: serpentinized harzburgite, lherzolite, and dunite, with minor amounts of rodingitized gabbro, amphibolitized microgabbro, oxide-rich metagabbro, oxide-rich clinopyroxenite, oxide-rich gabbronorite, feldspathic clinopyroxenite, hornblendite, and porphyritic diabase. Of the material recovered, 95% is serpentinized peridotite, with protoliths ranging from dunite to lherzolite, but harzburgite is the predominant lithology, forming 83% of the total recovery. The remaining 5% of the rocks recovered consists of variably deformed and metamorphosed plagioclase- and clinopyroxene-bearing plutonic and finer grained hypabyssal rocks. Thirteen units were identified in Hole 920D. Below they are listed in order, from the top to the base of the core (Table 3).

Unit 1 is a pyroxene-poor serpentinized harzburgite. It has a gradational contact with underlying Unit 2, a pyroxene-rich serpentinized harzburgite. Unit 3 is a pyroxene-poor serpentinized harzburgite similar to Unit 1.

Below Unit 3, the peridotite sequence is locally intruded by magmatic veins and intrusive plutonic rocks up to several centimeters, and rarely a few tens of centimeters, wide. These minor intrusions are both concordant and discordant with respect to the high-temperature crystal-plastic fabric. The largest of these intrusions have been designated as separate units. Unit 4 is the first of these magmatic units and includes two lithologies, a metagabbro, and an amphibolitized microgabbro without tectonic fabrics. The total recovered length of this unit is 37 cm, including three separate pieces. Note that recovery for this section of core was only 25%.

Unit 5 is another pyroxene-depleted serpentinized harzburgite similar to Unit 3, but with common altered pyroxenite veins. Unit 5 is in contact, at its base, with 3.3 m of moderately plagioclase-olivine porphyritic diabase, defined as Unit 6. It is petrographically similar to Unit 4 in Hole 920B. Unit 7 consists predominantly of serpentinized harzburgite, but also includes a few thin zones of serpentinized dunite and gabbroic veins. A 24-cm-long interval of rodingitized gabbro, consisting of seven pieces, is defined as Unit 8 (Fig. 6). Although Unit 9 is also predominantly serpentinized harzburgite, the unit has a larger range in total pyroxene contents than elsewhere in the core. The modal variation appears locally to be cyclic, occurring on a scale of meters. Unit 10 is a 24-cm-long interval of pegmatitic, oxide-rich metagabbro (Fig. 7). It is underlain by a serpentinized harzburgite, Unit 11, that is similar to Unit 7. Unit 12 is very coarse-grained oxide-rich metagabbro grading to pyroxenite (Fig. 8) recovered as one 16.5-cm-long piece. The remaining 94 m of Hole 920D are designated as Unit 13 and consist of a sequence of serpentinized peridotites that appear to vary cyclically between pyroxene-rich harzburgite, nearly lherzolite, to pyroxene-poor harzburgite and dunite. In general, Unit 13 is cut by small (millimeter size) to relatively large (centimeter size) pyroxenitic to gabbroic veins (Fig. 9) that are abundant in some intervals (e.g., ~153–155 mbsf).

Top and bottom contacts were recovered in two locations in the hole. The first is between the rodingitized gabbro (Unit 8) and serpentinized dunite of Units 7 and 9 (Fig. 6). The second occurs between the oxide-rich metagabbro of Unit 12 (Fig. 8) and the serpentinized harzburgite of Units 11 and 13. Partial contacts were also recovered between smaller gabbroic or pyroxenitic intervals that are too small to describe as individual units (Fig. 9), especially in Unit 13 (Fig. 10). These contact relationships will be described in detail in a subsequent section ("Igneous Petrology," this chapter).

As in Hole 920B, plagioclase-olivine phyric diabase (Unit 6) of Hole 920D is interpreted as having intruded the harzburgite because finer grained margins, attributed to chilling, were recovered adjacent to serpentinized harzburgite (Fig. 11).

IGNEOUS PETROLOGY

The predominant rock types recovered from Site 920 are serpentinized harzburgite, with lesser amounts of lherzolite, dunite, clinopyroxenite, and websterite along with variably altered olivine gabbro, gabbro, oxide-rich metagabbro, oxide-rich gabbronorite, oxide-rich clinopyroxenite, amphibolitized microgabbro, amphibolite, hornblendite, rodingitized gabbro, and plagioclase-olivine phyric diabase. Partially serpentinized harzburgite is the dominant rock type sampled and forms the bulk of the sections cored (see modal abundances section below). Harzburgites are believed to have experienced polybaric pressure-release melting and simultaneous deformation within a mantle melting column beneath the ridge axis prior to their exposure on the seafloor. The features in these cores contain information about the generation, segregation, and transport of magma in the subaxial mantle. This section reports on the results of macroscopic and petrographic descriptions, and of geochemical analysis of cores from Holes 920B and 920D. These holes provide the most complete record of the lithologic, petrologic, and textural variations within serpentinized ultramafics on a slow-spreading ridge.

All of the features observed in the peridotites from Hole 920A are observed in those from Holes 920B and 920D. Because the latter two holes provided significantly better recovery, they will form the basis of the detailed summary and discussion that follow. The petrological and geochemical descriptions and presentation of data from cores of Holes 920B and 920D are divided into three parts. The first section describes residual ultramafic tectonites; the second part describes subordinate intrusive rocks within the ultramafic sections; the third part addresses the geochemistry of the samples recovered. More detailed discussion of petrographic observations related to metamorphism and structural features can be found in the "Metamorphic Petrology" and "Structural Geology" sections of this chapter. In this section, the focus is on observations relating to determination of the primary lithology, mineralogy, textures, and geochemistry of these rocks.

Ultramafic Rocks

Ultramafic rocks were recovered in Units 1, 2, 3, and 5 in Hole 920B and in Units 1, 2, 3, 5, 7, 9, 11, and 13 in Hole 920D. These units are similar in most respects in that they were defined, with the exception of Unit 2 in both Holes 920B and 920D, on the basis of a succession of small pyroxenitic or gabbroic intrusives rather than the internal

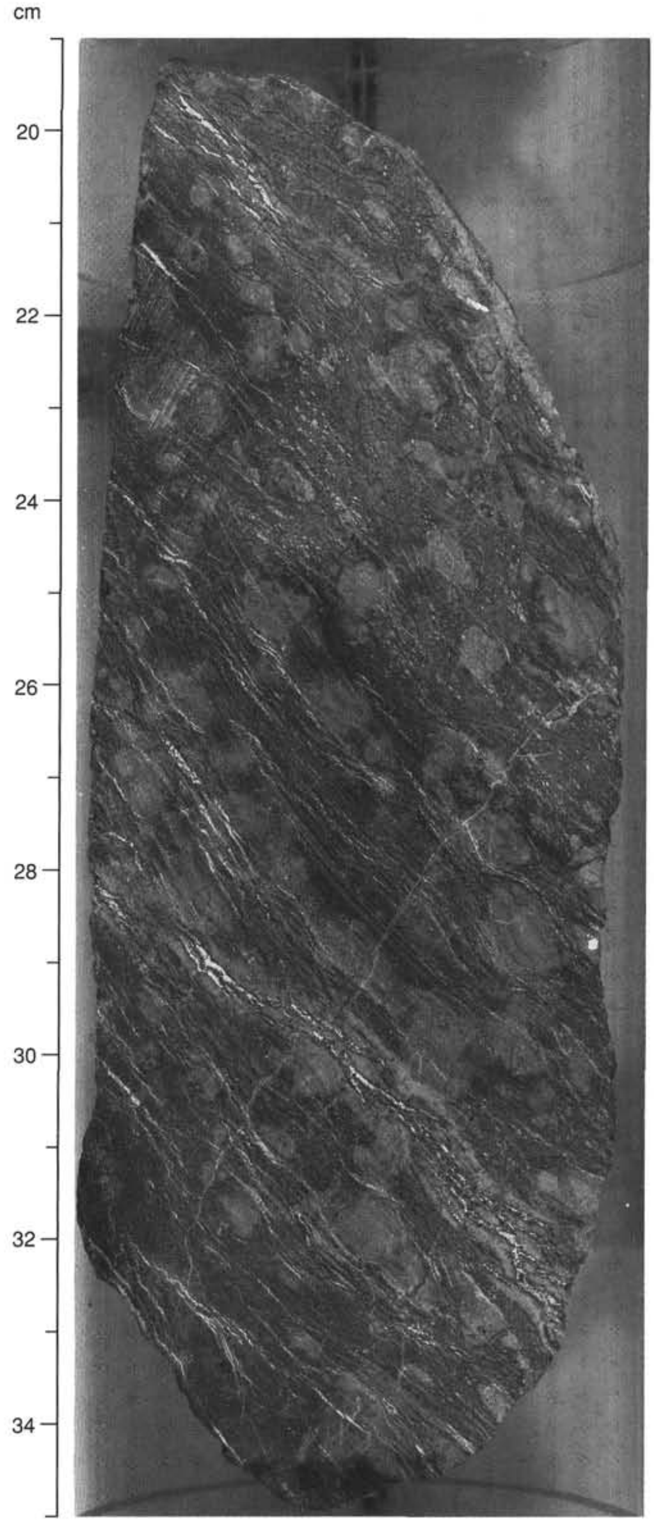

Figure 3. Typical serpentinized harzburgite with large, weakly elongated orthopyroxene porphyroclasts in a matrix of serpentinized olivine. Serpentinization in this sample is over 90%. Thin veins of serpentine and magnetite produce a prominent foliation. Unit 2, Hole 920B (Sample 153-920B-3R-1, 19–35 cm).

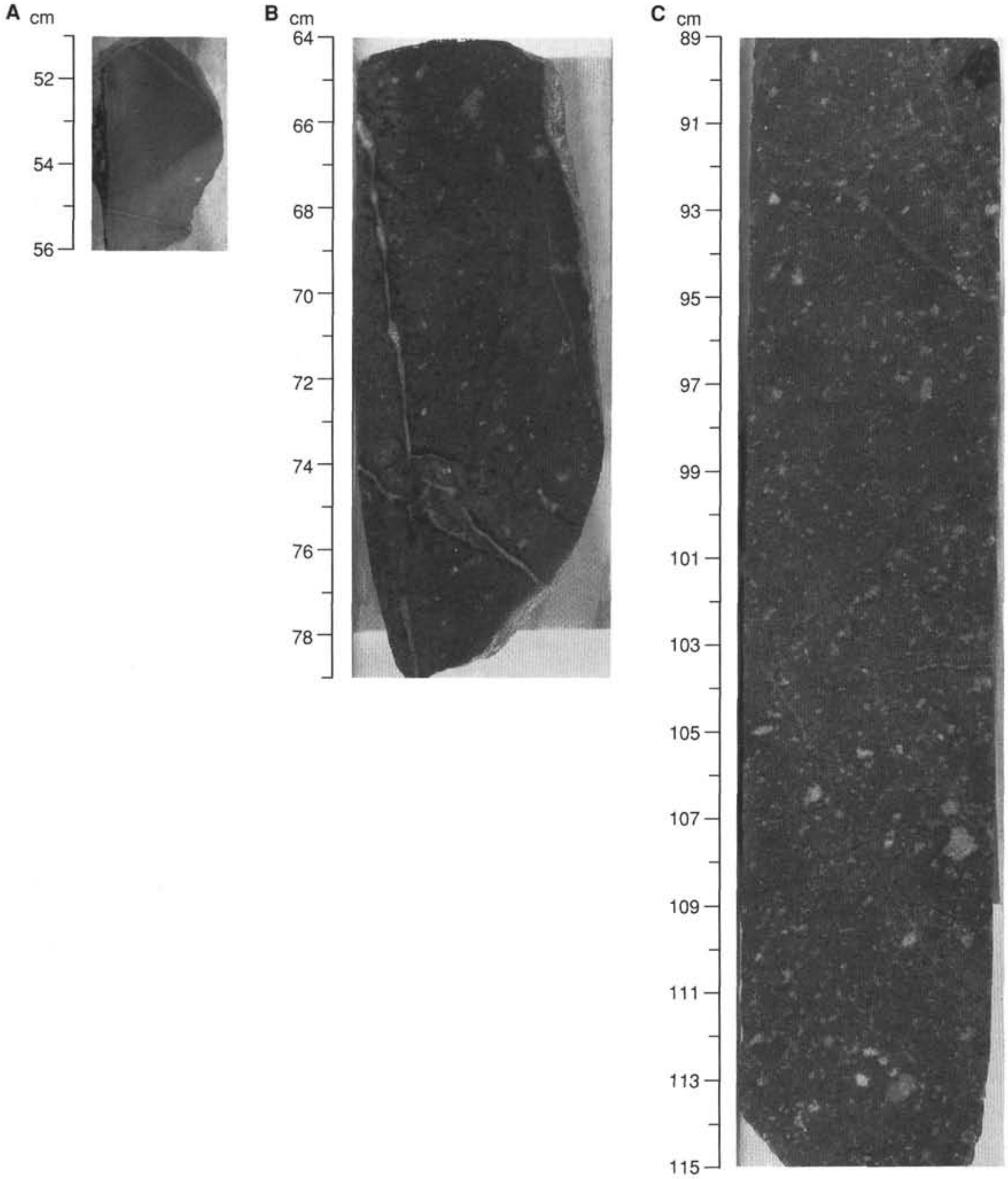

Figure 4. Sequence of samples showing a progressive reduction in grain size of diabase (Unit 4, Hole 920B) toward a chilled margin with harzburgite (not shown, Unit 3); the sequence is interpreted as indicating the intrusive nature of the contact. The contact was not recovered. **A.** Sample 153-920B-9R-3, 51–56 cm. **B.** Sample 153-920B-9R-3, 64–79 cm. **C.** Sample 153-920B-9R-3, 89–115 cm.

characteristics of the harzburgite. Unit 2, as defined from core recovered from Holes 920B and 920D, was described as a pyroxene-rich harzburgite on the basis of a marked increase in modal pyroxene (Fig. 2).

Modal Mineralogy

The most striking feature of these ultramafic rocks is that the primary mineralogy, which consists of olivine, orthopyroxene, clinopyroxene, and spinel, is now moderately to pervasively serpentinized or altered to a varying extent, generally from 50% to 100%, but averaging about 90% ("Metamorphic Petrology," this chapter). There are widely distributed zones of lower alteration downhole that appear to correlate with clinopyroxene-rich zones.

In general, pyroxene-rich and pyroxene-poor peridotites have distinctly different macroscopic appearances. In pyroxene-poor peridotites, the serpentine matrix is dark gray to black (Fig. 12A), homogeneous in appearance, and anastomosing veins sets are not abundant; thin, white, serpentine veinlets are discontinuous, fewer in number, and generally have a somewhat random orientation. Pyroxene-rich peridotites typically are characterized by abundant anastomosing vein sets that tend to be more continuous and define a more planar fabric element. Serpentine mesh textures after olivine are commonly preserved and are enhanced by a pale gray-green patchy bleaching that occurs where the cores of the mesh structures are large and have a paler green color than the crossing serpentine fibers. A fine dusting of magnetite, produced during serpentinization, is concentrated along

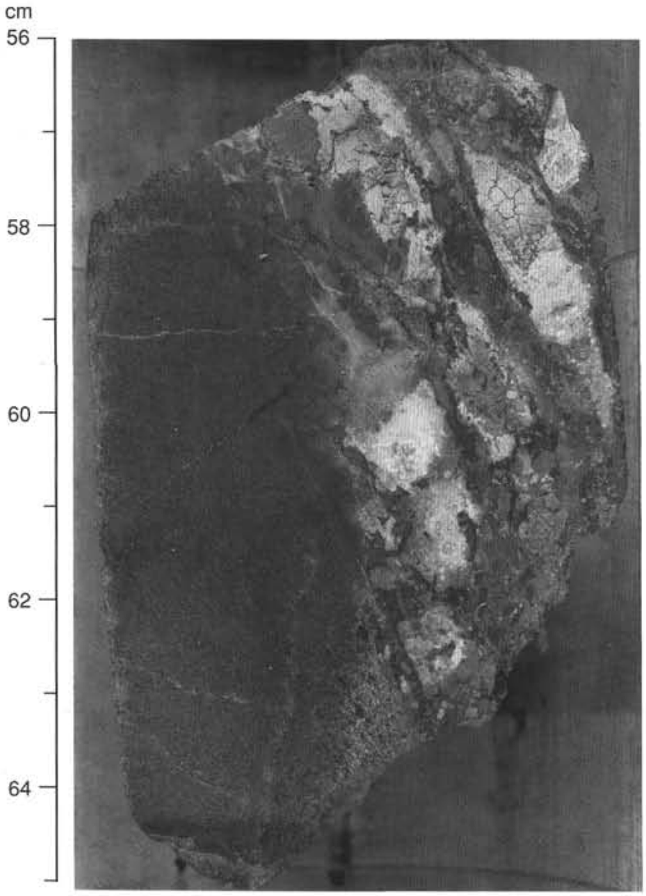

Figure 5. Contact between amphibolite and gneissic gabbro recovered from Hole 920B, Unit 7. Sample 153-920B-13R-4 (Piece 7, 56–65 cm). The contact is subparallel to the foliation both in the gabbro gneiss and amphibolite. Greenschist facies mineral assemblages in the gneissic gabbro are moderately abundant with only trace brown hornblende, whereas high temperature amphibolite facies mineral assemblages are abundant in amphibolites that lack retrograde minerals.

olivine kernel boundaries. Larger scale continuous veins filled with cross-fibered chrysotile or asbestiform serpentine commonly cut across the mesh textured serpentine.

A total of 150 thin sections of the various rock types examined in Holes 920B and 920D were prepared and used to characterize the modal abundances of phases present in rocks and to estimate the abundances of primary phases present prior to hydrothermal alteration of these rocks. The majority of thin sections were cut from the serpentinized harzburgites, dunites, and lherzolites (107 samples), which are the dominant lithology recovered at Site 920. Other lithologies were also sampled for thin-section studies (see below). Fifty-two of the samples chosen for thin sections were also analyzed by XRF for major and trace elements. Overall, in spite of the generally high level of serpentinization and alteration of olivine and/or pyroxenes in these ultramafic rocks, the original primary mineralogy, as well as textural relations, is partially preserved in most samples.

In thin section, olivine occurs as small (generally less than 0.1–1 mm) grains consisting of subangular to subrounded kernels separated by anastomosing serpentine veinlets. Where serpentinization is complete a polygonal mesh texture with structureless serpentine cores commonly is crosscut by extensional cross-fibered composite chrysotile-magnetite or chlorite veins. By observing clusters of olivine that are optically continuous and have similar optical interference colors, it is possible to reconstruct original (i.e., pre-serpentinization) grain sizes in thin sections. More subtle intracrystalline structures (e.g.,

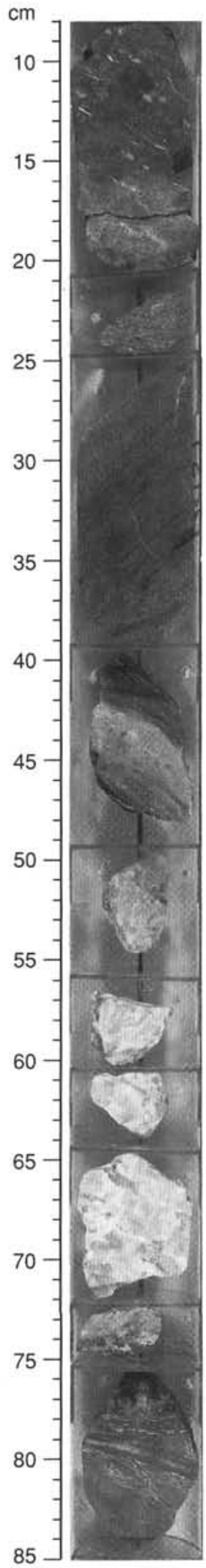

Figure 6. Rodingitized gabbro of Unit 8, Hole 920D (Sample 153-920D-11R-1, 8–85 cm). Notice that the peridotite above and below the gabbro are pyroxene-poor, with dunite occurring immediately adjacent to the gabbro and pyroxene abundance in harzburgite increasing progressively away from the gabbro.

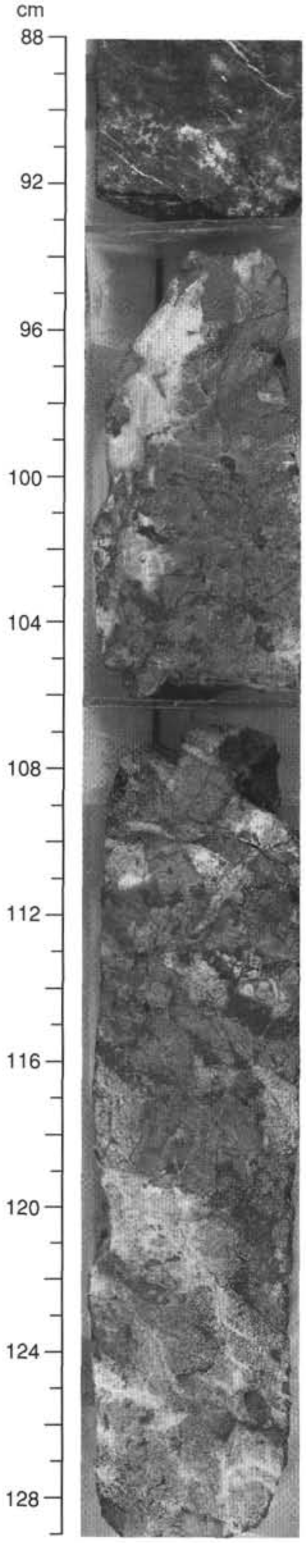

Figure 7. Sample 153-920D-12R-3, 88–129 cm, showing adjacent pieces at the contact between oxide gabbro (Unit 10) and depleted harzburgite (Unit 9). The gabbro grades from coarse clinopyroxenite at the contact into a coarse-grained, hypidiomorphic granular aggregate of clinopyroxene with interstitial iron-oxide minerals, plagioclase and sulfide minerals. Plagioclase is replaced by prehnite and clinopyroxene partially altered to amphibole. An increase in the density of prehnite veining and in the pegmatitic grain size between 120 and 129 cm suggests that this is close to the bottom margin of the gabbroic dike.

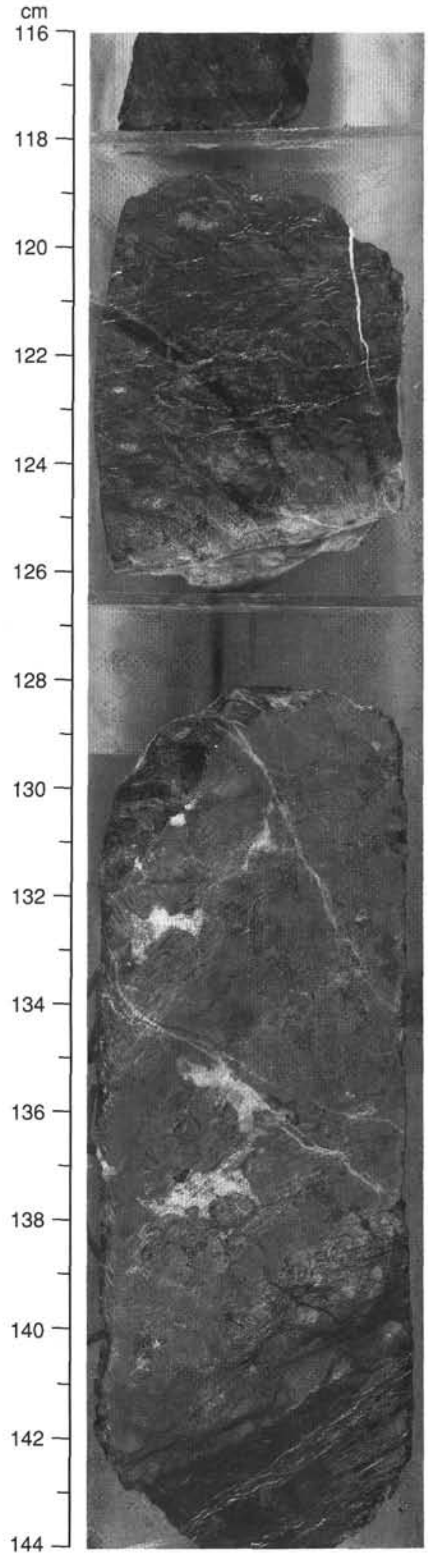

Figure 8. Sample 153-920D-13R-2, 116–144 cm (Unit 12), showing upper and lower contacts between pegmatitic pyroxenite and very depleted harzburgite. The upper contact is sharp and the lower diffuse; both preserve fresh olivine relicts and secondary clinopyroxene within a 1- to 2-cm-wide band in the adjacent harzburgite. The pyroxenite contains interstitial feldspar, now altered to prehnite and is crosscut by thin prehnite veinlets. Sulfide minerals are present along the upper contact.

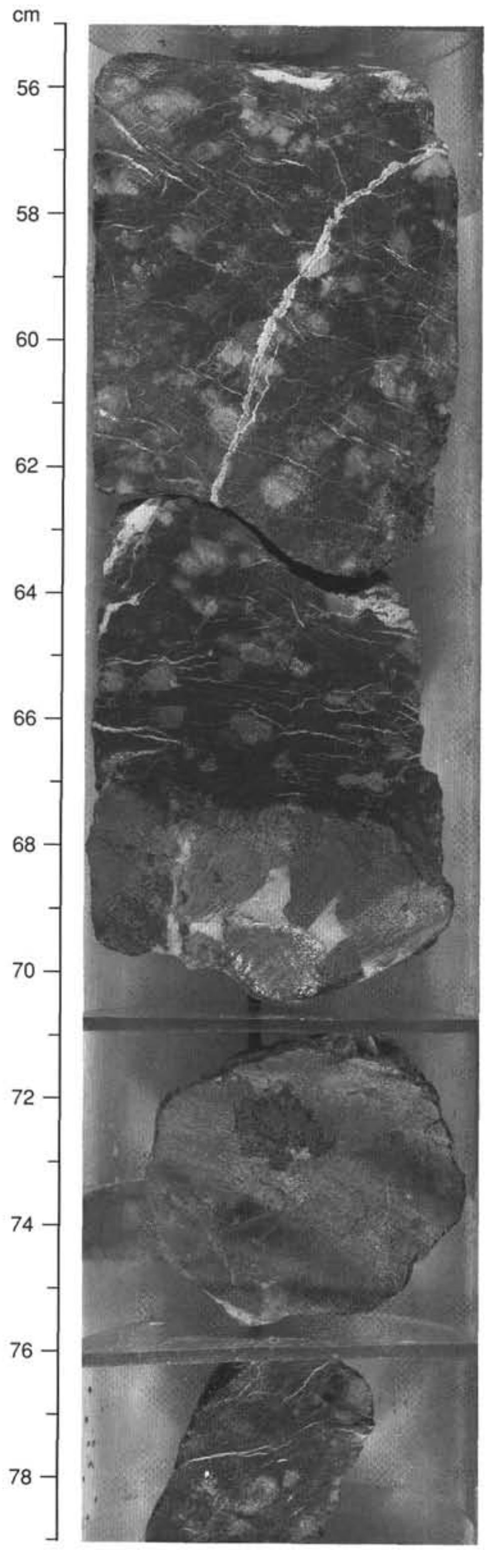

Figure 9. Sample 153-920D-13R-1, 55–79 cm (Unit 13), showing a contact between a pegmatitic gabbro and depleted harzburgite. Clinopyroxene at the margin shows a comb texture, defined by clinopyroxene crystals extending inward from the dike wall. Plagioclase, now altered to prehnite, is interstitial. The lower contact between gabbro and harzburgite was not recovered. The harzburgite shows a progressive increase in modal pyroxene away from the gabbro dike.

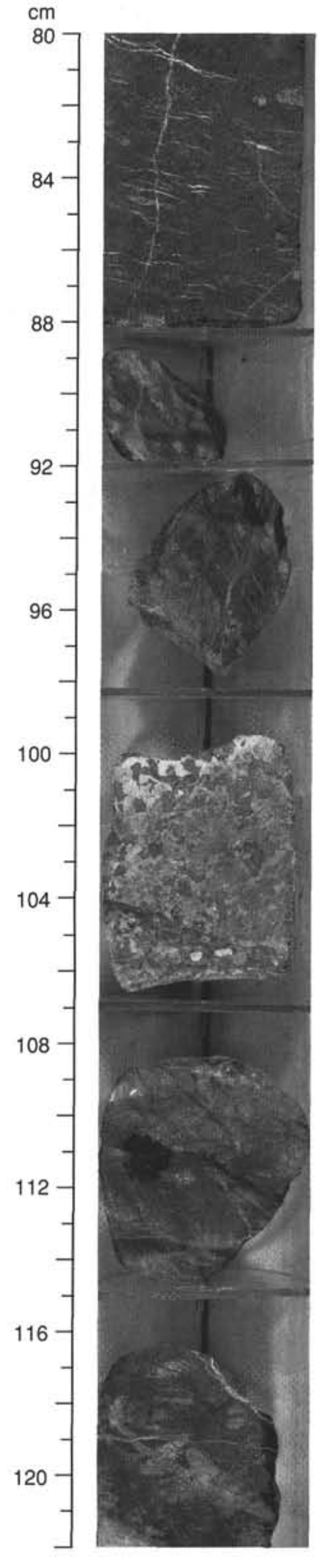

Figure 10. Sample 153-920D-18R-2, 80–122 cm (Unit 13), showing the contact relationship between coarse-grained gabbro and depleted harzburgite. Both upper and lower contacts are preserved as thin faces on the harzburgite pieces and are rimmed by selvages of fresh olivine and clinopyroxene in the serpentinized peridotite. The serpentinized harzburgite shows a progressive depletion in pyroxene toward the gabbro. Note the thin oxide mineral-rich layer within the gabbro (105–106 cm).

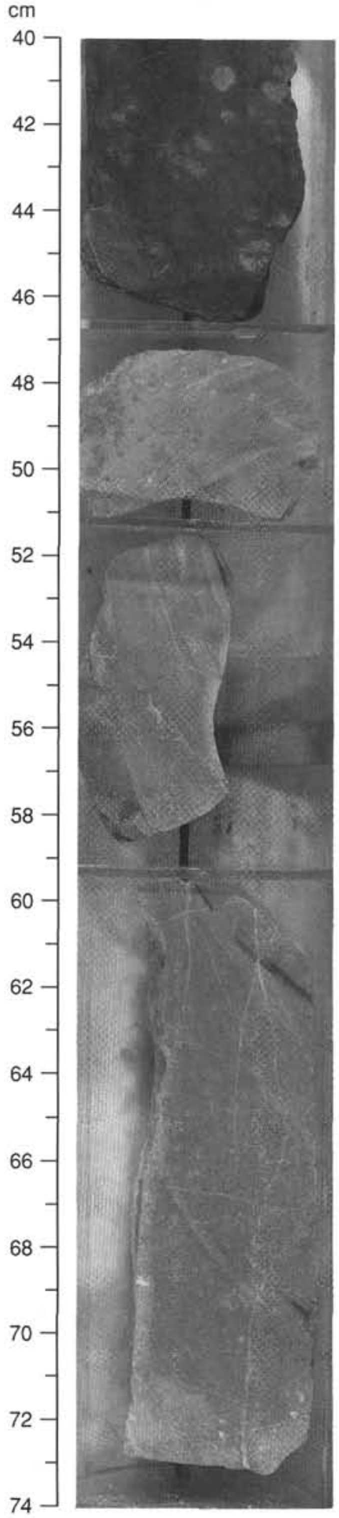

Figure 11. Sample 153-920D-8R-3, 40–74 cm, showing the upper margin of the diabase (Unit 6) in Hole 920D. There is a progressive reduction in grain size of the groundmass toward the margin. The rocks are sparsely phyric throughout the section shown, but become progressively more coarse-grained and moderately porphyritic downhole. Dark patches in the piece closest to the contact are part of an alteration halo around a small fracture on the edge of the piece. Adjacent harzburgite (Unit 5) is pyroxene-poor and shows weak crystal-plastic fabric development.

kink bands) within larger olivine grains that are now isolated in the serpentine network can also commonly be deduced using optical continuity relationships. In contrast, definition of the original grain size of olivine in hand sample was not possible because of the highly altered states of the peridotites and the pervasive vein-like and grain-dissecting nature of serpentine alteration of olivine.

Orthopyroxene is commonly replaced by bastite pseudomorphs, but the outer rims of orthopyroxene are commonly replaced by talc or fibrous chrysotile. Clinopyroxene is replaced by serpentine, tremolite-actinolite, and brown amphibole in some sections of the core, although clinopyroxene tends to be the least altered where present (see "Geochemistry" and "Metamorphic Petrology," this chapter). Chrome-spinel is generally well preserved, although black rims of ferrit-chromite or overgrowths of secondary magnetite (formed during serpentinization) are observed in many samples. Thus, in general, serpentine after olivine can be readily distinguished from the bastite pseudomorphs that replace pyroxenes so that original olivine modes could be estimated. Orthopyroxene and clinopyroxene could be distinguished from one another in most sections from relict unaltered cores of grains. Distinguishing between totally replaced orthopyroxene and clinopyroxene, however, is difficult, leading to uncertainties in the proportions of clinopyroxene to orthopyroxene for highly altered samples. For this reason, the total pyroxene content was found to be a better discriminator of modal variations in hand specimen than the clinopyroxene or orthopyroxene modal content. In areas of total alteration where relict cores are not present, alteration minerals that include mesh-textured serpentine and magnetite were assigned to olivine. Bastite pseudomorphs and any associated talc were assigned to orthopyroxene. Characteristic orthopyroxene intracrystalline structures such as kink bands as well as elongate shapes are commonly preserved in pseudomorphous grains, helping to distinguish altered orthopyroxene. Tremolite-actinolite and brown amphibole were assigned to clinopyroxene.

Although there is a wide range of alteration intensities in any interval, the least altered ultramafic sections (sample alteration as low as 20% to 60%) occur in three parts of the core: (1) at the very top of Hole 920D (8–20 mbsf), (2) in the middle of both holes at depths of 85–140 mbsf in Hole 920D and 50–85 mbsf in Hole 920B, and (3) toward the base of each hole below 110 m in Hole 920B and below 180 m in Hole 920D (see "Metamorphic Petrology").

The olivine matrix is typically pervasively altered to serpentine + magnetite (60%–100%, average is 90%). Within individual samples the normal order of replacement is olivine, orthopyroxene, clinopyroxene, and spinel. Because olivine forms the greatest proportion of the peridotites and appears to be most easily altered, there is an expected tendency for samples with the highest modal proportion of olivine to be more highly serpentinized. This also reflects the tendency for pyroxene to be less altered (average 30% for clinopyroxene and 60% for orthopyroxene; Table 4). In fact, the lowest extents of alteration, as deduced from the macroscopic and microscopic inspection of the core, from the H_2O content of geochemical samples (see "Geochemistry," this chapter), and from the serpentine-related magnetite volume as estimated from magnetic susceptibility and IRM measurements (see "Paleomagnetism," this chapter), occur in regions of the core that have high modal clinopyroxene content.

Modal variation was observed with depth on the scale of centimeters to larger scales ranging from meters to tens of meters. Figures 12A, 12B, and 12C illustrate the variation in modal abundance from pyroxene-bearing (1%–2%) dunite, to depleted harzburgite to pyroxene-rich harzburgite encountered in each hole. On the scale of centimeters there is variation in modal abundance caused by fine-scale modal layering (Fig. 12D) defined by sharp increases or decreases in pyroxene content. There is also significant variation in modal mineralogy that is more gradational, occurring on the scale of a few meters to tens of meters. This gradational variation is presented here as the downhole variation in modal olivine and total pyroxene based on the visual description logs for individual core pieces for Holes 920B and

Table 4. Summary of modes, grain sizes, and total alteration estimated from thin sections for olivine-bearing ultramafic rocks from Holes 920B and 920D.

	Modal data (%)				Grain-size data (mm)						
					Olivine		OPX		CPX		Total alteration
	Olivine	OPX	CPX	Spinel	Max.	Min.	Max.	Min.	Max.	Min.	(%)
Hole 920B											
Average:	80.50	17.60	2.50	1.10	2.23	0.27	7.37	1.32	2.07	0.51	89.80
1 s.d.:	7.80	7.70	1.70	0.90	1.60	0.30	3.20	1.10	1.60	0.90	13.90
Max.:	99.00	35.00	8.00	6.00	8.50	1.00	16.00	5.00	7.00	4.00	98.00
Min.:	65.00	0.90	0.00	0.20	1.00	0.02	1.20	0.08	0.01	27.00	72.00
Hole 920D											
Average:	83.20	14.60	2.20	1.10	2.55	0.50	7.23	0.67	1.91	0.33	85.00
1 s.d.:	6.50	5.90	1.50	0.70	1.40	0.90	3.40	0.50	1.20	0.30	16.40
Max.:	95.00	35.00	6.00	5.00	6.00	5.00	20.00	2.00	5.00	1.00	100.00
Min.:	60.00	4.00	0.00	0.50	0.04	0.04	2.60	0.04	0.10	0.04	17.50

Note: OPX = orthopyroxene, CPX = clinopyroxene, Max. = maximum, Min. = minimum, s.d. = standard deviation.

920D (Fig. 13). An example of variation on the scale of meters can be seen in the Unit 9 portion of Core 153-920D-12R, where the modal proportion of olivine varies from 80% to more than 90% over approximately 1 m, then decreases to about 70% over the next meter before returning to a value near 80%.

This type of cyclic variation is not equally well recorded throughout the core for two reasons. First, it requires that core recovery be sufficient to obtain enough of the section to observe the variation. With a core recovery of only 10%–20%, this type of variation might not be observable in a consistent way. Second, it requires that an estimate of modes be made over a sufficiently short length scale in the section to identify these trends, the latter being limited by the time available for core descriptions. Below 60 mbsf in Hole 920D, where the core recovery was high, the large-scale modal variations are particularly well displayed by variations in estimated modal pyroxene and olivine. Even where the recovery was more limited in the shallower parts of Hole 920D and in Hole 920B this large-scale cyclic modal variation is apparent.

Point-counting modal estimates for a limited number of samples were conducted on one to two standard-size thin sections or one oversized thin section, in order to "calibrate" the visual estimates. However, reconstructed modes of such extensively altered rocks must be viewed with some caution and the accuracy of standard-size thin-section visual estimates on very coarse-grained rocks is considered problematical. The modal abundance of clinopyroxene in these rocks is also ultimately uncertain because of the extent of alteration and the low modal abundances exhibited even in the least altered samples, and because of the difficulty of distinguishing completely altered orthopyroxene from altered clinopyroxene. In addition, no attempt has been made to adjust the estimated modal composition for the volume expansion that almost certainly occurred in the rock as a consequence of serpentinization. The volume may increase to 30% for serpentinized olivine and orthopyroxene (Komor et al., 1985). Thus, the reconstructed modal estimates probably overestimate serpentinized olivine and pyroxene abundances and underestimate those of unaltered pyroxene. However, the magnitudes of the corrections await shore-based studies on modal mineralogy, mineral chemistry, and bulk-rock chemistry and will help constrain the magnitude of adequate volume corrections. The lack of correction in the modal estimates presented here also allows direct general comparisons with extensive modal data sets from abyssal peridotites that were also reported without corrections for volume increases caused by serpentinization (e.g., Dick, 1989; Michael and Bonatti, 1985). Nevertheless, the thin-section estimates generally correlate with visual core descriptions and shipboard bulk-rock geochemistry data. A thin section was examined for each sample chosen for XRF analysis so that results could be correlated.

In the 107 olivine-bearing ultramafic samples (excluding pyroxenites) selected for thin-section studies, orthopyroxene is clearly the most abundant pyroxene, with modal abundances ranging from ~1% to 35%, with the typical range between 10% and 25% and a mean of 17.6% for Hole 920B and 14.6% for Hole 920D (Table 4). Clinopyroxene modes range from ~0% to 9% and the mean clinopyroxene mode was estimated at 2.5% for Hole 920B and 2.2% for Hole 920D. Histograms showing the estimated abundances of primary mineral phases are shown in Figure 14 for Holes 920B and 920D.

The ultramafic units recovered at Site 920 have been labeled serpentinized harzburgite units because this rock type represents the dominant lithology. This is reflected in the low estimated clinopyroxene modes for most of the samples. However, a small number of samples within these units were originally lherzolitic in composition prior to serpentinization. These sections are from regions of Hole 920B between 100 and 120 mbsf and of Hole 920D between 100 and 140 mbsf. Several thin-section samples from Holes 920B and 920D are classified as dunites although they generally contain ~1% to 9% total pyroxene, usually orthopyroxene with or without minor clinopyroxene.

Yellowish to reddish brown chrome-spinel (Fig. 15) is present in all peridotite samples, with modal abundances of 0.2% to ~2%. Exceptionally, the modal abundance of spinel reaches ~5%, although this is only observed in some dunitic samples (Samples 153-920B-12R-2, 139–144 cm, 153-920D-7R-1, 67–70 cm, and 153-920D-11R-1, 27–30 cm) and in one harzburgite sample (Sample 153-920B-12R-1, 117–121 cm). Spinel grain sizes range from 0.1 to ~2 mm.

The interrelationship between modal olivine, orthopyroxene, clinopyroxene, and spinel for thin sections studied for Holes 920B and 920D is depicted in Figure 16, which shows the wide range of compositions encountered. This figure includes the mafic (diabasic and gabbroic) and pyroxenite intrusives into the ultramafics. In harzburgites, dunites, and lherzolites, the same modal variations seen in the macroscopic core descriptions are apparent. Sampling for thin sections downhole in Hole 920B was more closely spaced than in Hole 920D, and there appear to be more systematic variations evident at these finer sampling intervals. Based on macroscopic core description, the average modal proportions of the major silicate phases in the residual ultramafic rocks recovered (excluding the pyroxenites) is olivine = 84%, orthopyroxene = 14%, and clinopyroxene = 2%. The modal proportions are similar for both Holes 920B and 920D, so the data from the two have been combined to arrive at this average. In general, the modal averages and ranges determined by the visual core description and thin-section studies (Table 4) form internally consistent data sets.

In summary, visual estimates of modal proportions of core material as well as thin section modal estimates suggest that a range of ultramafic compositions has been recovered. These compositions include, in order of abundance: harzburgite, dunite, and lherzolite with minor occurrences of pyroxenite and websterite. The harzburgitic, dunitic, and lherzolitic rocks are generally believed to be residual

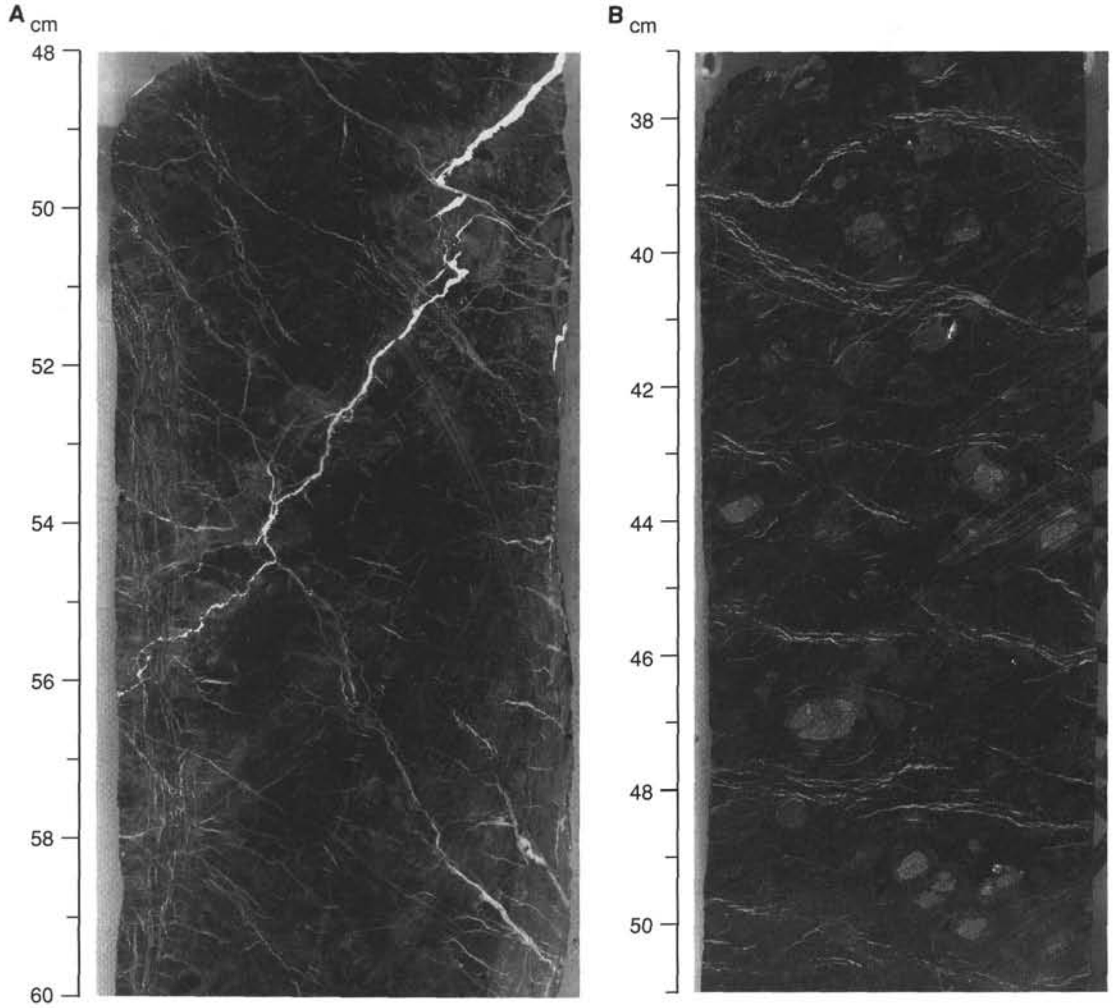

Figure 12. Representative range of modal variation and textural relationships of peridotite from Site 920 drill holes. **A.** Orthopyroxene-bearing dunite. White serpentine veinlets are short, discontinuous, and few in number. Olivine is almost completely altered to dark serpentine mesh texture having a homogeneous color and appearance. Sample 153-920B-1W-1, 48–60 cm. **B.** Pyroxene-poor harzburgite with weakly developed crystal plastic-fabric. Matrix olivine is altered to mesh-textured serpentine that appears dark and homogeneous except in dark-gray shadows marginal to pale-gray and fresh orthopyroxene porphyroclasts. Thin white serpentine veins are discontinuous, few in number, and localized into subparallel bands through the piece. Sample 153-920D-4R-2, 37–51 cm. **C.** Pyroxene-rich harzburgite in which the high-temperature crystal plastic-fabric is defined by elongation of orthopyroxene porphyroclasts. Thin discontinuous, anastomosing white serpentine veinlets wrap around these porphyroclasts; a late serpentine veinlet cuts the fabric. Sample 153-920B-3R-1, 80–95 cm. **D.** Sample 153-920B-1W-2, 130–140 cm, showing layering of pyroxene-rich and pyroxene-poor harzburgite on a centimeter scale. Thin, white discontinuous serpentine veins are both subparallel and oblique to the layering. The density of white anastomosing serpentine veins increases in pyroxene-rich layer. Anastomosing white serpentine vein sets commonly, but not always, mimic the orientation of the high-temperature elongated orthopyroxene foliation.

in origin. Dunites are typically orthopyroxene-bearing and therefore probably also of residual origin.

Textural Relationships and Grain-size Variation

Maximum and minimum grain sizes of the major minerals in the peridotites of Holes 920B and 920D were measured during visual core and thin-section descriptions. From thin sections, measurements were made using a micrometer ocular; the results for the 107 samples from Holes 920B and 920D are summarized in Table 4 and shown in histogram form in Figure 17. Because of the extreme level of alteration, grain sizes of olivine could not be estimated in hand samples. Figure 18 shows orthopyroxene and olivine maximum and minimum grain-size populations with depth, incorporating thin-section data and macroscopic core description.

Figure 17 shows the bimodal nature of the grain sizes in most ultramafics. This bimodal grain size distribution is caused by grain size reduction of olivine, orthopyroxene, and clinopyroxene resulting from high-temperature plastic flow and dynamic recrystallization (see "Structural Geology," this chapter). In general, the textures observed in the primary assemblages are inequigranular and coarse-grained as depicted in Figure 17. An example of this common texture is shown in Figure 19. Orthopyroxene generally exhibits the largest grain sizes (maximum = 20 mm) and forms porphyroclasts that are believed to reflect more closely the coarse, equigranular textures and grain sizes prior to the dynamic recrystallization that led to formation of the surrounding finer grained matrix. Clinopyroxene grains are also observed as remnant porphyroclasts; they usually have smaller grain sizes (2–6 mm). The matrix surrounding porphyroclasts consists of finer grained recrystallized olivine, orthopyroxene, and clinopyroxene showing a range of grain sizes typically between 0.1 and ~ 4 mm.

Coarse-grained equigranular textures, devoid of finer grained matrix material and sub-mylonitic porphyroclastic textures with highly recrystallized fine-grained matrices are also locally present. The coarse

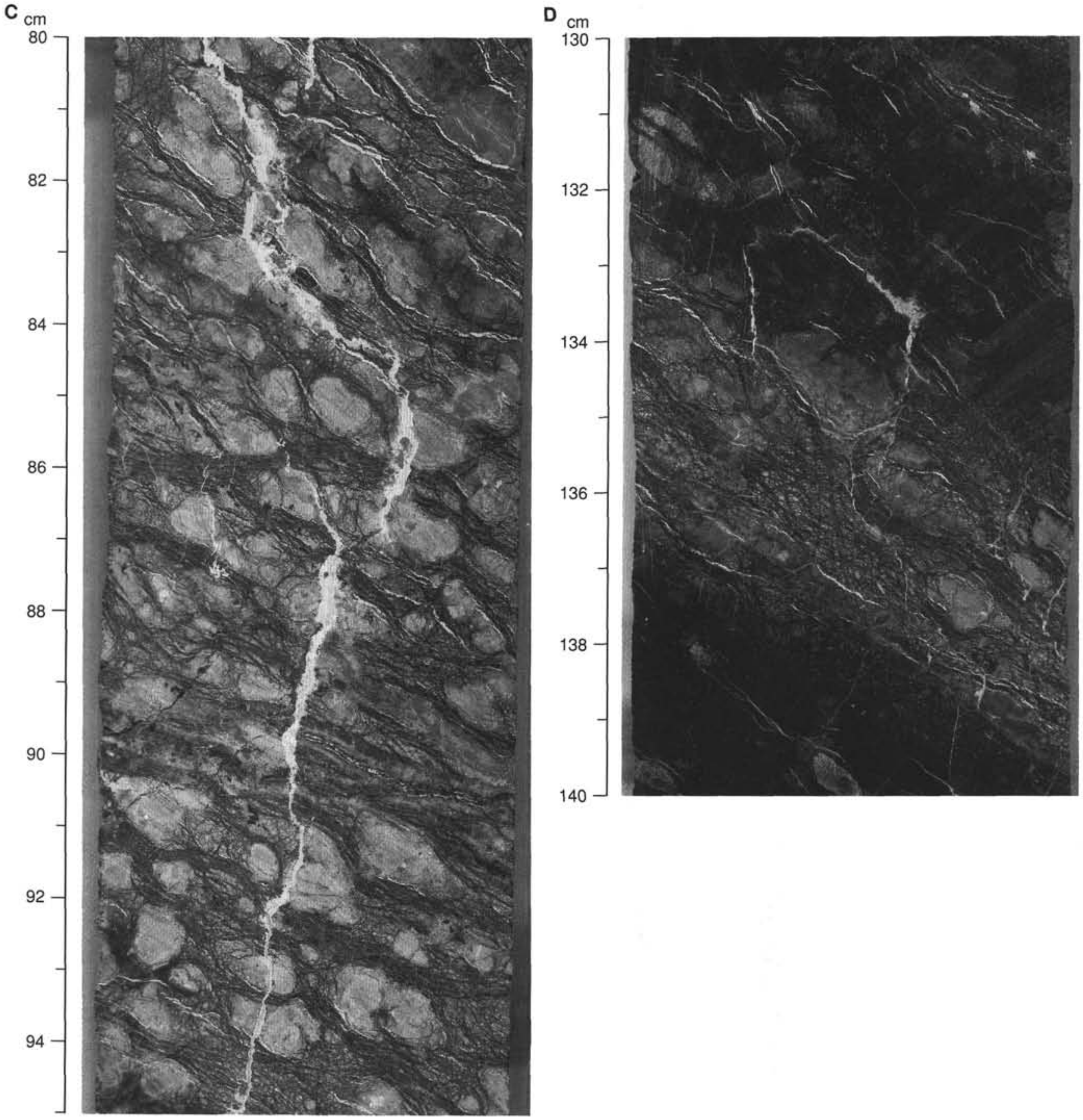

Figure 12 (continued).

equigranular textures have been observed adjacent to partially altered clinopyroxenite and gabbroic veinlets that crosscut harzburgite. These serpentinized harzburgites are locally plagioclase-bearing and appear to have been infiltrated by melts prior to alteration. The melts appear to have allowed the residual deformed mineralogy to recover and undergo grain growth in the presence of a melt phase, reestablishing coarse-grained equigranular textures. The association between magmatic veins and coarser grain sizes is striking and well displayed in thin section.

Igneous textures are commonly preserved within the harzburgite units in the form of magmatic clinopyroxene and plagioclase that have been observed in thin section as small undeformed interstitial phases in an otherwise deformed residual mantle matrix. Specifically, magmatically twinned clinopyroxene has been observed in several harzburgite thin sections (e.g., Samples 153-920B-3R-2, 122–125 cm, 153-920D-15R-4, 27–30 cm, and 153-920D-22R-7, 16–20 cm; Fig. 20). No clear connection to any clinopyroxenite veins or other intrusive features was associated with these occurrences of twinned clinopyroxene.

Spinel is abundantly preserved within the serpentinized harzburgites, although it is commonly rimmed by alteration products such as ferrit-chromite and magnetite. It occurs in trace amounts throughout

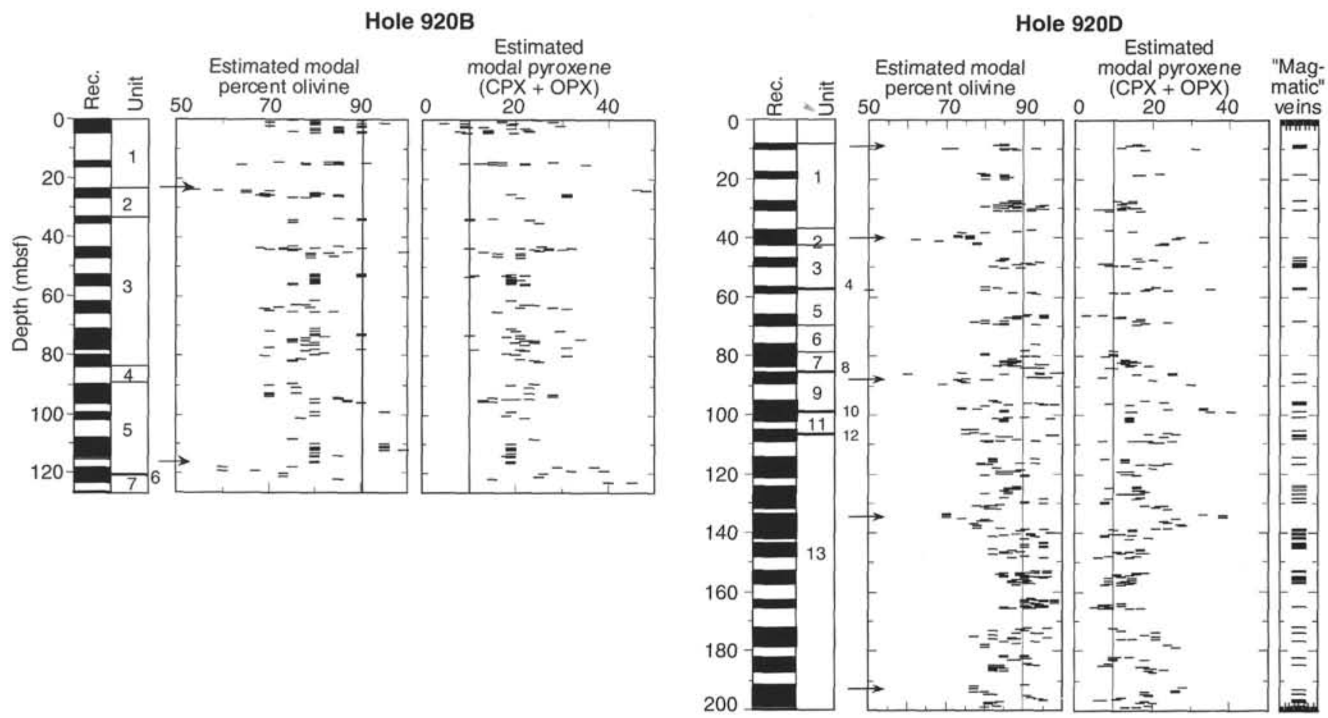

Figure 13. Variation of modal olivine and pyroxene with depth in Holes 920B and 920D as estimated from macroscopic core description. Arrows indicate horizons that are most olivine-poor and pyroxene-rich. Also shown is the downhole distribution of magmatic veins in Hole 920D.

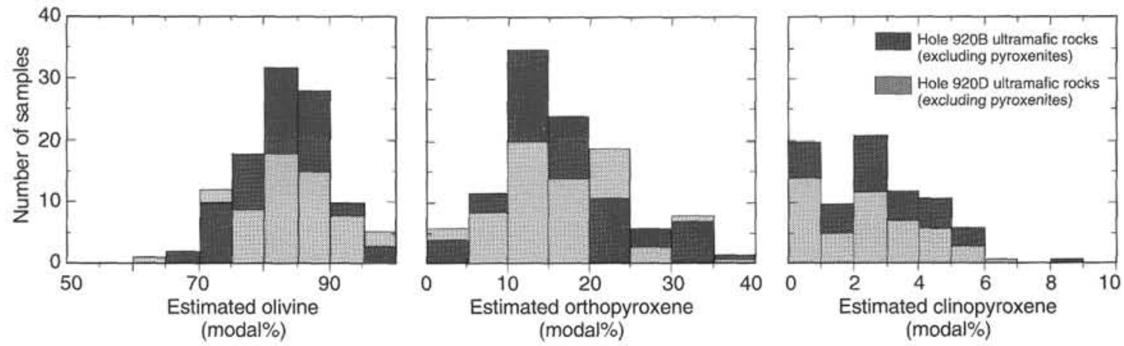

Figure 14. Histograms of modal mineralogy, both estimated and measured, from thin sections of peridotite from Holes 920B and 920D. N equals 107 for all plots. Note the similarity of the distributions between holes for all phases.

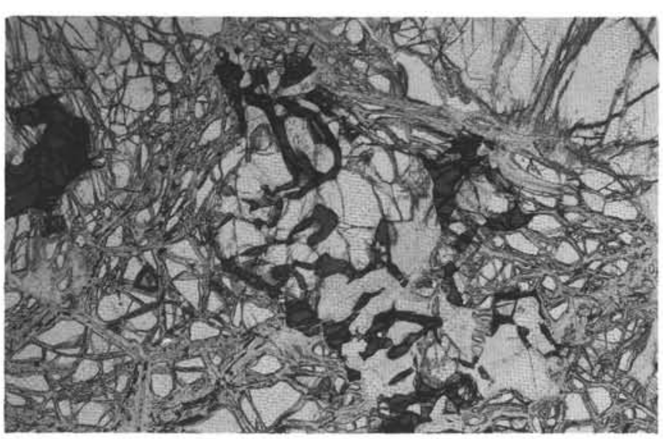

Figure 15. Photomicrograph of spinel-orthopyroxene-clinopyroxene intergrowth in harzburgite, Sample 153-920D-22R-7 (Piece 1, 16–20 cm). Such intergrowths could be the result of breakdown of garnet during mantle upwelling from the garnet to spinel-lherzolite facies. Field length is 2 mm.

the core as isolated grains, coarse grains, patches of grains, trains of fine intergranular grains (Fig. 21), and as vermiform intergrowths within pyroxene (Fig. 15). "Trains" defined by interconnected or discontinuous chains of spinel have been observed in core from Holes 920B and 920D. An example is depicted in Figure 21. They generally define a lineation on the cut core face. Dominantly they are observed as straight linear features, but also can form meandering traces through the rock with apparent random orientation. Some of these spinel trains are several tens of grains in length, and may be traceable for more than 10 cm. Some of these trains may crosscut the elongated orthopyroxene foliation at low to high angles. The grain size of spinel in these trains is variable, up to 2 mm long. Very small spinel trains are also commonly observed along orthopyroxene grain boundaries. In the case of trains along olivine grain boundaries, the spinels are closely associated with small amounts of orthopyroxene. In some cases these trains of spinel appear to cut across pyroxene porphyroclasts. Where spinel trains are present, the distribution of spinel in the rock tends to be heterogeneous and concentrated along these features. They may represent zones where melt percolated through the solid matrix along interconnected pore space or grain-scale fractures.

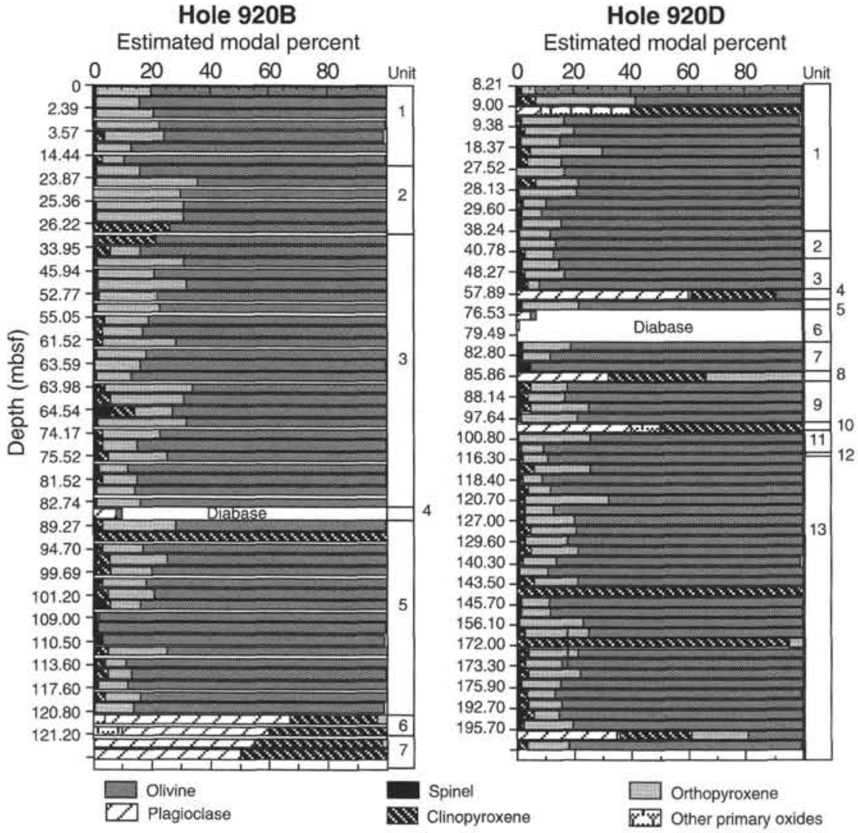

Figure 16. Modal proportions of the primary phases estimated in thin sections from Holes 920B and 920D. The depth scale provides a reference depth listed sequentially for each thin section, but the vertical scale is not linear.

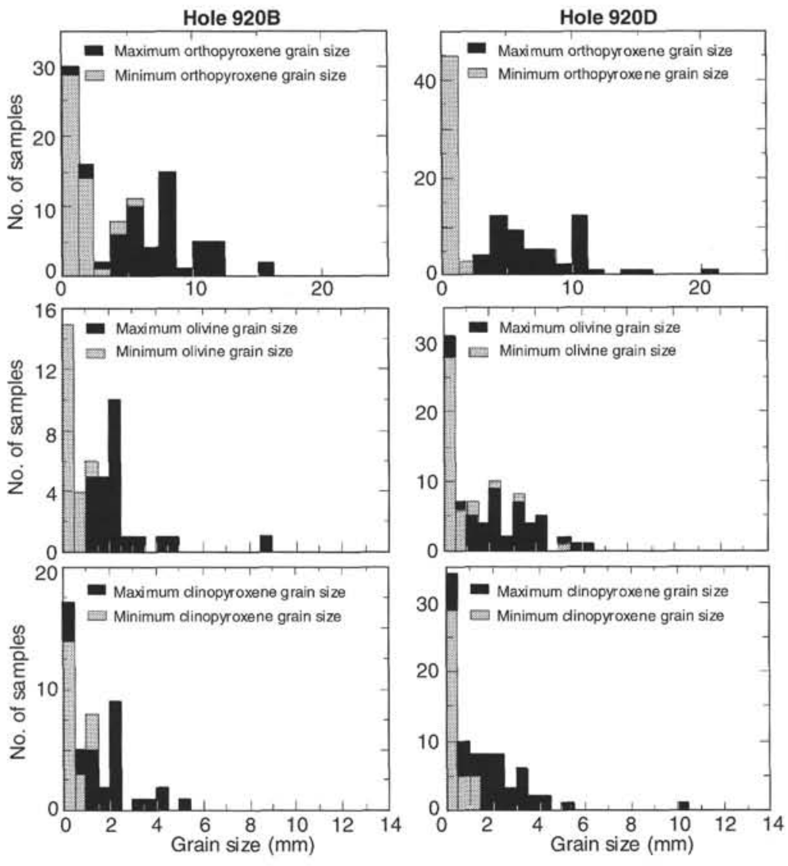

Figure 17. Distribution of measured maximum and minimum grain sizes from thin sections for orthopyroxene, olivine, and clinopyroxene in thin sections of peridotite from Holes 920B and 920D. Horizontal scales are the same for olivine and clinopyroxene grain sizes.

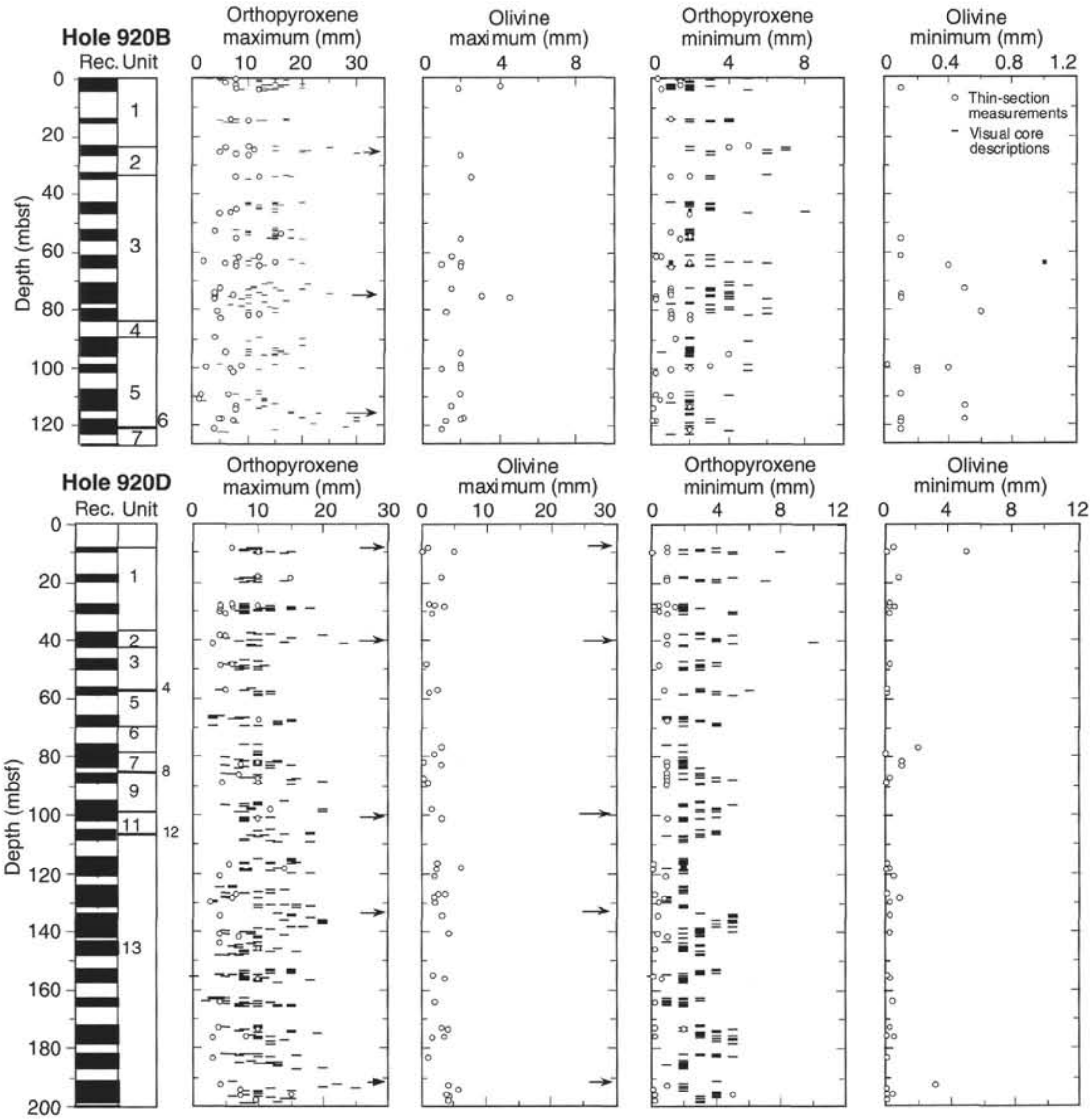

Figure 18. Variation with depth of maximum and minimum grain size of orthopyroxene and olivine in Holes 920B and 920D. Zones of maximum grain sizes of orthopyroxene (indicated with arrows) correlate with zones of higher pyroxene modal proportions (Fig. 13).

Centimeter- to millimeter-thick clinopyroxenite and gabbro veins crosscut the peridotites. The petrography of these small intrusive features is discussed more fully below. Many such small veinlets observed in hand specimen are bounded by concentrations of pyroxenes, with pyroxene-poor zones more distant from the vein boundaries. At smaller scales, trains of continuous to discontinuous clinopyroxene, similar to the trains of spinel, have also been observed in thin section. They are several millimeters to centimeters in length.

Plutonic and Hypabyssal Rocks

The extensive peridotite section recovered in the cores from Holes 920B and 920D is characterized by abundant plagioclase and/or clinopyroxene-bearing plutonic and hypabyssal rocks that intrude it. Such rocks, whose recovered length totals more than 10 cm were designated as separate units (Units 4, 6, and 7 in Hole 920B and Units 4, 6, 8, 10, and 12 in Hole 920D). Nonetheless, there are other pieces of gabbro, metagabbro, and pyroxenite that display well-developed hypidiomorphic granular textures but are less than 10 cm in recovered length. Commonly the size of these smaller intrusions is defined clearly, because both contacts with the harzburgite country rock are preserved in the core. The protoliths of these magmatic veins and dikes include olivine gabbro, oxide-rich gabbronorite, oxide-rich clinopyroxenite, clinopyroxenite, porphyritic diabase, and amphibolitized microgabbro.

Altered Clinopyroxenite and Composite Clinopyroxenite-gabbro Veins

In addition to the obviously magmatic coarse- and fine-grained intrusives, cores recovered from Holes 920B and 920D include numerous thin (1–50 mm thick) veins and veinlets. These veins are interpreted as magmatic, rather than hydrothermal, due to the presence of magmatic phases, such as pyroxene and/or plagioclase, or of alteration products after such minerals, such as aggregates of decussate tremolite/actinolite, radiating crystals of actinolite, some serpentine, and minor chlorite (see "Metamorphic Petrology," this chapter). Examples of these veins are depicted in Figure 22. Many of these veins are actually composite veins with clinopyroxenite margins and gabbroic centers. Sulfide minerals (typically pyrite) are present in minor proportions within these veinlets as interstitial grains that are probably magmatic in origin. Some sulfide minerals are, however, associated with late-stage serpentine veining. Igneous textures in the form of euhedral grain terminations of orthopyroxene, clinopyroxene, and plagioclase (Fig. 23) are commonly preserved in the least altered of these veins. The density of these clinopyroxene and composite clinopyroxenite gabbro veins varies downsection in Holes 920B and 920D (Fig. 14). They occur more commonly within pyroxene-poor peridotites (Fig. 24) and are associated with local enrichment of the host ultramafics in clinopyroxene (e.g., Fig. 22C). There is also a tendency for the thickest veins to be concentrated in the pyroxene-poor zones. This may indicate that the pyroxene-poor peridotites provided an easier pathway for fluids and/or melts than more pyroxene-rich rocks. Finally, small altered clinopyroxenite veins commonly developed near major intervals of metagabbro or pyroxenites (e.g., Section 153-920D-17R-1).

The altered clinopyroxenite and gabbroic veins show variable orientation with respect to the crystal-plastic foliation of the new ultramafics and could therefore be either syn-kinematic or post-kinematic with respect to this high-temperature fabric. However, textural observations such as euhedral crystal termination and the absence of strain-induced microstructures in the vein minerals suggest that they are dominantly post-kinematic, even when parallel to the foliation plane.

Coarse-grained to Pegmatitic Gabbro and Pyroxenite

Slightly larger scale, usually coarse-grained intrusions of gabbro, feldspathic pyroxenites, and oxide-rich pyroxenites occur as usually concordant veins or intrusive bodies ranging from ~21 to 37 cm (recovered length) thick. Concordant intrusions are those that are subparallel or parallel to the high-temperature foliation in the harzburgite tectonites. The most abundant rock type is coarse, pegmatitic gabbro/pyroxenite in which crystals of clinopyroxene up to 50 mm commonly form comb-structure along the walls with crystals protruding into the vein (Fig. 9). Comb structure is generally interpreted to form by in-situ crystallization along the walls or margins of a magma body. Generally this comb structure gives way to feldspathic rocks with intergranular textures. Only an intergrown mesh of alteration minerals was recovered for many veins, but others preserve intergranular plagioclase and/or iron oxide minerals. Sulfide minerals (typically pyrite or pyrrhotite) have also been observed in some gabbros (Sample 153-920D-13R-1, 8–9 cm) where they form blebs within the interstitial regions with reaction-free faces against adjacent iron oxide minerals. These sulfide minerals thus may be magmatic, but their common occurrence near veins of secondary actinolite and chlorite suggests that they are at least partially remobilized during later hydrothermal activity.

Clinopyroxene is typically brown and ranges from 95% modal abundance in pegmatitic clinopyroxenite to 25% for typical coarse-grained metagabbro. Plagioclase and iron oxide minerals are the next most abundant phases, with typical modal ranges of 2% to 60% and 1% to 43%, respectively. High modal abundances of iron oxide minerals occur within oxide gabbro (Unit 6, Hole 920B; Units 10 and 12, Hole 920D) and oxide pyroxenite (Section 153-920D-10R-2, Piece 1). One sample (Section 153-920D-11R-1, Piece 7) is a gabbronorite, containing 30% orthopyroxene pseudomorphs. The contacts between gabbros and serpentinized peridotite are typically sharp, although the lower contact in Sample 153-920D-13R-2, 138–140 cm, shows mild deformation. In Unit 8 in Hole 920D (Section 153-920D-11R-1, Piece 5) the contact between rodingitized gabbro and dunite occurs as a thin (20 mm) band of deformed metagabbro within dunite (Fig. 6). The relationship of this metagabbro with the rodingitized gabbro is unclear, but it could represent gabbro deformed and metamorphosed during intrusion of the gabbroic dike into relatively hot wall rocks.

The coarse gabbro/pyroxenite intrusions generally show systematic zonations internally and within the adjacent ultramafic wall rock. Figures 8, 9, and 10 show contact relationships between harzburgite and pyroxenite or gabbroic intrusions. In some cases, the residual harzburgite is characterized by a progressive decrease in pyroxene content toward the margin of the intrusion with a transition from harzburgite to dunite over a scale of less than 1 m where marked compositional changes take place. The contact zone between the residual rock and the larger pyroxenitic or gabbroic dikes or veins is generally between orthopyroxene- and clinopyroxene-bearing dunite and clinopyroxenite at the margin of the vein. Clinopyroxenites typically grade inward to feldspathic pyroxenite and gabbro (e.g., Fig. 10) with a common increase of oxide minerals and sulfide abundances (e.g., Figs. 6 to 10). Contacts with the host ultramafics range from sharp to transitional on a centimeter scale.

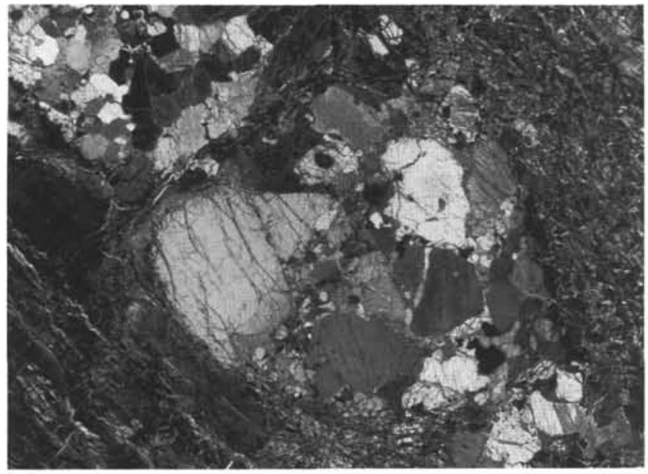

Figure 19. Photomicrograph of a polymineralic lens composed of porphyroclastic and recrystallized orthopyroxene, olivine, and less abundant clinopyroxene. Sample 153-920B-11R-1 (Piece 8B, 54–56 cm). Minerals within this type of lens commonly exhibit the lowest intensity of alteration, with local replacement as little as <5%–10%. Narrow rims (50–100 μm wide) of cummingtonite after orthopyroxene, talc after olivine, and traces of amphibole after clinopyroxene form an interconnected network within the aggregates. The lenses are enclosed in mesh-textured serpentine. Field length is 16 mm.

Amphibolite and Gneissic Gabbro

Below the porphyroclastic mylonite of Unit 6 in Hole 920B is a medium- to fine-grained amphibolite in vertical contact with a gneissic metagabbro (Fig. 5). Both rock types have a strong near-vertical lineation and foliation. They have been designated collectively as Unit 7 because of their common deformational fabrics (see "Structural Geology," this chapter). In Hole 920D, an amphibolitized microgabbro occurs in Unit 4.

The amphibolite in Unit 7 of Hole 920B has a well-developed foliation and consists of recrystallized plagioclase, clinopyroxene, brown hornblende, olivine, and magnetite, suggesting uppermost amphibolite facies metamorphism. The amphibolitized microgabbro from Hole 920D (Core 153-920D-7R) contains the same constituent minerals (i.e., olivine, clinopyroxene, brown hornblende, plagioclase, and iron oxide minerals). These rocks are different in grain size, mode of plagioclase twinning, and metamorphic structure. In both rocks, however, brown hornblende partially to completely replaces clinopyroxene, but also occur as discrete crystals. The amphibolite collected from Hole 920B shows a strong fine-scale gneissic texture defined by alternating clinopyroxene and hornblende-rich layers with plagioclase-rich segregations. In contrast, the amphibolitized microgabbro from Hole 920D has an equigranular igneous texture and shows no foliation or deformation (Fig. 25). The amphibolite in Hole 920B is finer grained than the amphibolitized microgabbro of Hole 920D. In addition, the amphibolitized microgabbro has a 5-cm-wide zone at the top that includes numerous xenocrysts of altered plagioclase, pyroxene, and

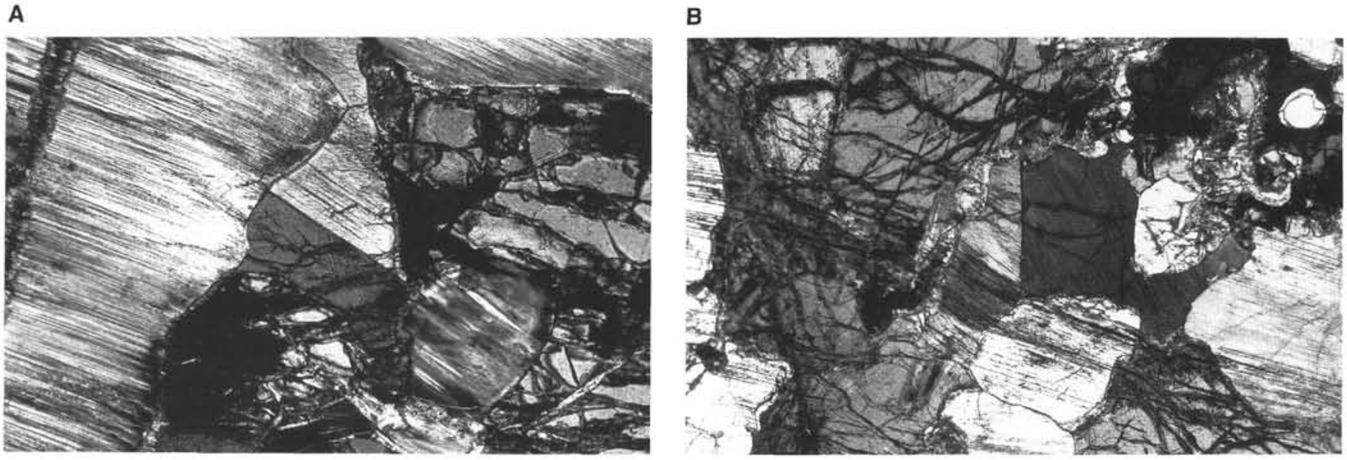

Figure 20. **A.** Photomicrograph of magmatic twin of clinopyroxene in Sample 153-920B-3R-2 (Piece 13, 122–125 cm). A twinned and strain-free clinopyroxene grain (center) is in contact with an orthopyroxene porphyroclast (left) and with strained olivine (right). Field length is 1 mm. **B.** Twinned clinopyroxene in harzburgite, Sample 153-920D-15R-4 (Piece 1, 27–30 cm). This interstitial clinopyroxene is in contact with strained olivine (left) and with orthopyroxene (below and right). Field length is 2 mm.

Figure 21. Photomicrograph of spinel train in serpentinized harzburgite. Sample 153-920D-22R-4 (Piece 1B, 31–35 cm). Field length is 6 mm.

olivine (up to 18 mm in size) that are interpreted as xenocrysts assimilated from a coarse-grained gabbro (not recovered) interpreted to have been intruded by the amphibolitized microgabbro.

The gneissic metagabbro in Unit 7 of Hole 920B has a coarse-grained porphyroclastic texture and contains an anhydrous mineral assemblage of clinopyroxene, plagioclase, and oxide minerals. Highly strained plagioclase and clinopyroxene porphyroclasts are surrounded by a fine-grained matrix of recrystallized plagioclase and clinopyroxene.

Porphyritic Diabase

Moderately olivine + plagioclase phyric diabases were recovered in both Holes 920B (Unit 4) and 920D (Unit 6). The two units are petrographically similar (Figs. 4 and 11) and believed to be from the same body. They are bounded by serpentinized harzburgite above and below and in neither hole was a contact with the surrounding peridotite observed. However, the diabase is finer grained and contains fewer phenocrysts at the top and bottom in Hole 920D, and at the top in Hole 920B (Fig. 4). From these relationships we infer that the diabase intruded the peridotite, even though the contact is not exposed. Since diabase was intersected at a shallower depth in Hole 920D (69.3 vs. 83.2 mbsf), it is probably an inclined tabular intrusive body; the difference in depth defines an apparent dip of 43° for the dike between the two holes. A longer section of diabase was recovered in Hole 920D (3.27 m) than in Hole 920B (1.39 m), but because the lower contact in Hole 920B was near a coring break, drilling losses may have been significant. Given that fine-grained margins were observed at both the top and bottom of the unit in Hole 920D, it is likely that most of the intrusive body was recovered in that hole, suggesting a thickness of 3.5 to 4 m. There is a high density of sulfide veins in the peridotite adjacent to the diabase, suggesting that the intrusion may have provided a heat source for hydrothermal activity and elemental mobilization.

The diabase has a porphyritic intergranular to subophitic texture and contains euhedral olivine (0%–10%) and tabular plagioclase (0%–10%) phenocrysts (Fig. 26). It is moderately altered but still preserves abundant primary plagioclase, clinopyroxene, and iron oxide minerals in the groundmass. Plagioclase phenocrysts have tabular euhedral shapes, are commonly zoned and contain altered melt inclusions. Their anorthite content (determined optically) ranges from An_{65} to An_{75}. Euhedral olivine phenocrysts, ranging from 0.5 to 3 mm, are now totally replaced by chlorite + amphibole + clay. The groundmass is composed of fine-grained plagioclase (40%–60%), clinopyroxene (11%–20%), altered olivine (15%–23%), and opaque iron oxide minerals in a smectite-chlorite matrix. Groundmass plagioclase laths range from 0.1 to 0.8 mm, anhedral interstitial clinopyroxenes from 0.1 to 0.7 mm, and euhedral magnetite and ilmenite from 0.02 to 0.04 mm. Some large clinopyroxene crystals, more than 1 mm long, subophitically enclose plagioclase laths.

GEOCHEMISTRY

The chemical data from Holes 920A, 920B, and 920D are considered together. A total of 52 samples from these three holes were analyzed during Leg 153 for major and trace elements by XRF (X-ray fluorescence). These data, as well as LOI (loss on ignition), H_2O, and CO_2 analyses, are reported in Table 5. Forty-five of these analyses were conducted on ultramafic samples (harzburgites, dunites, and lherzolites), three on plagioclase-olivine phyric diabase (one from Unit 4, Hole 920B, and two from Unit 6, Hole 920D), and the remainder on a metagabbroic vein (Hole 920B), an oxide gabbro (Unit 6, Hole 920B), an amphibolite (Unit 7, Hole 920B), and an amphibolitized microgabbro (Unit 4, Hole 920D). The results for major and trace elements are all reported on a volatile-free basis. The usual trace element procedures were modified for ultramafic rocks because of the high volatile contents, dominantly structural water, bound in serpentine and other hydrated minerals within the peridotites (see "Geochemistry" section of "Explanatory Notes," this volume). Tests conducted on serpentinized peridotite samples (by igniting the sample to drive off volatiles before trace element analyses)

Table 5. Bulk-rock geochemistry of ultramafic and mafic rocks from Holes 920A, 920B, and 920D.

Hole:	920A	920B	920B	920B	920B	920B	920B	920B	920B	920B
Core, section:	1W-1	2R-1	3R-2	4R-1	5R-3	6R-3	7R-1	7R-2	7R-3	8R-2
Interval (cm):	73–77	17–20	98–101	60–63	86–87	20–26	52–58	114–118	15–18	70–77
Depth (mbsf):	0.73	14.17	25.98	33.8	46.48	55.05	61.52	63.56	63.98	72.38
Piece:	6	2	10	7	5	2	1E	8	1	6
Rock type:	Serpentinized harzburgite	Serpentinized harzburgite	Serpentinized harzburgite	Serpentinized harzburgite	Serpentinized harzburgite	Serpentinized harzburgite	Serpentinized harzburgite	Serpentinized harzburgite	Serpentinized harzbugite	Serpentinized harzburgite
Major elements (wt%)										
SiO_2	44.61	44.14	43.74	44.97	44.29	46.16	44.49	44.02	44.86	44.22
TiO_2	0.02	0.02	0.02	0.02	0.02	0.01	0.01	0.02	0.02	0.01
Al_2O_3	1.14	1.41	1.29	1.83	1.52	1.56	1.44	1.24	1.39	1.22
Fe_2O_3	9.12	9.67	9.27	9.12	9.71	9.45	9.24	9.21	8.72	9.58
MnO	0.14	0.13	0.14	0.13	0.14	0.12	0.11	0.14	0.14	0.12
MgO	44.6	44.01	44.72	42.82	44.37	43.34	44.17	46.21	44.12	44.49
CaO	0.01	0.1	0.01	0.42	0.18	0.33	0.21	0.06	0.33	0.06
Na_2O	BDL	BDL	BDL	BDL	BDL	BDL	BDL	BDL	BDL	BDL
K_2O	BDL	BDL	BDL	BDL	BDL	BDL	BDL	BDL	BDL	BDL
P_2O_5	BDL	BDL	BDL	BDL	BDL	BDL	BDL	BDL	BDL	BDL
Total	99.65	99.47	99.19	99.32	100.23	100.97	99.67	100.91	99.58	99.71
LOI	12.78	12.1	12.81	11.51	12.26	11.41	11.97	13.22	12.04	12.51
CO_2	0.03	0.24	0.19	0.41	0.08	0.31	0.27	0	0.34	0.3
H_2O	13.1	12.72	15.98	11.11	15.44	12.41	12.55	13.37	11.55	14.55
Trace elements (ppm)										
Nb	BDL	BDL	BDL	BDL	BDL	BDL	BDL	BDL	BDL	BDL
Zr	5	5	5	5	5	6	5	4	4	4
Y	1	1	2	2	2	3	1	1	1	1
Sr	8	8	8	18	8	8	8	8	8	8
Rb	BDL	BDL	BDL	BDL	BDL	BDL	BDL	BDL	BDL	BDL
Zn	25	34	30	35	47	45	31	39	34	36
Cu	6	5	25	36	6	25	45	5	12	9
Ni	2609	2561	2757	2540	2526	2505	2565	2638	2529	2641
Cr	2147	2937	2576	3713	2770	3096	2681	2631	2967	2679
TiO_2	0.02	0.02	0.02	0.02	0.02	0.02	0.02	0.02	0.02	0.02
V	48	50	50	63	50	53	51	50	55	50
Ce	BDL	BDL	BDL	BDL	BDL	BDL	BDL	BDL	BDL	BDL
Ba	BDL	BDL	BDL	BDL	BDL	BDL	BDL	BDL	BDL	BDL

Note: BDL = below detection limit.

generally resulted in significant increases in measured trace element abundances (especially Cr and Ni) over unignited samples because of the large dilution effect and probable analytical X-ray absorption effects of these volatile constituents (usually ~11–16 wt% in serpentinized peridotites). These effects may not be similar in known standards which, relative to these samples, are highly depleted in volatiles. The results of pilot tests on a set of ultramafic samples run both ignited and unignited are displayed in Figure 27 and show significant increases in Ni abundances (>400 ppm) on ignited samples relative to unignited samples. Also shown is the inadequacy of simple adjustments made based on LOI. The trace element analyses for peridotites are reported on a volatile-free basis to simulate the abundances in the peridotite prior to hydration. To aid in the assessment of volatile and alteration effects on the bulk-rock chemistry, H_2O and CO_2 analyses were also conducted and are reported in the data (Table 5). Test runs conducted on ignited and unignited mafic rocks showed no significant differences in their trace element abundances. This is because of the generally lower degrees of hydration and the fact that any dilution effect is generally within the bounds of analytical error. Mafic samples were therefore measured with the more usual sample preparation techniques without igniting prior to trace element analyses. Below we present separate discussions for ultramafic and mafic rock analytical results.

Ultramafic Rocks

Bulk-rock analyses of ultramafic rocks show that the composition of all these rocks has been significantly modified by hydrothermal alteration and the addition of volatile constituents to the original ultramafic assemblage (Fig. 28). Most notably this led to the addition of 8.33–15.9 wt% H_2O.

CO_2 in ultramafic rocks ranges from 0.0 to 0.85 wt%, but varies inversely with increasing H_2O, indicating that the least altered horizons apparently concentrate CO_2 preferentially. The relationship between bulk-rock MgO and CO_2 (Fig. 28) also indicates that rocks highest in MgO (highest modal olivine) are least likely to concentrate CO_2. CO_2 abundances could be caused by the precipitation of carbonate, but may also reflect an original protolith rich in clinopyroxene (discussion below). Carbonate veins were observed in some samples, although efforts were made to sample away from major vein sets when sampling for geochemistry. In addition, although carbonate (aragonite) is a source of CO_2 (Table 5), the relatively low abundances and low concentrations of Sr, Ba, and CO_2 indicate a relatively small carbonate component. As expected, LOI tends to be 1–2 wt% below total volatile contents measured and thus does not fully account for volatile abundances (Fig. 28).

Pervasive hydrothermal alteration of the samples, as documented both by thin-section descriptions, visual core descriptions, and the high volatile content, could result in variable and possibly significant effects on the more mobile major and trace element chemistry of serpentinized ultramafic rocks. The range of alteration estimated in thin sections for the olivine-bearing ultramafic rocks analyzed for major and trace elements varies from 72% to 98% for Hole 920B (average 90%) and from 18% to 100% for Hole 920D (average 85%; Table 4). The effects of the alteration on the geochemistry of these rocks will be critically evaluated only after shore-based mineral chemistry, bulk-rock chemistry, and more quantitative modal analysis on oversized thin sections. However, several correlations with other collected data sets suggest that the bulk-rock chemistry reported on a volatile-free basis may, in part, still reflect the protolith composition.

Previous alteration studies from Site 670 in the MARK peridotites have shown that the mineral chemistry of pseudomorphs after olivine, orthopyroxene, and clinopyroxene do, in fact, reflect the original composition of the altered minerals (Hébert et al., 1990). This suggests that there is some potential for study and identification of the original protolith through bulk-rock chemistry or mineral chemistry of pseudomorphs, especially if the more immobile elements are evaluated. The extensive hydration of ultramafic rocks from the ocean basins has dissuaded most investigators from conducting bulk-rock

Table 5 (continued).

920B 8R-3 115–121 74.17 11 Serpentinized harzburgite	920B 9R-2 36–43 81.55 3B Serpentinized harzburgite	920B 9R-2 84–91 82 4C Serpentinized harzburgite	920B 9R-3 55–57 83.2 8 Pl-Ol phyric diabase	920B 10R-1 17–23 89.3 2A Serpentinized harzburgite	920B 10R-3 0–5 91.87 1 Metagabbroic vein	920B 10R-4 139–143 94.7 9 Serpentinized harzburgite	920B 11R-1 119–125 99.69 14 Serpentinized harzburgite	920B 12R-5 10–17 113.1 1A Serpentinized harzburgite	920B 13R-1 33–38 117.53 2B Serpentinized harzburgite	920B 13R-3 129–132 121.18 5B Oxide gabbro
44.61	43.87	44.71	46.64	43.97	47.16	43.88	44.3	43.81	42.63	49.84
0.02	0.01	0.02	1.04	0.03	0.18	0.02	0.02	0.02	0.02	2.89
1.33	1.06	1.42	18.05	1.51	9.21	1.33	1.48	1.4	1.27	16.93
9.03	9.42	9.1	9	9.93	3.35	9.5	9.2	9.22	9.21	13.38
0.13	0.12	0.13	0.25	0.13	0.21	0.13	0.13	0.14	0.13	0.19
44.41	45	44.37	13.03	43.95	15.32	45.33	43.44	43.55	45.98	3.14
0.13	0.14	0.04	8.92	0.08	24.53	0.23	0.37	1.01	0.88	8.1
0	0	0	2.2	0	0	0	0	0	0	4.63
0	0	0	0.01	0	0	0	0	0	0	0.09
0	0	0	0.05	0	0	0	0	0	0	0
99.66	99.63	99.8	99.19	99.59	99.96	100.42	98.94	99.15	100.12	99.18
12.75	12.41	12.77	4.29	12.23	4.17	13.82	11.25	11.86	12.6	1.26
0.31	0.3	0.13	0	0.3	0.79	0.03	0.26	0.52	0.33	0
14.4	13.22	13.07	5.87	15.44	4.05	13.05	12.32	12.4	14.32	2.29
1	0	1	1	1	0	1	0	1	0	4
4	4	4	70	4	4	4	4	4	4	67
2	1	2	18	1	6	1	1	1	1	24
8	8	8	190	8	15	8	8	8	8	395
1	2	1	1	2	1	1	1	1	2	1
36	36	35	97	30	26	35	47	39	41	164
9	3	3	16	5	6	2	48	17	24	41
2624	2772	2547	228	2475	335	2784	2647	2576	2762	69
2815	2615	2897	391	2677	387	2270	3349	2749	2577	36
0.02	0.02	0.02	0.94	0.02	0.22	0.02	0.02	0.02	0.02	2.71
54	44	57	214	58	178	48	58	57	44	365
0	1	1	7	2	4	1	0	1	0	11
0	0	0	1	0	0	0	0	0	0	27

studies and there is scarce comparative data from abyssal peridotites (e.g., Hamlyn and Bonatti, 1981). Dick (1989) used the approach of calculating bulk compositions from modal data and mineral chemistry on altered rocks. This approach may lead to a bias, as it tends to select the least altered samples, which commonly are also the high-clinopyroxene-rich ones, for modal point counting. Figure 29 depicts the major element bulk-rock composition of the peridotites sampled in Holes 920A, 920B, and 920C and of peridotites sampled in the same area at ODP Site 670 (Di Donnato et al., 1990), and along *Alvin* dive tracks (Casey, unpubl. data). Apart from changes in the Fe_2O_3/$FeO + Fe_2O_3$ ratios associated with serpentinization, large changes in MgO relative to FeO* (total Fe reported as FeO) can be evaluated by comparing the range of Mg# in minerals from previous studies of MARK peridotites from Site 670, Leg 109, with the bulk-rock Mg numbers reported here (Fig. 29). As is usual in residual mantle rocks, Mg numbers from MARK peridotites have previously been reported to cover a narrow range from 90.1 to 90.9 for olivine, 90.2–91.1 for orthopyroxene, and 90.4–93.43 for clinopyroxene (Komor et al., 1990; Juteau et al., 1990). The range of Mg numbers in bulk-rock olivine-bearing ultramafic rocks (harzburgites, dunites, and lherzolites), if not significantly modified by alteration, should also cover a similar range. Mg numbers at Site 920 show a comparable narrow range in Hole 920B from 89.7 to 90.9 (average = 90.4, s.d. = 0.004) and for Hole 920D from 88.5 to 90.7 (average = 90.2, s.d. = 0.003). This is similar to the range of bulk-rock compositions from Site 670 (Di Donnato et al., 1990; Humphris et al., 1990) and *Alvin* (Casey, unpubl. data) samples from the MARK region, also plotted in Figure 29. This indicates that relative iron and magnesium element mobility was not sufficient to alter substantially the original bulk rock Mg# values for most of the samples studied.

The major elements of most significance in the peridotites are MgO, SiO_2, FeO, Al_2O_3, and CaO. The range of compositions reflected at Site 920 is presented in Figure 29 against the background of previous analyses of peridotites from the MARK region.

FeO* abundances in core from Holes 920B and 920D vary from 7.84 to 9.80 wt%, MgO from 42.73 to 46.20 wt%, SiO_2 from 42.62 to 45.08 wt%, Al_2O_3 from 1.06 to 1.83 wt%, and CaO from 0.01 to 1.55 wt%. Average bulk-rock compositions for Site 920 peridotites are reported in Table 6. These compositions are compatible with a residual origin of the peridotites, as products of partial melting and subaxial mantle processes. This is also compatible with tectonite textures and fabrics for all of the harzburgite samples analyzed (see "Structural Geology," this chapter) and with evidence from previous MARK peridotite studies (Komor et al., 1990; Juteau et al., 1990; Cannat et al., 1990). In the more specific sense of residual mantle rocks, a wide range of residual mantle compositions were sampled in Holes 920B and 920D, although the data from Site 670 and *Alvin* sampling in the MARK region expand the range of compositions even more significantly. This is also reflected in the modal variation documented downhole.

The composition of MARK peridotites falls along a pyroxene depletion trend on an MgO/SiO_2 vs. Al_2O_3/SiO_2 diagram (Fig. 30). Also plotted are the compositional fields of olivine (black), clinopyroxene, and orthopyroxene (gray) from the MARK region (Komor et al., 1990; Juteau et al., 1990; Casey [unpubl. data]). Both ratios vary as a function of pyroxene content. As total pyroxene decreases, MgO/SiO_2 increases and Al_2O_3/SiO_2 decreases. The field of MARK peridotites essentially spans the range of most abyssal peridotites, with Site 920 results spanning the center of the MARK field. In addition, the bulk rock data trend also falls along mixing lines between analyzed olivine and pyroxenes from the MARK Area on an MgO vs. Al_2O_3 diagram (Fig. 30). Again these coherent trends in the bulk rock data are consistent with mineral chemistry results, indicating that elemental abundances in the peridotites sampled at Site 920 may not have been significantly affected by alteration.

Calcium metasomatism occurring during serpentinization of ultramafic rocks causes the production of Ca-rich solutions and can cause rodingitization of gabbroic rocks as, for example, observed in some gabbroic intrusions within the peridotites of Holes 920B and 920D (e.g., Unit 8). Calcium-rich solutions are probably released during serpentinization, especially if the ultramafic rock is rich in clinopyroxene (which contains ~21–23 wt% CaO). In this respect some of

Table 5 (continued).

Hole:	920B	920D	920D	920D	920D	920D	920D	920D	920D	920D
Core, section:	13R-4	2R-1	3R-1	4R-2	5R-2	5R-4	6R-2	7R-2	8R-1	8R-3
Interval (cm):	23–26	21–27	38–41	97–100	33–39	0–5	45–51	22–29	123–127	66–73
Depth (mbsf):	121.51	8.21	17.88	29.57	38.24	40.73	48.27	57.89	67.13	69.46
Piece:	3	4	3B	4	1A	1	9A	2B	15	8
Rock type:	Gneissic amphibolite	Serpentinized harzburgite	Serpentinized harzburgite	Serpentinized harzburgite	Serpentinized harzburgite	Serpentinized harzburgite	Serpentinized harzburgite	Amphibolitized microgabbro	Serpentinized harzburgite	Pl-Ol phyric diabase (chill)
Major elements (wt%)										
SiO_2	46.63	44.75	44.09	45.09	43.51	44.64	44.81	45.1	43.71	48.1
TiO_2	1.07	0.03	0.02	0.02	0.02	0.02	0.01	1.22	0.01	0.99
Al_2O_3	16.14	1.49	1.43	1.49	1.57	1.45	1.29	16.68	1.31	16.68
Fe_2O_3	11.88	9.3	9.21	9.04	9.21	9.02	9.29	12.97	9.6	8.86
MnO	0.19	0.12	0.12	0.12	0.14	0.15	0.13	0.23	0.14	0.25
MgO	11.75	43.56	44.17	42.74	43.99	43.6	43.66	12.07	43.61	14
CaO	9.68	0.33	0.07	0.39	0.1	0.01	0.02	8.61	0.08	7.73
Na_2O	2.4	0	0	0	0	0	0	2.33	0	2.7
K_2O	0.04	0.01	0	0	0	0	0	0.05	0	0.02
P_2O_5	0.02	0	0	0.01	0	0	0	0.04	0	0.04
Total	99.81	99.6	99.11	98.89	98.54	98.87	99.21	99.3	98.45	99.35
LOI	-0.39	11.67	12.06	11.01	12.35	12.07	12.5	2.56	12.09	4.49
CO_2	0.08	0.51	0.36	0.41	0.33	0.3	0.47	0.05	0.41	0.04
H_2O	0.71	10.94	12.46	11.48	12.16	12.21	10.98	4.13	13.01	5.75
Trace elements (ppm)										
Nb	0	0	0	1	0	0	0	1	0	1
Zr	52	8	4	4	3	4	4	67	4	65
Y	25	2	2	2	1	2	2	26	1	17
Sr	132	8	9	8	9	8	8	110	8	293
Rb	1	1	1	1	1	1	1	2	1	0
Zn	73	38	42	31	28	43	52	87	46	71
Cu	49	6	25	24	18	12	15	40	19	11
Ni	299	2564	2641	2469	2533	2600	2612	305	2663	274
Cr	382	2864	2910	2658	2921	2873	2909	343	2844	427
TiO_2	1.1	0.03	0.02	0.02	0.02	0.02	0.02	1.16	0.02	0.86
V	216	53	50	55	54	57	49	223	50	210
Ce	6	0	0	0	0	1	0	5	0	7
Ba	10	0	0	0	0	0	0	7	0	3

the orthopyroxene-rich harzburgites are especially depleted in calcium and lie below a mixing line between olivine and orthopyroxene (the most calcium-depleted pyroxene) on a CaO–Al_2O_3 plot (Fig. 31). This appears to indicate calcium depletion and mobility within some samples. Most samples, however, either lie along a mixing line between orthopyroxene and olivine or above it, suggesting that either wholesale calcium addition took place during serpentinization or that clinopyroxene was originally present in the protolith. The correlation between the downhole distribution of these CaO-rich zones and that of modal clinopyroxene (Figs. 32 and 33) suggest that this enrichment is not solely due to alteration.

Carbonate minerals have frequently been observed in oceanic ultramafic rocks that are serpentinized to high degrees (Hamlyn and Bonatti, 1981). At Site 920, aragonite veins were observed in many parts of the core (see "Metamorphic Petrology," this chapter). The carbonates are probably precipitated from Ca-rich solutions formed through serpentinization of Ca-bearing phases (dominantly clinopyroxene, but also orthopyroxene) during extensive alteration, or could have originated from seawater itself, as oceans are near saturation with $CaCO_3$. In general, the CO_2 species in descending seawater should be scrubbed out by reaction with calcic-aluminous phases in peridotites. CO_2 fixation in the peridotite will tend to localize in zones where calcic phases such as clinopyroxene are present during the serpentinization.

In downhole plots of CaO, we note that there are two CaO enriched zones in Hole 920D, and the shallowest zone occurs at the same depth in Hole 920B (Fig. 32). These zones correlate with general increases in modal clinopyroxene based on visual and thin-section descriptions (Fig. 33). We also note that these zones tend to be the most enriched in CO_2 (Fig. 34), suggesting that the release of Ca from pyroxene during serpentinization caused fixation of CO_2 preferentially where a CaO-rich protolith existed. The CaO in these zones is too high to be contained solely in aragonite (insufficient CO_2) and indicates that the CaO peaks downhole are probably controlled by the original protolith; the CaO was retained either within alteration products such as tremolite or within the original clinopyroxene. The CaO-rich zones also correspond to minima in alteration, LOI, and H_2O on downhole plots, and maxima in CO_2 and clinopyroxene modal abundances (Fig. 34). In fact, CO_2 abundances drop with increasing MgO content of the rock reflecting increases in modal olivine and decreases in modal pyroxene content.

Downhole plots of CaO and Al_2O_3 abundances (Fig. 32) show that these CaO-rich zones occur at depths between 20 and 50 mbsf and between 100 and 140 mbsf in Hole 920D and Hole 920B and between 180 and 200 mbsf in Hole 920D. In this figure, the cross-hole correlation is striking both for the shallowest CaO-rich region and for variations in Al_2O_3. For example, the pyroxene-rich harzburgite units (Unit 2 in both Holes 920B and 920D) show up as distinct Al_2O_3 peaks. Al_2O_3 can be used as a proxy for total pyroxene, irrespective of the ratio. As this figure shows, there appears to be significant variation in total pyroxene content downhole, as indicated by modal estimates during visual core descriptions. CaO, on the other hand, defines regions in the core in which the original protolith was clinopyroxene-rich. Further analysis of additional samples and evaluation of primary modal abundances and alteration processes are needed to verify whether the protolith is reflected in the bulk chemistry. Certainly on the basis of preliminary visual descriptions and thin-section work this seems to be a strong possibility.

Trace and minor element abundances also support the residual origin of the ultramafic rocks analyzed. The peridotites are depleted in incompatible elements with low distribution coefficients (e.g., TiO_2, Na_2O, K_2O, P_2O_5, Zr, Y, Nb, Rb, Ba, and Ce). Sr is highly incompatible during mantle melting, but it is also highly mobile during seawater hydrothermal circulation. The average Sr content is ~8 ppm (Tables 5 and 6), the same concentration as in seawater, suggesting that Sr is somehow buffered and was introduced during hydrothermal circulation. Residual peridotites also tend to be enriched in elements that have high distribution coefficients. These are concentrated in the residue during partial melting and include MgO, Ni, and Cr. Cr and Ni also tend to be immobile during alteration (Pearce, 1987; Hébert et al., 1990). Ni shows a strong positive correlation with increasing MgO and a negative correlation with increasing Al_2O_3 (pyroxene content) (Fig. 35). In contrast, Cr in the samples

Table 5 (continued).

920D	920D	920D	920D	920D	920D	920D	920D	920D	920D	920D
10R-1	10R-3	11R-2	11R-3	12R-2	12R-5	14R-3	15R-3	15R-3	16R-1	16R-7
57–60	74–80	63–69	22–28	119–125	23–29	82–88	40–45	48–54	98–104	54–60
78.67	81.7	87.35	88.14	97.64	100.76	117.85	126.91	126.99	134.38	141.53
7B	9A	4	1	11	3	3	2B	3A	5C	6
Pl-Ol phyric diabase (center)	Serpentinized harzburgite	Serpentinized harzburgite	Serpentinized harzburgite	Serpentinized harzburgite	Serpentinized harzburgite	Serpentinized harzburgite	Serpentinized harzburgite	Serpentinized harzburgite	Serpentinized harzburgite	Serpentinized harzburgite
50.21	44.11	43.7	44.48	43.68	43.8	43.26	42.85	43	43.79	44.02
1.11	0.01	0.02	0.03	0.01	0.02	0.01	0.01	0.01	0.02	0.01
14.93	1.34	1.49	1.48	1.28	1.35	1.41	1.49	1.34	1.5	1.3
9.55	9.52	9.92	8.84	9.31	9.12	9.08	10.46	9.36	8.99	9.52
0.28	0.14	0.15	0.14	0.12	0.15	0.14	0.16	0.14	0.15	0.13
15.08	44.09	43.54	43.87	43.83	44.29	43.52	44.05	44.23	43.97	44.39
6.21	0.29	0.03	0.29	0.23	0.26	1.55	0.58	0.99	1.15	0.12
3.36	0	0	0	0	0	0	0	0	0	0
0.02	0	0	0	0	0	0	0	0	0	0
0.04	0	0	0	0	0	0	0	0	0	0
100.79	99.49	98.84	99.13	98.47	98.98	98.98	99.59	99.07	99.57	99.5
4.58	11.9	12.26	12.42	12.44	12.76	10.36	12.34	11.91	11.23	12.16
0.06	0.76	0.55	0.73	0.74	0.85	0.73	0.54	0.82	0.74	0.4
5.71	10.8	12.75	12.11	12.46	11.7	10.35	12.09	10.05	10.65	12.51
1	0	1	1	1	0	1	0	0	0	0
70	4	5	5	4	4	5	4	4	4	4
19	1	2	2	1	2	2	2	1	2	1
312	8	8	8	16	8	7	7	7	8	7
1	1	1	0	1	2	1	1	1	1	2
106	38	40	38	42	36	45	53	80	41	40
6	17	12	9	19	19	20	11	27	22	16
310	2733	2622	2579	2662	2566	2529	2560	2691	2541	2720
473	2609	3395	3297	2580	2907	2974	3629	2896	2821	2683
0.91	0.02	0.02	0.03	0.02	0.02	0.02	0.02	0.02	0.02	0.02
214	50	54	59	49	56	51	51	50	51	48
7	0	1	1	2	0	3	0	1	0	0
6	0	0	0	0	0	0	0	0	0	0

from Holes 920B and 920D tends to decrease in abundance with increasing MgO, which probably reflects reductions in modal pyroxene. Cr/Ni ratios show a strong positive correlation with Al_2O_3 content (taken to correlate with total modal pyroxene). These data indicate that Cr behaves as a mildly incompatible element and Ni as a highly compatible element during melting and/or pyroxene depletion (Fig. 35); this Cr/Ni ratio will become smaller in the residuum with pyroxene depletion (or increased extents of melting). A Cr/Ni ratio vs. CaO plot shows that most of the Site 920 peridotites can be explained as mixtures of orthopyroxene and olivine, whereas the high CaO component causes a spread in the data compatible with increasing clinopyroxene or CaO enrichment during alteration (as discussed above). Cu, Zn, and V show weak negative correlations with increasing MgO and weak positive correlations with Al_2O_3 (similar to Cr), suggesting that each is behaving mildly incompatibly during mantle depletion and melting.

Lastly, the downhole plots for various major and trace elements seem to correlate with modal cyclicity documented by visual core description and thin-section modal data presented previously. Figure 36 shows Hole 920B and 920D downhole plots for Al_2O_3 (which is a function of pyroxene and spinel abundance) and Ni (which is a function olivine abundance) and shows a cyclicity similar to that observed in modal plots (Fig. 13). The strong peak in Al_2O_3 near the top of both holes corresponds to Unit 2, which is pyroxene rich. Note the depleted Ni contents at the same level. The base of Hole 920D also corresponds to a more pyroxene-rich zone, which is reflected in Al_2O_3 and Ni content.

Mafic Rocks

Bulk rock analyses of mafic rocks from Holes 920B and 929D include a range of intrusive types within each of the holes (Table 5). Most of the samples are from Hole 920B: a sample of plagioclase-olivine phyric diabase from Unit 4, an oxide gabbro from Unit 6, an amphibolite from Unit 7, and a metagabbroic vein, all intruded into the harzburgite. Samples from Hole 920D include two samples of olivine-plagioclase diabase from Unit 6 and an amphibolitized microgabbro from Unit 4.

These mafic rocks have very different histories and modes of solidification. All samples analyzed are altered to varying degrees and show significant loss on ignition. H_2O is variable and ranges from ~4–6 wt% in all olivine-plagioclase phyric diabases and in the gabbroic vein and from 0.71 to 2.29 in the remainder of the samples. The three diabase dike samples of Unit 4 (Hole 920B) and Unit 6 (Hole 920D) are all characterized by high MgO (13.03–15.08 wt%; Fig. 37). The amphibolite and the amphibolitized microgabbro have similar compositions. Apart from the unusually high MgO and high Mg# values of these rocks (up to 0.74), they are generally similar to N-MORB in various trace element abundances. Relative to previously reported chemical compositions of MARK basaltic rocks (Bryan et al., 1994), however, they are the most MgO-rich and incompatible-element-depleted basaltic compositions documented thus far from the MARK region (e.g., see Bryan et al., 1994). This is well displayed on a Zr vs. Y plot (Fig. 38) showing the field for MARK basalts from Bryan et al. (1994). Because of the altered state of these rocks, we have utilized mainly immobile trace elements in their discrimination. It should be noted, however, that primary mineralogy is still abundant in the diabasic rocks even with the high H_2O content.The questions of these unusually primitive "appearing" basalts and the alteration effects on the major and trace element compositions await more detailed shore-based studies.

The high Mg# (0.90) of the gabbroic vein in Sample 153-920B-10R-3, 0–5 cm, and its strong depletion in highly incompatible element abundances (Fig. 37) preclude it from representing a liquid composition. It appears to represent a very primitive gabbroic cumulate with intrusive contacts into the peridotite. The Mg# of the bulk rock is indistinguishable from the peridotite Mg numbers, indicating that these solidification products derived were close to equilibrium with the adjacent mantle assemblages or that extensive enrichment in MgO relative to FeO* occurred during alteration. The oxide gabbro of Sample 153-920B-13R-3, 129–132 cm, is very fractionated with respect to the other mafic samples analyzed (its Mg# is about 0.32; Fig. 37).

Table 5 (continued).

Hole:	920D	920D	920D	920D	920D	920D	920D	920D	920D	920D
Core, section:	17R-3	18R-3	19R-2	20R-1	20R-2	20R-4	21R-2	22R-2	22R-5	22R-7
Interval (cm):	37–43	75–81	13–19	103–109	24–30	38–44	40–46	86–92	104–110	16–22
Depth (mbsf):	145.74	156.1	163.8	172.93	173.3	175.92	183.15	192.66	195.67	197.49
Piece:	1C	4	1	13B	1B	3A	1C	1D	6B	1
Rock type:	Serpentinized harzburgite	Serpentinized harzburgite	Serpentinized harzburgite	Serpentinized harzburgite	Serpentinized harzburgite	Serpentinized harzburgite	Serpentinized harzburgite	Serpentinized harzburgite	Serpentinized harzburgite	Serpentinized harzburgite
Major elements (wt%)										
SiO_2	43.98	43.63	44.27	43.79	44.29	43.9	43.55	43.58	44.72	43.94
TiO_2	0.02	0.01	0.02	0.01	0.01	0.01	0.01	0.01	0.01	0.01
Al_2O_3	1.51	1.39	1.34	1.36	1.64	1.48	1.5	1.45	1.61	1.49
Fe_2O_3	9.25	10.9	9.71	9.34	9.05	9.11	9.09	8.83	8.77	8.88
MnO	0.14	0.15	0.14	0.14	0.15	0.14	0.14	0.13	0.14	0.14
MgO	43.9	42.74	43.33	44.14	43.49	43.85	43.95	42.93	43.22	43.22
CaO	0.39	0.14	0.25	0.23	0.26	0.39	0.73	1.41	0.57	1.39
Na_2O	0	0	0	0	0	0	0	0	0	0
K_2O	0	0	0	0	0	0	0	0	0	0
P_2O_5	0	0	0	0	0	0	0	0	0	0
Total	99.19	98.97	99.07	99.01	98.89	98.88	98.96	98.34	99.06	99.08
LOI	12.17	12.1	11.86	12.3	11.83	12.02	12.21	9.62	11.99	10.97
CO_2	0.51	0.38	0.48	0.63	0.63	0.56	0.46	0.45	0.55	0.71
H_2O	11.79	12.02	11.21	12.35	12.05	11.48	10.72	8.33	11.42	11.26
Trace elements (ppm)										
Nb	0	0	0	0	1	1	1	1	1	0
Zr	4	5	5	4	5	4	4	4	5	5
Y	2	1	1	2	1	2	1	1	1	1
Sr	8	7	7	8	8	8	8	8	8	8
Rb	1	2	1	2	2	1	2	2	2	1
Zn	47	47	42	43	40	40	43	39	36	44
Cu	11	10	9	18	13	18	24	29	27	18
Ni	2642	2501	2637	2648	2441	2582	2628	2514	2396	2522
Cr	3409	3071	2898	2900	3264	3191	3177	2664	3051	2640
TiO_2	0.02	0.02	0.02	0.02	0.02	0.02	0.02	0.02	0.02	0.02
V	55	55	53	51	63	56	54	49	57	52
Ce	0	0	1	0	2	0	0	0	0	3
Ba	0	0	0	0	0	0	0	0	0	0

Discussion

The ultramafic rocks recovered from Holes 920B and 920D dominantly have textural, modal, and compositional characteristics consistent with an origin as residues from mantle melting. However, Figures 16 and 31 suggest that there is no systematic relationship between the orthopyroxene and clinopyroxene abundances, as might be expected in a melting trend. If correct, this may indicate that, in places, the mantle has been enriched in clinopyroxene components after it was depleted. In fact, evidence for melt impregnation and clinopyroxene addition to the mantle assemblage is present in the core in the form of clinopyroxenite veins and of trails of spinel and of interstitial, undeformed clinopyroxene, which commonly show magmatic twins (Fig. 20). The geochemical data provide further evidence that there is little systematic relationship between orthopyroxene and clinopyroxene modal abundances in the core.

The range of modal variations in the ultramafic rocks is large and spans nearly the entire range of modal compositions documented in the extensive study of plagioclase-free abyssal spinel peridotites from the Indian and Atlantic oceans by Dick (1989). These modal variations take place in the core on a scale of centimeters to tens of meters. They appear to show cyclicity on a scale of ~30 to 100 m in both Holes 920B and 920D. Some of the smaller scale modal variations appear to be related to variations in the frequency of clinopyroxenite and gabbroic veins (Fig. 24). This may reflect melt wall/rock interactions, or incongruent melting along these melt pathways. Alternatively, this could represent original mantle heterogeneity. In this case, the preferred spatial association of the most depleted ultramafics with melt infiltration zones would be consistent with experimental evidence that shows that near-monomineralic rocks may be more permeable to melt (Kolstedt, 1992).

A series of mafic rocks ranging in scale from a few millimeters to a minimum of 4 m has intruded the ultramafic rocks. The coarse-grained gabbroic and pyroxenitic intrusions show a range of compositions, with Mg# numbers that range from 0.90 to 0.32 (Fig. 37). This suggests that these were derived from a range of melts, from those that

Table 6. Average bulk-rock analyses and standard deviation (in parentheses) for serpentinized peridotite from Holes 920B and 920D.

	Hole 920B (18 analyses)	Hole 920D (27 analyses)
Major element oxides (wt%)		
SiO_2	43.90 (0.70)	44.29 (0.54)
TiO_2	0.01 (0.005)	0.01 (0.006)
Al_2O_3	1.43 (0.17)	1.37 (0.09)
Fe_2O_3	9.32 (0.28)	9.31 (0.48)
MnO	0.13 (0.008)	0.13 (0.009)
MgO	43.69 (0.87)	44.38 (0.45)
CaO	0.45 (0.28)	0.25 (0.45)
Na_2O	0.00 (0)	0.00 (0)
K_2O	0.00 (0)	0.00 (0)
P_2O_5	0.00 (0)	0.00 (0)
Total	99.02	99.77
LOI	11.87 (0.64)	12.35 (0.69)
CO_2	0.55 (0.14)	0.24 (0.15)
H_2O	11.53 (1.36)	13.38 (0.99)
Mg#	90.20 (0.003)	90.4 (0.004)
FeO*	8.38 (0.25)	8.38 (0.43)
Trace elements (ppm)		
Nb	0.37	0.8
Zr	4.4	4.4
Y	1.5	1.3
Sr	8.1	8.5
Rb	1.2	1.2
Zn	42.7	36.3
Cu	17.3	15.8
Ni	2585	2614
Cr	2964	2785
V	53.0	52.2
Ce	0.5	0.5
Ba	0.0	0.0

Note: Mg# calculated with all iron as FeO. (*) = standard deviation.

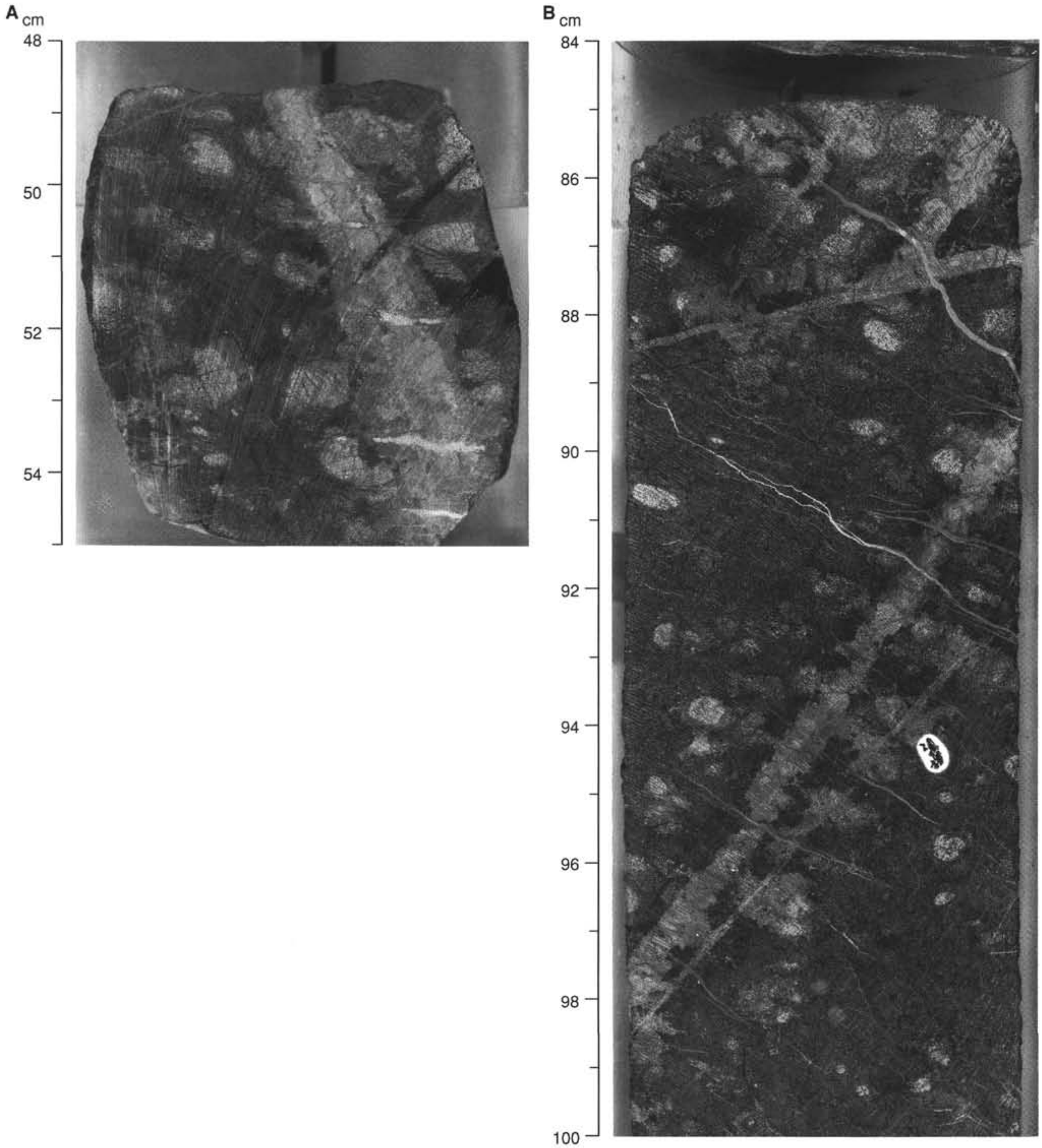

Figure 22. **A.** Harzburgite crosscut by an 8- to 12-mm-vein of pyroxenite with a partially altered rim and intensely altered tremolite(?) ± chlorite core. The crystal-plastic fabric is weakly developed in this piece. Subhorizontal gashes crosscutting the pyroxenite vein are filled by green and white serpentine ± aragonite. Sample 153-920D-10R-2, 48–55 cm. **B.** Weakly lineated, pyroxene-poor harzburgite cut by a set of planar, discordant pyroxenites or composite clinopyroxenite/gabbro veins. Clinopyroxene grains are altered to tremolite, actinolite, chlorite, and talc but retain primary grain shape in the thickest vein. The veins appear to form a conjugate set, one of which is near-perpendicular to the high-temperature crystal-plastic fabric and to thin, white discontinuous serpentine veins. Light grains in harzburgite are fresh orthopyroxene cores. Sample 153-920D-18R-3, 84–100 cm. **C.** Thin gabbroic veins consisting of interstitial plagioclase (altered to prehnite), clinopyroxene (altered to chlorite and tremolite), and accessory iron oxide minerals. These veins have diffuse margins with the host pyroxene-poor harzburgite. Light gray patches in harzburgite are comparatively less serpentinized than the darker groundmass. Sample 153-920D-18R-3, 44–59 cm. **D.** Pyroxene-poor harzburgite crosscut by a 1.5 mm gabbro veinlet containing altered pyroxene + interstitial plagioclase. The harzburgite does not possess a strong high-temperature fabric. Sample 153-920D-3R-1, 89–93 cm.

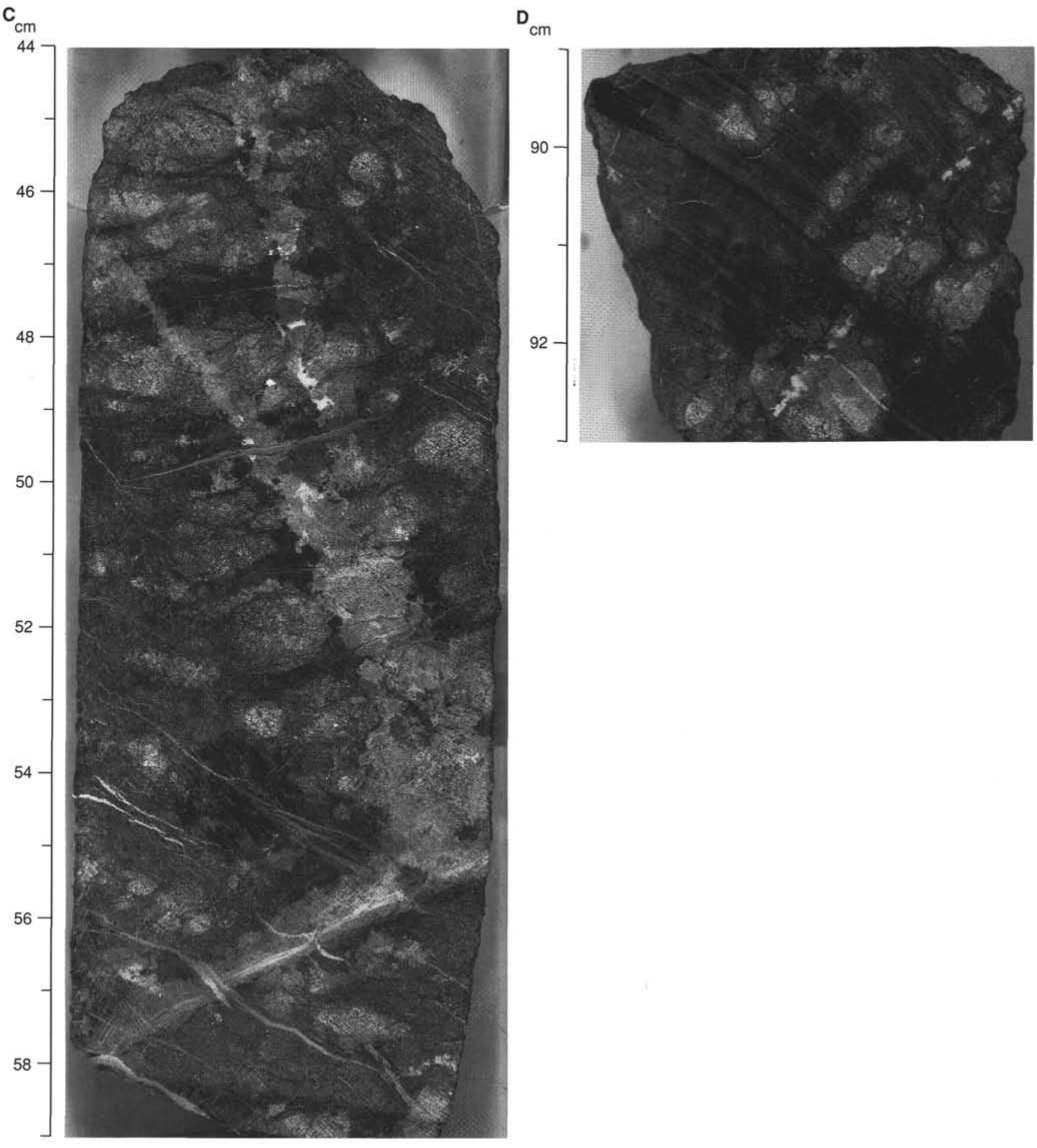

Figure 22 (continued).

were close to equilibrium with mantle assemblages to melts that were highly fractionated relative to most MORBs erupted at the surface.

The fine- to medium-grained intrusions, including the diabases in Holes 920B and 920D, the amphibolitized microgabbro of Hole 920D, and the amphibolite of Hole 920B, although now altered, appear to have similar compositions. Relative to other basalt analyses from the MARK region (Bryan et al., 1994), they are depleted in highly incompatible trace elements and enriched in MgO, Ni, and Cr (Figs. 37 and 38). The fact that the amphibolite and amphibolitized microgabbro are similar in composition to the diabase dikes suggests that they are derived from a diabase protolith. Dike intrusions in the ultramafics may thus have occurred during three distinct episodes, one characterized by high-temperature ductile deformation and hydration (amphibolite), one characterized by high-temperature static hydration (amphibolitized microgabbro), and finally a last episode characterized by lower temperature static hydration (porphyritic diabases).

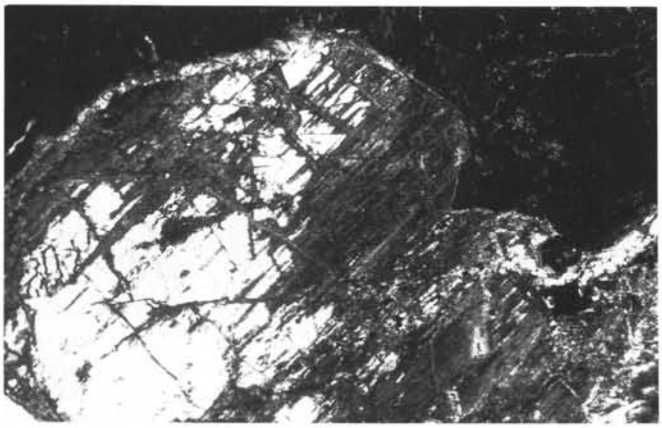

Figure 23. Photomicrograph of euhedral termination of orthopyroxene grain along the wall of a composite clinopyroxenite-gabbro vein in harzburgite host rock. Euhedral terminations also occur in plagioclase and clinopyroxene grains along this wall and indicate that the melt channel was dominantly melt rather than a solid matrix. Sample 153-920B-11R-2, 119–122 cm. Field length is 2 mm.

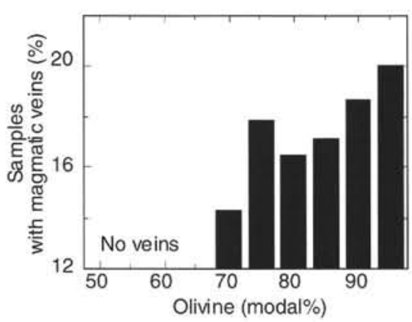

Figure 24. Histogram showing the percentage of ultramafic samples with magmatic veins as a function of modal percentage of olivine (compare with histogram shown in Fig. 14). Note the higher frequency of vein occurrences within harzburgites with high olivine modal contents and within dunites (>90 modal% olivine).

Figure 25. Photomicrograph of amphibolitized microgabbro with small euhedral plagioclase laths enclosed in hornblende grain. Sample 153-920D-7R-2 (Piece 2B, 22–29 cm). Field length is 2 mm.

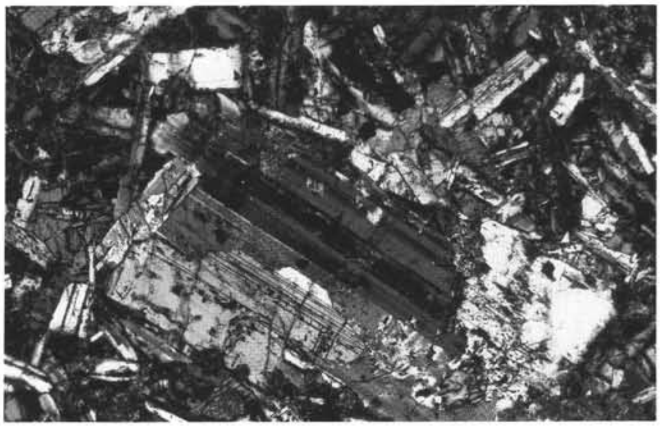

Figure 26. Photomicrograph of zoned plagioclase phenocryst and subophitic texture in the coarse interior of a diabase intrusion. Sample 153-920B-9R-3, 123–126 cm (Unit 4). Field length is 2 mm.

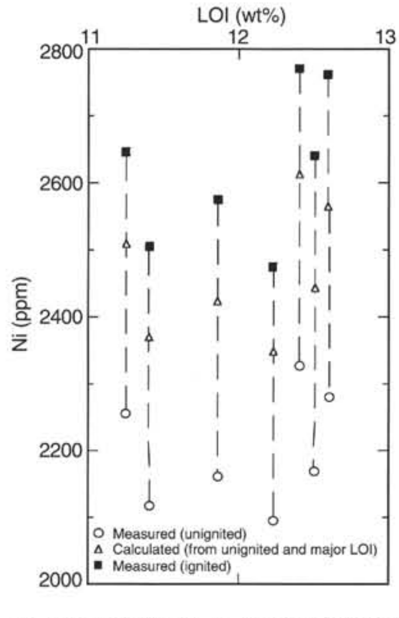

Figure 27. Results of test conducted on ignited and unignited ultramafic samples for measuring trace element abundances in highly serpentinized ultramafic rocks. Plot shows Ni abundances measured on ignited and unignited samples and calculated based on LOI. Note large increases in measured Ni abundances after devolatilization. The calculation based on LOI fails to adjust the composition to the appropriate ignited value. All trace element measurements on ultramafic samples therefore were conducted on ignited samples to approximate their anhydrous abundances prior to hydration and dilution.

METAMORPHIC PETROLOGY

Introduction

Variably altered and deformed ultramafic, gabbroic, and diabasic rocks recovered from Site 920 (Holes 920A, 920B, and 920D) represent the first significant sampling of upper mantle and intercalated lower crustal rocks formed in a slow-spreading environment. The coherent recovery of nearly continuous sections in many cores allows characterization of metamorphic and hydrothermal processes on vertical scales, ranging from centimeters to 100 m and offers a unique opportunity to assess the temporal and spatial evolution of deep-seated alteration and deformational processes in submarine environments. The ultramafic and gabbroic lithologies record a complex history involving substantial metamorphic and hydrothermal modification, with subsequent unroofing by extensional tectonics. These samples provide an important reference section for comparison of magmatic and hydrothermal processes in similar spreading environments and in ultramafic and gabbroic rocks recovered during ODP Leg 147 from fast-spreading East Pacific Rise crust exposed in the Hess Deep Rift.

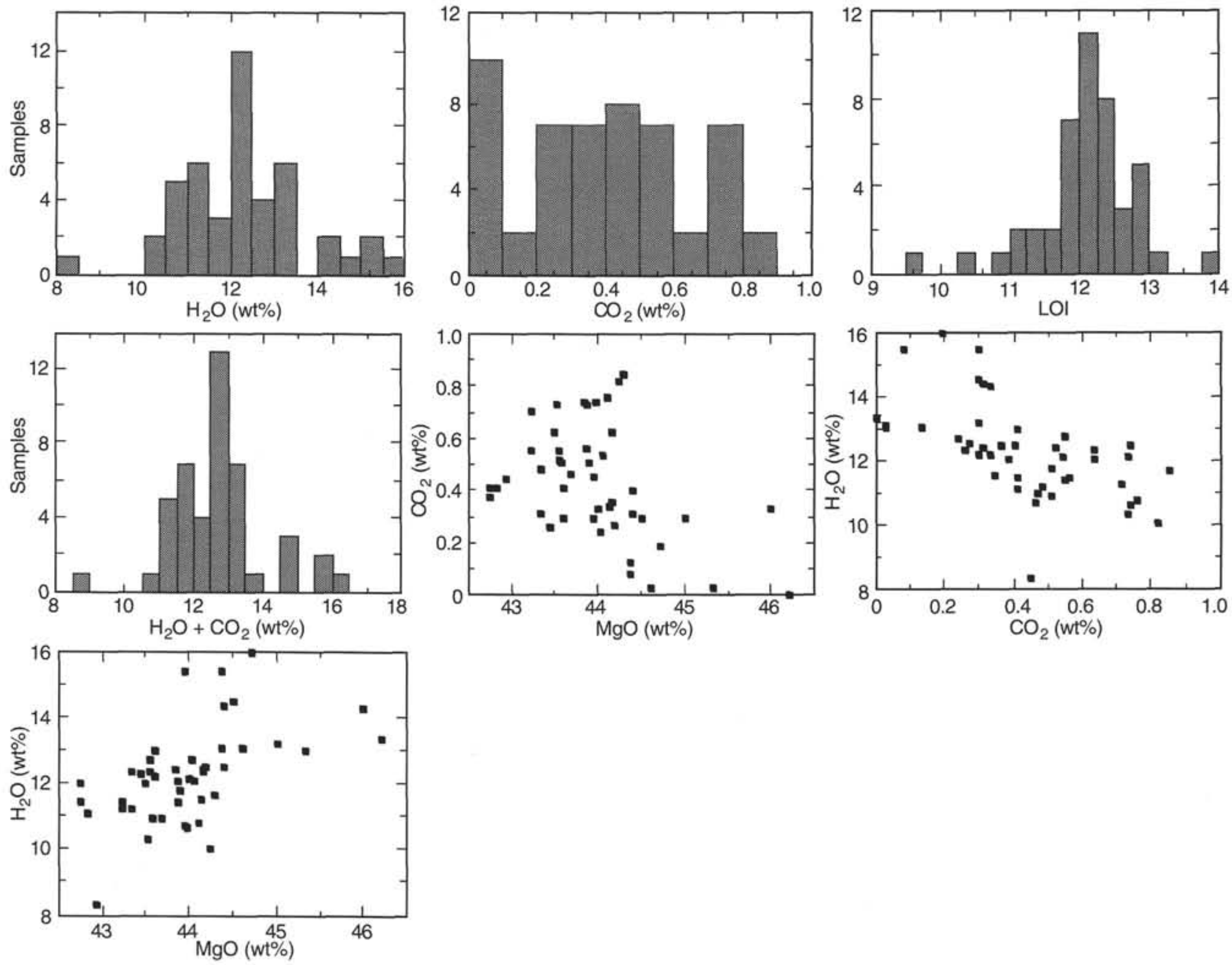

Figure 28. Histograms showing the abundances of H_2O, CO_2, LOI, and total $H_2O + CO_2$ for residual harzburgites from Holes 920B and 920D (Table 5). Ultramafic rocks are strongly hydrated and, as expected, LOI does not match total volatile abundances. Also shown is the negative correlation between total H_2O and CO_2, the weak positive correlation between H_2O and MgO, and the weak negative correlation between CO_2 and MgO.

All ultramafic lithologies recovered at Site 920 are extensively altered and are characterized by the pervasive development of mesh-textured serpentine with minor amounts of talc, amphibole, and chlorite. The pervasive alteration is associated with multiple generations of microscopic to mesoscopic veins, the earliest of which include intrusion by pyroxenitic and gabbroic melts and concomitant wall-rock reaction. The magmatic veins were commonly reactivated during later hydrothermal episodes involving brittle deformation and resulted in the development of four to five distinct vein sets. The veins are typically serpentine-bearing, though actinolite, chlorite, talc, carbonate minerals, pyrite, and iron oxide minerals are present in some veins as well.

Gabbroic, pyroxenitic, and diabasic rocks, which occur as discrete intervals within the ultramafic suite, are typically moderately to highly altered. Secondary mineral phases include brown hornblende, tremolite-actinolite, and chlorite with lesser amounts of epidote, prehnite, clay, and zeolite minerals. Evidence from apatite-hosted, primary fluid inclusions within the gabbroic rocks indicates that the earliest fluids to circulate were magmatic in origin. Later crosscutting veins include variable amounts of amphibole, prehnite, zeolite, epidote, and carbonate minerals. Alteration and vein-filling mineral assemblages require that subsequent fluid circulation occurred under amphibolite to zeolite facies conditions, with resultant pervasive alteration to greenschist facies mineral assemblages.

The following sections describe metamorphic and alteration relationships in the ultramafic, gabbroic, and diabasic suite recovered from Site 920. Downhole variation between the various rock units and intra-hole variations are discussed, and a summary of the hydrothermal and metamorphic history preserved in these rocks is presented.

Alteration of the Serpentinized Peridotite Suite

All ultramafic lithologies recovered at Site 920 are generally affected by significant secondary replacement of primary minerals, with most intervals exhibiting 85%–100% alteration (Fig. 39). Olivine is commonly the most intensely altered mineral phase, and, as a consequence, the most pervasive replacement by secondary phases generally occurs in pyroxene-poor dunitic zones.

Porphyroclastic Harzburgites

Porphyroclastic serpentinized harzburgites exhibit variable and heterogeneous alteration with the most intense alteration occurring in orthopyroxene-poor zones, where alteration is typically 95%–100% (Figs. 39 and 40; Table 7). The pervasive alteration of olivine is linked to a dense microscopic network of serpentine-bearing veinlets (<0.03–0.05 mm wide) that consist of cross-fibered serpentine with cores of very fine grained, iron oxide minerals. The veinlets form a mesh texture and are cut by discontinuous veins of serpentine and

Table 7. Site 920 metamorphic mineral summary.

Lithology	Mineralogy: Primary	Mineralogy: Secondary	Facies/alteration intensity
Harzburgite	Olivine	Chrysotile, antigorite(?) chlorite talc, clay minerals, brucite, magnetite	Upper greenschist to zeolite, 50% to >90% altered
	Orthopyroxene	Cummingtonite, tremolite, Mg-rich chlorite, talc, bastite, magnetite	
	Clinopyroxene	Tremolite-actinolite, pyrite, magnetite	
Gabbric rocks	Olivine	Secondary olivine, talc, magnetite, amphibole ± chlorite, clay minerals	Transitional granulite to amphibolite, to zeolite, slightly rodingitized, 50%–100% altered
	Clinopyroxene	Brown amphibole, green amphibole, colorless amphibole, chlorite, secondary clinopyroxene, pyrite, magnetite	
	Orthopyroxene	Cummingtonite, tremolite, chlorite, magnetite	
	Plagioclase	Secondary plagioclase, prehnite, epidote, zoisite, zeolite minerals, chlorite, actinolite, carbonate minerals	
Diabase	Plagioclase	Tremolite-actinolite, prehnite, chlorite, clay minerals, secondary plagioclase, hydrogrossular, zeolite minerals, epidote, carbonate minerals	Amphibolite to zeolite, 30%–80% altered
	Olivine	Chlorite, clay minerals, serpentine, amphibole	
	Clinopyroxene	Brown amphibole, magnetite, green amphibole	
	Plagioclase	Chlorite, clay minerals, amphibole?	

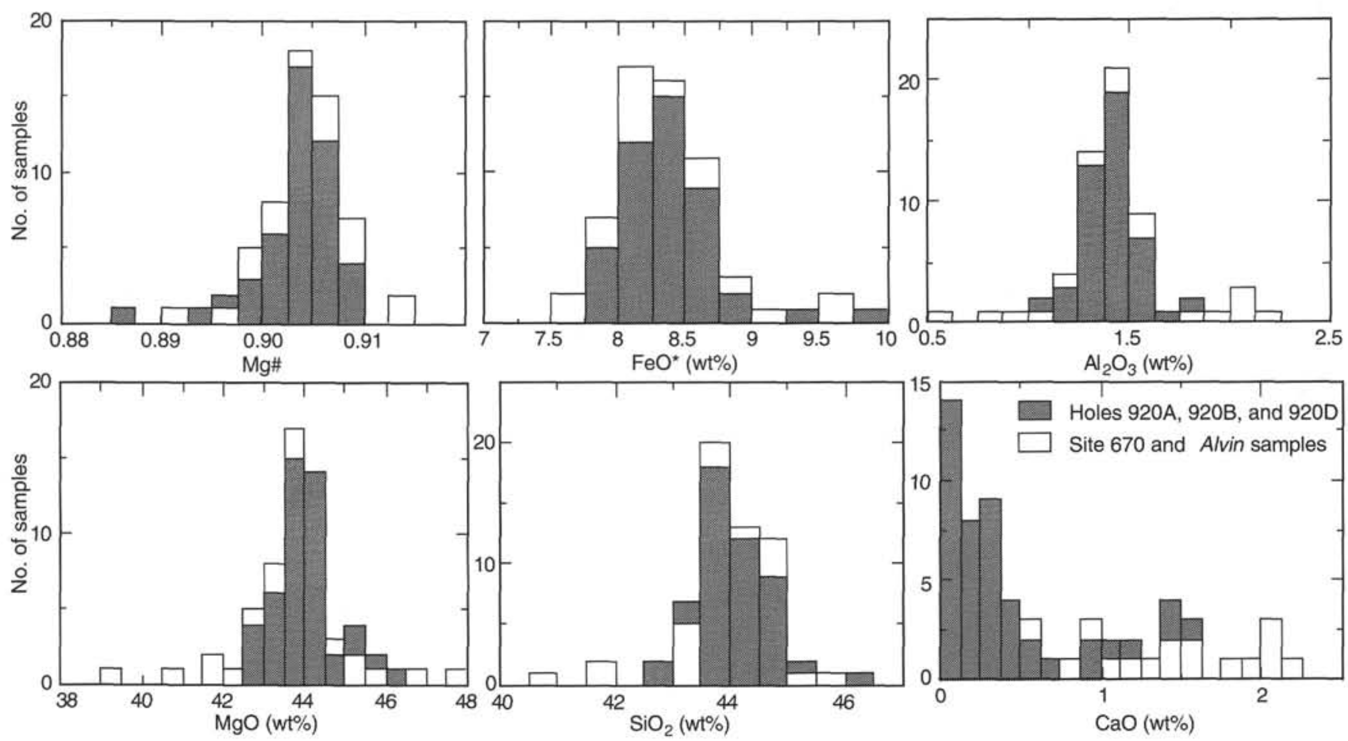

Figure 29. Histograms showing the bulk-rock major element compositions of harzburgites from Holes 920A, 920B, and 920D, and from Site 670 (Di Donato et al., 1990) and *Alvin* samples (Casey, unpubl. data).

serpentine + clay mineral veins. Locally, the serpentine forms anisotropic polygonal networks after olivine.

Within the harzburgites, composite lenses of segmented and elongated aggregates of porphyroclastic and recrystallized orthopyroxene, olivine, and less abundant clinopyroxene commonly exhibit the lowest intensity of alteration, with local replacement as little as <5%–10% (Figs. 19 and 41). Narrow rims (50–100 μm wide) of cummingtonite after orthopyroxene, talc after olivine, and trace amounts of amphibole after clinopyroxene form an interconnected network within the aggregates (Fig. 19). Fine-grained fibrous amphibole and serpentine also rim the aggregates. In domains separating the polymineralic lenses, veined and highly serpentinized orthopyroxene and olivine are common.

The aggregates of orthopyroxene, olivine, and clinopyroxene are commonly wrapped by an anastomosing subparallel network of composite, <1-mm-wide wispy, white asbestiform serpentine, and serpentine + magnetite veinlets (Fig. 41). In hand sample, the aggregates commonly consist of apple-green cores (Fig. 41) where fresh to slightly altered, and they become mottled gray-green to olive green where more intensely altered. With progressive alteration of the orthopyroxene porphyroclasts and mineral aggregates, minor amphibole intergrown with serpentine, chlorite, and fine-grained oxide minerals completely replace most of the primary phases (Fig. 42). Spinel grains in these highly altered zones are commonly rimmed by fine-grained oxide minerals and enclosed by halos of chlorite. In the most intensely altered samples, ghosts of the porphyroclasts and aggregates are completely replaced by bastite and serpentine, respectively.

Away from the polymineralic lenses, secondary mineral assemblages such as cummingtonite and talc occur only in trace amounts,

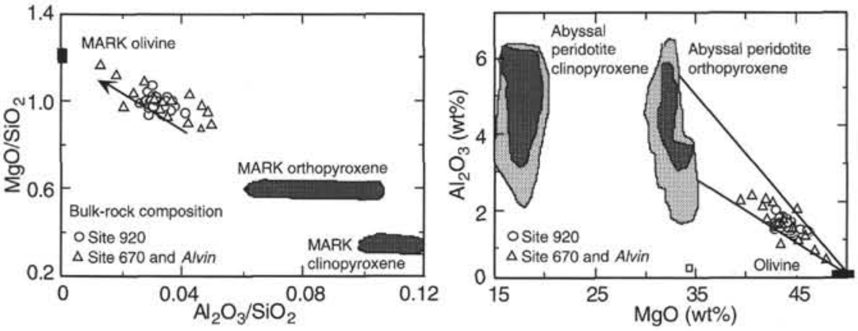

Figure 30. MgO/SiO_2 vs. Al_2O_3/SiO_2 and Al_2O_3 vs. MgO diagrams showing the bulk rock compositions of peridotites from Holes 920B and 920D, and from other samples in the MARK area (referred to in Fig. 29). Also plotted are fields for the mineral compositions (olivine, clinopyroxene, and orthopyroxene) measured on Site 670 peridotites (Komor et al., 1990; Juteau et al, 1990). The fields of clinopyroxene and orthopyroxene compositions in abyssal peridotites from the Atlantic (Bonatti et al., 1992) are also shown in the Al_2O_3 vs. MgO diagram (light gray). The arrow in the MgO/SiO_2 vs. Al_2O_3/SiO_2 diagram shows the trend in bulk compositions corresponding with decreasing modal abundances of pyroxene. The two lines in the Al_2O_3 vs. MgO diagram are mixing lines between olivine and the range of orthopyroxene compositions measured in the MARK area samples.

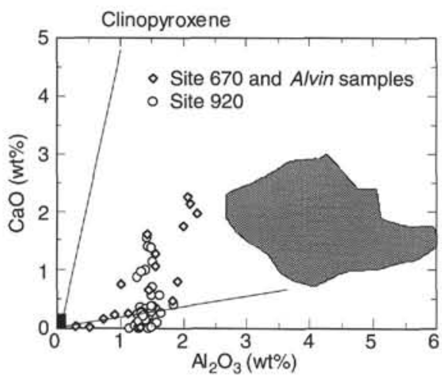

Figure 31. Al_2O_3 vs. CaO from bulk rock chemistry from Sites 920 and 670 and *Alvin* samples (referred to Fig. 29). Gray field shows the range of orthopyroxene compositions measured on Site 670 peridotites (Komor et al., 1990; Juteau et al., 1990). Subhorizontal line is a mixing line between olivine and the most depleted orthopyroxene composition measured on Site 670 peridotites. Subvertical line is a mixing line between olivine and clinopyroxene (composition measured on Site 670 peridotites).

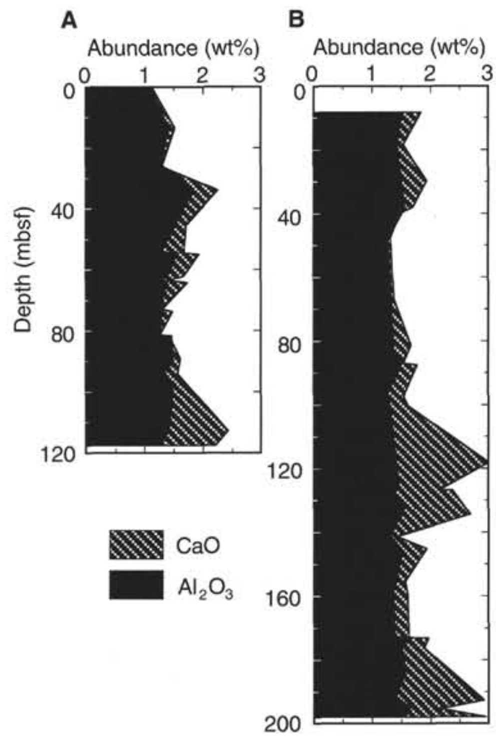

Figure 32. Downhole plot of the abundances of CaO and Al_2O_3 bulk rock chemistry abundances for (**A**) Hole 920B and (**B**) Hole 920D, reflecting modal variations in total pyroxene (indicated by variation in Al_2O_3) and possibly clinopyroxene/orthopyroxene abundances indicated by the abundance of CaO. The zones of increased CaO generally correlate with zones of increased clinopyroxene abundances as determined from thin-section studies (Fig. 16).

while lower-temperature serpentine and clay minerals are pervasive. Olivine kernels that represent relict islands become progressively rare and generally exhibit a reduction in size away from the aggregates because of more extensive replacement by serpentine-magnetite mesh. In intensely altered areas, harzburgites typically show patchy alteration with replacement of olivine kernels by white serpentine with yellow-green rims (Fig. 43). Concentrated patches of the white and green serpentine that are enclosed in a dark brown-black to olive green serpentine mesh give samples a patchy appearance.

Serpentinized Harzburgite and Dunite-hosted Porphyroclastic Mylonite Zones

Intense localized deformation form 2- to 20-cm-wide bands of porphyroclastic mylonite in some harzburgite samples. These bands commonly juxtapose intervals of gabbro and/or clinopyroxenite with adjacent peridotite (Fig. 44; e.g., Samples 153-920D-2R-1, Piece 13, 116–119 cm, and 153-920D-2R-1, Piece 14, 138–141 cm). The foliation in the mylonite zones is defined by discontinuous lenses of polygonal, neoblastic olivine grains, strong elongation of olivine and orthopyroxene porphyroclast, and wrapping magnetite-ilmenite rich stringers. Deformation and extensive recrystallization in both ultramafic and gabbroic material has resulted in elongation of olivine porphyroclasts and extensive grain-size reduction of primary phases. Retrograde alteration of olivine is limited to minor replacement by fine-grained iron oxide minerals and fine serpentine networks of interstitial to polygonal olivine grains. The mylonites exhibit the lowest intensities of alteration in Hole 920D ultramafics.

Elongate and ribbon- to sigmoidal-shaped orthopyroxene porphyroclasts in the mylonites exhibit undulose and patchy extinction, deformation lamellae and kink bands, and are partially recrystallized into fine polygonal grains. The recrystallized assemblage adjacent to the orthopyroxene porphyroclasts is typically comprised of neoblastic olivine, and lesser amounts of clinopyroxene and orthopyroxene, which form enclosing aureoles. The neoblastic olivine locally grows subparallel to parallel to orthopyroxene porphyroclastic grain boundaries, mimicking formation of tails on the porphyroclasts. Recrystallized olivine grain size progressively increases away from the orthopyroxene porphyroclasts.

In the ultramafic-rich zones of the mylonite, equant and recrystallized porphyroclasts of clinopyroxene containing blebs of brown amphibole are commonly enclosed in polymineralic lenses of fine-grained olivine, orthopyroxene, and clinopyroxene neoblasts. The grain sizes

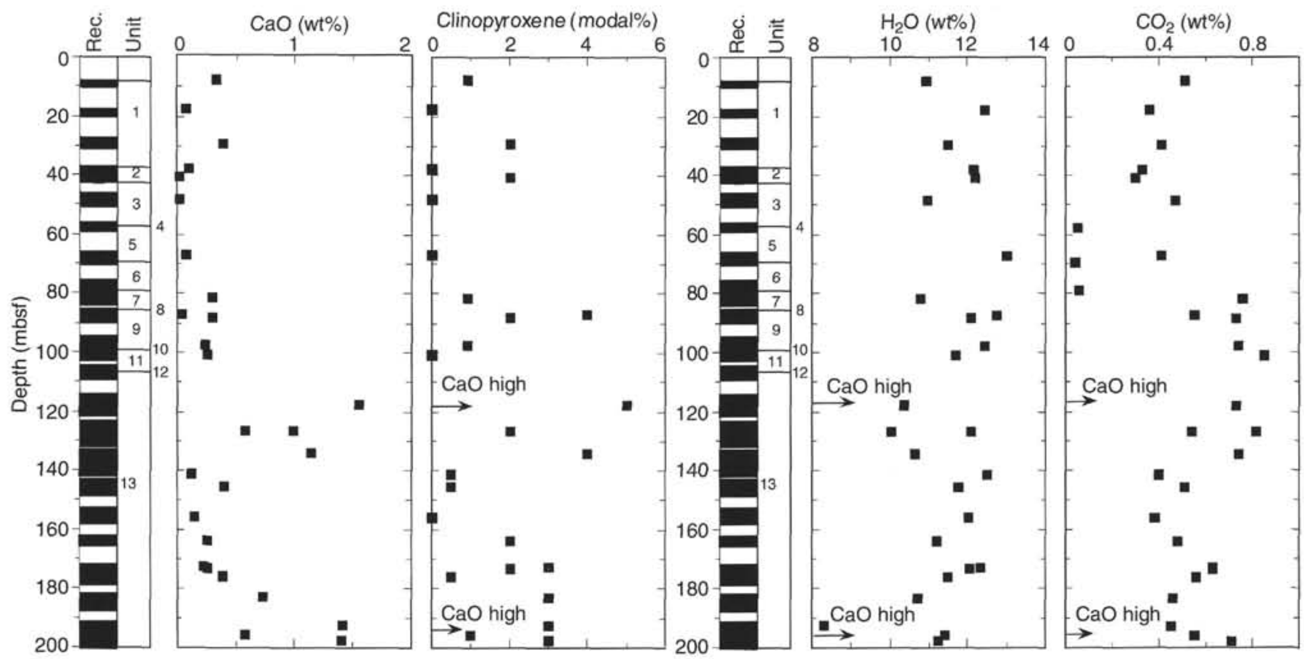

Figure 33. Downhole plots of bulk rock CaO, H_2O, and CO_2 contents and of modal clinopyroxene (thin-section estimates) in serpentinized harzburgites of Hole 920D, showing the correlation between CaO-rich and clinopyroxene-rich zones. Zones of highest alteration (H_2O) are also zones where CO_2 is the lowest, suggesting that CO_2 abundances cannot be explained by the extent of alteration.

in these polymineralic recrystallized zones are notably smaller than in olivine-dominated aggregates. Similar to the porphyroclastic harzburgite intervals, retrograde alteration of pyroxene-rich zones in the mylonites is minor. Secondary minerals after the porphyroclasts include green amphibole and fine-grained magnetite.

Deformation in the mylonitic shear zones has resulted in the common transposition of metagabbroic or metapyroxenitic lenses into the mylonitic foliation (Fig. 45). The aggregates of recrystallized plagioclase and pyroxene derived from the gabbro or clinopyroxenite form a somewhat diffuse interfingering between the recrystallized ultramafic assemblages. Porphyroclastic grains and associated polymineralic lenses associated with the ultramafic material are bounded by discontinuous and anastomosing zones composed of isolated fine-grained porphyroclasts of orthopyroxene, olivine, clinopyroxene, and rare plagioclase, apatite, and zircon. The porphyroclasts are enclosed in a fine-grained colorless matrix of chlorite. The boundaries of these bands are rimmed by fine-grained brown amphibole, actinolite, chlorite, and fine stringers of magnetite ± ilmenite that form alternating bands with extremely fine-grained olivine and an isotropic polygonal-shaped mineral after olivine.

Alteration of Pyroxenite and Oxide-rich Gabbro Veins in the Serpentinized Peridotites

In the peridotites, complex macroscopic pyroxenite and gabbroic veins crosscut the pervasive background mesh-textured serpentine (Figs. 45 to 48) and typically comprise the earliest vein assemblage in the serpentinized peridotites (Table 8). These pods and veins, which reach up to several centimeters in size, comprise <1% of the core and are most commonly associated with orthopyroxene porphyroclast-poor areas (see discussion in "Igneous Petrology," this chapter). They are inferred to be the products both of crystallization and wall-rock interaction. Though igneous textures are preserved in some samples, the magmatic veins are generally pervasively altered and higher temperature secondary mineral assemblages are better preserved in the veins than in the serpentinized peridotite host (Fig. 39 and Table 7).

Pyroxenite Veins

Pyroxenite veins in the peridotites are pervasively altered (80%–100%) and replacement minerals commonly partially to completely obscure the primary mineralogy (Figs. 45 and 46). Identification of vein protolith in pervasively altered samples, in which original primary igneous textures were obscured, is based on secondary mineral assemblages and presence of minor to trace relict igneous phases and pseudomorphs. Veins dominated by cummingtonite, tremolite and/or actinolite after pyroxenes, and which lack remnant plagioclase or prehnite are inferred to have been derived from pyroxenites.

The margins of the pyroxenite veins are commonly diffuse on a thin-section and hand-sample scale, resulting both from enhanced growth of clinopyroxene along vein margins and in adjacent host rock, and from the common preservation of fresh olivine kernels adjacent to vein margins (Fig. 45). This enhanced grain growth of primary wall-rock phases may reflect melt infiltration and/or diffusion into the surrounding host rock during vein formation (see "Igneous Petrology," this chapter). Alteration of the bounding peridotite away from the localized zones of pyroxene and olivine preservation is commonly pervasive, with almost complete replacement of harzburgitic and dunitic material by mesh-textured serpentine. These intensely altered zones are commonly devoid of iron oxide minerals, in contrast to the normal association of serpentine and iron oxide minerals in these rocks (e.g., Sample 153-920D-17R-1, Piece 4, 46–51 cm). Vein and host-rock contacts in some samples are characterized by a <1- to 1-mm-wide talc-dominated zone. This zone is intergrown with fibrous tremolite-actinolite and serpentine, which encloses relict anhedral islands of orthopyroxene and chlorite-rimmed spinel. More commonly, however, the contact is marked by the development of fine-grained to well-crystallized radiating amphibole crystals growing perpendicular to the vein walls. Relict orthopyroxene along some vein margins is pervasively amphibolitized in these zones. Associated rimming amphibole commonly grows perpendicular to the pyroxene host, where it forms radiating euhedral crystals that penetrate into the vein. Tremolite is well-developed and forms columnar aggregates and long prismatic crystals with intermixed fibrous patches (Fig. 45).

Table 8. Vein summary, Holes 920A, 920B, and 920D.

Host rock	Vein type/mineralogy	Color	Width	Orientation/form	Comments
Peridotite	Gabbro and pyroxenite	Green, white, brown	1 mm to >100 mm	Discordant or concordant to crystal and plastic foliation	Commonly postdates crystal plastic foliation but some veins are sheared, typically form first generation of veins and are pervasively altered to amphiboles, and Ca-bearing phases
Peridotite	Serpentine + magnetite	Green black to white	submillimeter	Define anastomosing serpentine foliation	Forms pervasive serpentine mesh and wraps porphyroclasts
Peridotite	Serpentine + actinilite + chlorite + talc	Dark green to black	1–10 mm	Commonly discordant to anastomosing foliation, but may run parallel to it	Some contain narrow chlorite+serpentine alteration halos, generally postdate foliation
Peridotite	Serpentine + magnetite	White to black	<1 mm	Commonly discordant to anastomosing foliation, but some composite arrays oriented perpendicular to it	Wispy, white asbestiform and en echelon arrays, thickest at widest point of porphyroclasts, intensity is dependent on porphyroclast abundance
Peridotite	Serpentine + magnetite ± carbonate minerals ± pyrite	Chalky white to aqua	>5 mm	Branching, randomly oriented	Commonly massive and wide
Peridotite	Carbonate minerals + pyrite ± clay minerals	White	<1–3 mm	Branching, randomly oriented	Commonly reactivate earlier serpentine veins, pyrite and clay minerals form hairline stringers
Peridotite, gabbro, and pyroxenite veins	Serpentine	White to aqua	1–3 mm	Commonly discordant to magmatic veins	Form discontinuous sigmoidal shaped veins
Gabbro and clinopyroxenite intervals	Actinolite + chlorite	Green to dark green	<1–1 mm	Randomly oriented	Commonly cut relict plagioclase
Gabbro intervals	Prehnite + zeolite ± carbonate minerals ± clay minerals	White	1/17 mm	Randomly oriented	Associated with incipient Ca-metasomatism of wall rock
Diabase	Prehnite + zeolite ± clay minerals	White	2–3 mm	Branching, randomly oriented	Minor to moderate alteration of host rock

Talc decreases in abundance toward the core of magmatic veins with a corresponding marked increase in very well-crystallized coarse- to medium-grained secondary amphibole. The amphibole exhibits pleochroic pale-green cores and rims, and a high extinction angle (~25°), indicating that it is probably cummingtonite. The cummingtonite(?)-rich patches are locally associated with fibrous, to well-crystallized tremolitic-actinolitic amphibole. Chlorite is commonly associated with the amphibole-rich pods. In these zones, chlorite forms well-crystallized rosettes and exhibits anomalous blue birefringence. Relict anhedral clinopyroxene is present in low to moderate modal amounts. The cores of the metapyroxenite veins contain medium- to coarse-grained cummingtonite, tremolite, and chlorite (Fig. 46). Reactivation of the pyroxenite veins during the formation of later serpentine veins is common, resulting in complex composite veins with cores of serpentine enclosed in a chlorite-amphibole matrix. The early magmatic veins generally are crosscut by serpentine veins that are <1 to 1–2 mm wide, discontinuous, and aqua-green to white, and more rarely they are crosscut by carbonate mineral veins. Alteration halos, generally 2–3 mm wide, of serpentine ± intergrown actinolite and chlorite rim vein margins (Fig. 45).

Gabbroic Veins

Gabbroic veins in which both contacts are preserved range from 1–2 mm to 45 mm wide; however, core breakage along the veins is not uncommon, and therefore, only one vein-host rock contact is preserved in many samples. The gabbroic veins typically do not exhibit extensive deformation (Fig. 47), though moderately deformed and recrystallized coarse-grained gabbros do occur. Alteration intensity of the gabbroic rocks is pervasive and alteration to Ca-bearing phases is common (Table 7). In the most highly altered samples, in which primary mineralogy is almost completely obscured by formation of secondary minerals, abundant actinolite, and prehnite after clinopyroxene and plagioclase, respectively, are interpreted to indicate a gabbroic protolith.

Coarse-grained clinopyroxene crystals within the gabbroic veins are commonly turbid due to replacement by fluid inclusion- and oxide-rich secondary clinopyroxene and fine-grained amphibole. They are altered to variable amounts of brown hornblende and subradiating aggregates of prismatic and columnar sprays of actinolite, which commonly exhibit dusty margins. Boundaries of relict grains are perva-

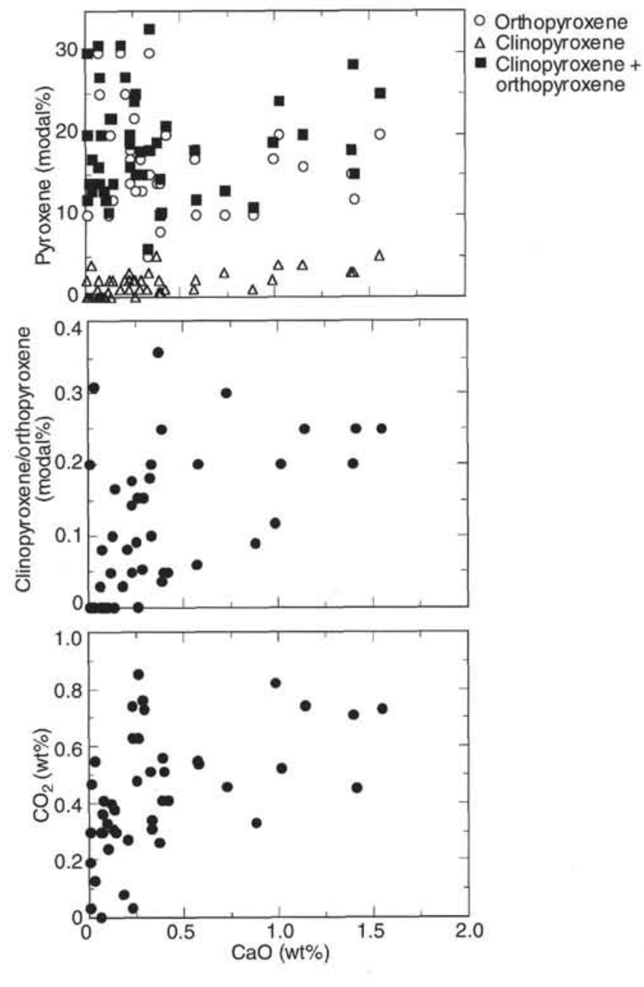

Figure 34. Bulk-rock CaO vs. thin-section estimates of modal clinopyroxene and orthopyroxene contents showing positive correlation with clinopyroxene content, but no correlation with total pyroxene or orthopyroxene content. Correlation between high-CaO rocks and CO_2 suggests that CO_2 concentrations are highest in clinopyroxene-rich zones.

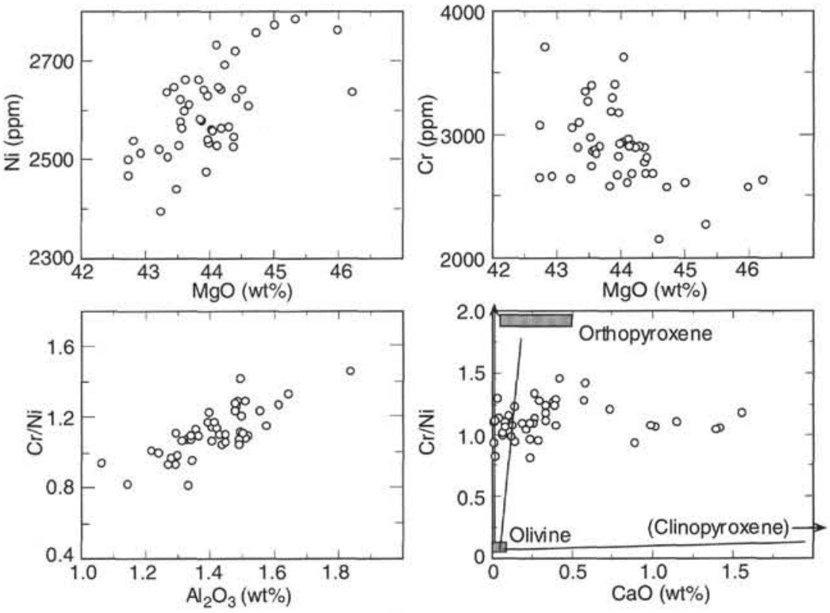

Figure 35. Bulk-rock Ni vs. MgO, Cr vs. MgO, Cr/Ni vs. Al_2O_3, and Cr/Ni vs. CaO diagrams for Holes 920B and 920D peridotites. Rectangles in Cr/Ni vs. CaO diagram indicate range of mineral compositions for olivine and orthopyroxene in peridotites from Site 670 (Komor et al., 1990; Juteau et al., 1990). Lines are mixing trends between olivine and orthopyroxene and clinopyroxene compositions.

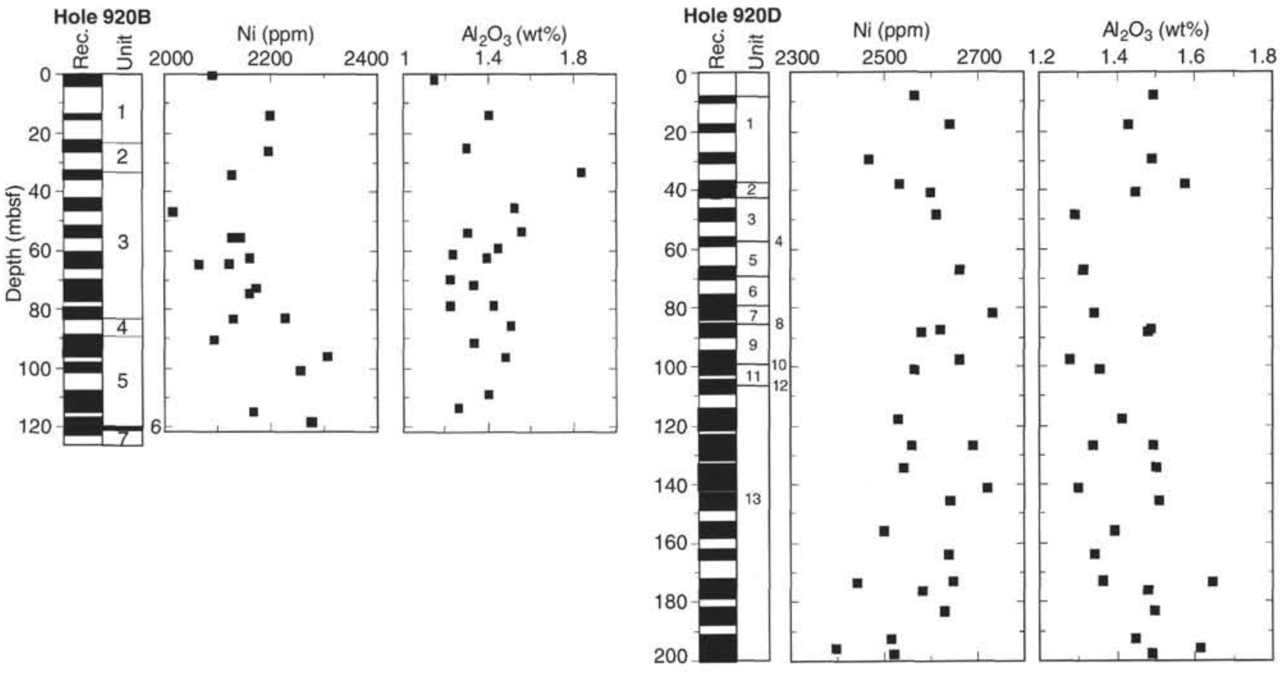

Figure 36. Downhole plots of bulk-rock abundances of Ni and Al_2O_3 in serpentinized harzburgites in Holes 920B and 920D.

sively replaced by amphibole that is fine-grained and green to colorless. Other alteration minerals include fine-grained magnetite, pyrite, and clay minerals. The pyroxene grains are commonly slightly to moderately deformed, with well-developed deformation bands, sutured grain boundaries, and minor to moderate subgrain development. They are locally recrystallized to secondary clinopyroxene and brown amphibole (e.g., Sample 153-920D-12R-3, Piece 5, 93–96 cm). Orthopyroxene grains are typically pervasively replaced by amphibole with replacement along cleavage planes by fine-grained cummingtonite. In the most intensely altered zones they are completely pseudomorphed by chlorite.

Alteration of plagioclase is heterogeneous and generally most intense adjacent to crosscutting hydrothermal veins (Figs. 47 and 48). Relict grains exhibit patchy and undulatory extinction, and anhedral grain boundaries with subgrain development is common in some samples. Plagioclase grains typically exhibit extensive replacement by prehnite and lesser amounts of actinolite, chlorite, zoisite, hydrogrossular garnet, and carbonate, zeolite and clay minerals (Fig. 49). The abundance of hydrous calcium-aluminum silicates in the gabbroic veins indicates that many of these samples have undergone incipient rodingitization.

Apatite and zircon grains are relatively common in the gabbroic veins as accessory magmatic phases. They occur as medium- to fine-grained, anhedral and highly-strained grains, which exhibit subgrain development and embayed grain boundaries. They are commonly partially overgrown by amphibole and chlorite. Primary and secondary, vapor-dominated, fluid inclusions within apatite are common, but are rare in zircon.

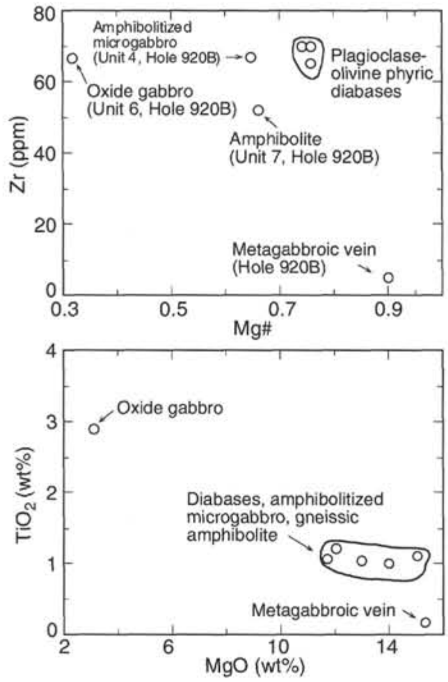

Figure 37. Mg# vs. Zr and MgO vs. TiO_2 diagrams in mafic rocks from Holes 920B and 920D.

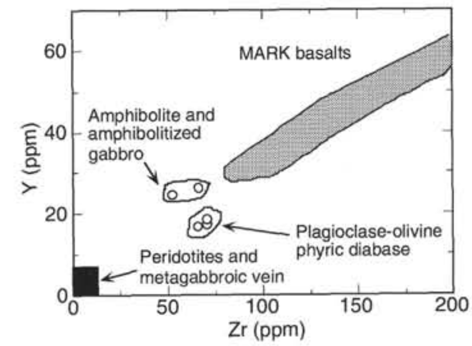

Figure 38. Zr vs. Y bulk-rock composition diagram showing the field for MARK basalts (gray field) from Bryan et al. (1994), the composition of mafic samples (except for the metagabbroic vein of Sample 153-920B-10R-3, 0–5 cm) from Holes 920B and 920D (open circles), and the composition of peridotites and the metagabbroic vein from these holes (black field).

Hydrothermal Veins within the Serpentinized Peridotites

In the serpentinized peridotites, hydrothermal veins are typically dominated by serpentine minerals, though variable amounts of other phases may be associated as well (Table 8). Composite and discrete veins can include brucite, talc, prehnite, smectite, aragonite and other carbonate minerals, sulfide, and clay minerals (Fig. 40B). On the basis of the most common crosscutting textural relationships observed in hand sample and thin-section analyses, four successive generations of macroscopic hydrothermal veins can be recognized within the harzburgites (Fig. 50; see "Structural Geology," this chapter). Although crosscutting relationships of the different vein generations are commonly consistent, there are exceptions to this general chronology of the mesoscopic veins. Mineralogy of the different vein generations was characterized in hand sample and confirmed by thin-section analyses. Identification of fine-grained vein filling minerals was facilitated by shipboard XRD studies on representative samples (Fig. 51). Below we describe the characteristics of hydrothermal veins and provide a general chronology of the veining events.

Serpentine + Magnetite Veins

The earliest serpentine veins in the ultramafic suite are represented by an array of very fine serpentine veinlets (0.03–0.05 mm wide) that postdate the intrusion of the pyroxenite, gabbro, and oxide-rich gabbroic veins (Fig. 50 and Table 8). These early veinlets commonly mimic and overprint the high-temperature plastic fabric in the serpentinized peridotites and are associated with the pervasive background alteration in the peridotites to serpentine after olivine, and bastite after orthopyroxene. The veinlets form a ubiquitous set of microscopic, fine, dark-green to white serpentine + magnetite veinlets that characterizes mesh-textured serpentine. Fine-grained aligned magnetite grains form the cores of the microveinlets and are rimmed by fibrous low-birefringent serpentine (lizardite + chrysotile). These veinlets enclose relict olivine grains and form fine, individual or clustered sets of subparallel veins.

Serpentine + Amphibole ± Chlorite ± Talc

Relatively rare veins composed of fibrous or very fine-grained serpentine + actinolite ± chlorite ± talc typically form the second generation of hydrothermal veins (Figs. 50 and 52). These dark-green to black veins are commonly 2–3 mm wide and are generally highly discordant to the anastomosing serpentine foliation in the ultramafics, although some veins run parallel to it. The veins are commonly zoned with amphibole-rich cores and chlorite + serpentine rims. Typically, there is a diffuse zone of chlorite ± serpentine ± amphibole along the bounding wall rock, forming a narrow alteration halo (Fig. 52).

Serpentine + Magnetite

This third set of veins is the most common throughout the peridotites and occurs as a network of thin (up to 1 mm), anastomosing wispy white and black serpentine + magnetite veins (Figs. 41, 48, 50, and 53; Table 8). The occurrence and abundance of the serpentine and magnetite veins is heterogeneous downcore, with the highest abundances occurring in areas of high orthopyroxene porphyroclast content (see "Structural Geology," this chapter). These veins form isolated wisps of asbestiform serpentine, and they also occur as swarms with black magnetite-rich veins and alternating white serpentine-rich veins (Fig. 53). The serpentine-rich veinlets are composed of very thin serpentine fibers that exhibit a relatively high-birefringence (chrysotile), undulose extinction and fiber growth both parallel and perpendicular to the vein margins. Fine-grained iron oxide minerals are intergrown between the serpentine fibers and locally clay minerals are present. The veins form an anastomosing network that wraps around orthopyroxene porphyroclasts and locally produces an anastomosing serpentine foliation. Less commonly these veins are oriented at a high angle to this foliation.

Serpentine ± Carbonate Minerals ± Pyrite ± Clay Minerals

This set of veins is characterized by the development of wide (>5 mm) white to green "chalky" veins that are randomly oriented and filled by fibrous to massive serpentine, and contain lesser amounts of aragonite, and sulfide and clay minerals (chalcopyrite and pyrrhotite) (Fig. 54). XRD determinations indicate that the serpentine in these veins is typically chrysotile and that the carbonate mineral is commonly aragonite (Fig. 51). Aragonite typically coats fracture surfaces forming radiating prismatic aggregates. The chalky white to green serpentine veins may be temporally associated with a set of aqua-green to light blue-gray serpentine veins that commonly cut the gabbroic veins; however, the timing of this vein set is not well-constrained because crosscutting relationships are absent (Fig. 50). The aqua-green serpentine veins typically form sigmoidal arrays up

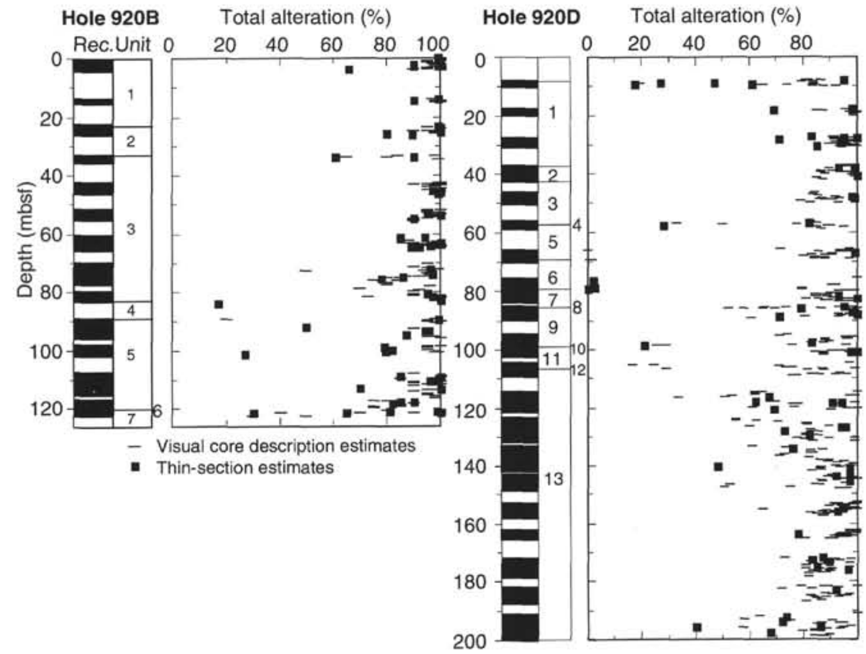

Figure 39. Depth vs. percent abundance of secondary minerals, as estimated in core samples, for Holes 920B and 920D. Core recovery is indicated by black bars. Alteration intensities are generally similar in Holes 920A, 920B, and 920D. The lowest alteration intensities are in harzburgitic and gabbroic mylonite zones in Hole 920D, and in rare amphibolite gneiss and amphibolitized metagabbro intervals recovered in Holes 920B and 920D.

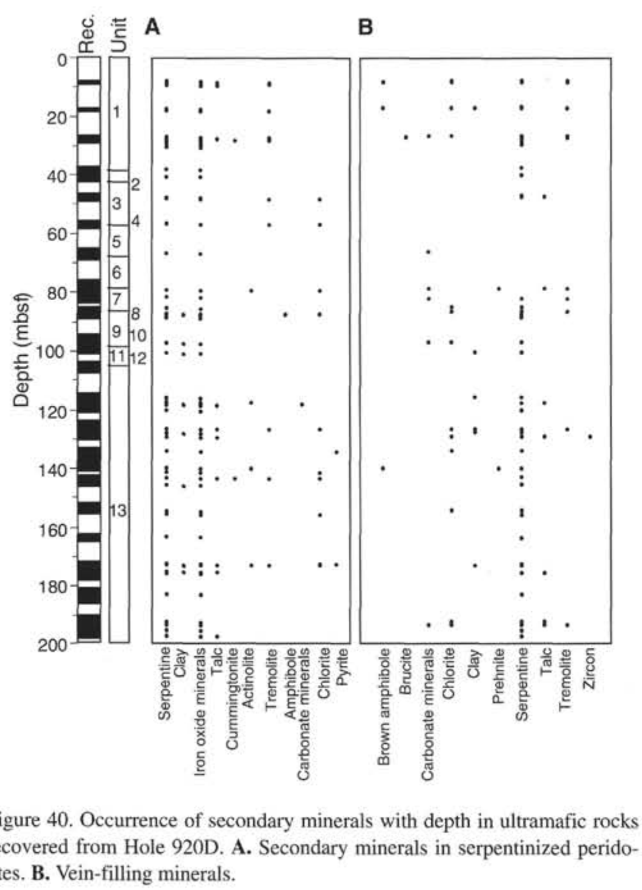

Figure 40. Occurrence of secondary minerals with depth in ultramafic rocks recovered from Hole 920D. **A.** Secondary minerals in serpentinized peridotites. **B.** Vein-filling minerals.

to 4 mm wide and are composed of amorphous, submicroscopic serpentine ± clay minerals.

Carbonate Minerals ± Pyrite ± Clay

The latest veins in the serpentinized peridotites are thin (<1 to 1 mm wide) and are marked by infilling of carbonate mineral, carbonate minerals + pyrite minerals, and pyrite (Figs. 50 and 54). These veins are randomly oriented and commonly reactivate earlier-formed serpentine veins (Fig. 54); also they occur locally as isolated veins. Where carbonate minerals are associated with serpentine veins, they typically line the outer margins of the veins. Pyrite-rich veinlets occur as very thin, discontinuous stringers that may be altered locally to hematite (Fig. 54).

Alteration of Clinopyroxenite

Medium- to fine-grained clinopyroxenite intervals recovered in Hole 920D are moderately to highly altered and mildly deformed. Alteration is dominated by formation of secondary clinopyroxene and amphibole after clinopyroxene. The coarse- to medium-grained clinopyroxene grains, which exhibit exsolution blebs of brown amphibole and fine-grained magnetite, are moderately to pervasively altered. Alteration minerals include well-developed, light-brown amphibole and fibrous, colorless to pale-green amphibole, which typically rim grain boundaries. Olive-green amphibole after brown amphibole is common. In deformed zones, coarse-grained clinopyroxene exhibits undulatory extinction, deformed cleavage planes, embayed grain boundaries, extensive subgrain development, and recrystallization to secondary clinopyroxene. Secondary clinopyroxene is poorly developed and is mottled and dusty in appearance due to abundant fine-grained inclusions of magnetite and vapor-dominated fluid inclusions. Alteration is most intense (80%–90%) in fine grains and in grains near veins containing intergrown prehnite, tremolite, and rare granular epidote. Plagioclase is rare, and where it is present it is pervasively altered to prehnite, epidote, trace amounts of clay minerals, and chlorite and actinolite when adjacent to clinopyroxene grains. Apatite is commonly associated with magnetite and sulfide minerals where it occurs as fine-grained inclusions. In some samples, apatite grains form concentrated aligned zones of fine- to medium-grained crystals, which exhibit patchy extinction. They also contain abundant secondary, and less commonly primary, vapor-dominated fluid inclusions (<5 µm). These inclusions are rare in associated zircon. Alignment of the apatite grains may represent migration of vapor-saturated melts along interstitial grain boundaries during the later stages of crystallization. Titanomagnetite, which has exsolved ilmenite, is pervasively altered to titanite along exsolution lamellae.

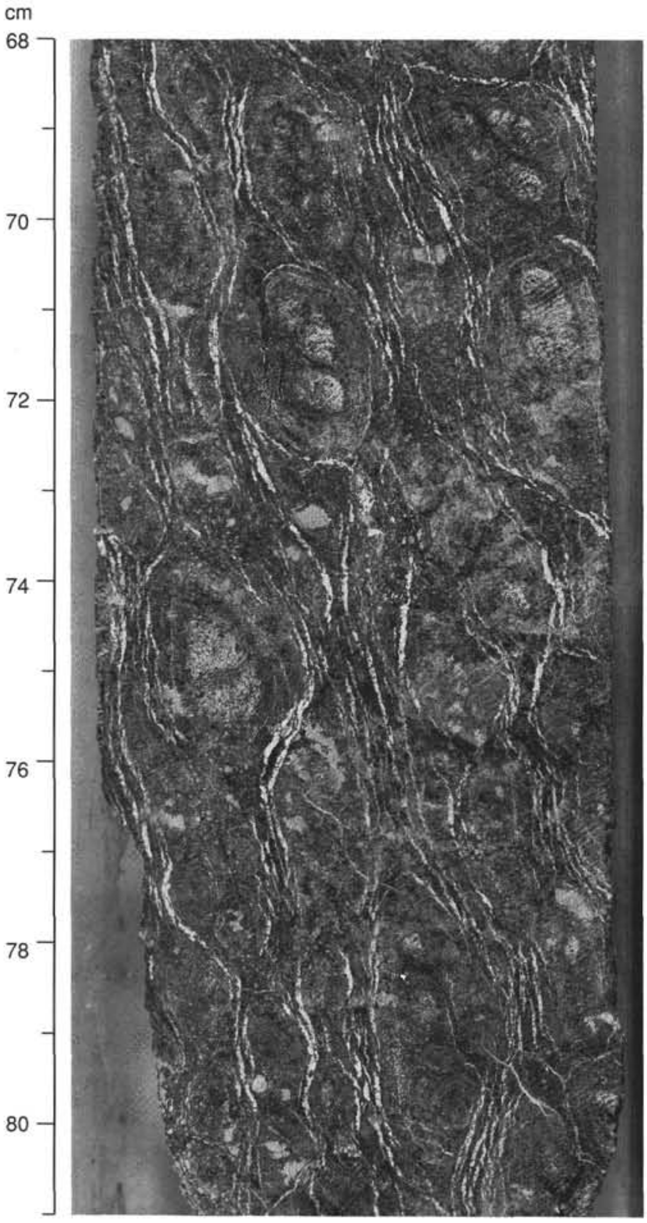

Figure 41. Pervasively serpentinized harzburgite with porphyroclasts of orthopyroxene, and polymineralic aggregates of orthopyroxene, clinopyroxene, and olivine. The primary phases are set in a matrix of mesh-textured serpentine (Sample 153-920D-14R-5, Piece 5, 68–81 cm). Orthopyroxene porphyroclasts and polymineralic aggregates are wrapped by wispy white asbestiform serpentine + magnetite veinlets, which enhance a steeply dipping anastomosing serpentine foliation.

Figure 42. Orthopyroxene porphyroclast partially pseudomorphed by bastite in pervasively serpentinized harzburgite. Sample 153-920D-15R-3 (Piece 3, 48–54 cm). Field of view is 0.5 mm long.

Alteration of Gabbroic Rocks

Intervals of variably altered and deformed gabbroic rocks recovered from Site 920 are characterized by a pervasive background static metamorphism, with most lithologies exhibiting over 50% replacement of primary minerals (Table 7). Mineral assemblages reflecting high-grade thermal metamorphism are associated with mylonite and gneissic zones, in which minerals have been altered under amphibolite to transitional granulite conditions. Retrograde alteration in these zones is generally minor. In less deformed zones, except for the presence of brown amphibole after clinopyroxene, most samples record static metamorphism under greenschist to zeolite facies conditions. Overprinting of higher temperature mineral assemblages by lower temperature phases is common. In the gabbroic rocks, the pervasive replacement of hydrous calcium-aluminum silicates after primary phases, indicates that these samples have undergone incipient rodingitization. Alteration intensity downhole is heterogeneous and there is no apparent difference in the occurrences of alteration minerals, both downhole and between Holes 920A, 920B, and 920D.

Metagabbros and Oxide Metagabbros

Alteration of gabbroic rocks is typically high to pervasive (Fig. 55), with alteration most intense near vein margins and in brittlely deformed zones. In the gabbroic rocks, coarse-grained plagioclase grains are moderately to pervasively altered (20%–100%) with alteration intensity increasing adjacent to veins. Plagioclase is locally highly strained as evidenced by undulose and patchy extinction, abundant deformation twins, and minor subgrain development. In zones of pervasive alteration plagioclase is commonly replaced by prehnite, colorless chlorite with gray-green anomalous birefringence, and radiating sprays of zeolite minerals. In some samples, extensive formation of well- to poorly-crystallized prehnite, and associated clay and zeolite minerals may obscure the primary textures. Light green to colorless amphibole forms microveinlets that cut plagioclase. Amphibole rims plagioclase grain boundaries with adjacent clinopyroxene. Other alteration minerals after plagioclase include granular epidote, smectite, and clay minerals. Along healed microfractures within plagioclase, liquid-dominated secondary fluid inclusions are common.

Coarse- to medium-grained clinopyroxene grains are moderately to pervasively altered. In highly altered samples, clinopyroxene exhibits ragged grain boundaries and is typically dusty in appearance due to abundant fine-grained iron oxide minerals, amphibole, and clay minerals. Narrow alteration rims of fibrous amphibole and chlorite are common. Deformed clinopyroxene grains exhibit bent cleavage planes and locally grain boundaries are fragmented, with finer grains enclosed in fine-grained amphibole. Blebs of brown amphibole, which may be retrograded to olive-green amphibole are common in the cores of clinopyroxene and less common along grain boundaries. Rare orthopyroxene is pervasively replaced by clay minerals, exhibits ragged grain boundaries, and is rimmed by chlorite and fine-grained colorless amphibole.

Titanomagnetite grains, which enclose fine-grained clinopyroxene and plagioclase grains are locally rimmed by green to blue-green amphibole and chlorite with anomalous purple-blue birefringence. Highly altered grains exhibit ilmenite lamellae and are altered to titanite. Brown and green amphibole commonly rims fine-grained magnetite after clinopyroxene and coarse-grained primary magnetite. Accessory minerals consisting of apatite and zircon, which contain abundant vapor-rich to vapor-dominated fluid inclusions, are common.

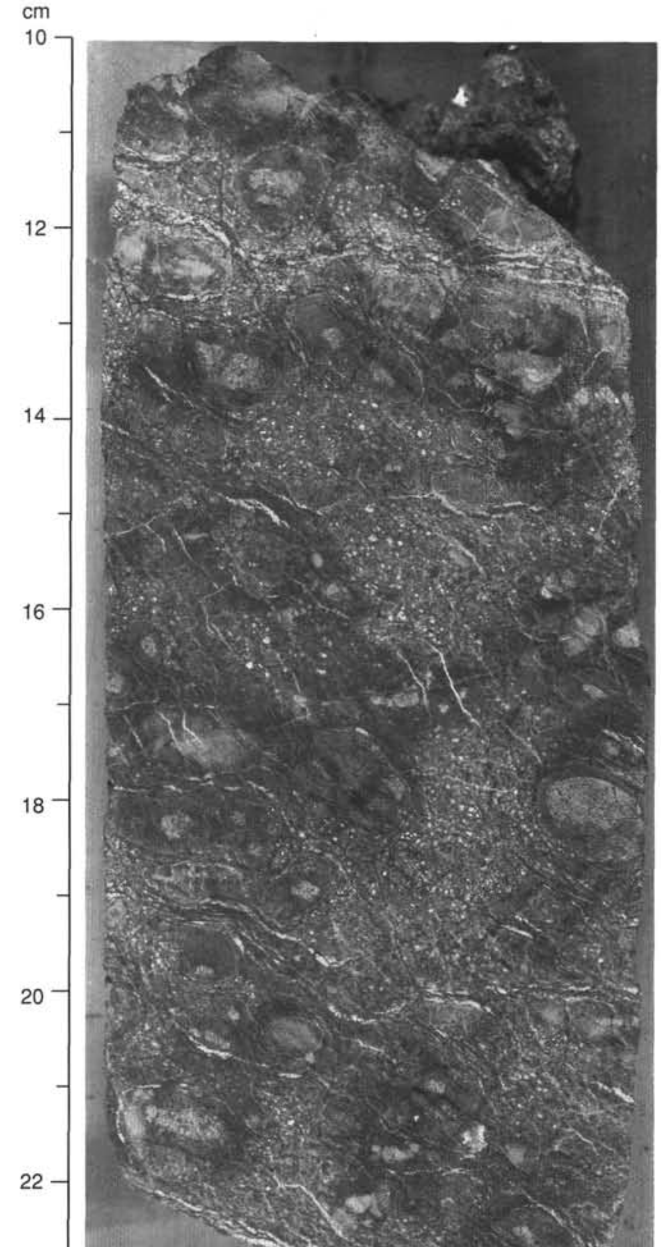

Figure 43. Patchy alteration in harzburgite due to replacement of olivine by white cores of serpentine with yellow-green rims. Sample 153-920B-8R-5 (Piece 2, 10–23 cm). Alteration of this type is common throughout the core in pyroxene porphyroclast-rich zones. Fine, wispy serpentine + magnetite veinlets define an anastomosing foliation.

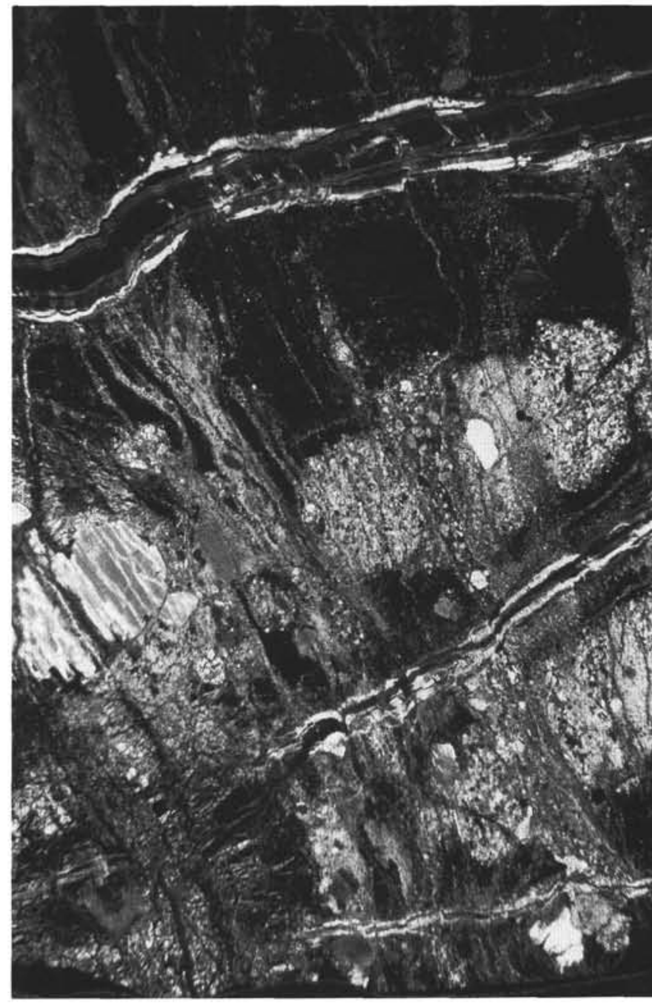

Figure 44. Photomicrograph of porphyroclastic mylonite in serpentinized pyroxene-poor harzburgite and in an adjacent gabbro interval. Deformation in the mylonite has resulted in the interfingering of metagabbroic material and adjacent ultramafic assemblages into the mylonitic foliation. Sample 153-920D-2R-1 (Piece 14, 138–141 cm). Field of view is 45 mm long.

Amphibolites

In Hole 920B, an interval of amphibolite that is in vertical contact with a gneissic metagabbro was recovered (Unit 7, see "Lithologic Units," this chapter). In the amphibolite (Figs. 5 and 56) well-developed neoblastic brown amphibole after clinopyroxene forms fine-grained, millimeter-wide anastomosing and discontinuous bands. The bands contain porphyroclasts of medium- to fine-grained strained olivine, clinopyroxene with inclusions of brown amphibole, and magnetite stringers. They are bounded by segregations and layers of neoblastic plagioclase, which is fine- to medium-grained, equigranular, and commonly exhibits a mosaic texture (Fig. 57; Sample 153-920B-13R-4, Piece 3, 18–26 cm). The alternating bands define a moderately developed foliation. Elongated crystal shapes define a well-developed lineation. The association of olivine, clinopyroxene, and brown amphibole, in near textural equilibrium with plagioclase, indicates formation at temperatures of ~600–800°C under low-pressure conditions. Evidence of subsequent interaction with lower temperature fluids in these rocks is rare, as alteration phases indicating retrograde reactions are absent.

An amphibolitized microgabbro interval defining Unit 4 of Hole 920D exhibits static metamorphism under similar amphibolite facies conditions (e.g., Sample 153-920-7R-2, Piece 2B, 22–29 cm). Medium-grained clinopyroxene enclosed in a fine-grained matrix of plagioclase, clinopyroxene, and secondary brown amphibole contains fine-grained inclusions of euhedral plagioclase and anhedral brown hornblende and magnetite (Fig. 25). Moderately coarse-grained olivine exhibits undulose extinction and deformation bands. Grain boundaries exhibit minor alteration to talc and magnetite. Alteration intensity in olivine is generally less than 10%. Locally, finer grained olivine is pervasively altered (80%–100%) to talc and magnetite with lesser amounts of amphibole, chlorite, and smectite. Fine-grained plagioclase exhibits patchy extinction, glide twins, and moderate development of sutured grain boundaries. Clinopyroxene grains are pervasively replaced by fine- to medium-grained brown amphibole and

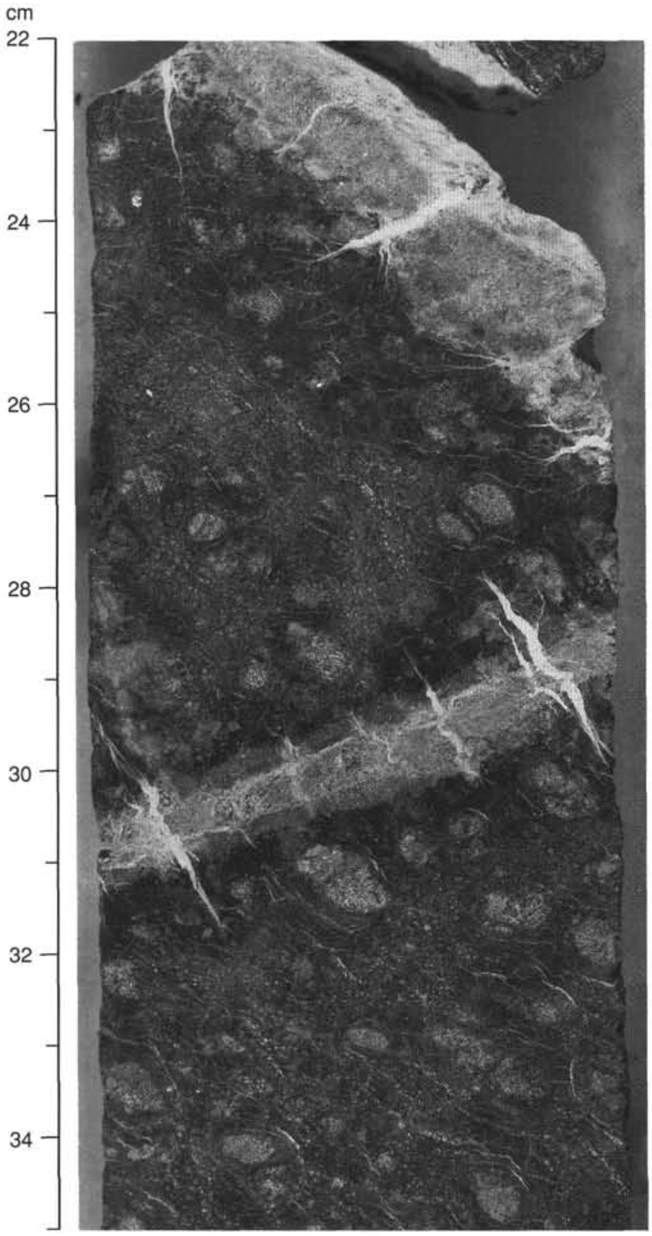

Figure 45. Altered pyroxenite veins (light) in porphyroclastic harzburgite. Sample 153-920D-15R-2, 22–35 cm. Pyroxenite veins are pervasively altered (80%–100%). Replacement minerals include abundant cummingtonite, tremolite and/or actinolite after relict pyroxene. The altered pyroxenite veins are cut by serpentine veinlets that are sigmoidally shaped and aqua to white in color.

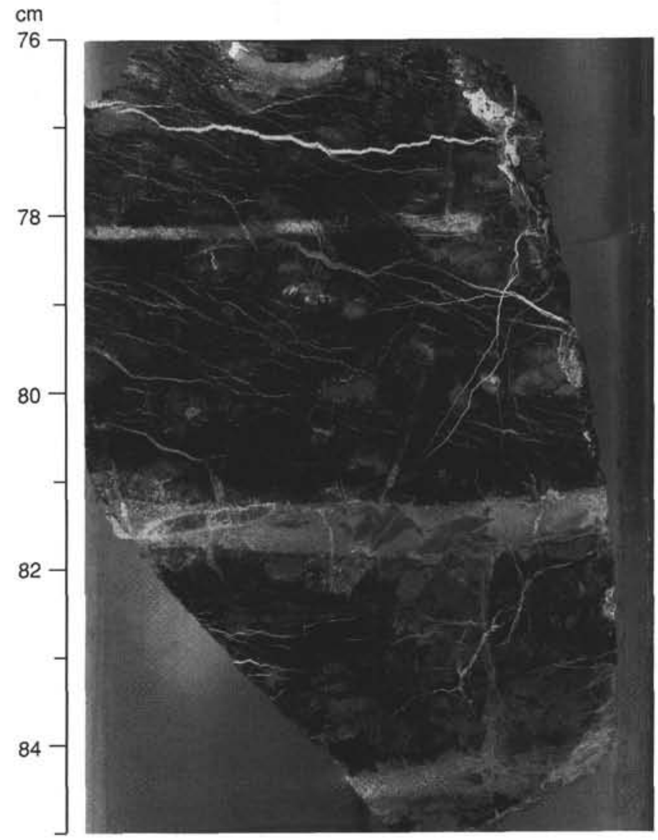

Figure 46. Altered gabbroic vein with euhedral, light-brown amphibole enclosed in a tremolite, actinolite, and chlorite matrix. Fine amphibole + serpentine + chlorite veinlets form offshoots from the main vein. Alteration of the harzburgitic wall rock is pervasive to mesh-textured serpentine. Sample 153-920D-11R-3 (Piece 6, 76–85 cm).

magnetite. Crystallization of amphibole is heterogeneous. Well-developed, blocky grains of brown amphibole after clinopyroxene enclose fine-grained, euhedral to subhedral plagioclase and anhedral magnetite. Aggregates of poorly-crystallized brown amphibole + magnetite replace clinopyroxene. Retrograde reactions involving brown amphibole are heterogeneous in the unit and are most pervasive adjacent to diffuse veins of actinolite and chlorite. In highly altered zones, patches of pale green fibrous amphibole intergrown with chlorite and magnetite may be after clinopyroxene; however, relict crystals of the latter are absent. Chlorite and clay minerals fill fine veinlets that are <1 mm wide. The amphibolite lacks a preferred mineral orientation and segregation bands are absent, in contrast to amphibolite in Unit 7 of Hole 920B.

Porphyroclastic Metagabbro

In Hole 920B, Unit 7, the amphibolite is in contact with a porphyroclastic metagabbro gneiss that exhibits minor to moderate retrograde alteration under greenschist facies conditions (Fig. 5). The contact is subparallel to the foliation both in the porphyroclastic gneiss and amphibolite (Fig. 58) and is underlined by a narrow magnetite and ilmenite-rich ribbon. It is probably tectonic in origin (see "Structural Geology," this chapter). Extensive recrystallization of minerals along this zone indicates that deformation along the contact occurred at probable temperatures of 700°–800°C.

Coarse-grained, elongate plagioclase porphyroclasts in the gabbroic gneiss are highly strained as indicated by sutured grain boundaries, extensive subgrain development, patchy and undulatory extinction, and formation of deformation twins. Augen are commonly rimmed by magnetite stringers with trace amounts of fine-grained amphibole and mosaic to sutured, fine- to very fine-grained neoblasts of plagioclase (Fig. 58). Medium-grained magnetite-ilmenite stringers enclose apatite, plagioclase, orthopyroxene, and clinopyroxene. In plagioclase, crosscutting arrays of liquid to vapor-dominated fluid inclusions along healed microfractures are abundant. The inclusions commonly contain multiple birefringent daughter minerals and crosscut porphyroclast and neoblast grain boundaries.

Coarse-grained orthopyroxene porphyroclasts are slightly to moderately altered (15%) with fine rims of intergrown cummingtonite and talc. Where in contact with plagioclase, the orthopyroxene porphyroclasts are altered to moderately well-developed green amphibole. Small cummingtonite-rich pods completely replace fine-grained orthopyroxene. Coarse-grained clinopyroxene, with embayed grain bound-

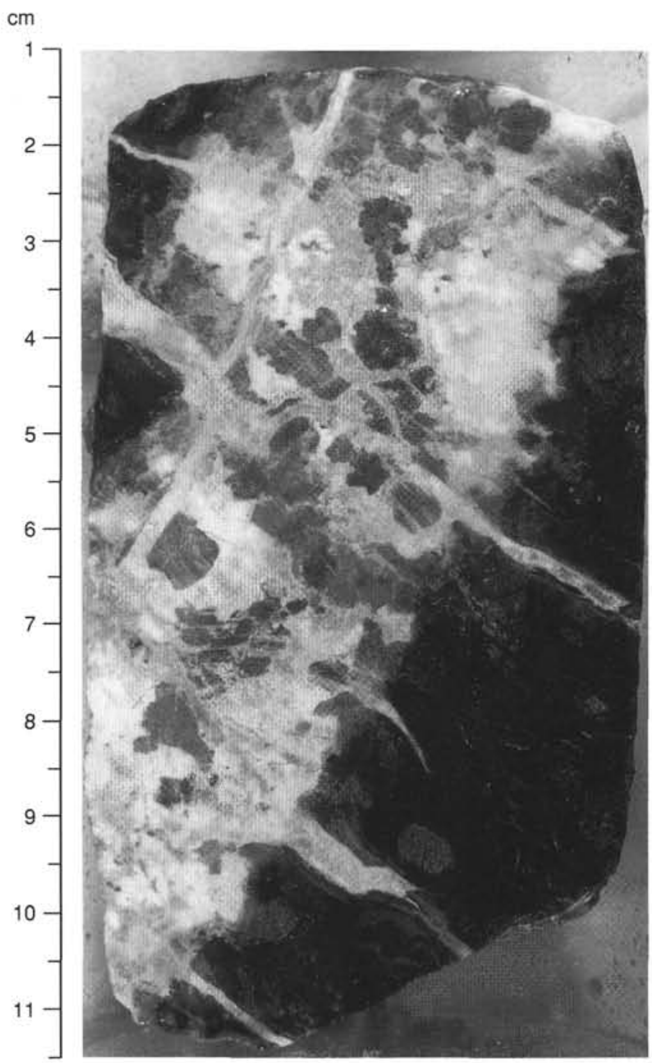

Figure 47. Gabbroic vein in Sample 153-920B-10R-3 (Piece 1, 1–11.5 cm), residual harzburgite. The coarse-grained gabbro is moderately deformed and recrystallized, and is pervasively replaced (90%) by Ca-bearing secondary phases. The gabbroic vein is cut by light prehnite veins, which change composition to serpentine near the vein boundary and into the ultramafic host rock.

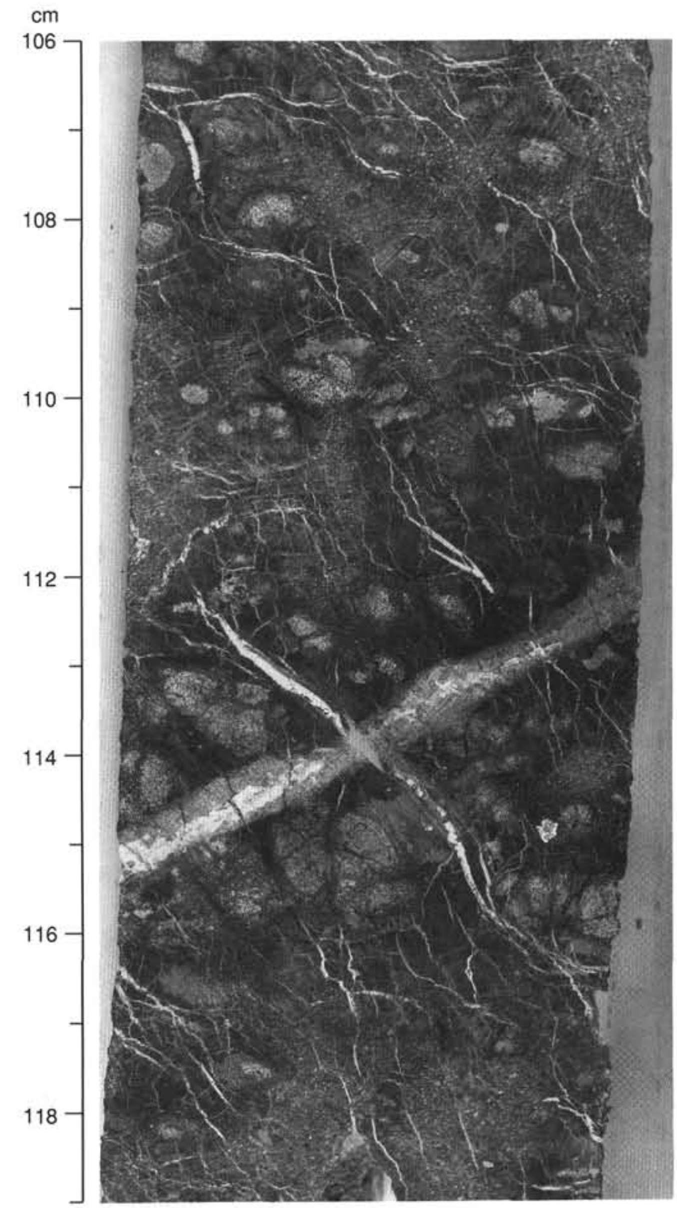

Figure 48. Narrow metagabbroic vein in serpentinized harzburgite. The vein exhibits a somewhat diffuse margin due to development of a 3-mm-wide light-gray halo of amphibole + serpentine ± chlorite, enhanced pyroxene growth, and local preservation of olivine kernels adjacent to the vein. The core of the vein is composed of prehnite after plagioclase, and actinolite + chlorite, with minor amounts of relict pyroxene. The magmatic vein is cut by discontinuous veins of aqua to white serpentine. These serpentine veinlets change color from white in the harzburgite, to light green where they transect the gabbro vein. Sample 153-920D-22R-4 (Piece 4, 106–119 cm).

aries, ophitically enclose fine-grained, euhedral plagioclase grains. Clinopyroxene is rimmed locally by pale green amphibole, trace blebs of very fine-grained brown amphibole, and oxide minerals. The pyroxene porphyroclasts are enclosed in a fine-grained matrix composed of recrystallized plagioclase neoblasts, amphibole, and clay minerals(?). Composite augen of medium- to fine-grained clinopyroxene, orthopyroxene, and plagioclase commonly are moderately altered to pale green, fine-grained, fibrous amphibole and minor chlorite.

There is an abrupt discontinuity in secondary mineral assemblages at the contact between the porphyroclastic gneiss and the amphibolite; brown hornblende only occurs as trace amounts in the augen gneiss, and greenschist facies mineral assemblages that are present in the porphyroclastic gneiss are absent in the amphibolite.

Porphyroclastic Metagabbroic Mylonite

One piece of porphyroclastic metagabbroic mylonite was recovered from Hole 920B, at the base of Sample 153-920B-13R-3 (Piece 6, 133–139 cm) (Fig. 59). Rocks recovered directly below the mylonite, from Section 153-920B-13R-4, include amphibolite and porphyroclastic gneiss (Figs 5 and 58); above the mylonite, the contact with overlying relatively undeformed gabbro (Fig. 55) is absent. The mylonite has an oxide gabbro protolith, as defined by elongate augen of highly deformed, coarse-grained plagioclase porphyroclasts, rounded aggregates and isolated grains of clinopyroxene and orthopyroxene, abundant oxide minerals, and apatite and zircon as accessory phases (Fig. 59).

Alteration in the mylonite sample is heterogeneous ranging from 60% to 100%, and includes secondary clinopyroxene, olive green to pale green amphibole ± chlorite, and magnetite, with trace blebs of

Figure 49. Photomicrograph of altered plagioclase in gabbroic vein. Sample 153-920D-10R-3 (Piece 1, 0–5 cm). Hydrogarnet (hygnt), light green to colorless amphibole (Amph), and carbonate minerals (CC) in a highly altered plagioclase grain. Field of view is 1 mm.

brown amphibole, which probably formed as inclusions in now 100% altered primary clinopyroxene. Orthopyroxene is altered to colorless to pale green amphibole, which forms concentrated pods and fine narrow rims around grain boundaries. Plagioclase augen exhibit undulose and patchy extinction, sutured grain boundaries, and extensive neoblast development. They are commonly rimmed by anastomosing ilmenite-rich stringers. Plagioclase neoblast development has proceeded in at least two stages as evidenced by medium-grained, recrystallized plagioclase in aggregates of clinopyroxene, plagioclase, and apatite that are enclosed in a matrix of fine- to very fine-grained, neoblastic plagioclase. Secondary inclusions enclosed in plagioclase, which are vapor to liquid-dominated, are entrapped along healed microfractures and have a morphology similar to that of methane-bearing inclusions in gabbros from ODP Hole 735B (Kelley et al., 1993; Vanko and Stakes, 1991). The inclusions arrays, which cut plagioclase porphyroclasts, both cut and are truncated by recrystallized fine-grained plagioclase. These inclusions may represent syn- to post-deformational migration of immiscible methane and water-rich fluids in this shear zone. Secondary mineral assemblages in the mylonites formed under greenschist facies conditions, indicating temperatures of ~300°C to <500°C.

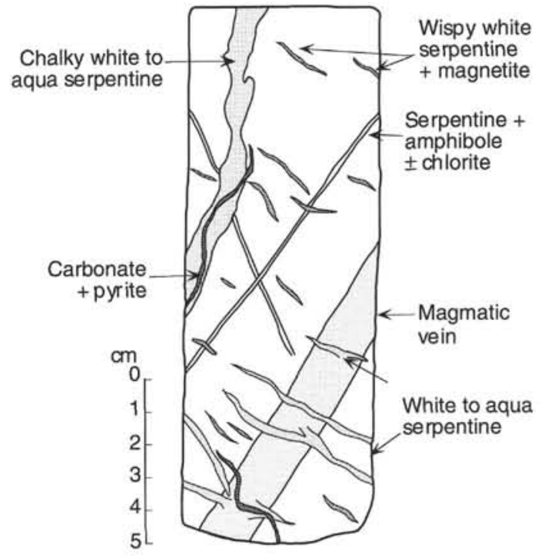

Figure 50. Schematic illustration of relationships and relative timing of macroscopic veining events in the serpentinized peridotites. In general, in addition to the magmatic veins, five successive generations of macroscopic hydrothermal veins can be recognized within the serpentinized harzburgites. From oldest to youngest, these include (1) serpentine + magnetite veinlets that are associated with the pervasive background alteration of the ultramafics; (2) serpentine + amphibole ± chlorite ± talc veins; (3) serpentine + magnetite veins that are wispy white and black; (4) serpentine ± carbonate ± pyrite ± clay mineral veins which are typically composed of wide (>5 mm) white to aqua-green "chalky" serpentine, aragonite, and sulfide and clay minerals; and (5) carbonate minerals ± pyrite ± clay mineral veins, which commonly reactivate earlier formed veins.

Hydrothermal Veins in the Gabbroic Rocks and Magmatic Veins

Composite prehnite veins within the gabbroic rocks are commonly associated with the incipient formation of Ca-bearing alteration mineral assemblages. The veins, up to 1.7 cm wide (Fig. 55) are filled with coarse- to fine-grained prehnite. Well-developed prehnite forms cockscomb crystals in vuggy veins and is associated with minor concentrations of aragonite and well-crystallized zeolite minerals. The prehnite and zeolite minerals line and radiate out from vein walls, indicating open space filling. In some samples, these veins are associated with light rose-colored veins of zoisite (e.g. Sample 153-920B-10R-1, Piece 3, 46–55 cm). Other vein-filling minerals (Table 8) include botryoidal aragonite with associated euhedral pyrite, commonly observed on broken surfaces of the core. Mesoscopic actinolite ± chlorite veinlets cut plagioclase, though macroscopic veins of actinolite ± chlorite are rare.

Alteration of Diabase

The diabase sections recovered in Hole 920B (Unit 4) and Hole 920D (Unit 6) are moderately to highly altered with alteration intensity controlled by the formation of clay minerals and chlorite after groundmass mesostasis (Fig. 60). Groundmass plagioclase and glomerocrysts are moderately to pervasively altered (20%–100%). Alteration is dominated by formation of secondary plagioclase, which forms jagged, irregular patches, and prehnite as radiating mats and well-developed crystals. Alteration is heterogeneous with coarser-grained areas commonly pervasively replaced by well-developed prehnite. Other alteration minerals after plagioclase include trace granular epidote, rare chlorite + actinolite as microveinlets, and clay minerals, with minor amounts of zeolite minerals. Liquid-dominated, secondary inclusions in plagioclase delineate healed microfractures, and irregularly-shaped fluid inclusions in patches are common. Olivine phenocrysts are pseudo-

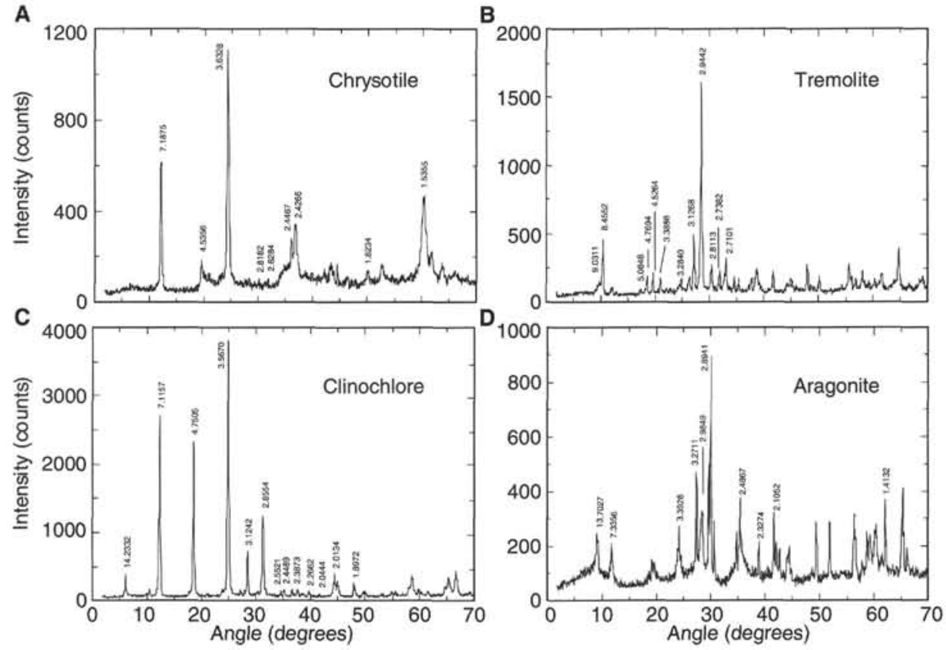

Figure 51. X-ray diffraction patterns of vein material in magmatic and hydrothermal veins hosted in the serpentinized peridotites. **A.** Chrysotile polymorph of serpentine veinlet cutting a pyroxenite vein. Sample 153-920D-16R-6 (Piece 8, 45–55 cm). **B.** Tremolite after pyroxene in altered pyroxenite vein. Sample 153-920D-18R-1 (Piece 7, 53–57 cm). **C.** Clinochlore in irregular, thin veinlet crosscutting a gabbroic veinlet. Sample 153-920D-14R-1 (Piece 1, 0–6 cm). **D.** Radiating sprays of aragonite coating open fractures, which are associated with serpentine. Sample 153-920D-4R-3 (Piece 10, 56–77 cm).

morphed by zoned, euhedral pods containing cores of serpentine + chlorite + clay minerals. These pods are rimmed by fine-grained fibrous amphibole. Relict, anhedral, and embayed clinopyroxene forms discontinuous, fine-grained islands that are enclosed by very fine-grained, colorless to pale green amphibole and chlorite. Groundmass clinopyroxene exhibits slight to pervasive alteration to actinolite with minor amounts of chlorite. In pervasively altered patches, zeolite and clay minerals, chlorite, and fibrous amphibole completely obscure the primary mineralogy. Titanomagnetite, with exsolution lamellae of ilmenite, is altered to titanite. Alteration mineral assemblages indicate metamorphism under greenschist down to zeolite facies conditions.

Veins in the Diabasic Rocks

Veins within the diabase are commonly filled by prehnite, with lesser amounts of zeolite and clay minerals (Figs. 60 and 61). They typically form 2–3 mm wide sets of branching and crosscutting networks. Prehnite within the veins is well developed and forms medium-grained cockscomb crystals that are intergrown with radial acicular sprays of zeolite minerals. The minerals line and radiate out from vein walls, indicating open space filling (Fig. 61).

Fluid Inclusions in the Gabbroic and Diabasic Rocks

Multiple populations of fluid inclusions in the variably altered and deformed gabbroic and pyroxenitic samples indicate that fluid circulation at Site 920 involved fluids of widely varying compositions and temperatures, starting at late magmatic conditions. Inclusions are most abundant in plagioclase augen hosted in gneissic intervals and in apatite in oxide-rich gabbros, though they are present in metagabbros and diabase as well. The inclusions typically occur along anastomosing arrays of healed microfractures in plagioclase, and as primary inclusions trapped during growth of magmatic apatite. They are relatively rare in zircon. Primary and secondary inclusions are not common in secondary and vein-filling minerals, which likely reflects the inherent difficulty of minerals such as actinolite, chlorite, and prehnite to trap inclusions. Based on petrographic analyses at room temperature, the inclusions were classified into three main types (Fig. 62).

Type 1: Liquid-dominated, daughter-mineral-absent inclusions. Type 1 inclusions are liquid-dominated inclusions that are moderately common in plagioclase and less common in apatite, secondary amphibole, and clinopyroxene. Inclusion sizes are variable and range from <1 µm to 15 µm. The liquid-dominated inclusions occur as two subtypes within the gabbroic and pyroxenitic rocks. Type 1a inclusions are hosted in plagioclase, amphibole, secondary clinopyroxene, and apatite. They exhibit negative to anhedral crystal habits, contain a small, liquid-rimmed, vapor bubble (<50 vol%), and they commonly form anastomosing, crosscutting arrays along healed microfractures. These inclusions are typically secondary in origin. In apatite, these inclusions occur both as primary and secondary inclusions, they exhibit a very small vapor-to-liquid ratio, and show Brownian motion at room temperature. Type 1b inclusions form rare, concentrated zones of irregularly-shaped, ragged inclusions and occur in highly-altered patches of plagioclase. Type 1b inclusions most commonly occur in diabase, but are present in the gabbros as well. They may be primary in origin, although textural evidence for primary origin is not conclusive.

Type 2: Vapor-dominated, daughter-mineral-absent inclusions. Vapor-dominated inclusions are moderately common in oxide gabbro, gabbro, pyroxenite, and are rare in mylonite and augen gneiss intervals. They are moderately abundant as primary and secondary inclusions in apatite (Fig. 62A), and are rare as secondary inclusions in plagioclase. In apatite, the inclusions range in size from <1 to 12 µm, and they contain up to ~100% of a vapor phase (Fig. 62A). The large extent of vapor-filling indicates that the inclusions likely contain $CO_2 \pm H_2O$; however, shore-based studies are needed to confirm composition. In some samples, the vapor-dominated inclusions are spatially associated with halite-bearing inclusions (Fig. 62C).

Type 3: daughter-mineral-bearing inclusions. Daughter-mineral-bearing inclusions occur as two types in the gabbro samples. Type 3a inclusions are only hosted in plagioclase where they are secondary in origin and are liquid-dominated to vapor-rich. Daughter mineral

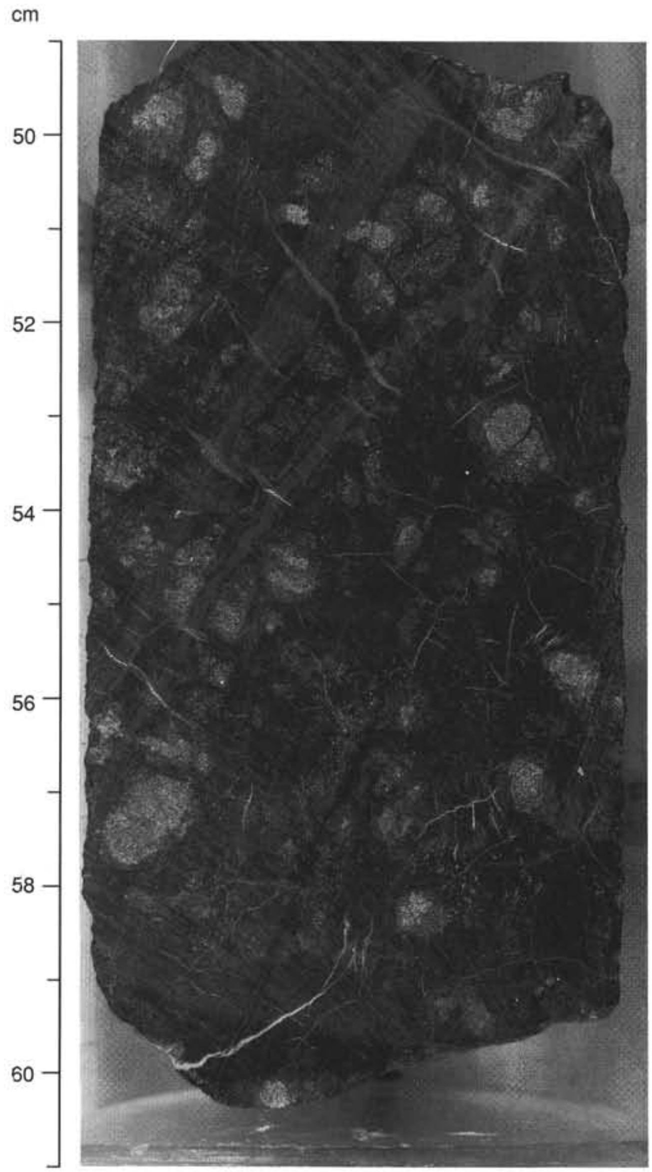

Figure 52. Narrow actinolite + chlorite veinlets in pervasively altered harzburgite. Sample 153-920B-6R-1 (Piece 5, 49–61 cm). The dark green to black veinlets contain a core of actinolite + chlorite with a serpentine ± chlorite rim. These veins postdate both the magmatic veins and fine serpentine veinlets associated with pervasive alteration of the harzburgite to mesh-textured serpentine. They are cut by later, pale-green serpentine veins.

phases are extremely abundant and include fibrous and elongate highly birefringent crystals (amphibole?), subrounded to cubic, birefringent daughter minerals, and rare, opaque minerals. Rare, vapor-rich inclusions, which occur in the mylonite zone at Hole 920B, are pervasive in plagioclase augen (Fig 62B). The inclusions delineate healed microfractures, which cut plagioclase augen, and both extend across and terminate at augen grain boundaries. These relationships suggest that they formed during or after deformation associated with augen development. The vapor-rich inclusions are similar petrographically and in their occurrence to vapor-rich, methane-bearing inclusions in gabbroic rocks from ODP Hole 735B in the Southwest Indian Ocean (Kelley and McDuff, 1993; Kelley and Frantz, unpubl. data). Type 3b inclusions are primary and secondary halite-bearing inclusions, hosted in magmatic and secondary(?) apatite (Fig. 62C). The halite daughter phases typically host singular, fine-grained opaque minerals, and inclu-

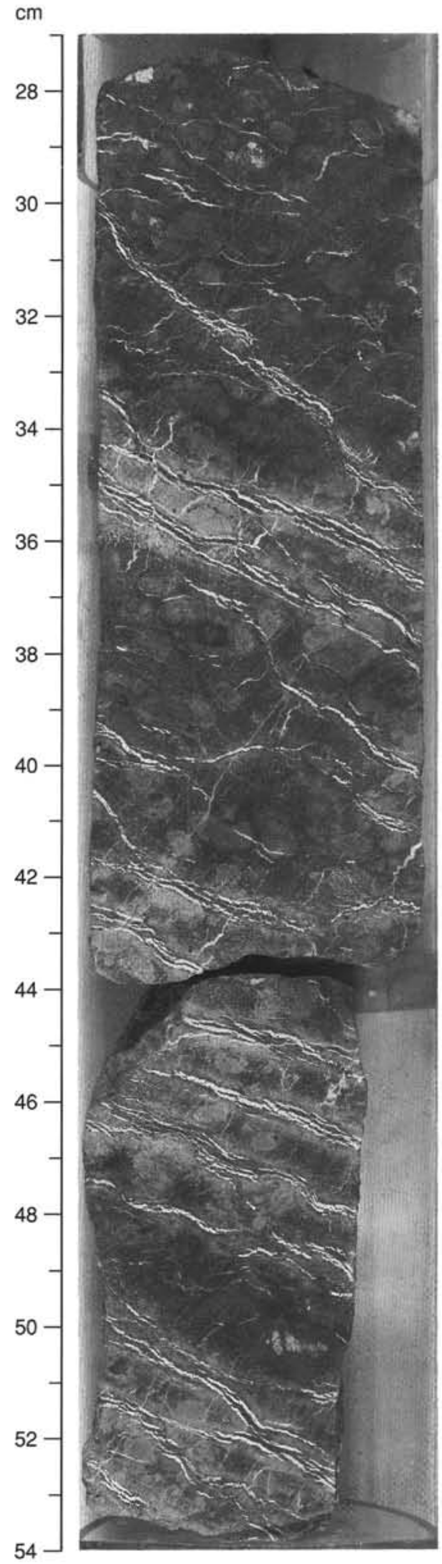

Figure 53. Anastomosing, wispy white and black serpentine + magnetite veins. Sample 153-920B-5R-3 (Piece 4, 27–54 cm). The veins form isolated wisps of asbestiform serpentine and occur as swarms with black magnetite-rich veins alternating with white serpentine-rich veins.

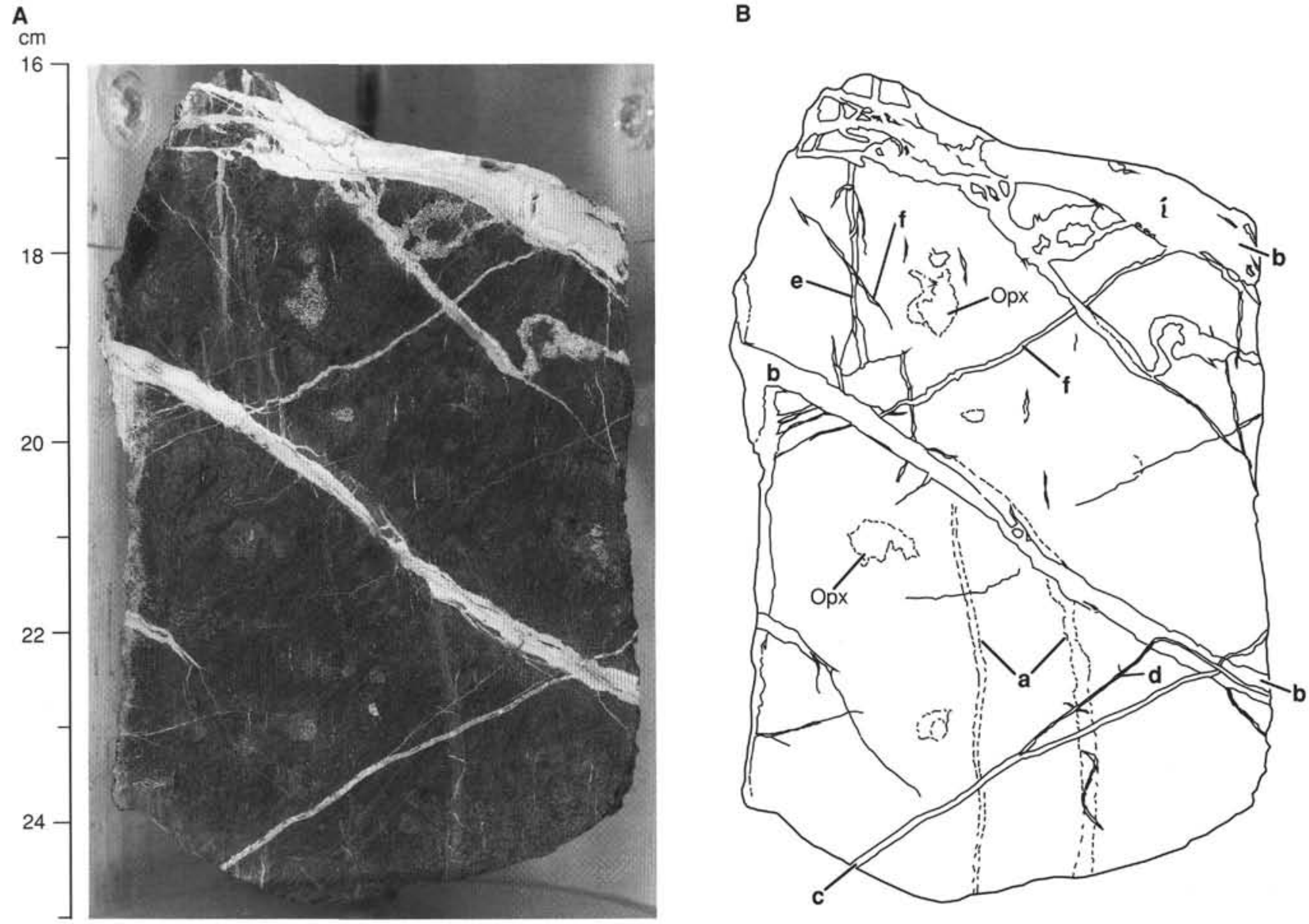

Figure 54. Sample 920D-8R-1 (Piece 3, 16–25 cm). **A.** Pervasively serpentinized (95%–98%) orthopyroxene-poor harzburgite cut by multiple generations of veins. Bastite after orthopyroxene is common. **B.** Drawing of **A.** An early set of actinolite + chlorite ± serpentine veins (a) is cut at a high angle by 2 to 3 sets of veins. Chalky white serpentine veins (b), which are highly discordant to the actinolite-bearing veins, are reactivated by a later set of yellow-green serpentine + pyrite + carbonate mineral veinlets (c) and pyrite + carbonate mineral stringers (d). Fine, aqua-green serpentine veins (e) are cut by a later serpentine + carbonate mineral vein (f). Opx = orthopyroxene porphyroclasts.

sion sizes vary from <5 to 20 μm. The brine inclusions are spatially associated with conjugate vapor-dominated inclusions, indicating that the fluids were entrapped under immiscible conditions.

Down- and Intrahole Variation in Alteration

There is no apparent difference in the occurrences of alteration minerals between Holes 920A, 920B, and 920D, and alteration intensities are broadly similar between the three holes (Figs. 39 and 40). A decrease in alteration intensity is observed in Hole 920D at depths of ~10, 100, and 200 mbsf, but is not as clearly defined in Hole 920B. The lowest alteration intensities are in interfingered harzburgitic and gabbroic mylonite zones in Hole 920D, and in rare amphibolite and amphibolitized metagabbro intervals recovered in Holes 920B and 920D. Secondary minerals within the serpentinized peridotites commonly reflect interaction with fluids under lower temperature conditions than those indicated by alteration phases in the gabbroic rocks and alteration intensities are generally lower in the gabbroic rocks.

Discussion

The metamorphic history recorded in the ultramafic, gabbroic, and diabasic rocks recovered from Holes 920A, 920B, and 920D is variable and complex. Deformational and metamorphic relationships reflect the integrated effects of polyphase deformational episodes, localized intrusion of melts that produced pyroxenitic and gabbroic pockets and veins, and multiple hydrothermal pulses. The effects of these processes on the rocks have resulted in variable styles, grades, and intensities of alteration both within individual lithologies and throughout the recovered sections.

In the peridotite suite, the pervasive coarse-grained crystal-plastic fabric defined by the elongation of orthopyroxene and olivine porphyroclasts and recrystallization of the finer-grained matrix has been noted in other oceanic regions, ophiolites, and in mantle xenoliths. Generally, these fabrics are interpreted to form during recrystallization and deformation at minimum temperatures of 800°C–1000°C (Kirby, 1983). Mineralogical evidence for high-temperature (>500°C) interaction with hydrothermal fluids is generally minor or absent in the peridotites, except in the mylonite zones. In these intensely deformed zones, ribbons of metagabbroic and metapyroxenitic material, moderately rich in fine-grained hornblende, are interfingered between the recrystallized ultramafic assemblages. These mineralogical and textural relationships indicate that shearing and limited hydration occurred at minimum temperatures of 700°C to 900°C (Spear, 1981). Retrograde mineral assemblages in these deformed zones of pale green amphibole, chlorite, and chrysotile + lizardite indicate that interaction with hydrothermal fluids continued down to at least greenschist facies conditions.

Away from these intensely deformed zones, there is little evidence in the ultramafic rocks for interaction with high-temperature fluids. The minor occurrence of talc and cummingtonite after orthopyroxene

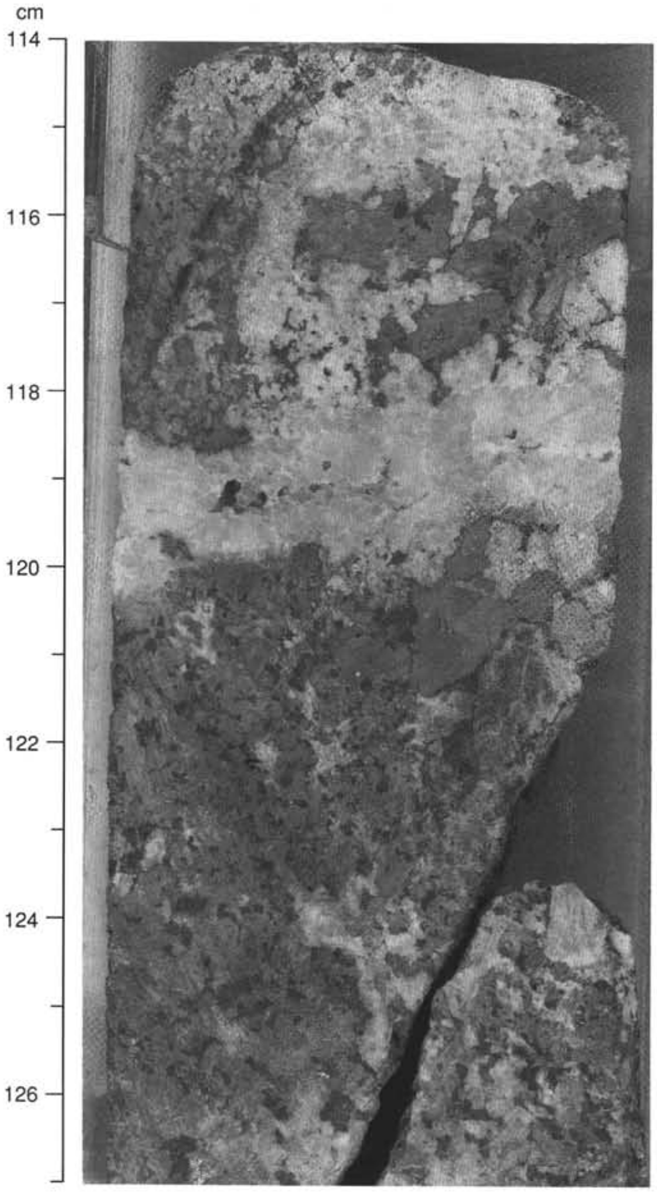

Figure 55. Moderately to pervasively altered oxide gabbro. Sample 153-920-13R-3 (Piece 5, 114–127 cm). Sample is cut by a 1.7-cm-wide vuggy prehnite vein with radial acicular zeolites. Coarse-grained plagioclase grains are slightly to pervasively altered with alteration intensity increasing adjacent to prehnite vein. Secondary minerals after plagioclase include prehnite, pale-yellow to olive-green amphibole, chlorite, granular epidote, smectite, and clay minerals. Pale brown to green clinopyroxenes exhibit ragged grain boundaries and are dusty in appearance due to abundant fine-grained iron-oxide minerals, amphibole, and clay(?) minerals. Accessory minerals consisting of apatite and zircon are common.

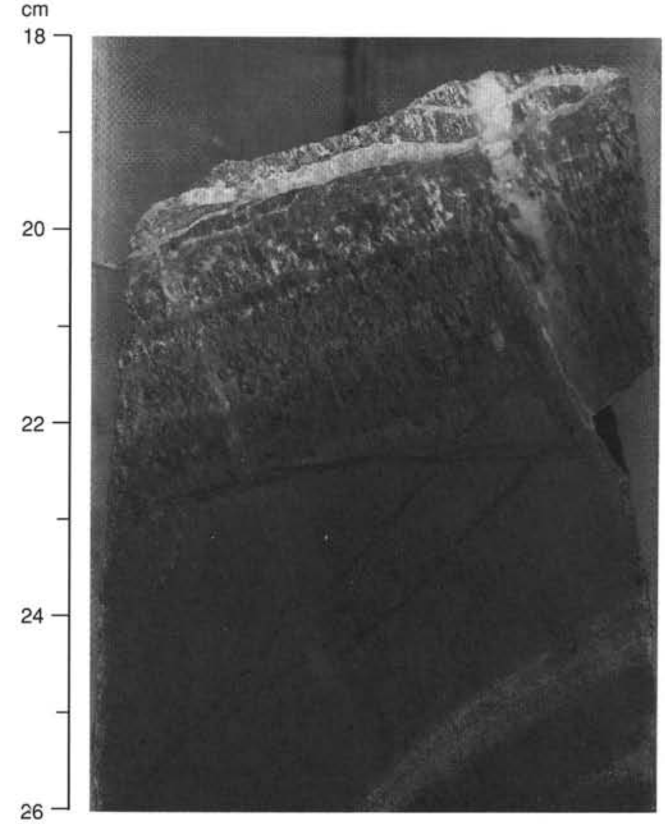

Figure 56. Amphibolite recovered in Hole 920B. Sample 153-920B-13R-4 (Piece 3, 18–26 cm). Well-developed linear mafic aggregates of neoblastic brown amphibole and associated porphyroclasts of olivine, clinopyroxene, and magnetite form fine-grained, anastomosing and discontinuous bands. The mafic bands are bounded by segregations of neoblastic plagioclase. A 20 to 30 mm wide alteration halo at the top of the piece is associated with narrow prehnite + zeolite veinlets. Secondary minerals in this zone include actinolite, chlorite, prehnite, and clay and zeolite minerals.

in slightly altered polymineralic lenses and adjacent to magmatic veins suggests that at least local penetration by hydrothermal fluids into the peridotites occurred under amphibolite to greenschist facies conditions (Mottl and Holland, 1978). The relative scarcity of high-temperature secondary phases may reflect either non-pervasive high-temperature fluid circulation in the harzburgites, or the ubiquitous overprinting of high-temperature phases by the background mesh-textured serpentine associated with circulation of lower temperature fluids.

Within the ultramafic suite, a significant component of the pervasive background alteration is associated with the formation of polymineralic veins that commonly exhibit evidence for reactivation during multiple hydrothermal events. The earliest veining episode is marked by intrusion of gabbroic to pyroxenite veins and veinlets. Primary aqueous and possibly CO_2-bearing fluid inclusions that are abundant in vein-hosted apatites within the gabbro and pyroxenite intervals indicate that the initial hydrothermal event(s) involved fluids of magmatic origin. The association of zircon, apatite, and aqueous fluids in these zones is consistent with high degrees of fractionation and exsolution of fluids from melts of evolved compositions.

The primary mineralogy of the magmatic veins is generally partially to completely obscured by the formation of well-developed pale brown amphibole (cummingtonite?), tremolite, and actinolite, and ubiquitous disequilibrium textures marking lower temperature overprint events. In the gabbroic veins, secondary minerals include prehnite after plagioclase, with lesser amounts of epidote, zoisite, chlorite, and hydrogrossular garnet. Intense alteration of the gabbroic veins to calcium-bearing phases is associated with later veining events involving prehnite, zoisite, and tremolite-actinolite-bearing veins. The abundance of hydrous calcium-aluminum silicates associated with alteration of the gabbroic rocks indicates that, locally, some of these samples have undergone incipient rodingitization. The secondary mineralogy is consistent with initial alteration at temperatures of >500°C with progressive fluid flow and alteration down to zeolite facies conditions.

The occurrence of incipiently calcium-metasomatized rocks within the peridotites is similar to those described in gabbroic rocks from the Mid-Atlantic Ridge (Honnorez and Kirst, 1975), the Garret Transform (Bideau et al., 1991), and more recently to rodingites recovered during Leg 147 from Site 895, fast-spreading crust exposed at Hess Deep

Figure 57. Microphotograph of amphibolite. Sample 153-920B-13R-4 (Piece 3, 23–26 cm). Neoblastic brown amphibole, strained olivine, clinopyroxene, and magnetite mafic stringers form alternating segregations with fine-grained mosaic plagioclase, defining a moderately developed foliation and a well-developed lineation. The association of olivine, clinopyroxene, and brown amphibole, in near textural equilibrium with plagioclase, indicates formation at transitional granulite to amphibolite facies conditions. Field of view is 30 mm in length.

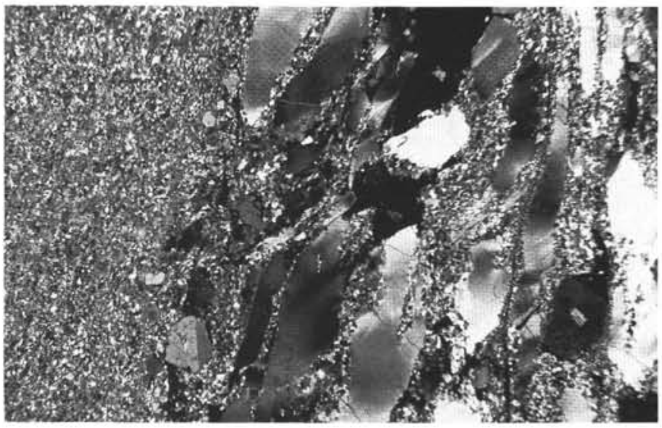

Figure 58. Microphotograph of the contact between amphibolite and gneissic metagabbro recovered from Hole 920B, Unit 7 (Sample 153-920B-13R-4, Piece 5, 42–45 cm). Coarse-grained, elongate plagioclase porphyroclasts in the metagabbro gneiss are rimmed by magnetite stringers. Alternating lenses of elongate plagioclase augen, fine-grained plagioclase neoblasts, and magnetite-rich stringers define a well-developed anastomosing foliation. Field length is 33 mm.

(Gillis, Mével, Allan, et al., 1993). The close association of these intensely altered rocks at Site 920 with pervasively serpentinized harzburgites suggests that local migration of Ca-enriched fluids produced during serpentinization of the ultramafic rocks resulted in the incipient alteration. The occurrence of tremolite, prehnite, epidote, zoisite, and trace hydrogarnet in these samples, is consistent with circulation of Ca-enriched fluids under greenschist facies conditions at temperatures of 300°C–400°C.

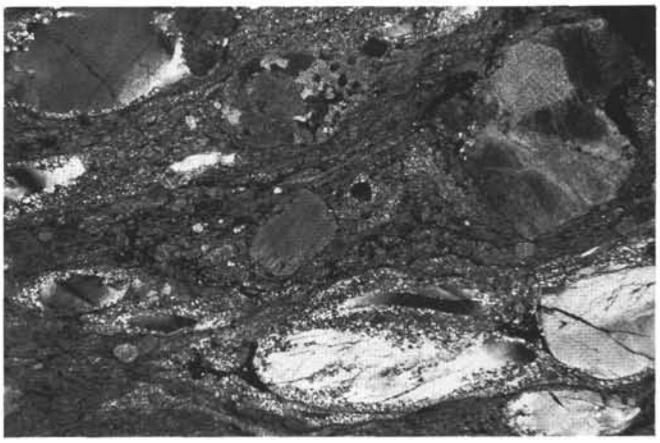

Figure 59. Porphyroclastic mylonite recovered from Hole 920B, at the base of Sample 153-920B-13R-3 (Piece 6, 133–139 cm). Elongate augen of highly deformed, coarse-grained plagioclase porphyroclasts, rounded aggregates, and isolated grains of clinopyroxene and orthopyroxene partially replaced by amphibole are commonly rimmed by anastomosing ilmenite-rich stringers. Augen are enclosed in a matrix of fine- to very fine-grained neoblastic plagioclase. Field length is 28 mm.

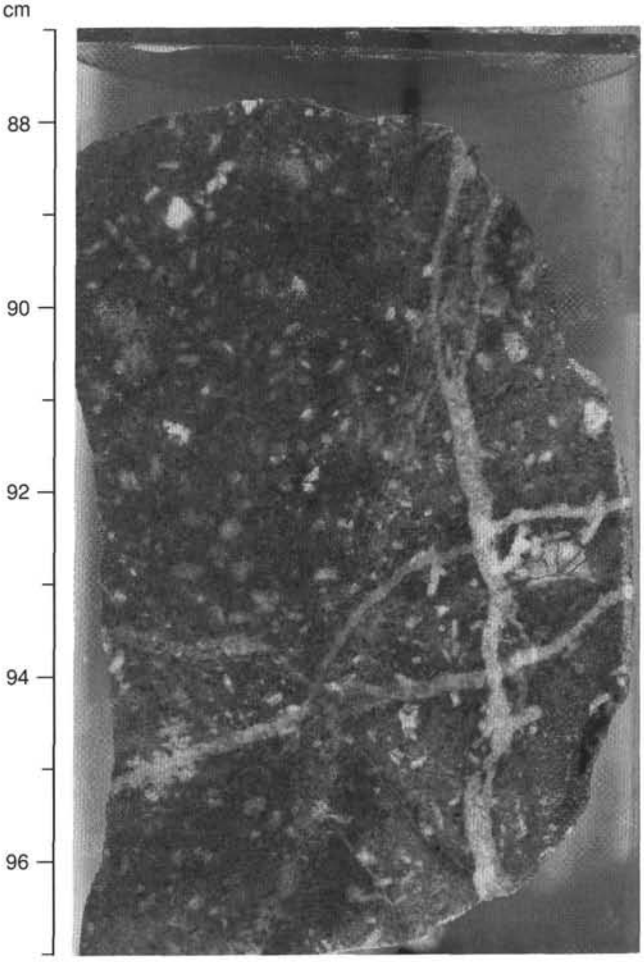

Figure 60. Diabase sample from Hole 920D exhibits moderate to high intensities of alteration. Sample is cut by prehnite + zeolite mineral-filled veins. Sample 153-920D-9R-1 (Piece 10, 87–97 cm).

Figure 61. Microphotograph of prehnite + zeolite vein. Sample 153-920D-9R-1 (Piece 10, 93–97 cm). Prehnite forms medium-grained cockscomb crystals, which are intergrown with radial acicular sprays of zeolite minerals. The minerals line and radiate out from vein walls indicating open space filling. Field length is 2 mm.

Away from the magmatic veins, intense static background alteration of the peridotites is governed by fracturing and hydration in the form of multiple generations of mesoscopic and macroscopic serpentine veins, which are common throughout the peridotite sections. The occurrence of chrysotile and lizardite in the early vein sets, indicates that much of the hydration in the peridotites occurred at temperatures below 400°C. Cross-fibered serpentine veins and veinlets (common throughout the harzburgites) indicate dilation and concomitant growth during tension that likely enhanced fluid circulation into the ultramafic rocks. Reactivation of these veins during later tensional events and formation of carbonate mineral + pyrite veinlets may be related to emplacement of the ultramafic rocks along the rift valley walls attendant with extensional tectonics. Formation of the carbonate mineral + pyrite veinlets and composite veinlets of serpentine + zeolite and clay minerals marks the general cessation of fluid flow in the ultramafic suite.

The metamorphic relations documented in the serpentinized peridotites of Holes 920B and 920D record a history of progressive strain localization and metamorphic recrystallization that occurred under conditions of decreasing temperatures and increasing hydration. This is overprinted by extensive low-temperature hydration that has affected nearly all of the peridotites regardless of their previous deformation and metamorphic history.

In contrast to the relative absence of high-temperature secondary phases characteristic of the ultramafic suite, mineralogical and textural features within the gabbroic to diabasic intervals, record intense high-temperature hydrous alteration both under dynamothermal and static conditions. In Hole 920B this high-temperature event is closely linked with intensely deformed, high-temperature shear zones composed of amphibolite, porphyroclastic gabbroic gneiss, and porphyroclastic mylonite intervals. Metamorphic mineral assemblages within these gabbroic sections that include recrystallized olivine, neoblastic clinopyroxene, and brown hornblende in near textural equilibrium with plagioclase indicate that dynamic metamorphism occurred under upper amphibolite to transitional granulite facies conditions (600°C–800°C). Retrograde alteration within these zones is strikingly sparse, with only minor alteration by greenschist facies mineral assemblages. In these deformed intervals, the occurrence of vapor-dominated inclusions entrapped along healed microfractures that are petrographically similar to methane-bearing fluids in gabbroic rocks from Hole 735B in the Southwest Indian Ocean indicates that these zones may have acted as channelways for the highly reduced fluids. Shore-based studies, however, are needed to confirm the compositions of these fluids.

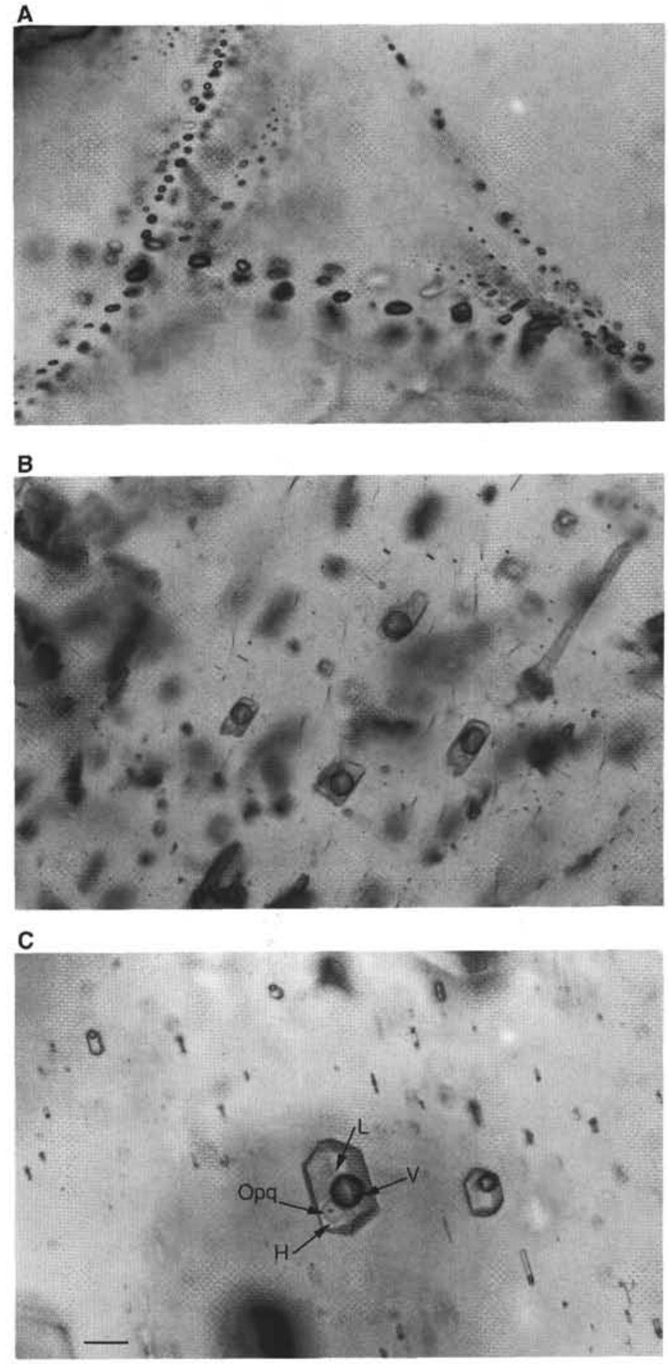

Figure 62. Photomicrographs of fluid inclusions in gabbro and pyroxenitic samples recovered from Holes 920B and 920D. **A.** Type 2: Apatite-hosted, vapor-dominated, daughter-mineral-absent inclusions along healed microfractures. The inclusions range in size from <1 to 12 µm and contain up to ≈100% of a vapor phase. Sample 153-920B-10R-3 (Piece 1, 0–5 cm). **B.** Type 3A: vapor-rich fluid inclusions in porphyroclastic mylonite. Sample 153-920B-13R-3 (Piece 6, 133–139 cm). The inclusions delineate healed microfractures, which cut plagioclase augen and are both cut and extend into fine-grained zones of neoblastic plagioclase. **C.** Type 3B: Halite-bearing inclusions in magmatic apatite. Sample 153-920D-20R-1 (Piece 4, 14–18 cm). The fluid inclusions contain a moderate-sized vapor bubble (V), rimmed by a high-salinity liquid (L), and contain daughter minerals of halite (H) + an opaque (Opq). Inclusion sizes vary from <5 to 20 µm. Scale bar is equal to 10 µm.

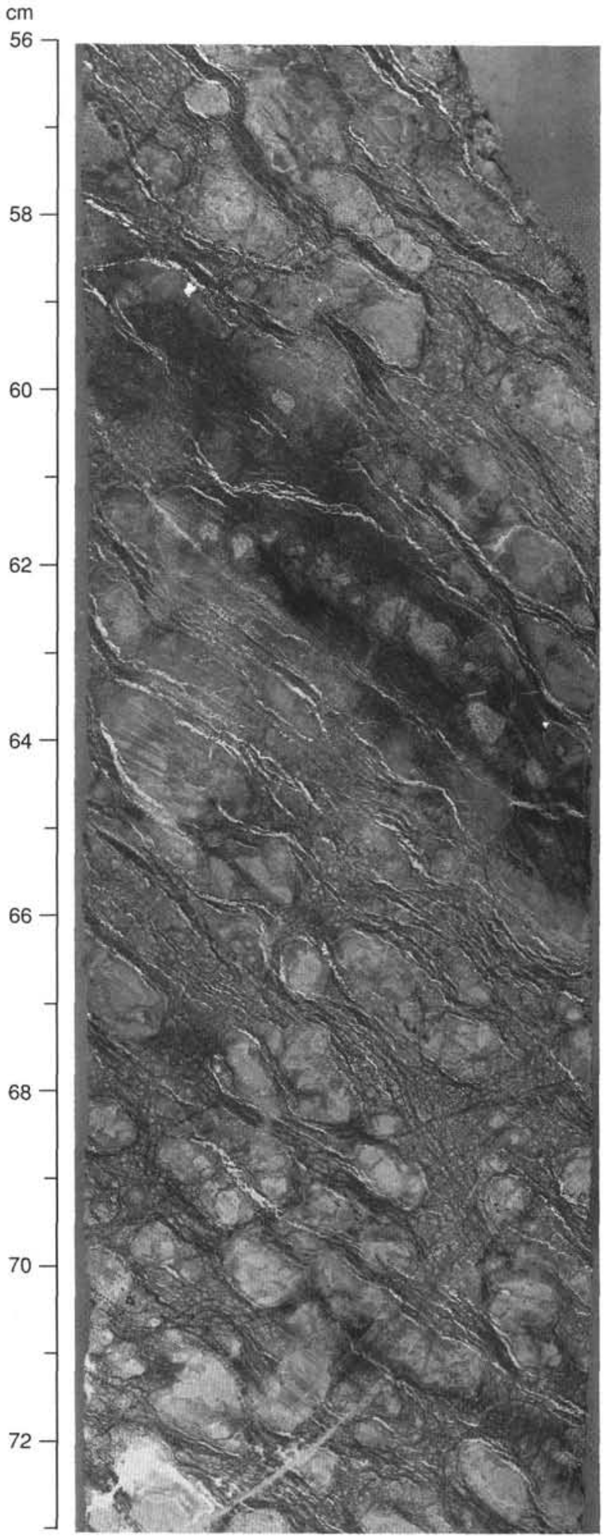

Figure 63. Elongated porphyroclastic texture in serpentinized harzburgite. Sample 153-920B-3R-1, 56–73 cm. Orthopyroxene porphyroclasts have a shape-preferred orientation that defines the crystal-plastic foliation. The thin white serpentine veins (V2) overprint and align closely with the anastomosing foliation defined by dark serpentine seams. The dark band at 65 cm has a lower modal abundance of orthopyroxene. The white serpentine veining and anastomosing foliation are less developed in this dark band.

STRUCTURAL GEOLOGY

Introduction

Cores from Site 920 are particularly valuable for structural studies of spreading center processes as they provide a high-resolution record of polyphase deformation over a total length of more than 327 m in serpentinized peridotites with minor metagabbro, amphibolite gneiss, and diabase. Although the absolute ages of deformation episodes are unconstrained, the structural relations identified in Holes 920A, 920B, and 920D constrain the deformation paths of mantle-derived lithologies during their exhumation. Furthermore, it has been possible to partially reorient 34 planar structures, measured in the core reference frame, using magnetic declination corrections (see "Paleomagnetism" section of "Explanatory Notes," this volume). These corrections provide preliminary constraints for placing the extensive structural data set acquired at Site 920 (over 1000 readings) within the kinematic framework of the MARK area.

The structures measured on core from Holes 920B and 920D are discussed within two broad divisions of deformation, the first involving dominantly crystal-plastic fabric and the second involving mainly brittle features. An overview of the structural characteristics of the crystal-plastic fabrics in the ultramafic lithologies is followed by an overview of the brittle deformation, including vein arrays and faults. The deformation of gabbroic and amphibolite units is then described. The downhole structural variations for Holes 920B and 920D are then discussed, followed by preliminary interpretations.

Hole 920A recovered only small fragments of serpentinized peridotite with weakly deformed orthopyroxene porphyroclasts forming an elongate porphyroclastic texture. No further discussion of Hole 920A will be included in this section (for lithological details, see "Igneous Petrology" section, this chapter).

Crystal-plastic Fabric in Serpentinized Peridotites

The predominant crystal-plastic fabric in serpentinized peridotites through both Holes 920B and 920D consists of a variably elongated porphyroclastic texture (e.g., Samples 153-920B-3R-1, 56–73 cm, and -920D-5R-2, 3–15 cm; Figs. 63 and 64). The downhole variations in the aspect ratios of orthopyroxene porphyroclasts suggest that there may be significant variations in strain on scales from centimeters to several meters. Some intervals appear undeformed, preserving equidimensional orthopyroxene grains (e.g., Samples 153-920D-14R-2, 30–64 cm and 110–123 cm, and -22R-4, 31–85 cm, and -22R-2, 0–86 cm; Fig. 64B). Gradients in porphyroclast ellipticity are preserved in single pieces. For example, in Sample 153-920D-5R-2, 3–15 cm (Fig. 64A), the orthopyroxene porphyroclasts have a weak preferred orientation at the base of the piece, and appear more elongate toward the top of the piece (4–5 cm). At the top of the piece, they seem to have fragmented into separate clasts, with lower elliptical ratios. The aspect ratios of orthopyroxene porphyroclasts in Holes 920B and 920D reach maximum values of about 5:1, but reconstruction of the fragmented porphyroclasts suggests that higher aspect ratios (6:1 to 8:1) may have existed. This ellipticity must constrain the lower limit of qualitative strain as recovery and recrystallization can maintain equant grain shapes even after large strains during high-temperature deformation. Serpentinite veins that transect orthopyroxene porphyroclasts also divide them into fragments. These fragments have different elliptical ratios to that of the original strained porphyroclast, introducing some error into the qualitative strain estimates. Serpentinization has obscured porphyroclast aspect ratios. It was assumed in these cases that the pre-serpentinization orthopyroxene porphyroclast shape was generally preserved and the shape was still used to estimate crystal-plastic fabric intensity estimates.

Observations of three-dimensional orthopyroxene porphyroclast geometries in four cuts parallel and perpendicular to the foliation in the working half of the core suggest that orthopyroxene porphyroclasts are predominantly oblate spheroids. One location contained

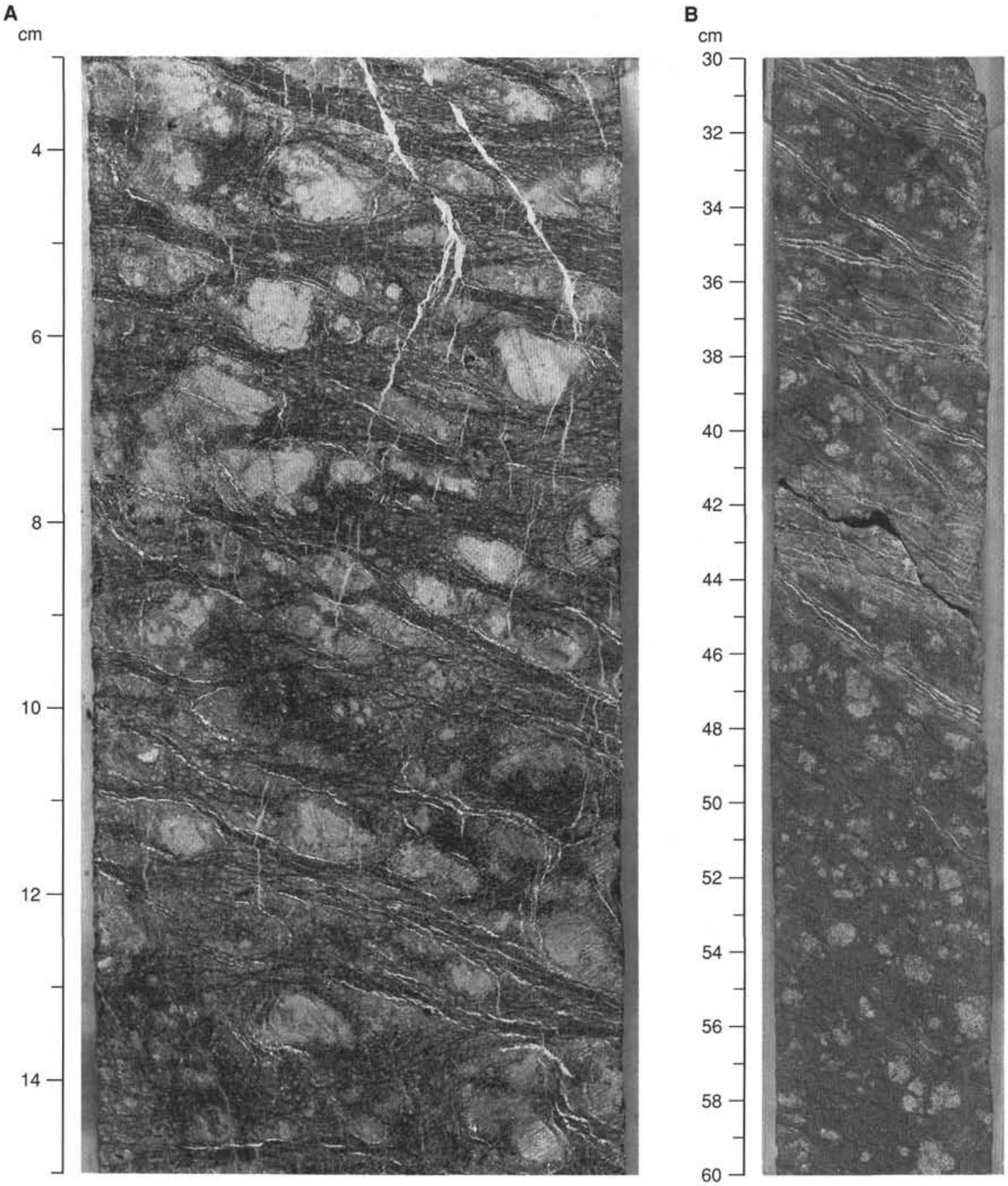

Figure 64. **A.** Elongate porphyroclastic texture in serpentinized harzburgite, Sample 153-920D-5R-2, 3–15 cm. Orthopyroxene porphyroclasts show a weaker shape-preferred orientation than in Fig. 63. Elongation appears to increase toward the top of the piece. The anastomosing serpentine foliation (black seams) is mirrored by white serpentine veins (V2). In contrast to Fig. 63, minor V2 arrays have also formed at a high angle to the foliation. **B.** Weakly deformed serpentinized harzburgite, Sample 153-920D-14R-2, 30–60 cm. Equidimensional orthopyroxene crystals at the base of the piece appear to grade upward into weakly elongated porphyroclastic texture, where a weakly anastomosing serpentine foliation (highlighted by wispy white veins) has overprinted the crystal-plastic fabric. The upper half of the piece also has a higher pyroxene content than the lower half. The change in modal composition coincides with an increase in the intensity of the anastomosing serpentine foliation and thin white serpentine veins (V2).

prolate geometries (Sample 153-920B-7R-2, 80–90 cm). Quantitative strain estimates for these apparent strain variations await detailed shore-based studies.

Thin-section studies indicate that in some cases aggregates of medium-grained olivine, orthopyroxene, and clinopyroxene (Figs. 19 and 65D) have been mistaken for orthopyroxene porphyroclasts during mesoscopic core description. In some samples, these aggregates appear less strained than the surrounding, finer grained matrix (Sample 153-920D-22R-4, 31 cm; Fig. 65D) based on relatively weak undulose extinction and weak subgrain development.

Orthopyroxene

In some thin sections orthopyroxene porphyroclasts display subgrain and fine-grained neoblast development in "tails" and "mantles." These recrystallized grains are commonly replaced during serpentini-

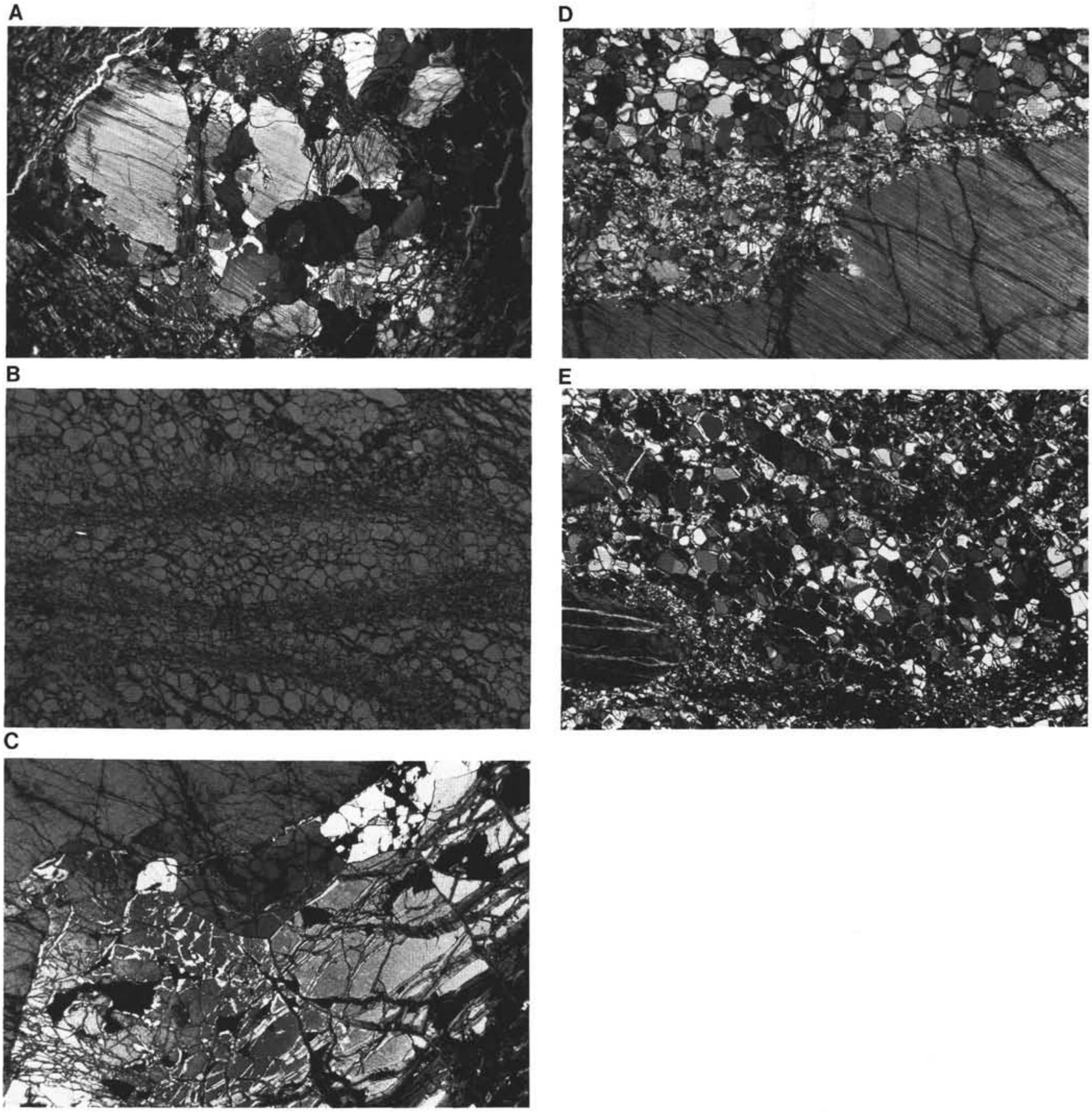

Figure 65. **A.** Thin-section 153-920D-2R-1, 116 cm, field of view = 3.4 mm. Porphyroclastic texture in a serpentinized harzburgite mylonite. Orthopyroxene (bottom) occurs as coarse elongated porphyroclasts with core-mantle microstructure. The porphyroclasts are mantled by olivine and orthopyroxene equidimensional neoblasts. Olivine neoblasts have a bimodal grain-size distribution with peaks at 100 (upper part of photography) and 20 µm (closer to orthopyroxene porphyroclast). **B.** Thin-section 153-920D-2R-1, 116 cm, field of view = 3.4 mm. Mylonitic serpentinized harzburgite. Olivine mosaic shows bimodal grain-size distribution that corresponds to alternating zones of relatively coarse (100 µm) and fine (20 µm) grains. **C.** Thin-section 153-920D-22R-2, 86 cm, field of view = 3.4 mm. Strongly annealed porphyroclastic harzburgite. The view shows part of a large (8 mm) subhedral orthopyroxene crystal (upper left) and a few equant olivine crystals displaying straight grain boundaries, triple junctions at 120°, and a recovered substructure. Olivine grain size ranges from 3 to 5 mm. Most harzburgites drilled at Site 920 display a similar texture, with variable grain sizes. **D.** Thin-section 153-920D-22R-4, 31 cm, field of view = 8.6 mm. Cluster of clinopyroxene, orthopyroxene, and olivine. This type of cluster is relatively resistant to serpentinization. **E.** Thin-section 153-920D-2R-1, 116 cm, field of view = 3.4 mm. Mylonitic harzburgite. Orthopyroxene porphyroclast in lower left is mantled by fine-grained (10–20 µm) neoblasts that extend as a tail with sinistral asymmetry. Olivine occurs as a mosaic of neoblasts with an average grain size of 100 µm. Two larger olivine grains in the upper left are strongly elongated and contain subgrain boundaries that are oriented at a high angle to the foliation defined by the porphyroclast tail. The obliquity between the long axes of these grains and the foliation also indicates sinistral shear.

zation. The orthopyroxene porphyroclasts in other samples show only limited evidence for crystal-plasticity in the form of broad kinks, kinked cleavages (also evident in hand specimens), and neoblasts less than 0.1 to 1 mm in size. The relatively coarse neoblasts (1 mm) develop at the edge of porphyroclasts, forming a mosaic cluster of equant orthopyroxene grains. The finer grained neoblasts are confined to mylonitic shear zones (Fig. 65), where they form elongate tails associated with the highly deformed porphyroclasts. Most orthopyroxene porphyroclasts in the core have low aspect ratios (1:1.5 to 1:2) and contain medium-grained (1–2 mm) olivine aggregates in the tail regions. The maximum grain sizes for orthopyroxenes range between 1 and 16 mm for Hole 920B and from 2.5 to 12.5 mm for Hole 920D. The minimum grain sizes range from submicroscopic to 2.5 mm (Hole 920B) and 6 mm (Hole 920D) (see "Igneous Petrology," this chapter). A spectrum of grain sizes from 6 mm to a few hundred microns can be observed in a single thin section.

Olivine

In thin section, olivine generally displays a medium-grained (1–2 mm) mosaic texture with straight-to-lobate grain boundaries and well-developed 120° triple junctions (Fig. 65C, D). Larger olivine grains (up to 9 mm) with irregular shapes occur in some samples where they appear to have been partially replaced by millimeter-sized grains. The presence of subgrains in the large olivine grains may be the precursors of the millimeter-sized grains generated during dynamic recrystallization. Many of the coarser olivine grains (2–3 mm) are located close to orthopyroxene grains or within aggregates of orthopyroxene and olivine in the tails of orthopyroxene porphyroclasts. Olivine grains are generally smaller than orthopyroxene grains, but they still show a spectrum of grain sizes: rocks from Hole 920B display minimum olivine grain size from submicroscopic to 1.5 mm, and the maximum grain size is 1 to 9 mm. In rocks from Hole 920D the minimum grain size ranges from a few hundred micrometers to 5.5 mm, whereas the maximum grain size ranges up to 6.5 mm (Fig. 18H). The embayed margins of some of the coarse olivine and orthopyroxene grains may have been caused by subsolidus grain boundary migration, or may have an igneous origin (Fig. 20). Lobate grain boundaries and subgrain boundaries are present in both medium and coarse olivine grains. Most olivine grains are equant. In some samples, however, olivine porphyroclasts have a shape-preferred orientation (aspect ratios generally less than 1:1.5) subparallel to the pyroxene porphyroclast elongation (Fig. 65E). The subgrain boundaries are commonly oriented at high angles to this weak olivine elongation (Fig. 65E). A pronounced crystallographic preferred orientation has been observed in some thin sections, indicated by the common extinction of most olivine grains. Mosaic textures with significantly reduced olivine grain sizes (a few tens of millimeters or less) are found in rare mylonitic shear zones, associated with finely recrystallized elongated orthopyroxene grains (Fig. 65A, B, and E).

Clinopyroxene and Spinel

Clinopyroxene grains are present as relict porphyroclasts with grain sizes varying between 2 and 6 mm. They also occur as dynamically recrystallized grains and in aggregates with orthopyroxene and olivine, with grain sizes varying between 0.1 and 4 mm. Undeformed clinopyroxene grains are found as interstitial phases in the deformed serpentinized harzburgites. Some of these interstitial grains display magmatic twins (see "Igneous Petrology," this chapter).

Spinel occurs as isolated grains, aggregates, or trails of grains (Fig. 20), localized along both linear and irregular paths, and as vermiform intergrowths with pyroxene (Fig. 15). Some isolated spinel grains display shape-preferred orientations that parallel the crystal-plastic foliation (e.g., Sections 153-920B-7R-2, Piece 8, and 153-920D-13R-2, Piece 6). Further shore-based studies are needed to determine whether the spinel grains were penetratively deformed or whether their elongate shapes resulted from a primary crystallization morphology. Some spinel grains display cuspate and holly leaf morphologies (e.g., Sections 153-920D-12R-1, Piece 1, and -16R-3, Piece 5). In some locations, both linear and nonlinear trains of isolated spinel grains and aggregates are oriented at a high angle to the crystal-plastic foliation. The trains can be traced for several centimeters (>10 cm) (e.g., Section 153-920D-5R-3, Piece 10). In these cases the trail of spinel may have formed after the generation of the crystal-plastic foliation.

Crystal-plastic Shear Zones in the Ultramafics

Rare mylonitic and ultramylonitic shear zones were recovered in core from both Holes 920B and 920D (e.g., Samples 153-920D-2R-1, 16–19 cm, and 137–140 cm, and -920B-2R-1, 43–53 cm; Figs. 65 and 66). These shear zones are typically a few millimeters to a few centimeters wide. Zones of strong porphyroclast elongation were noted as potential shear zone locations during core examination. As the elongation of the orthopyroxene is often obscured by anastomosing serpentine veins, the shear zones were subsequently confirmed by thin-section evidence for dynamic recrystallization and shear displacements.

Within mylonitic shear zones, the tails of dynamically recrystallized orthopyroxene porphyroclasts contain equant (10 to 100 μm) subgrains (Figs. 65A, B, and E). In these zones olivine shows a bimodal grain size where zones of extreme grain-size reduction (less than tens of microns) alternate with slightly coarser grained (10–100 μm) zones. Several zones of intense crystal-plastic fabric are spatially associated with gabbroic and clinopyroxenite dikelets (e.g., Section 153-920D-4R-1, Piece 12). Other strong foliations are preserved in small fragments (Section 153-920D-013R-2, Piece 3) or with pyroxene-poor ultramafic horizons (e.g., Sample 153-920B-7R-1, 15–65 cm).

Brittle Features

Anastomosing Serpentine Fabric

A dominantly planar fabric, comprising an anastomosing foliation, is present throughout the serpentinized peridotite sections and overprints the crystal-plastic deformation (Figs. 3 and 67). This fabric is defined by arrays of serpentine veins that do not consistently define a planar fabric. Dark green to black serpentine and magnetite veins that form this anastomosing foliation are deflected around, but in some instances cross, orthopyroxene porphyroclasts. In most cases the anastomosing serpentine foliation appears to be oriented subparallel to the crystal-plastic foliation but there are some exceptions (see below). Cross fibers are evident in the dark serpentine veins in thin section (Fig. 68). The wavelengths of the anastomosing foliation vary from individual pyroxene grain-scale to greater than 10 cm and the amplitudes can exceed 2 cm. Variations of the dips of the anastomosing foliation through both Holes 920B and 920D may also reflect longer wavelengths of the anastomosing fabric.

The intensity of the anastomosing foliation (Fig. 13, "Explanatory Notes," this volume) appears to mirror that of the crystal-plastic fabric in several places. For example, in Section 153-920D-5R-1 (Pieces 9 and 10) the anastomosing foliation intensifies and becomes more planar, and the crystal-plastic foliation also intensifies, approaching the gradational boundary with lithologic Unit 2; in Section 153-920D-5R-4 (Pieces 9–11) a drop in the intensity of the anastomosing foliation coincides with a reduction in the pyroxene content of the harzburgite at the lithologic Unit 2/3 boundary. Observations of this anastomosing foliation in thin section show that it is dominantly a dilational fabric (Fig. 68). Serpentine fibers in the thin serpentine and magnetite veinlets that define this foliation grow perpendicular to the veinlet walls. Evidence for shearing along this fabric, in the shape of serpentine fibers growing oblique to the veinlets walls or being deformed within the veinlets, is uncommon.

The anastomosing foliation is overprinted by arrays of thin, white serpentine veins of about 1–3 cm long that locally form narrow (5 cm) en-echelon arrays subparallel to the trace of the foliation. Veins of the same general appearance also form minor arrays in zones oriented

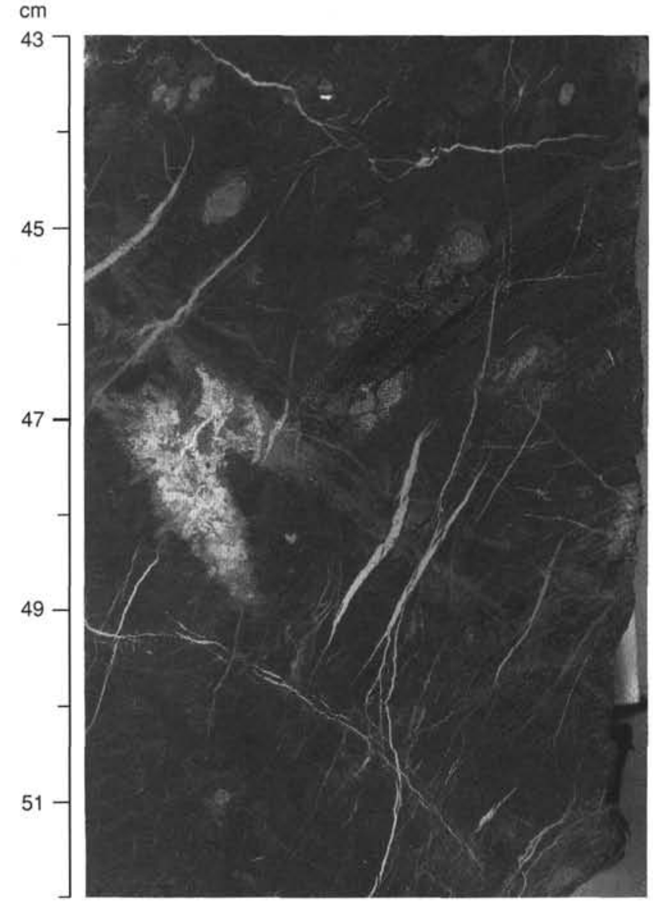

Figure 66. Altered metagabbroic patch (white) at the margin of a thin mylonitic shear zone (Sample 153-920B-2R-1, 43–52 cm) in the serpentinized harzburgite. Both the metagabbroic patch and the shear zone are cut by pale green serpentine veins (V3 generation). The V3 veins thicken as they cross the shear zone. They also cut sparse, thin white serpentine veins (V2) that trend subparallel to the shear zone.

perpendicular to the foliation (Section 153-920D-5R-4, Pieces 1–3). These veins are present in both Holes 920B and 920D, diminishing to trace (<1%) quantities in pyroxene-poor horizons (Fig. 12D). The white serpentine veins are thickest at the widest point of the porphyroclasts that are surrounded by vein traces (Fig. 63). The thicknesses of the veins vary between <1 and 3 mm. In several locations the spacing and distribution of these veins appear to be strongly dependent on the orthopyroxene content of the host harzburgite; abrupt increases in pyroxene content in units in both Holes 920B and 920D correspond to an increase in the density and thickness of veins and the intensity of the anastomosing foliations (Fig. 12D). For example, in Section 153-920D-5R-1 (Pieces 8 and 9) the junction between a pyroxene-bearing dunite and harzburgite exhibits an increase in the abundance of white serpentine veins in the harzburgite relative to the dunite (see also Samples 153-920B-12R-6, 44–69 cm, -13R-2, 70–130 cm, and -920D-11R-3, 0–30 cm). Even where the white serpentine veins are abundant the distribution is not always even. In some locations they cluster in zones (1–5 cm wide) where a slightly stronger porphyroclastic fabric is evident (Section 153-920D-14R-5). Although the white serpentine veins are nearly ubiquitous through both Holes 920B and 920D, veins are absent and only dark green serpentine and chlorite veins are present in some exceptional intervals (e.g., Section 153-920D-14R-2).

The coarser orthopyroxene grain sizes, combined with high orthopyroxene contents, also correspond to regions of high-angle vein deflections around the grain margins (e.g., Samples 153-920B-12R-6, 28–44 cm, -13R-1, 10–100 cm, and -13R-2, 73–100 cm). The orientations and distribution of the white serpentine veins, however, vary considerably. In some pieces, white serpentine veins form two sub-perpendicular arrays (e.g., Section 153-920D-4R-3, Piece 5). In other cases the veins become less planar and form broad segmented rings around porphyroclasts (Section 153-920D-20R-1, Pieces 12 and 13).

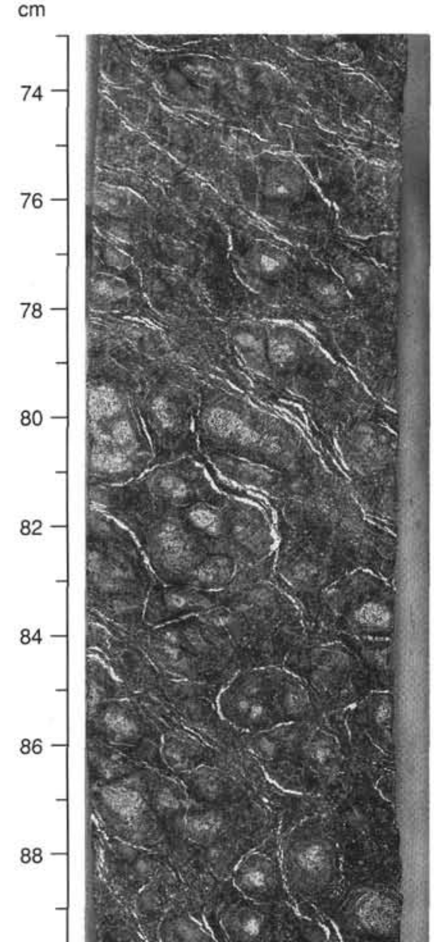

Figure 67. Strongly anastomosing foliation and white serpentine veins, deflected to high angles around orthopyroxene porphyroclasts in a pyroxene-rich interval. Sample 153-920B-13R-2, 73–100 cm.

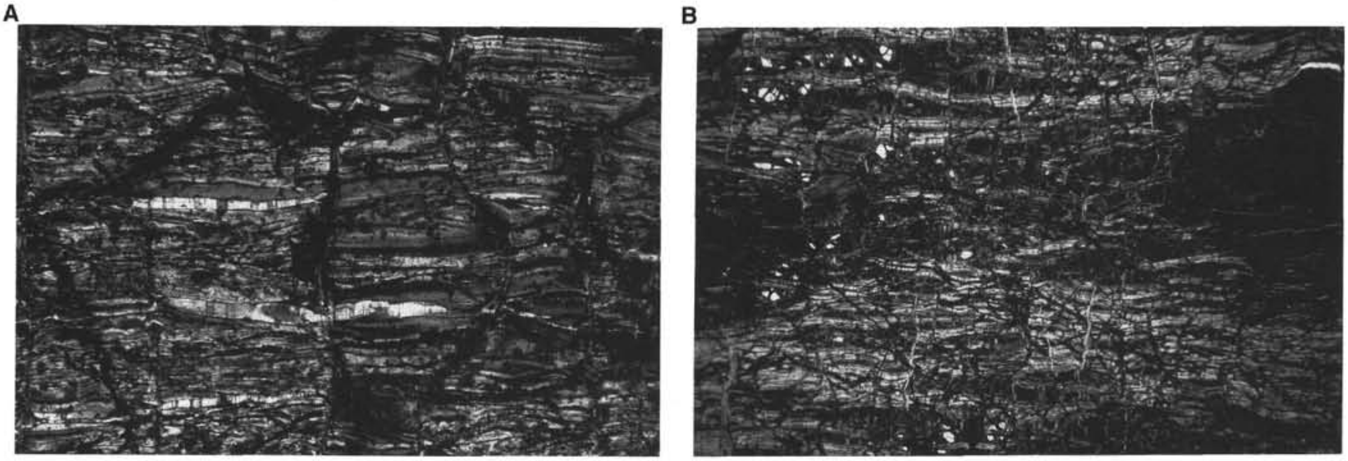

Figure 68. **A.** Thin-section 153-920B-12R-1, 117 cm, field of view = 3.4 mm. Set of closely spaced parallel serpentine veins in serpentinized harzburgite defines the anastomosing serpentine foliation. Serpentine fibers in the veins are perpendicular to vein walls, indicating that the large volume change associated with serpentinization was strongly anisotropic. **B.** Thin-section 153-920B-14R-3, 143 cm, field of view = 3.4 mm. Closely spaced serpentine veins in serpentinized harzburgite wrap around and cut through two bastite crystals (former orthopyroxene porphyroclasts). The vein fabric is weakly developed in the tails of these two bastites.

Although the anastomosing foliation appears generally oriented parallel to the crystal-plastic foliation defined by orthopyroxene porphyroclasts there are several instances in both Holes 920B and 920D where these two foliations are oblique to each other (e.g., 20° in Section 153-920D-4R-2, Piece 14; 90° in Sections 153-920D-3R-1, Piece 12, 153-920B-12R-2, Piece 6, and 153-920D-22R-5, Piece 6; Fig. 69).

Veins

A preliminary assessment of the vein chronology for both Holes 920B and 920D is graphically shown in Figures 50 and 70. Magmatic veins or dikelets that are oriented either concordantly or discordantly to the crystal-plastic fabrics predate the anastomosing foliation (Fig. 71; see "Igneous Petrology" and "Metamorphic Petrology," this chapter). These veins (termed "MV" for core description) consist of variably metamorphosed gabbro and clinopyroxenite; they are discussed below with the deformation of mafic lithologies. "V0" was used to indicate veins where cross-cutting relations suggested that a vein belonged to the earliest generation of veins, but where extensive alteration obscured any pre-existing magmatic textures (Fig. 70). Some of the dark-green serpentine veins of the anastomosing foliation cross the magmatic and V0 veins. The magmatic and V0 veins are also cut by discrete serpentine veins (V1). The "V1" veins are characterized by cross fibers (1–10 mm) of dark green serpentine and chlorite with minor actinolite and talc. In many cases these veins (V1) cut the anastomosing foliation at a high angle, but locally they run subparallel to it. In the latter case, some crosscutting relations are unclear and do not exclude an overlap between the generation of V1 veins and the anastomosing serpentine foliation. Most of the crosscutting relations, however, indicate that the V1 veins generally postdate the anastomosing foliation.

A second stage of veining (V2) is characterized by the thin, white discontinuous serpentine and magnetite veins that trend mainly subparallel, but in places perpendicular, to the anastomosing foliation (described above). In some locations, the foliation-perpendicular veins have localized along the trace of the pre-existing V1 veins (Sample 153-920B-1W-1, 48–60 cm; Fig. 12A; see "Igneous Petrology," this chapter).

A third stage of veining (V3) is characterized by more discrete, commonly branching, veins of pale green-white, "chalky" serpentine associated with carbonate, pyrite, and magnetite, with widths in many cases exceeding 0.5 cm. Later generations of veins (V4 and V5) are characterized by thin carbonate veins, some of which contain sulfide and clay minerals. These veins cross the V2 and V3 veins and reactivate some of the early dark green serpentine veins (V1). The orientations of the different generations of veins are discussed below.

Faults and Serpentinite Shear Zones and Joints

No major cataclastic fault zones were observed in rock from any of the Site 920 holes. Aligned serpentine fibers coating several joints indicate shear displacements, but these could not be measured. The most extensive serpentinite deformation occurs in Section 153-920D-10R-2, Piece 2. This piece contains crenulated and microfaulted serpentine fibers (Fig. 72).

Some pale-green serpentine veins contain fibers oblique to their margins (Fig. 73) and offset short (1 cm) segments of white and pale green serpentine veins that are orthogonal to the sheared vein margins. These "sheared" veins offset and are also cut by minor thin, green serpentine veins developed at high angles to their walls. Not all of the short veins are offset; some cut across the fibrous serpentine. In these cases, the crosscutting veins thicken (2–3 mm) and change color, usually becoming paler. Offsets of up to 1 cm were recorded. Shear senses derived from fiber orientations indicate a normal displacement in several locations (e.g., Sections 153-920D-18R-3, Piece 5, and -5R-4, Piece 1). Strongly aligned serpentine fibers (sometimes with talc) on exposed surfaces may also represent shear planes (e.g., Sections 153-920D-11R-2, Piece 12, -15R-6, Piece 7, and -16R-1, Piece 4). The timing of offset on the serpentine shear zones may vary, but they all appear to postdate the anastomosing serpentine foliation. For example, in Section 153-920B-12R-1, two steeply dipping serpentine veins cut the anastomosing foliation above a shear zone at the base of the section. One fault offsets a pyroxenite vein (Section 153-920D-5R-4, Piece 1). The crosscutting relationships between light green serpentine veins with oblique fibers and other veins suggest that they also postdate V2 veins and may have accommodated repeated displacements at different stages during the development of the V3 and V4 generations (Fig. 73).

Other possible indications of the existence of faults that were not recovered include brecciated fragments (Sample 153-920D-6R-2, 31–35 cm; Fig. 74) and rubble (Section 153-920D-15R-6, Pieces 1, 3, and 6). In Sample 153-920D-6R-2, 31–35 cm, an amphibole, calcite, and serpentine vein network forms a "jigsaw puzzle" texture (Fig. 74) that may indicate local hydrofracturing, but no fault rocks were recovered adjacent to or within this interval. The surfaces of rubble fragments appear to be fresh and do not show any evidence for frictional sliding prior to drilling. In some cases the rubble fragments occur close to sheared serpentine fibers (e.g., Section 153-920D-20R-5, Piece 5). Several open joint surfaces are evident toward the base of

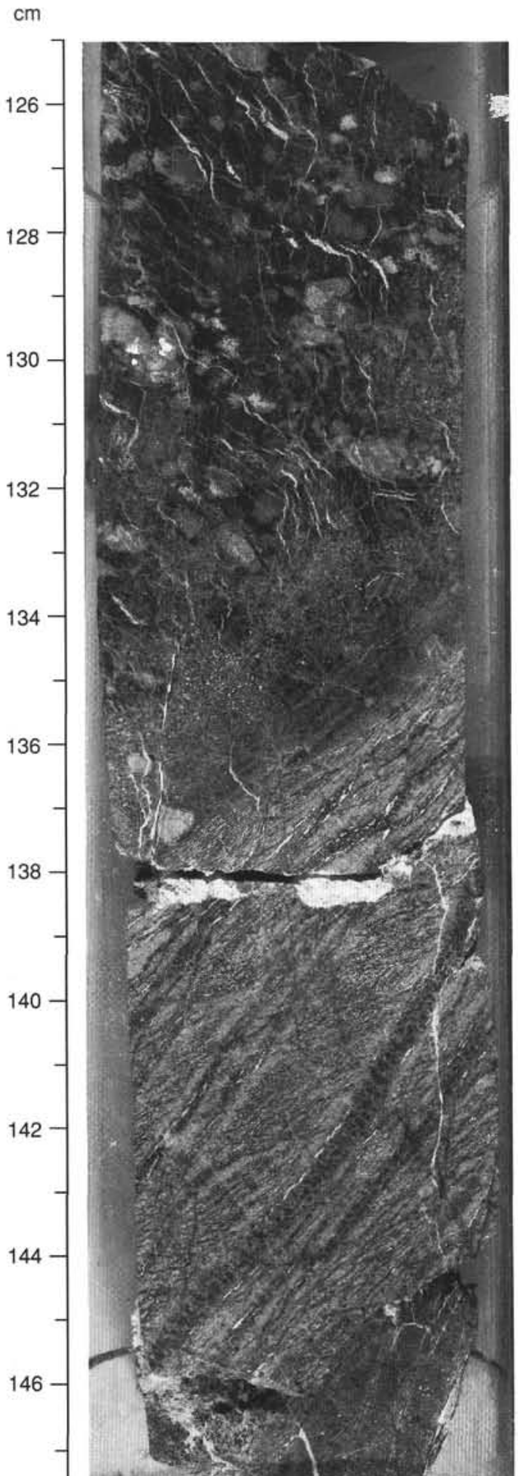

Figure 69. Intense serpentine veining in a pyroxene-depleted (dunitic) interval in the lower half of Sample 153-920B-12R-2, 125–148 cm, defines an anastomosing foliation. A thick serpentine vein crosses this anastomosing foliation from 137 to 147 cm. This zone is unusual in that its anastomosing foliation is oriented obliquely to the V2 veins and the anastomosing foliation in the overlying harzburgite (125–134 cm) and dips in the opposite direction.

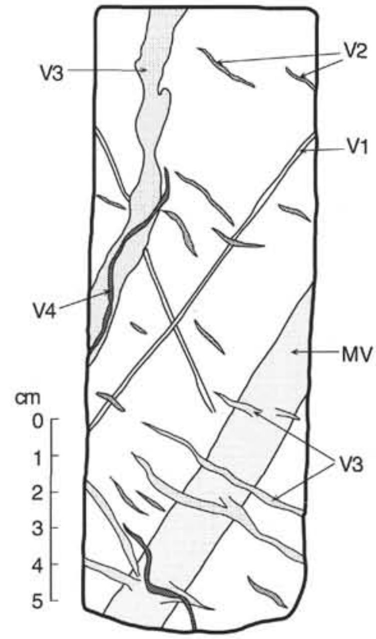

Figure 70. Chronology of veins determined from crosscutting relations in Holes 920B and 920D. MV represents "magmatic veins or dikelets" that are variably metamorphosed. A V0 vein (not shown) would occupy the same chronological position as the MV but would contain no relict magmatic phases. The numbers V1 to V4 represent successively later generations of veins. The mineralogy of these veins is shown in Figure 50. The relationship of these veins to penetrative fabrics is shown in Figure 75.

both Holes (e.g., Section 153-920D-14R-5, Pieces 6 and 9). Some sections contain closely spaced, orthogonal joint sets, with joints localized along the white serpentine veins (V2). Many of the ends of core pieces were formed along pre-existing joints.

Structures in Mafic Rocks

Holes 920B and 920D include a range of mafic lithologies that show varying degrees of deformation and different timing of deformation relative to the peridotite crystal-plastic fabrics. In Hole 920B these lithologies include variably altered pyroxenite, diabase, gabbro, metagabbro, and amphibolite. In Hole 920D they include rodingitized gabbro, amphibolitized microgabbro and oxide-rich metagabbro, oxide-rich clinopyroxenite, oxide-rich gabbronorite, feldspathic clinopyroxenite, hornblendite, and porphyritic diabase.

The first group of these mafic lithologies broadly can be considered as a group of structures referred to as "magmatic veins" (see "Veins," and "Igneous Petrology," this chapter) that consist mainly of variably altered metagabbroic and clinopyroxenite veins (Fig. 71). These veins are oriented both concordantly and discordantly to the penetrative fabrics (crystal-plastic foliation and anastomosing serpentine foliation). Magmatic veins that are discordant on the crystal-plastic fabric are generally thicker (1 mm to 5 cm) than the concordant veins (1–2 cm). They do not form organized arrays (e.g., Section 920D-16R-5, Pieces 2, 3, and 4) and generally they are weakly deformed or undeformed, regardless of their orientation. However, shear zones with a strongly elongated porphyroclastic texture are located in many cases in the pyroxene-poor margins of the magmatic veins (e.g., Sections 153-920D-12R-1, Piece 9, -12R-2, Piece 1, -12R-3, Pieces 3 and 4, -12R-5; Samples 153-920D-13R-1, 33–46 cm, -15R-3, 0–6 cm; and Section 153-920D-4R-1; Fig. 71). In Section 153-920D-13R-2, Piece 7, a magmatic vein is weakly deformed with minor kinking and distortion of clinopyroxene grains. The contact with the host serpentinized dunite is highlighted by numerous

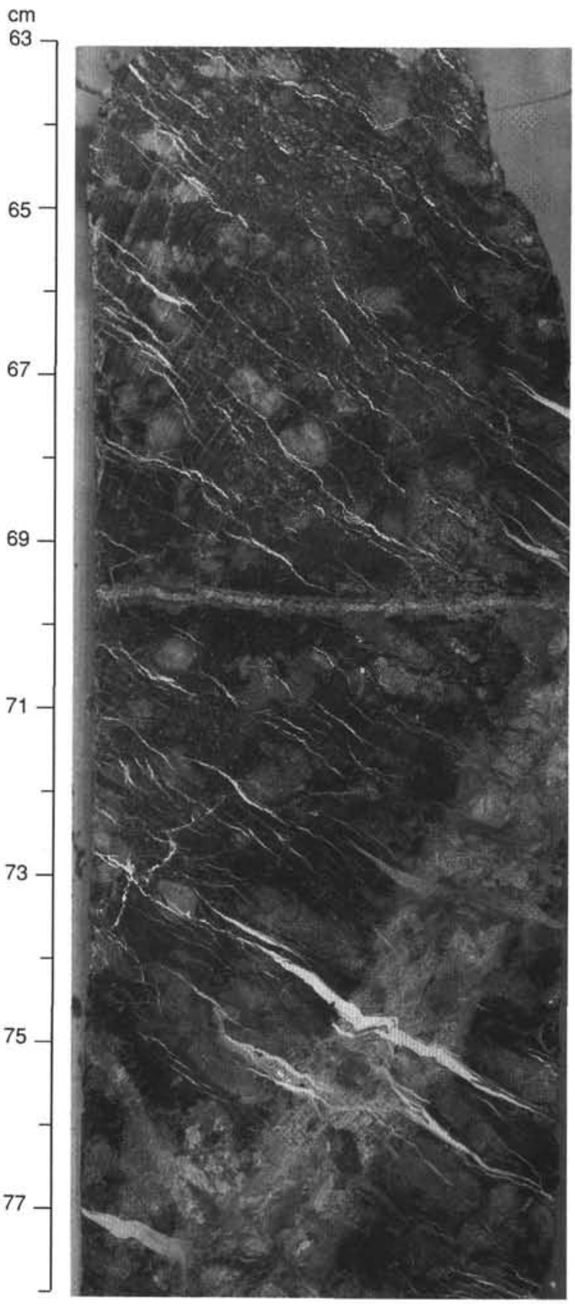

Figure 71. Example of a magmatic vein that cuts the crystal-plastic fabric at a large angle. Sample 153-920B-7R-3, 63–78 cm. Thin dark serpentine veins of the anastomosing foliation are parallel to the crystal-plastic foliation and cut the magmatic vein. The magmatic vein is also cut by V2 and V3 veins, which thicken as they cross the magmatic vein. At 70 cm a thin (2 mm) magmatic vein crosses the piece at an angle of about 30° to the crystal-plastic foliation plane.

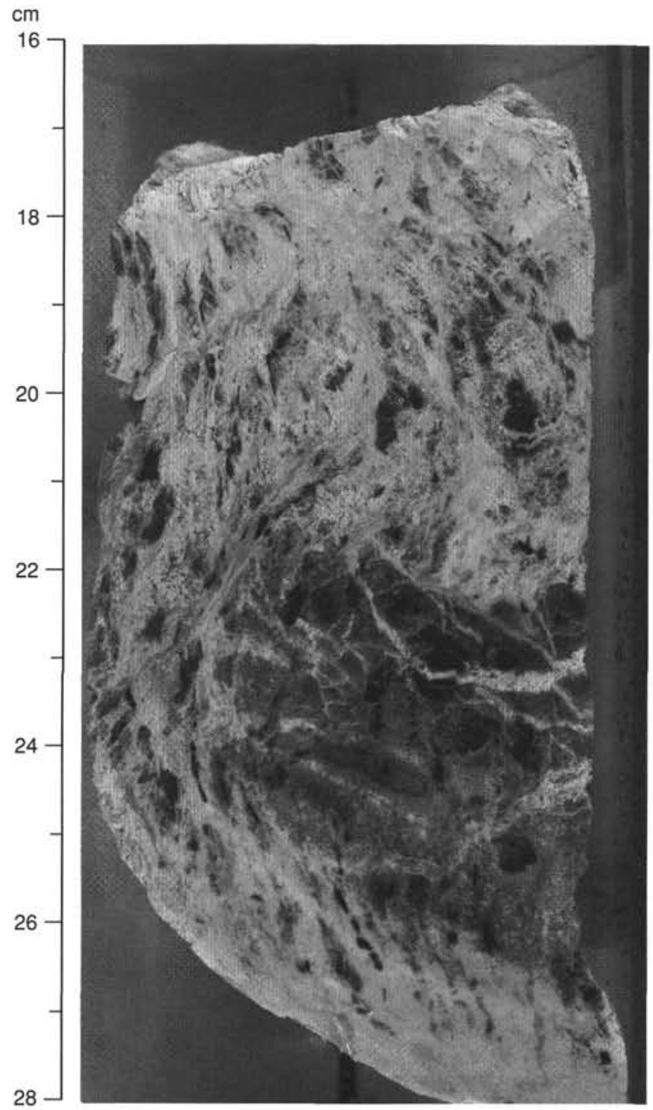

Figure 72. Sheared serpentinite, Sample 153-920D-10R-2, 16–28 cm. The center of the piece contains crenulation cleavages where the serpentine fibers have been tightly folded. Streaks of spinel grains have also been sheared and folded in the deformed serpentine matrix.

wispy white serpentine veins roughly parallel to the contact, which is adjacent to a crystal-plastic shear zone (see also Section 153-920D-11R-1, Pieces 5 to 7). One strongly deformed metagabbroic vein occurs in Piece 7 of Section 153-920D-18R-3, where grain-size reduction in tremolite and fractures in actinolite are evident.

The magmatic veins represent discrete lithologies within the peridotites but there are also more diffuse trails of clinopyroxenes, often steely gray, that transect the peridotites. Similar to the magmatic veins, these trails occur as both concordant and discordant features (Sections 153-920D-6R-1, Pieces 10A and 10B, and -12R-1, Pieces 5, 6, and 7) and mainly appear to postdate the crystal-plastic fabric.

Other gabbroic rocks recovered as isolated pieces may also have been magmatic veins with similar structural relations, but their contacts were not recovered. Some are pervasively altered, with the textures of the alteration phases closely resembling primary igneous textures (e.g., Section 153-920D-7R-1, Piece 18). Weak deformation of the metagabbro units is implied by kink bands in clinopyroxene and distorted plagioclase grains (e.g., 153-920D-11R-1, Pieces 6 to 10). A fine-grained, weakly foliated oxide gabbro may also represent a magmatic vein, but its contacts are not preserved (153-920D-2R-1, Piece 11).

A few of the mafic units are strongly deformed. In Unit 6 of Hole 920B a porphyroclastic mylonite separates weakly deformed gabbro (Sample 153-920B-13R-3, 104–133 cm) from the amphibolite and gneissic gabbro of Unit 7. This mylonite (Sample 153-920B-13R-3, 134–138 cm) represents the strongest crystal-plastic fabric in Hole 920B. In thin section, this shear zone appears as an extremely fine-grained matrix surrounding dynamically recrystallized feldspar porphyroclasts, displaying core and mantle structures (Fig. 59).

The amphibolite of Unit 7 has a strongly lineated to linear-schistose (L-S) fabric (Figs. 5 and 56). The fabric is defined by the preferred orientation of elongate hornblende, olivine, and clinopyrox-

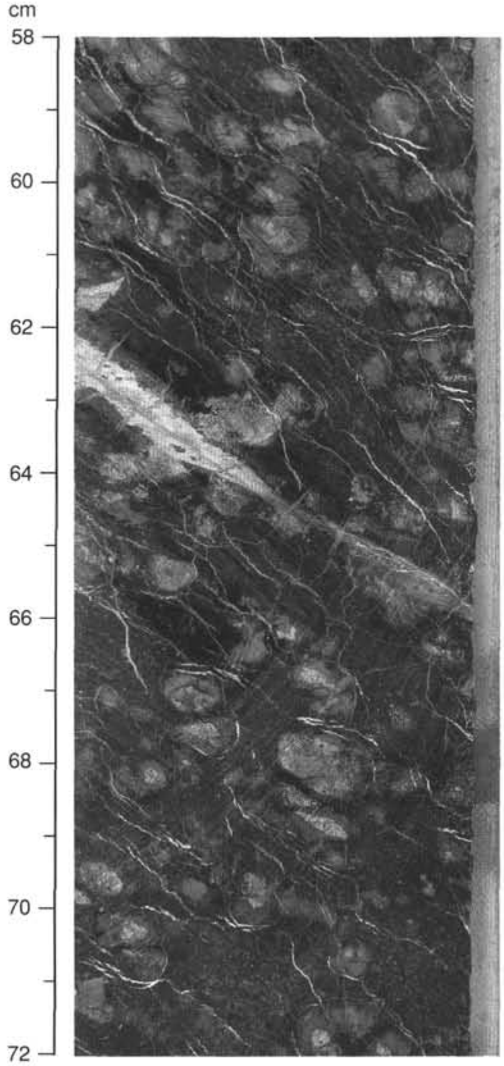

Figure 73. An example of a pale green serpentine vein with fibers oblique to the vein margins. Sample 153-920B-8R-3, 58–72 cm. Short vein segments cross the margins of this low-temperature shear zone, but are offset by a small (2 mm) right-lateral offset along a central zone approximately 1 mm wide. Crosscutting relations on these veins suggest that they may have been reactivated at different stages to accommodate minor displacements during low-temperature deformation.

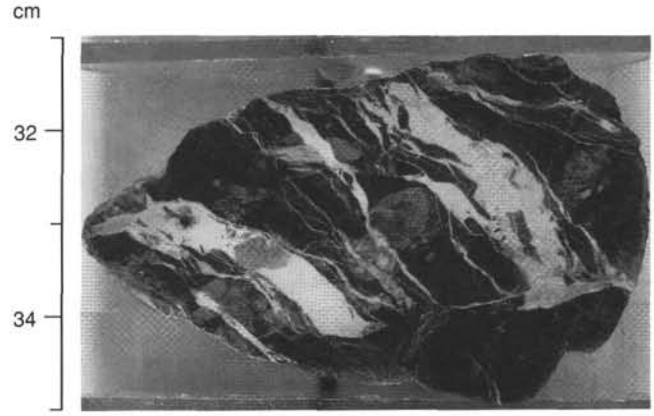

Figure 74. Brecciated fragments of serpentinized harzburgite in a matrix of prehnite, carbonate, and sulfide minerals. Sample 153-920D-6R-2, 31–35 cm. The "jigsaw puzzle" texture of breccia fragments may indicate locally high pore-fluid pressures and possible hydrofracturing.

ene grains and aggregates. A weak foliation is evident in some pieces, defined by fine-scale segregations of mafic-rich and plagioclase-rich layers. The adjacent gneissic gabbro is strongly foliated, containing porphyroclasts of clinopyroxene and plagioclase surrounded by a fine-grained recrystallized matrix of plagioclase and clinopyroxene (Fig. 58). The contact between these units is sharp, limited to a zone a few millimeters thick (Fig. 5). Thin-section examination shows this boundary to be tectonized with reduced grain size in both lithologies adjacent to the boundary. Penetrative crystal-plastic deformation is present along the subvertical contact where oxides have localized and where there is also a weak microfracture overprint.

In addition to penetrative crystal-plastic fabrics, discrete brittle features also deform metagabbro units. In the gabbroic unit at the base of Hole 920B, vuggy prehnite, zeolite, and carbonate veins are present but are undeformed (Sample 153-920B-13R-3, 110–130 cm; Fig. 55). The only deformation evident in a pegmatitic oxide gabbronorite in Hole 920D is represented by steeply dipping amphibole and prehnite veins (Section 153-920D-12R-3, Pieces 5 and 6). Porphyritic diabase units were recovered in both Holes 920B and 920D and are thought to belong to the same intrusive body (See "Igneous Petrology," this chapter). They are only weakly deformed by discrete veins, containing prehnite with clays and zeolites (Fig. 60). These veins have widths from 1 mm to about 1 cm and form irregular branching networks with no preferred orientation (see "Metamorphic Petrology," this chapter). In Section 153-920D-9R-1, the veins can be broadly divided into steeply dipping and subhorizontal arrays. Branching prehnite veins in the diabase show no preferred orientation (1–3 mm; 153-920D-7R-2). The crosscutting relations of veins in the diabase and metagabbro to serpentine veins in the peridotites are unknown.

Downhole Structural Variations

The downhole variations in intensity (see Fig. 13, "Explanatory Notes" chapter, this volume) and dip of the crystal-plastic and anastomosing serpentine foliations, as well as variations in the distribution and dips of the different types of magmatic and hydrothermal veins, are described below. Intensity and dip of the crystal-plastic foliation have been determined from macroscopic study of the core only. They may be modified following shore-based microscopic fabric studies.

Downhole Variations: Hole 920B

Crystal-plastic Fabric

The crystal-plastic fabric intensity in core from Hole 920B mainly varies between weak and moderate intensities. The strongest intensities (intensity values of 3 or 4; see Fig. 13, "Explanatory Notes" chapter, this volume) are spaced at 10- to 30-m intervals. Fabric intensity estimates, combined with shear zone locations confirmed with thin section observations, indicate strain gradients over 1-m intervals (e.g., Samples 153-920B-5R-2, 70–140 cm, and 153-920B-12R-2, 10–105 cm, Fig. 75). Section 153-920B-2R-1 (Piece 4) contains a strong crystal-plastic fabric, but the surrounding zone in core from the top of the hole down to Section 153-920B-3R-1 (Piece 1) is weakly deformed. The crystal-plastic fabric in rock below this section intensifies toward Section 153-902B-4R-1 (Piece 4), coinciding with the lower boundary of lithologic Unit 2, an orthopyroxene-rich peridotite. This increase in intensity persists to Section 153-920B-5R-2 (Piece 1). A shear zone is located at the base of Section 153-920B-5R-2, overlying a zone of increased crystal-plastic fabric intensity at Section 153-920B-5R-3 (Piece 1). Through lithologic Unit 3 (Sections 153-920B-4R-1, Piece 4, to -9R-3, Piece 8) there is a gradational increase in the overall intensity of the crystal-plastic fabric (Fig. 75). Peaks in the crystal-plastic fabric intensities occur at Sections 153-920B-5R-3 (Piece 1), -7R-1 (Piece 4), and -8R-3 (Piece 7). Below this last piece there is an overall reduction in crystal-plastic fabric intensity with

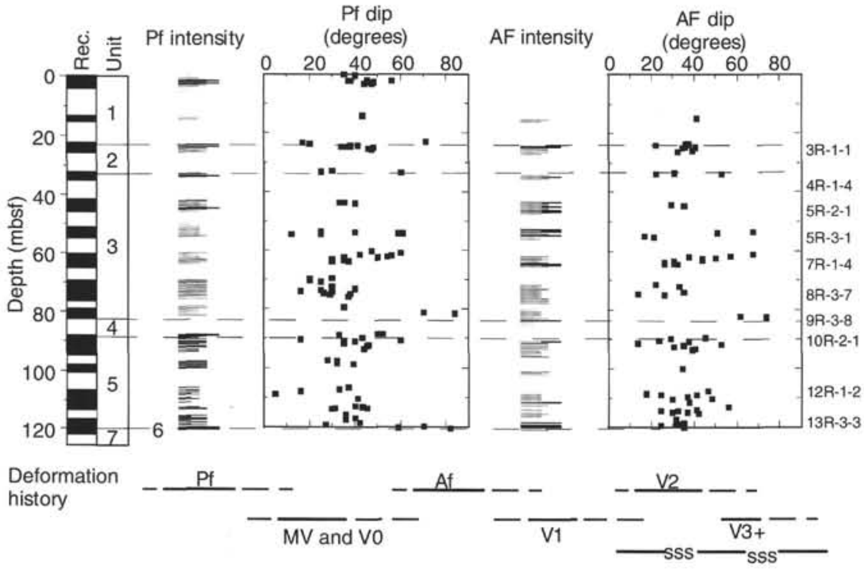

Figure 75. Fabric intensities and downhole dip variations for the plastic fabric (Pf) and anastomosing serpentine foliation (AF) in Hole 920B. The left column shows the recovered (black) intervals and lithologic units. The relative intensity scales have four bar lengths. (see Fig. 13, "Explanatory Notes" chapter, this volume). Piece numbers on right refer to the composite structural log in Figure 78. A schematic deformation history for the penetrative fabrics and veins is shown below. Time proceeds to the right. MV and V# = successive generations of veins; see text. The "s" lines represent the formation of sheared serpentine veins and their reactivation.

localized zones of increased intensity approaching the contact with the diabase dike (Section 153-920B-9R-3, Piece 8). Toward the base of the core, strong crystal-plastic fabric intensities are associated with mylonitic shear zones. These shear zones are located at the base of Section 153-920B-12R-1 (Piece 2) and within orthopyroxene-rich intervals in Cores 153-920B-12R and -13R. The peridotites are truncated by a gabbroic intrusion in Core 13R that marks the transition to the penetratively deformed gabbroic gneiss and amphibolite.

The apparent flattening plane of the orthopyroxene porphyroclasts has a true dip that varies primarily between 25° and 60° with extreme values of less than 5° and up to 85° (Figs. 75 and 76). The mean dip is 35° and the mean strike, in the core reference frame, is 352° (Fig. 76). Magnetic declination corrections suggest that the dominant strike azimuth is about 010° to 015° and that the dominant dip direction is to the east (see "Paleomagnetism" section, this chapter). Downhole plots of crystal-plastic fabric dip with depth suggest that significant variations occur over comparatively short intervals (Fig. 75). For example, between 20 and 30 mbsf, dip values range between 18° and 70°, but there does not appear to be a systematic change from low to high dips or vice versa. It appears that at least four such zones coincide with the location of the highest crystal-plastic fabric intensities. It is difficult, however, to evaluate the significance of these trends without the intervening dip record from the unrecovered borehole sections that may be just as varied.

Anastomosing Serpentine Foliation

The intensities of anastomosing foliation, qualitatively defined by the density and amplitude of the dark serpentine vein arrays (see Fig. 13, "Explanatory Notes," this volume), are dominantly weak to moderate throughout Hole 920B. The V2 veins are closely associated with the anastomosing foliation, and their intensity variations commonly co-vary. The strongest foliation intensities (intensity values of 3 or 4) are spaced at 2- to 20-m intervals. In core from the top of the hole the anastomosing fabric intensity increases gradually to a peak in Section 153-920B-3R-1 (Piece 1). A similar increase in the anastomosing foliation intensity occurs toward Section 153-920B-4R-1 (Piece 4), coinciding with the base of lithologic Unit 2. Below this (Section 153-920B-5R-2, Pieces 1–24), compositional layering introduces centimeter-scale variations in the intensity of the anastomosing foliation and white serpentine veins that overprint it. Dunitic intervals in these layers have only sparse veining and either a weak or absent anastomosing foliation. The anastomosing foliation intensity increases again at Section 153-920B-5R-3 (Piece 1), diminishing to Section 153-920B-7R-1 (Piece 4). Directly above the contact with the diabase dike the anastomosing foliation intensity increases but the white serpentine veins are only weakly developed, becoming steeply dipping in the two sections above the contact. Two of the strongest anastomosing foliation intensities are located at the base of Sections 153-920B-12R-1 and 153-920B-12R-2, where the orthopyroxene content decreases to less than 10% (see "Igneous Petrology," this chapter). The first of these (Section 153-920B-12R-1) is unique for Hole 920B in that it is the only zone where an intense, but more planar, foliation lies at a high angle to the thin white veins, the anastomosing foliation and the crystal-plastic fabric in the adjacent orthopyroxene-depleted serpentinized harzburgite. Directly above and below this zone the dips of the thin white vein arrays (V2) steepen to over 60° (Fig. 75).

The dips of the anastomosing foliation mainly range between 25° and 60°, with peak values to 85° and minimum values of about 15° (Figs. 75 and 76). The mean dip is 37° and the mean strike in the core reference frame is 356°, similar to that of the crystal-plastic fabric. Although the anastomosing foliation and the crystal-plastic fabric typically have extremely similar orientations they do not always coincide. For example, above the strongly foliated zone in Section 153-920B-12R-2 the crystal-plastic fabric dips at about 5°, oriented at about 60° to the anastomosing foliation.

Veins

The consistent cutting of cores perpendicular to the dominant foliation makes it possible to assess the relationship of vein orientations to penetrative fabrics on one stereoplot. In Hole 920B, poles to magmatic veins and "V0" have a wide scatter with dips ranging from subhorizontal to subvertical, but they have a weak preferred strike orientation that parallels the mean strike of the anastomosing foliation (Fig. 76). The V1 veins (dark green serpentine) have a similar wide range of dips with no consistent pattern of dips downhole or preferred strike orientation (Figs. 76 and 77). The V2 veins (white serpentine) cluster around a mean dip of 36° that overlaps with the strike and dip measurements of the anastomosing foliation poles and the crystal-plastic fabric (Fig. 76). V3 vein orientations have a small concentration for a mean dip of 22° but no downhole trends are evident (Fig. 77), and dips vary between 10° and vertical.

Faults and Serpentinite Shear Zone

Only minor faults were recovered in Hole 920B. There is a distinct zone of 22 m in Hole 920B that contains discrete serpentine veins with strongly oblique fibers that cut across the thin white serpentine veins and penetrative fabrics (Samples 153-920B-8R-3, 56–57 cm,

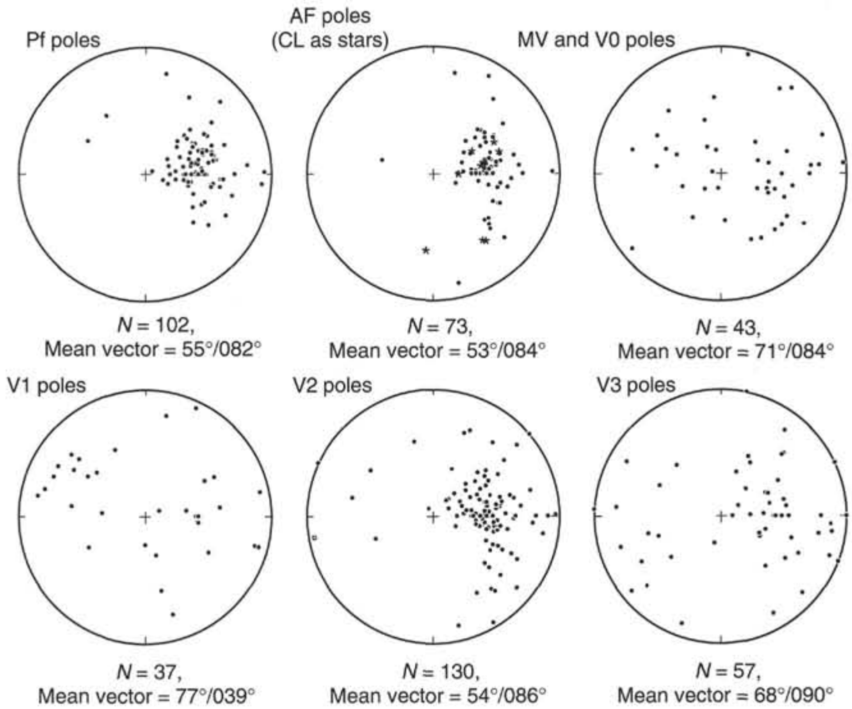

Figure 76. Equal-area stereoplots of the poles to planar fabrics and veins in Hole 920B, measured in the core reference frame.

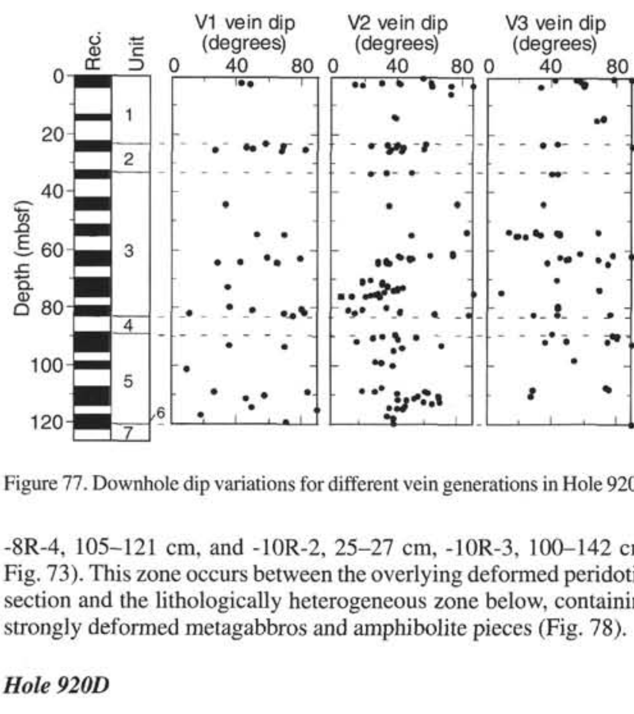

Figure 77. Downhole dip variations for different vein generations in Hole 920B.

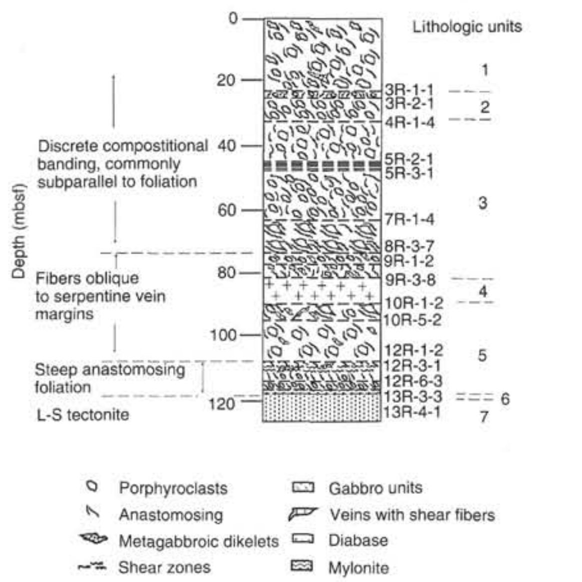

Figure 78. Composite structural log for Hole 920B. The sample numbers next to the lithologic units column correspond to the limits of the structural domain depicted in the figure.

-8R-4, 105–121 cm, and -10R-2, 25–27 cm, -10R-3, 100–142 cm; Fig. 73). This zone occurs between the overlying deformed peridotite section and the lithologically heterogeneous zone below, containing strongly deformed metagabbros and amphibolite pieces (Fig. 78).

Hole 920D

Crystal-plastic Fabric

Crystal-plastic fabric intensities in Hole 920D mainly show weak to moderate fabrics with peak intensities spaced at 10 to 50 m (Fig. 79). Variations in fabric intensity suggest strain gradients on centimeter and meter scales (e.g., Samples 153-920D-15R-3, 3–45 cm, and 153-920D-11R-1, 0–70 cm). Lithologic Unit 1 (top to Section 153-920D-5R-2, Piece 1) has a weak to moderately intense crystal-plastic fabric. Approaching the boundary with Unit 2, the fabric becomes more intense and has a shallower dip (Section 153-920D-5R-1, Pieces 9 and 10). From this boundary there is an overall decrease in crystal-plastic fabric intensity toward Section 153-920D-6R-1 (Piece 7). Between Sections 153-920D-5R-1 (Piece 10) and -6R-1 (Piece 7) there are several zones of intense crystal-plastic fabric. The fabric intensifies directly above Section 153-920D-8R-3 (Piece 7) and below Section 153-920D-10R-1 (Piece 1) on each side of the diabase dike forming Unit 6. The crystal-plastic fabric intensity remains relatively strong down to Section 153-920D-11R-3 (Piece 1). Below this there is a moderate crystal-plastic fabric, punctuated by strong fabric intervals down to a shear zone in Section 153-920D-13R-2 (Piece 6). There is also an apparent decrease in the dip of the crystal-plastic foliation from Section 153-920D-11R-3 (Piece 1) to -13R-2 (Piece 6). At Section 153-920D-14R-2 (Piece 8) a very weak crystal-plastic fabric is present, which strengthens toward a flat-lying crystal-plastic fabric in Section 153-920D-16R-1. In Sec-

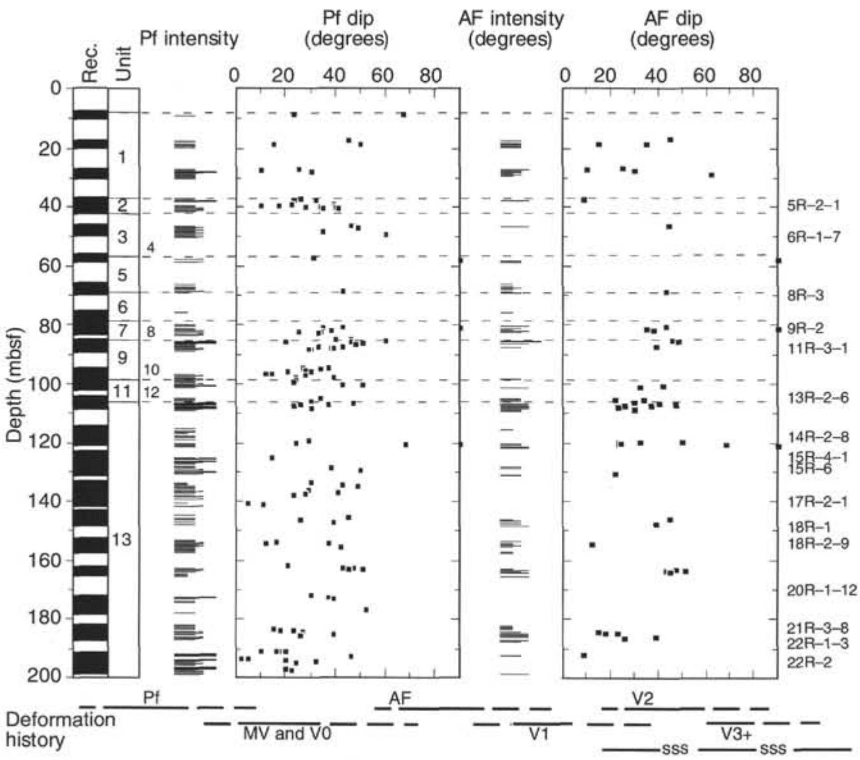

Figure 79. Fabric intensities and downhole dip variations for the plastic fabric (Pf) and anastomosing foliation (AF) in Hole 920D. Symbols are the same as for Figure 75. Piece numbers on right refer to the composite structural log in Figure 83.

tions 153-920D-16R-6, -16R-7, and -17R-1 several magmatic veins are associated with a strong, flat-lying crystal-plastic fabric. A pyroxene-poor horizon forms a distinct, weak crystal-plastic fabric zone at the top of Section 153-920D-18R-1, but the crystal-plastic fabric strengthens again at Section 153-920D-22R-1 (Piece 3) toward the base of the core recovered from the hole.

Overall the dips of plastic fabric for Hole 920D are shallower than Hole 920B, although they cluster mainly between 15° and 55° (Figs. 79 and 80). The dips range from subhorizontal to subvertical with a mean dip of 25° and a mean strike of 358° in the core reference frame. As in Hole 920B, high intensities of crystal-plastic fabric correspond to wide variations in dip over short intervals. Examples of these dip variations are located at the upper and lower boundaries of lithologic Unit 11 and within lithologic Unit 2 (Fig. 79). However, there are wide (more than 40°) variations in dip in the intervening zones and the data could be biased by the recovery locations.

Anastomosing Serpentine Foliation

The anastomosing serpentine foliation in Hole 920D appears to be less intense than in Hole 920B. The reduced number of anastomosing foliation measurements reflects this lower intensity (Fig. 79). Downhole intensity plots suggest that the anastomosing foliation is strongest in the upper half of core from the hole, and absent in several intervals below 120 mbsf (Fig. 79). From the top of the core down to Section 153-920D-5R-2 (Piece 1) there is weak to moderate anastomosing foliation intensity. The anastomosing serpentine foliation intensity increases toward the boundary of lithologic Unit 2 but is absent in several places between Sections 153-920D-5R-1 (Pieces 9 and 10) and -6R-1 (Piece 7). The anastomosing foliation intensity increases at Section 153-920D-8R-3 (Piece 7) above the contact with Unit 6. Below Unit 6, the anastomosing foliation intensity remains relatively strong until Section 153-920D-13R-2 (Piece 6), where the intensity diminishes. Below Section 153-920D-14R-2 (Piece 8) there is a virtual absence of anastomosing foliation and the thin white serpentine veins that overprint it. In Section 153-920D-14R-5 the white serpentine veins reappear but they have wavy profiles and steeper dips and the anastomosing fabric is not present.

Similar to the plastic fabric, the dips of the anastomosing foliation show a corresponding decrease in dip relative to Hole 920B. The mean dip is 38° and the mean strike is 009° in the core reference frame. Although generally very similar, the dips of the crystal-plastic fabric and the V2 veins that commonly overprint the anastomosing fabric do not always correspond. For example, in Sample 153-920D-3R-1, 121–137 cm, the V2 veins are subperpendicular to the crystal-plastic foliation. In Section 153-920D-4R-2, the V2 veins are oriented at an angle of about 60° to the crystal-plastic foliation.

Veins

There are two horizons in Hole 920D where magmatic veins are particularly abundant (Section 153-920D-6R-2; Sections -16R-5, Piece 2, to -17R-1, Piece 1; Sections -18R-2, Piece 9, to -18R-4, Piece 1). The metagabbroic and pyroxenite dikelets and V0 veins have a broad scatter of dips down the core with a mean dip of 20° (Figs. 80 and 81). Similar to rocks from Hole 920B, these vein orientations also have a slight concentration that gives a strike orientation close to that of the crystal-plastic fabric and anastomosing foliation. The V1 veins have a wide scatter of dips through the core with both subhorizontal and vertical dips. There is a weak downhole trend that suggests that the V1 veins may steepen with depth (Fig. 81) but no strong preferred orientation is evident. Toward the lower half of core from the hole the V2 veins have more variable geometries than those of Hole 920B. For example, in Sample 153-920D-22R-6, 24–35 cm, the V2 veins become strongly anastomosing and in some intervals form subperpendicular arrays (Fig. 82); In Sample 153-920D-15R-6, 40–70 cm, the V2 veins exhibit long wavelengths (>20 cm). The mean dip for the V2 veins is 26° with a mean strike of 356° in the core reference frame. Two intervals of Hole 920D are unique in their complete lack of V2 veins and preservation of V1 veins in weakly deformed horizons containing 17% to 20% pyroxene (Samples 153-920D-14R-8, 5–125 cm, and -22R-7, 0–50 cm). The V3 veins show a very broad scatter of dips reflecting their typically irregular, branching nature. The mean strike is 348°, close to the strike of the penetrative fabrics and magmatic veins. No downhole trends are evident.

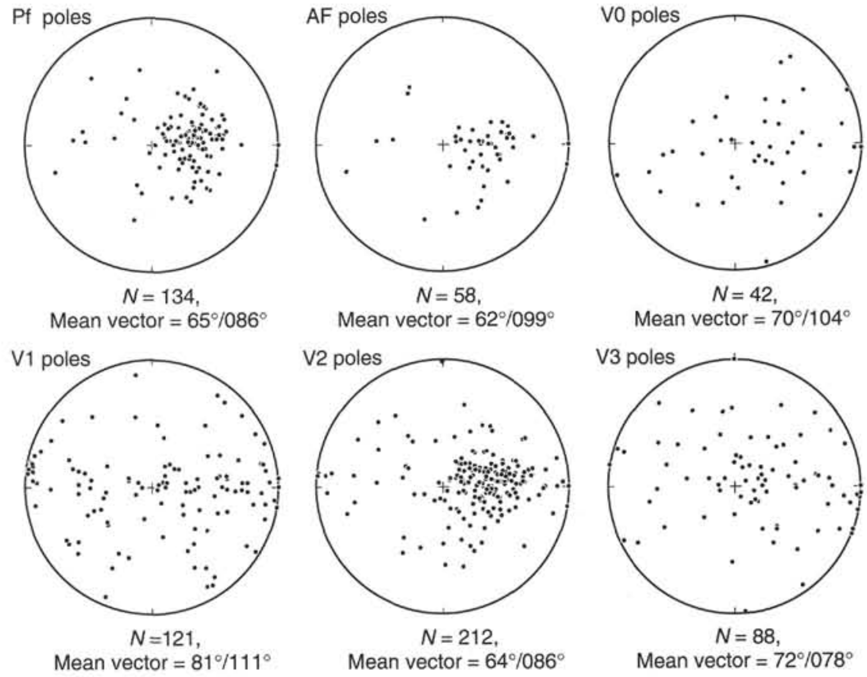

Figure 80. Equal-area stereoplots of poles to planar fabrics and veins in Hole 920D, measured in the core reference frame.

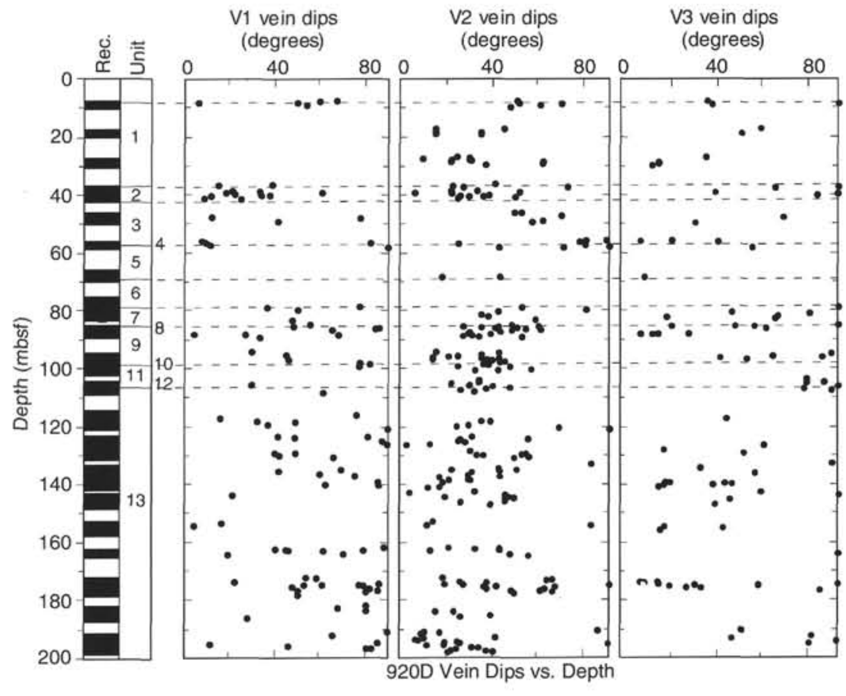

Figure 81. Downhole dip variations for different vein generations in Hole 920D.

Faults and Fractures

The lower sections of Hole 920D (below Section 153-920D-13R-1) contain several strongly fragmented core pieces that display fresh fracture surfaces with no slickenlines. Some pieces can be reconstructed along joint sets that parallel the anastomosing foliation or are subperpendicular to it (Section 153-920D-21R-4, Pieces 2, 4, 5, 7, and 8). Two perpendicular arrays of V2 veins are associated with zones of open fractures (e.g., Samples 153-920D-14R-5, 0–9 cm, -16R-1, 80–90 cm, and -22R-5, 65–120 cm) and may indicate the presence of unrecovered faults that cut the anastomosing foliation and V2 veins. Talc and serpentine assemblages form fault surfaces in Sections 153-920D-10R-2, -12R-2, and -15R-6, whereas in Hole 920B the small number of identified, minor faults are predominantly mineralized with serpentine.

Summary of Downhole Variations

Downhole variations in structural style reflect the overprinting of early-formed crystal-plastic fabrics by the anastomosing foliation and polyphase veining. Downhole variations in the intensities of one or more of the fabrics described above have been used to delineate decimeter-meter-scale domains of more or less uniform structural style with either discrete or gradational boundaries (Figs. 78 and 83).

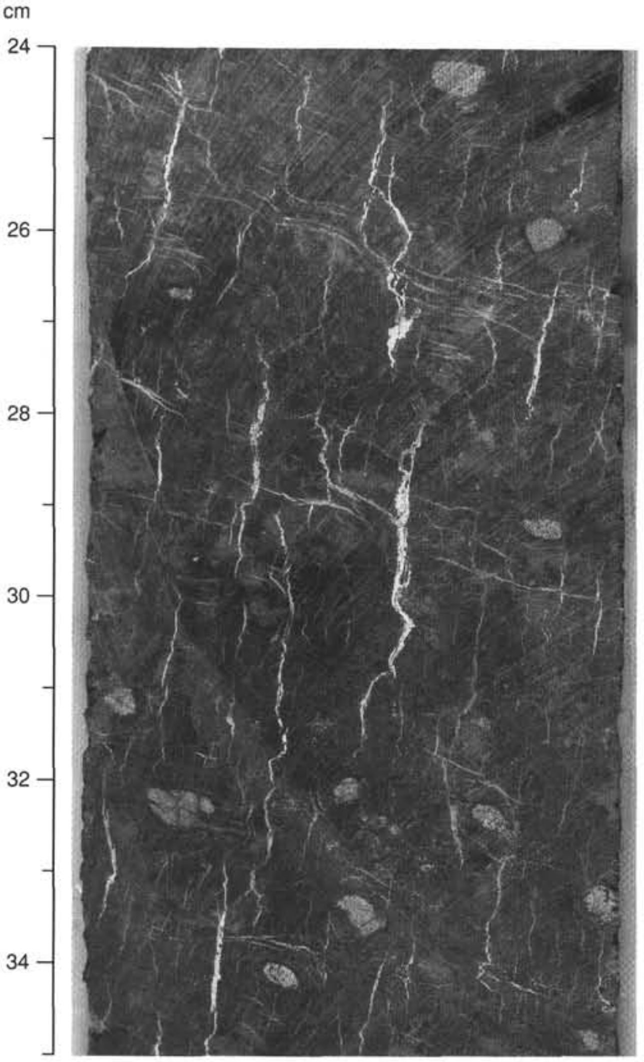

Figure 82. Subperpendicular arrays of V2 veins in an interval of low pyroxene content in a serpentinized harzburgite. Sample 153-920D-22R-6, 24–35 cm.

Some caution is necessary for interpreting such domains due to the discontinuous nature of the core record. The graphic structural log in Figure 78 is a simplified and schematic representation of recovered core sections, expanded to fill the drilled interval. They do not necessarily form an accurate representation of the depths and thicknesses of structural domains.

Several of the domain boundaries coincide with changes in intensity of both the anastomosing foliation and the crystal-plastic fabrics and several major lithologic boundaries (e.g, the lower boundary of Unit 2, Section 153-902B-4R-1, Piece 4; the upper contact of Unit 6, Section 153-920D-8R-3, Piece 7) and compositional variations (e.g., orthopyroxene-rich zones in Cores 153-920B-12R and -13R). Many of the peak anastomosing foliation and crystal-plastic fabric intensities also coincide with domain boundaries.

From Hole 920B, meter-scale variations in the crystal-plastic fabric intensity can be summarized as follows: it is generally moderate to weak in the upper half of the hole down to Section 153-920B-7R-1, Piece 4 (i.e., from 0 to ~62 mbsf), strong down to Section 153-920B-10R-5, Piece 2 (i.e., down to ~95 mbsf), and again moderate to weak down to the gneiss in Unit 7. The diabase unit forms an undeformed interval within the zone of strong crystal-plastic fabric. Superimposed on these meter-scale variations, numerous centimeter- to meter-thick intervals with a strong crystal-plastic fabric are scattered throughout the hole. Thin mylonitic shear zones are concentrated close to the gneiss unit (Unit 7) but are also recognized higher up in the hole, commonly on the margins of magmatic veins.

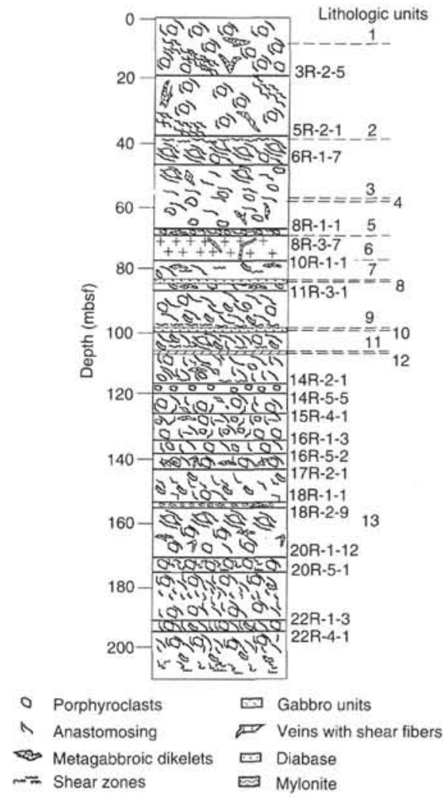

Figure 83. Composite structural log for Hole 920D. The sample numbers next to the lithologic units column correspond to the limits of the structural domain depicted in the figure.

The anastomosing serpentine foliation is generally strong and moderately dipping down to Section 153-920B-9R-1, Piece 2 (i.e., about 75 mbsf), weak and steeply dipping around the diabase unit, down to Section 153-920B-12R-1, Piece 2 (~110 mbsf), and again strong down to the gneiss in Unit 7. As in the case of the crystal-plastic fabric, centimeter-scale variation in anastomosing foliation intensity is superimposed on this trend. Other centimeter-scale variations are observed between Sections 153-920-B-5R-2, Piece 1, and -5R-3, Piece 1, and are correlated with centimeter-scale compositional banding.

At the top of Hole 920D the crystal-plastic fabric is weak to moderate down to Section 153-920D-5R-2, Piece 1 (i.e., ~38 mbsf) and more strongly developed down to Section -14-R-2, Piece 1 (i.e., ~115 mbsf) in an interval including the undeformed diabase (Unit 6). Below this the crystal-plastic fabric is weak down to the bottom of the core from the hole, except in an interval between 150 and 160 mbsf, where it is strongly developed. As in Hole 920B, numerous centimeter- to decimeter-thick intervals showing a strong crystal-plastic fabric are scattered throughout the hole, and mylonitic shear zones are commonly associated with magmatic veins.

As in Hole 920B, the intensity of the anastomosing foliation presents both large-scale and small-scale variation. However, a distinct interval in Section at 153-920D-14R-2, Piece 8, is very different from any of the structural styles encountered in Hole 920B. This interval is characterized by a very weak crystal-plastic fabric and a virtual absence of thin white serpentine veins and no anastomosing foliation. Dark-green irregular serpentine veins form a network around the porphyroclasts.

Discussion

The earliest mesoscopic deformation in the serpentinized harzburgites from Holes 920B and 920D has generated a variably elongated,

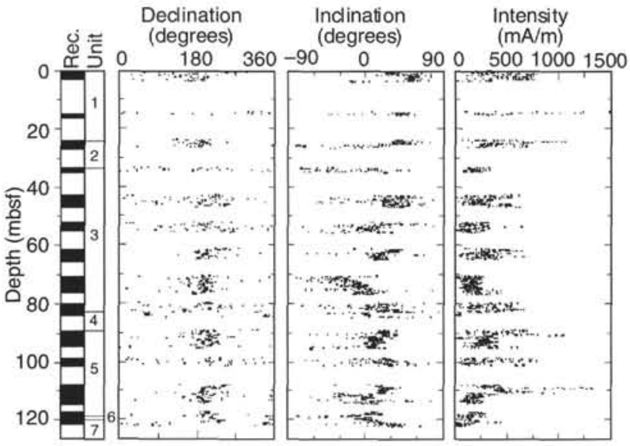

Figure 84. Downhole remanence data for Hole 920B archive half-cores after demagnetization at 20 mT. Note the consistency of the declination and inclination values.

medium- to coarse-grained porphyroclastic texture that comprises mainly orthopyroxene porphyroclasts (or clusters of orthopyroxene, clinopyroxene, and olivine) surrounded by a matrix comprising dynamically recrystallized olivine with minor orthopyroxene and clinopyroxene. The primary minerals in serpentinized harzburgites display a wide range of microstructures that suggest variable stress and/or strain conditions during progressive deformation at elevated temperatures. The relatively large, partly recrystallized olivine grains observed in some samples may be interpreted as the relics of a coarse-grained equigranular texture produced during dynamic recrystallization at high temperature and low deviatoric stress conditions. Textural relations, at least locally, are also compatible with high-temperature annealing, which may have been locally contemporaneous with intergranular melt migration. The medium-grained mosaic texture of recrystallized olivine is the most volumetrically significant texture and probably developed during a later stage of crystal-plastic deformation, possibly under higher, although still moderate, deviatoric stresses. Temperature conditions during this event are believed to have been quite high, as well-developed triple junctions and commonly lobate grain boundaries suggest grain-boundary migration. Finally, the fine-grained olivine that recrystallized in discrete mylonite shear zones may indicate relatively high deviatoric stresses for this later stage of crystal-plastic deformation.

Qualitative strain estimates of the crystal-plastic fabric based on porphyroclast elongation and the degree of preferred alignment provide a framework for a qualitative assessment of strain variations through the core. These fabric intensities have helped to identify local centimeter- to meter-scale strain gradients.

The magmatic veins and diffuse trails of clinopyroxene that transect the serpentinized peridotites are interpreted as syn- to post-kinematic melt migration channels preserved in the serpentinized harzburgite host. Trails of spinel grains may also represent zones of syn- and post-kinematic melt percolations (see "Igneous Petrology," this chapter). Only a small proportion of these veins are deformed. However, the spatial association between these magmatic veins and mylonitic shear zones suggests that they may be genetically linked, with melt segregations enhancing strain localization and/or shear zones providing transient melt migration paths.

The anastomosing foliation formed by fine, dark-green serpentine veins and overprinted by thin, white serpentine veins forms the dominant low-temperature (<550°C) fabric in the serpentinized peridotites. The intensity of this foliation is clearly influenced by lithologic variations but also varies within homogeneous units. The majority of the dark green serpentine veins appear to have a dilational origin. A few examples of fibers oblique to the margins of serpentine veins within the anastomosing foliation suggest that some shearing may have been associated with its development, but is very limited.

The white serpentine veins (V2) may have been generated by stress release as the peridotites were exhumed, reflecting variations in stored elastic strain in the orthopyroxene-rich horizons. The thin white, discontinuous vein fibers are also generally perpendicular to the vein margins suggesting that they accommodate a dilation. The differential volume change between the olivine matrix and the orthopyroxene porphyroclasts during serpentinization may have also contributed to extensional veining around the margins of the porphyroclasts controlled by the pre-existing fabric anisotropy. The changes in the orientations of the white serpentine veins may reflect change in the local stress field during their generation. Variations in the geometries of the white serpentine veins are strongly influenced by the modal abundance and grain size of orthopyroxene porphyroclasts.

Later generations of veins (V3 and later) include some veins with oblique fibers that suggest syn-kinematic growth during shear displacements. Some of these minor, low-temperature shear zones appear to have been reactivated two or three times. High anastomosing serpentine foliation intensities in some intervals may also be linked with low-temperature shear zone development.

PALEOMAGNETISM

Introduction

Paleomagnetic measurements were made on all archive half-rounds and a total of 148 minicores (approximately one sample per section) taken from Holes 920B and 920D. The aims of the measurements were to characterize the magnetic properties of the serpentinized peridotites and to determine characteristic remanence directions that could serve as a basis for reorienting structures observed in the cores from this slow-spreading area.

Whole-core Measurements

All archive half-cores from Holes 920B and 920D were measured at an interval of 3 cm with the pass-through cryogenic magnetometer. In most cases, the natural remanent magnetization (NRM) intensities proved too high to yield reliable data. The maximum number of flux counts (9999) on the 2G magnetometer corresponds to a total magnetic moment of approximately 1.5 emu. Thus, discrete sample (~10 cm^3 volume) magnetizations of 150 A/m may theoretically be measured. The much larger effective volume (factor of ~50) of the archive half-cores, however, is sufficient to overwhelm the counters at relatively modest magnetization values (~3 to 5 A/m). Most archive half-cores from Site 920 therefore were measured after demagnetization at 20 mT, with additional demagnetization steps at lower peak fields when time permitted.

Half-core remanence data from Hole 920B show broadly consistent declination and inclination values downhole (Fig. 84), despite the considerable scatter resulting from small unoriented pieces and edge effects at piece boundaries. The clustering of declination values near 180° reflects the systematic slicing of the cores parallel to the dip of the dominant foliation and therefore a consistent relationship of this foliation to the measured declination throughout the core. Inclinations are predominantly in the region of 20°–40°, in general agreement with the values expected from an axial geocentric dipole (41°) or the present field inclination (42°) at the site. Inclination values from much of Hole 920D are significantly steeper (~60°) and declinations more scattered, possibly as the result of a spurious magnetization acquired during demagnetization. Frequent demagnetization of the shield surrounding the AF coils was found to be necessary to prevent the acquisition of an anhysteretic remanence (primarily along the z-axis, the last axis to be demagnetized) during demagnetization. Although highly scattered, Hole 920D declinations cluster around 180° as seen in Hole 920B.

The archive half-core data allow an estimate of the characteristic remanence direction in continuous core pieces longer than ~15–20 cm. For example, long continuous pieces in Core 153-920D-22R can be

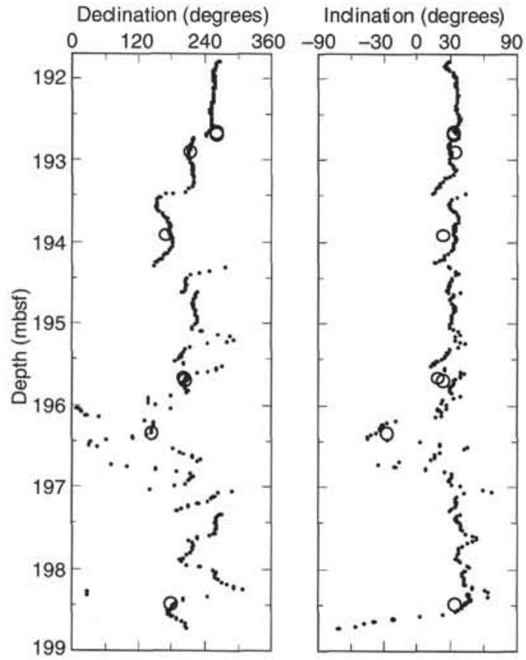

Figure 85. Correlation of whole-core (dots) and discrete sample (open circles) declination and inclination data obtained for Core 153-920D-22R. The negative inclination values near 196.3 mbsf are the result of a piece (Section 153-920D-22R-6, Piece 2) originally curated in an inverted position and subsequently corrected.

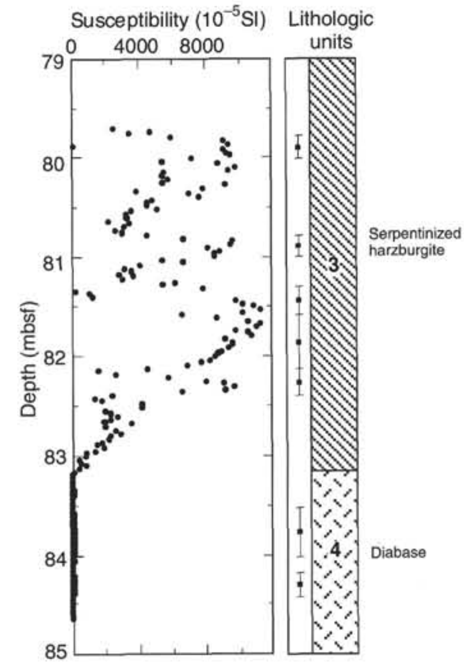

Figure 86. Whole-core susceptibility data from Core 153-920B-9R across the contact between serpentinized harzburgite (Unit 3) and diabase intrusion (Unit 4). Center column shows the distribution of core pieces longer than 15 cm. Data from 81.4–81.8 mbsf have been corrected for probable meter overrange.

easily recognized in the downhole remanence data as sections of uniform declination and inclination, the declination measured of single sections being related to the orientation of the core splitting surface chosen (Fig. 85). Inclination values for the larger pieces in this core lie near +30°, in good agreement with the discrete sample data.

Whole-core susceptibility measurements were made at 3 cm spacing on most core sections from Holes 920A and 920B. The majority of the serpentinized peridotites have high susceptibilities (>0.05 SI), which in some cases evidently exceeded the measurement range (0.1 SI) of the Bartington susceptibility meter. Through comparison with the size and distribution of core pieces, intervals of likely overrange measurements can be identified and corrected. For example, the interval from 81.4 to 81.8 mbsf in Hole 920B has been corrected (Fig. 86) because this portion of the core contained several continuous pieces with discrete sample susceptibilities on the order of 0.1 SI. The most notable feature of the susceptibility data is the striking contrast between serpentinized peridotite and diabase samples (<0.001 SI), evident in the downhole data from Core 153-920B-9R (Fig. 86).

Discrete Sample Measurements

The natural remanent magnetization and initial susceptibility were determined for ~150 discrete samples from Holes 920B and 920D (Table 9). The NRM magnetizations are remarkably homogeneous, in both intensity and inclination (Fig. 87). The mean NRM intensity (11.8 ± 4.9 A/m) is nearly an order of magnitude higher than that of serpentinites drilled on Leg 109 (Hamano et al., 1990) at a site only ~25 km from Site 920. NRM inclination values measured from discrete samples are generally between +20° and +60°. Volume susceptibility values for the discrete samples are typically 0.01–0.1 (SI units), consistent with the values determined from the whole-core measurements. The corresponding Koenigsberger ratios (the ratio of the remanent to induced magnetization, Q) for the serpentized peridotites range from 2 to 8. The mean Koenigsberger ratio (4.7 ± 1.5) indicates an approximately 20% (~2.5 A/m) contribution from induced magnetization in the serpentinites.

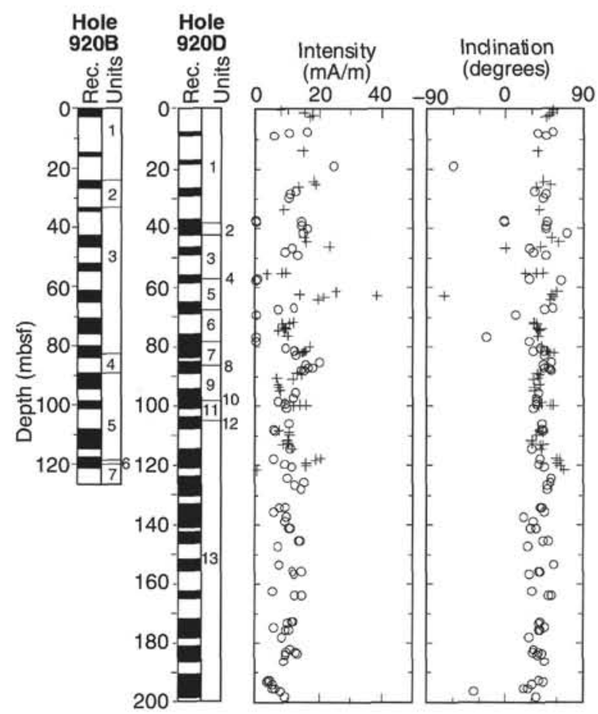

Figure 87. NRM inclination and intensity values determined from discrete samples from Holes 920B (crosses) and 920D (circles).

The majority of the discrete samples were stepwise AF demagnetized and the best fit characteristic magnetization directions determined by principal component analysis (Kirschvink, 1980). Most samples showed only a small to negligible drilling-induced magnetization component that appeared to be fully removed by 10 mT demagnetization (Fig. 88). Further demagnetization to 20 mT revealed single compo-

Table 9. Summary of magnetic properties of discrete samples from Site 920.

Core, section, interval (cm)	Piece	Depth (mbsf)	K (SI)	NRM (A/m)	Magnetic fabric			Cleaned direction				
					P	L	F	Dec.	Inc.	MAD	Lower (mT)	Upper (mT)
153-920B-												
1W-1, 55–58	6	0.55	0.0531	7.72	1.203	1.078	1.116	244.0	36.0	1.4	8	25
1W-2, 24–27	1C	1.29	0.0857	15.10	1.114	1.017	1.095	181.0	38.3	1.2	5	25
1W-2, 95–98	6	2.00	0.0717	18.04	—	—	—	159.0	38.5	0.7	12	25
1W-3, 46–49	4	2.94	0.1002	17.03	1.111	1.045	1.064	187.5	35.8	0.7	8	25
2R-1, 17–20	2	14.17	0.0933	14.75	1.109	1.035	1.071	294.2	30.3	0.8	5	25
3R-1, 65–68	5	24.15	0.0910	18.13	1.219	1.056	1.154	193.1	27.7	0.8	5	20
3R-2, 36–39	4	25.36	0.0765	18.82	1.120	1.073	1.044	163.6	35.1	0.4	6	25
3R-2, 98–101	10	25.98	0.0874	13.36	1.213	1.085	1.117	196.5	32.6	0.9	5	20
4R-1, 60–63	7A	33.80	0.0607	8.76	1.107	1.050	1.054	266.5	35.1	0.7	8	25
5R-1, 52–55	9	43.22	0.0830	15.10	1.170	1.111	1.053	217.5	32.2	0.8	8	20
5R-2, 60–63	10A	44.74	0.0865	15.76	1.188	1.046	1.135	204.8	39.0	1.0	6	20
5R-3, 61–64	5	46.23	0.0750	23.00	1.088	1.058	1.029	207.2	37.1	2.4	12	25
5R-3, 99–102	6	46.61	0.0595	11.43	1.189	1.094	1.087	182.7	33.0	0.7	6	25
6R-3, 20–23	2	55.05	0.0769	9.39	1.089	1.049	1.038	228.2	37.3	1.4	5	25
6R-3, 23–26	2	55.08	0.0616	8.02	1.073	1.024	1.047	239.1	39.8	0.7	6	20
6R-3, 57–60	7	55.42	0.0287	3.31	1.064	1.054	1.010	222.1	28.7	1.2	6	25
7R-1, 55–58	3E	61.55	0.0801	25.44	1.198	1.120	1.070	209.5	38.1	2.0	6	20
7R-2, 5–8	1A	62.47	0.0990	13.80	1.266	1.028	1.231	176.2	31.5	1.5	6	20
7R-2, 42–45	4	62.84	0.1076	38.44	1.239	1.097	1.130	194.7	31.2	0.7	8	20
7R-2, 91–94	8	63.33	0.1114	21.64	1.186	1.048	1.132	178.3	34.2	0.5	6	20
7R-3, 15–18	1	63.98	0.0985	19.75	1.158	1.052	1.100	193.1	32.6	1.2	6	20
8R-2, 24–27	2	71.92	0.1008	11.58	1.254	1.049	1.196	195.0	32.7	1.2	6	20
8R-2, 70–73	6B	72.38	0.1191	10.21	1.126	1.065	1.057	187.0	30.5	0.7	4	20
8R-2, 73–76	6B	72.41	0.1085	8.33	1.074	1.041	1.032	—	—	—	—	—
8R-3, 69–72	7	73.71	0.1048	8.66	1.170	1.056	1.108	190.2	34.4	0.8	4	20
8R-3, 115–118	11	74.17	0.1004	9.52	1.156	1.100	1.050	214.8	35.0	1.0	5	25
8R-3, 118–121	11	74.20	0.1009	9.15	1.152	1.060	1.087	213.8	37.0	1.1	4	20
8R-4, 11–14	2A	74.48	0.0946	6.73	1.123	1.018	1.104	189.0	36.5	0.8	6	20
8R-5, 62–65	5	76.36	0.0933	9.82	1.192	1.059	1.125	185.2	36.6	0.7	6	20
9R-1, 41–44	3	80.11	0.1045	17.08	1.138	1.107	1.028	200.4	34.8	1.4	6	25
9R-2, 36–39	3B	81.52	0.1101	15.57	1.111	1.046	1.062	236.7	37.4	0.6	4	20
9R-2, 39–42	3B	81.55	0.1004	15.01	1.104	1.050	1.051	—	—	—	—	—
9R-2, 84–87	4C	82.00	0.0860	14.78	1.148	1.007	1.140	—	—	—	—	—
9R-2, 87–90	4C	82.03	0.0826	14.28	1.139	1.022	1.114	194.9	40.5	1.7	6	20
9R-3, 123–126	12B	83.88	0.0004	0.008	—	—	—	93.7	36.5	1.6	15	60
9R-4, 10–13	2	84.22	0.0005	0.007	—	—	—	342.3	33.6	1.4	25	60
10R-1, 17–20	2A	89.27	0.0904	12.99	1.201	1.048	1.146	—	—	—	—	—
10R-1, 20–23	2A	89.30	0.1072	14.37	1.212	1.005	1.206	216.8	34.6	1.2	5	25
10R-2, 2–5	1A	90.48	0.0781	6.52	1.069	1.032	1.036	192.5	30.4	0.7	8	25
10R-2, 70–73	3	91.16	0.0821	11.54	1.296	1.063	1.220	207.7	34.7	0.4	8	25
10R-3, 120–123	8	93.07	0.0787	6.95	1.164	1.024	1.137	189.1	35.7	0.9	10	25
10R-4, 64–67	3	93.95	0.0849	7.13	1.182	1.032	1.145	222.9	32.9	1.1	5	25
10R-5, 13–16	1	94.87	0.0983	7.54	1.113	1.044	1.066	208.3	31.7	0.7	5	25
11R-1, 70–73	8	99.20	0.0514	9.27	1.269	1.050	1.208	206.2	30.0	0.7	8	25
11R-1, 119–122	14	99.69	0.0691	13.75	1.232	1.026	1.201	250.8	35.5	1.4	10	25
11R-1, 122–125	14	99.72	0.0849	15.88	1.226	1.029	1.191	—	—	—	—	—
11R-2, 10–13	1	100.06	0.0752	11.73	1.286	1.053	1.221	206.0	26.9	1.2	5	25
12R-1, 51–54	2	108.21	0.0725	7.26	1.168	1.021	1.143	245.8	33.6	1.1	8	25
12R-1, 100–103	3	108.70	0.0858	10.40	1.181	1.051	1.124	183.1	43.7	0.9	0	25
12R-2, 50–53	4	109.65	0.0723	10.48	1.180	1.025	1.151	193.6	34.7	0.9	8	25
12R-3, 80–83	8	111.45	0.0750	9.74	1.264	1.037	1.218	224.0	29.1	1.0	8	25
12R-4, 80–83	4	112.52	0.0961	10.35	1.216	1.025	1.186	197.0	30.5	0.9	2	25
12R-5, 10–13	1	113.10	0.0832	8.45	1.241	1.047	1.185	214.3	34.7	0.5	8	25
12R-5, 13–16	1	113.13	0.0873	10.04	1.194	1.078	1.107	—	—	—	—	—
12R-6, 16–19	1	114.52	0.0735	11.46	1.201	1.035	1.161	196.9	37.8	0.3	8	25
13R-1, 60–63	2D	117.80	0.0854	20.33	1.205	1.045	1.153	204.8	37.8	0.9	8	25
13R-1, 94–97	2F	118.14	0.0847	18.94	1.267	1.081	1.172	211.0	38.6	2.1	12	25
13R-2, 80–83	7	119.37	0.0822	15.98	1.236	1.052	1.174	223.9	37.9	1.6	8	25
13R-3, 36–39	1	120.25	0.0821	15.88	1.102	1.006	1.096	230.4	42.3	1.4	5	25
13R-4, 23–26	3	121.51	0.0016	0.16	1.033	1.016	1.017	5.7	41.4	0.8	12	25
153-920D-												
2R-1, 21–24	4	8.21	0.0805	16.23	1.127	1.036	1.089	134.3	49.2	0.9	6	20
2R-1, 24–27	4	8.24	0.0703	10.67	1.113	1.053	1.057	118.2	28.7	0.6	6	20
2R-1, 116–119	13	9.16	0.0385	5.76	1.082	1.049	1.032	164.2	37.2	0.6	12	30
3R-2, 49–52	4	19.49	0.0999	24.73	1.147	1.031	1.112	170.6	36.3	1.4	8	25
4R-1, 22–25	5	27.52	0.1011	12.64	1.163	1.099	1.059	222.8	30.6	0.7	5	25
4R-2, 17–20	3	28.77	0.0995	11.04	1.104	1.050	1.052	214.2	43.1	0.6	5	25
4R-3, 35–38	5	30.19	0.0872	10.75	1.190	1.008	1.18	207.4	37	1.1	8	25
5R-1, 56–59	8	37.46	0.0790	—	1.156	1.101	1.05	—	—	—	—	—
5R-2, 33–36	1A	38.24	0.0950	—	1.081	1.012	1.069	—	—	—	—	—
5R-2, 36–39	1A	38.27	0.0929	14.65	1.141	1.019	1.119	188.2	32.9	0.6	6	20
5R-3, 20–23	2	39.47	0.0930	14.41	1.094	1.089	1.005	265.3	31	2.9	12	25
5R-3, 127–130	13	40.54	0.0823	16.26	1.270	1.027	1.236	205.9	29.2	0.7	6	20
5R-4, 93–96	7	41.66	0.0960	15.10	1.118	1.066	1.049	145.7	33.1	0.8	8	20
6R-1, 53–56	6B	47.03	0.0942	11.30	1.185	1.139	1.04	217.7	27.2	2.1	6	20
6R-2, 48–51	9A	48.3	0.0781	9.03	1.148	1.010	1.136	273.3	32.7	1.9	12	25
6R-3, 54–57	7	49.6	0.0861	13.33	1.141	1.070	1.066	200.2	34.6	1.3	10	20
7R-1, 124–127	17	57.44	0.0010	0.42	—	—	—	198.4	23.9	0.6	20	70
7R-2, 22–25	2B	57.89	0.0008	0.004	—	—	—	—	—	—	—	—
8R-1, 141–144	16	67.31	0.0923	12.07	1.272	1.022	1.245	4.0	35.4	0.5	12	15
8R-2, 43–46	3	67.77	0.0701	7.08	1.136	1.036	1.097	167.2	40.9	1.5	4	25
8R-3, 74–77	9	69.54	0.0004	0.005	—	—	—	—	—	—	—	—
9R-2, 52–55	4A	77.37	0.0005	0.002	—	—	—	—	—	—	—	—
10R-1, 54–57	7B	78.64	0.0005	0.003	—	—	—	—	—	—	—	—

Table 9 (continued).

Core, section, interval (cm)	Piece	Depth (mbsf)	K (SI)	NRM (A/m)	Magnetic fabric P	L	F	Cleaned direction Dec.	Inc.	MAD	Lower (mT)	Upper (mT)
10R-2, 134–137	6	80.83	0.1097	9.45	1.101	1.025	1.074	202.1	35.9	0.8	6	20
10R-3, 74–77	9A	81.7	0.0870	12.57	1.195	1.030	1.16	201.5	41.5	1.0	6	20
10R-3, 77–80	9A	81.73	0.0896	12.08	1.202	1.019	1.18	—	—	—	—	—
10R-4, 80–83	7	83.24	0.0921	12.94	1.222	1.080	1.132	233.2	38.9	0.7	6	20
11R-1, 27–30	4	85.57	0.1288	20.27	1.218	1.035	1.177	37.6	31.9	1.5	6	20
11R-1, 125–128	13	86.55	0.0846	16.00	1.264	1.052	1.202	198.6	33.4	0.7	5	25
11R-2, 63–66	4	87.35	0.0974	18.10	1.201	1.033	1.162	223.7	36.5	0.9	8	25
11R-2, 66–69	4	87.38	0.0812	16.85	1.216	1.019	1.193	—	—	—	—	—
11R-3, 22–25	1	88.14	0.0796	14.42	1.234	1.050	1.175	—	—	—	—	—
11R-3, 25–28	1	88.17	0.0890	15.64	1.173	1.026	1.143	222.3	40.2	0.9	5	25
12R-1, 104–107	6	96.04	0.0799	12.99	1.259	1.077	1.169	181.7	30.6	1.2	7	25
12R-2, 119–122	11	97.64	0.1030	11.83	1.262	1.038	1.216	205.2	30.3	0.9	5	25
12R-3, 86–89	4	98.59	0.0552	6.91	1.240	1.073	1.155	246.2	31.5	0.9	5	25
12R-4, 54–57	2	99.57	0.0879	9.07	1.119	1.035	1.082	219.1	32.4	0.4	5	25
12R-5, 26–29	3	100.79	0.0713	9.80	1.320	1.066	1.237	120.2	31.1	0.6	5	25
13R-2, 84–87	3	106.33	0.0655	10.38	1.213	1.159	1.047	270.1	28.8	1.0	10	25
13R-3, 126–129	19	108.19	0.0424	5.57	1.266	1.010	1.254	175.6	32.7	1.0	10	25
13R-4, 41–44	6	108.74	0.0557	6.30	1.143	1.073	1.065	188.5	32.6	0.8	10	25
14R-1, 58–61	5	114.88	0.0897	10.84	1.217	1.122	1.086	196.3	28.8	0.9	6	20
14R-3, 82–85	3	117.85	0.0507	5.50	1.143	1.045	1.094	109.5	32.4	1.0	8	25
14R-4, 137–140	8	119.86	0.0778	9.17	1.280	1.197	1.069	159.8	35.6	1.1	4	20
14R-5, 69–72	5	120.59	0.0914	11.23	1.318	1.004	1.312	212.0	36.7	1.1	8	20
15R-1, 80–83	4C	124.7	0.0743	9.98	1.303	1.031	1.264	195.0	33.9	0.4	6	20
15R-2, 92–95	3	126.04	0.0783	15.54	1.203	1.033	1.164	213.7	36.4	1.9	6	20
15R-3, 48–51	3A	126.99	0.0672	12.14	1.212	1.066	1.138	237.6	33.1	1.0	8	20
15R-4, 72–75	3B	128.47	0.0813	14.31	1.316	1.043	1.262	208.7	34	0.9	6	20
16R-1, 98–101	5C	134.38	0.0881	9.05	1.173	1.088	1.078	—	—	—	—	—
16R-1, 101–104	5C	134.41	0.0724	7.69	1.138	1.108	1.027	206.2	33.6	0.6	6	20
16R-3, 5–8	1A	135.97	0.0594	5.54	1.081	1.040	1.039	249.6	30.4	1.6	6	20
16R-4, 82–85	1C	137.8	0.0917	9.87	1.338	1.031	1.297	189.2	20.5	0.9	5	25
16R-5, 80–83	4A	138.93	0.0768	9.01	1.235	1.050	1.176	223.8	29	0.9	8	25
16R-7, 54–57	6	141.53	0.0813	10.89	1.237	1.064	1.163	—	—	—	—	—
16R-7, 57–60	6	141.56	0.0990	10.58	1.237	1.073	1.153	278.0	25	2.9	8	25
17R-3, 37–40	1C	145.74	0.0882	14.22	1.161	1.043	1.113	—	—	—	—	—
17R-3, 40–43	1C	145.77	0.0840	13.81	1.163	1.043	1.115	222.0	33.9	1.7	5	20
17R-4, 103–106	3	147.69	0.0838	6.88	1.311	1.048	1.252	228.8	32	1.7	10	30
18R-1, 123–126	14	153.83	0.0747	7.45	1.104	1.015	1.088	344.0	26	0.9	15	30
18R-3, 75–78	4	156.1	0.0872	11.66	1.159	1.040	1.114	—	—	—	—	—
18R-3, 78–81	4	156.13	0.1255	14.78	1.126	1.066	1.057	198.2	35.6	0.7	8	25
18R-4, 12–15	1	156.85	0.0769	12.06	1.204	1.110	1.084	190.8	27.7	0.9	10	25
19R-1, 18–21	3A	162.48	0.0645	5.26	1.158	1.117	1.158	212.8	32.5	0.6	0	30
19R-2, 13–16	1	163.8	0.0987	14.76	1.198	1.076	1.113	NA	NA	NA	NA	NA
19R-2, 16–19	1	163.83	0.0847	12.17	1.188	1.066	1.115	195.2	37.5	0.9	10	25
20R-1, 103–106	13B	172.93	0.0921	11.84	1.213	1.126	1.078	197.2	37.7	0.4	6	20
20R-1, 106–109	13B	172.96	0.0858	11.28	1.204	1.128	1.068	—	—	—	—	—
20R-2, 24–27	1B	173.3	0.0754	10.11	1.196	1.124	1.064	200.9	35.4	0.6	8	20
20R-3, 80–83	2C	174.93	0.0402	5.61	1.232	1.034	1.191	247.8	36.1	0.6	10	20
20R-4, 38–41	3A	175.92	0.0777	9.48	1.180	1.043	1.131	202.7	34.3	0.7	6	20
20R-4, 41–44	3A	175.95	0.0831	10.72	1.132	1.098	1.032	—	—	—	—	—
20R-5, 98–101	4	177.98	0.0803	8.45	1.248	1.080	1.156	188.8	26	1.2	6	20
21R-1, 93–96	12	182.43	0.0731	10.90	1.374	1.061	1.295	205.9	29.1	0.7	7	20
21R-2, 40–43	1C	183.15	0.0678	9.76	1.295	1.058	1.224	196.7	32	1.4	5	20
21R-2, 43–46	1C	183.18	0.0907	12.60	1.253	1.051	1.192	—	—	—	—	—
21R-2, 97–100	4	183.72	0.0854	13.07	1.272	1.231	1.033	170.6	28.9	0.6	7	20
21R-3, 22–25	1B	184.32	0.0644	9.42	1.311	1.035	1.266	232.2	26.6	0.8	10	20
21R-4, 68–71	6	186.28	0.0732	8.54	1.204	1.032	1.167	222.2	33.2	2.2	5	20
22R-2, 86–89	1D	192.66	0.0316	3.80	1.190	1.048	1.135	—	—	—	—	—
22R-2, 89–92	1D	192.69	0.0383	4.51	1.211	1.053	1.151	260.9	32.3	1.0	10	20
22R-3, 17–20	1A	192.9	0.0342	3.62	1.058	1.030	1.028	215.6	33.7	1.2	5	20
22R-4, 50–53	1B	193.93	0.0468	5.16	1.235	1.074	1.15	170.4	24.1	0.8	5	20
22R-5, 104–107	6B	195.67	0.0501	5.11	1.342	1.074	1.25	201.1	19.6	1.9	6	20
22R-5, 107–110	6B	195.7	0.0532	6.14	1.316	1.082	1.217	204.6	23.9	1.3	6	20
22R-6, 15–18	2A	196.35	0.0649	7.90	1.284	1.051	1.222	234.0	26.5	1.6	6	20
22R-7, 111–114	8	198.44	0.0936	9.33	1.263	1.084	1.166	179.8	34.2	1.4	6	20

Note: Susceptibility (K), natural remanent magnetization (NRM), magnetic fabric parameters (P, L, F: see Fig. 7), Dec., Inc. = characteristic magnetization declination and inclination with associated maximum angular deviation (MAD) angle and alternating field treatment steps over which the cleaned direction was defined. NA = not available.

nent magnetizations with inclinations within the range 30°–40° (Fig. 89). Inclination values from the two holes are statistically indistinguishable, yielding a combined mean inclination of 33.7° (alpha = 1.0°, where alpha is the half-angle of the asymmetric 95% confidence interval, kappa = 150; calculated with method of McFadden and Reid [1982]). The mean characteristic inclination is broadly compatible with the inclination expected from a geocentric axial dipole (41°) or the present field direction (42°). The similarity of the observed and expected inclination values suggests that, to a first-order approximation, the remanent declination might be used to reorient structural features within the core.

Anisotropy of magnetic susceptibility was also determined for the majority of the discrete samples. The degree of anisotropy (as defined by the ratio K_1/K_3, where K_1 and K_3 are the maximum and minimum principal axes of the susceptibility ellipsoid, respectively is generally high (Fig. 90) and in many cases sufficient to significantly deflect the remanent magnetization. Although adjacent (within 5 cm) minicore samples generally have similar magnetic fabrics, the high variability in the degree of anisotropy on the scale of tens of centimeters (e.g., Table 9; Hole 920B, 89–91 mbsf) obscures any correlation with other downhole characteristics. The low susceptibility of diabase samples precluded accurate determination of the magnetic fabric; the substan-

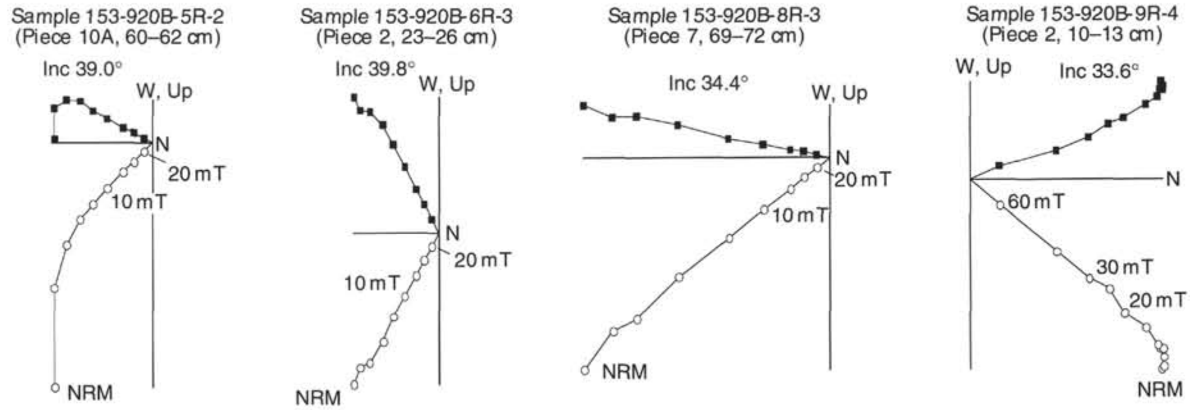

Figure 88. Vector endpoint diagrams for AF demagnetization of representative discrete samples. Squares (circles) are projections of the vector onto the horizontal (vertical) plane.

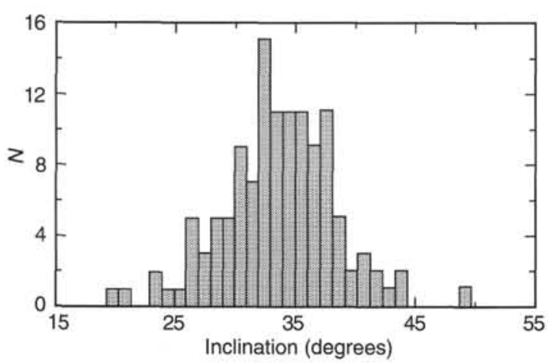

Figure 89. Characteristic inclinations of Site 920 discrete samples. The mean value is 33.7° ± 1.0° as compared to the expected geocentric axial dipole inclination (41°).

tial noise level resulting in a statistically isotropic susceptibility tensor. The majority of peridotite samples have an oblate magnetic fabric, presumably reflecting the anisotropic distribution of magnetite within serpentinized peridotites. Thin-section analysis supports the view that the dominant magnetite orientation is associated with the extensive development of subparallel serpentine veins (MacDonald and Ellwood, 1988). Acquisition of isothermal remanence in two representative peridotite samples indicate saturation is reached by approximately 0.15 T, with no indication of contribution from higher-coercivity phases (Fig. 91). Together with the low (<10 mT) median destructive fields (the alternating field necessary to reduce the NRM to half), these data are also compatible with magnetite as the dominant magnetic mineral.

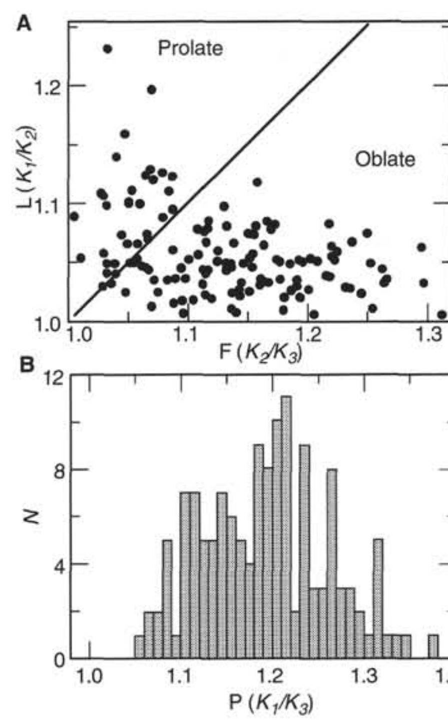

Figure 90. Magnetic fabric of serpentinized peridotites from Site 920. **A.** Magnetic fabric lineation (L) vs. foliation (F) illustrating dominantly oblate susceptibility ellipsoid shape. **B.** Anisotropy degree (P) for Site 920 serpentinized peridotites.

Implications of Paleomagnetic Data

The characteristic remanence directions provide a basis for reorienting structural features within the core, given an estimate of the in-situ magnetization direction. Although the mean inclination (33.7°) of peridotites from Site 920 is distinct from the expected axial dipole inclination (41°), the two values are similar enough to suggest that a first-order reorientation may be accomplished by a simple vertical axis rotation. Thus, an initial reorientation of the cores was accomplished simply by rotating the declination of each core piece to an azimuth of 360°, under the assumption that the remanence represents a normal polarity magnetization. The remanent magnetization in peridotites from Site 920 is related to serpentinization and therefore can provide information on the relative timing of alteration and tectonism affecting the peridotite body. Remanence acquisition may have occurred before, during or after tectonism; however, the general similarity of the inclination to that expected from an axial geocentric dipole suggests that relatively little horizontal axis rotation has occurred since remanence acquisition.

Although more complex rotations cannot be excluded (see below), this simplest-case scenario results in a remarkably consistent structural picture. The minimum susceptibility axes, after reorientation of the characteristic remanence direction to a declination of 360°, are well clustered near 265° and 35° (Fig. 92). Using this approach, the strike of the magnetic foliation is approximately north–south, dipping ~55°E. Similarly, the dominant composite foliation (comprising a V2 vein set, anastomosing foliation, and orthopyroxene elongation; see "Structural Geology," this chapter) and vein fabrics within the peridotites may be reoriented using the paleomagnetic remanence data. For example, reorientation of the V2 vein set yields a strike of approximately N15°E and dip of ~35°SE (Fig. 92), toward the median valley axis. Thus, the magnetic foliation and mesoscopic composite foliation are roughly co-incident. This similarity strongly suggests that the magnetic fabric formation is associated with the composite foliation in the peridotites. The inferred north–south in-situ strike of these features is also compatible with the local trend of the ridge axis.

The well determined mean characteristic inclination (33.7° ± 1°) of discrete samples from Site 920 may allow more detailed analysis of the rotational history associated with mechanical extension in this slow-spreading area. The size (n = 148) and consistency (alpha = 1°) of the data set involved indicate that the mean inclination is statistically distinct from the geocentric axial dipole inclination of 41°. However, the remanence directions observed are a product of both the anisotropic fabric and the rotational history of the peridotite body.

In strongly anisotropic rocks the remanent magnetization will be deflected from the ambient field direction toward the plane containing the maximum and minimum principal susceptibility axes. The magnitude of this deflection is a function of the degree of anisotropy as well as the orientation of the magnetic fabric relative to the applied field direction. A 5% anisotropy may result in a deflection of up to 3° (Stacey and Banerjee, 1974), and therefore the degree of anisotropy in the Site 920 peridotites suggests a possible offset of ~10°. However, several observations suggest that anisotropy is not the sole factor controlling the shallow inclinations observed from Site 920. If anisotropy is entirely responsible for the inclination variation, one would expect a strong correlation with the dip of the magnetic foliation and the percent anisotropy (Fig. 93). Although a small number of samples with high degrees of anisotropy do have correspondingly low remanent inclinations, the overall correlation is poor (y = 1.7X – 7.8; r2 = 0.17). In addition, the mean inclination (35.2° ± 1.4°; n = 48) of the least anisotropic samples (P < 1.16) is still distinct from the expected dipole direction. Finally, progressive demagnetization should reduce remanence deflection (Stacey and Banerjee, 1974), resulting in characteristic remanence directions being less affected by the magnetic fabric.

Tectonic rotations provide an alternative, but not mutually exclusive, explanation for the shallow inclinations. The data suggest a rotation of the magnetic remanent inclination from 41° (at time of acquisition) to the measured 33°. The magnetic data alone, however, do not constrain the azimuth of the axis of rotation. Extension in the northern portion of the MARK area is asymmetric with an eastward-dipping detachment surface (Karson et al., 1987; Brown and Karson, 1988; Mével et al., 1991). Thus, the axis of rotation reasonably may be assumed to be subparallel to the overall strike of faults in the area (±10° from north-south). Additional geological observations (e.g., slickensides, petrofabrics) may further constrain the sense of rotation. Assuming a horizontal rotation axis and minimal contribution from magnetic anisotropy, the amount of rotation of the footwall required to produce the observed shallow magnetic inclination is in the region of 20°–30°, depending on the axis azimuth and sense of rotation (Fig. 94).

The nonuniqueness inherent in rotation schemes based on azimuthally unoriented cores prohibits unambiguous separation of the effects of extensional tectonism and magnetic anisotropy. However, shore-based studies of magnetic fabrics should aid evaluation of the importance of anisotropic properties on the deflection of the remanence, and hence the amount of tectonic rotation.

PHYSICAL PROPERTIES

Introduction

Determinations of horizontal compressional-wave velocity (V_p), resistivity, and index properties (bulk density, grain density, water content, porosity, and dry density) were made on 117 minicore samples located in representative sections of the core (away from fractures and large veins) from rocks cored at Site 920 (Tables 10 and 11). Thermal conductivities were determined from 45 half-round archive sections of core (Tables 12 and 13). Densities were also determined

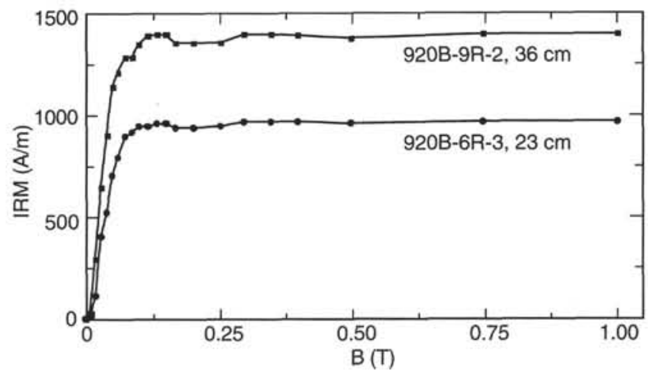

Figure 91. Isothermal remanent magnetization vs. induction (B) for two serpentinized peridotite samples from Hole 920B. Saturation at low levels (<0.15 T) is consistent with magnetite as the dominant magnetic phase within the peridotites.

from the gamma-ray attenuation porosity evaluator (GRAPE) on whole cores using the multisensor track. A description of experimental methodologies is provided in "Explanatory Notes" (this volume) and "Explanatory Notes" of the Leg 147 Initial Reports (Shipboard Scientific Party, 1993). The following constitutes preliminary analyses of the physical properties of the rocks obtained from Holes 920B and 920D, followed by a comparative analysis of the physical properties representing Site 920.

Data

Hole 920B

The predominant rock type sampled in Hole 920B was serpentinized peridotite, with rare diabase (84 mbsf) and gneissic gabbro (122 mbsf; see "Igneous Petrology"). Bulk densities determined from the serpentinized harzburgite and lherzolite minicore samples (Table 10) are 2.58 to 2.85 g/cm^3 with a median value of 2.65 g/cm^3. Porosity in these rocks is 1.77% to 8.57% with a median value of 4.04%; V_p measurements ranged from 3651 to 4979 m/s with a median value of 4378 m/s (measured at atmospheric temperature and pressure). Bulk densities of the diabase and gabbroic rocks are 2.86 and 3.05 g/cm^3, respectively (Table 10); porosity is 3.16% in the diabase and less than 0.2% in the gabbro; V_p measurements were 5132 m/s and 5764 m/s for the diabase and gabbroic samples, respectively. Thermal conductivities of serpentinized harzburgite range from 2.22 to 3.34 W/m°C, with a median value of 2.91 W/m°C, whereas the thermal conductivity of diabase is about 2.1 W/m°C (Table 12).

Variations in rock resistivity, V_p, porosity, density, thermal conductivity, and alteration as a function of depth for Hole 920B are shown in Figure 95 adjacent to bars indicating core recovery and unit boundaries determined from considerations of primary mineralogy and texture (see also "Igneous Petrology," this chapter).

Resistivity measurements began with samples from about 50 mbsf in Hole 920B. Resistivities of the serpentinized peridotite and attendant diabase and metagabbroic rocks below this depth fall in the 102–104 Ωm range (Fig. 95), similar to values observed elsewhere in oceanic crust (Pezard et al., 1991). V_p falls in the 3500–6000 m/s range (Fig. 95), similar to values elsewhere observed for the rock types encountered here (e.g., Christensen, 1982). Resistivity and velocity appear generally to vary sympathetically such that low velocity corresponds with low resistivity. Notable velocity lows occur at 26 mbsf in pyroxene-rich serpentinized harzburgite of Unit 2 and in serpentinized harzburgite at the base of Unit 3 (81.5 mbsf). Velocity highs are associated with the diabase and gabbroic Units 4 and 7, as described previously.

Porosity and density variations as a function of depth are shown in Figure 95. Porosity variations downhole are considerable, with

Table 10. Index properties, horizontal compressional-wave velocities (V_p), resistivities, and water contents of crystalline rocks recovered from Hole 920B.

Core, section, interval (cm)	Piece	Depth (mbsf)	V_p (m/s)	Resistivity (Ωm)	Wet-bulk density (g/cm^3)	Dry-bulk density (g/cm^3)	Grain density (g/cm^3)	Void ratio	Porosity (%)	Water content (%)	Alteration estimate (%)	LOI (%)	$H_2O + CO_2$ (%)	Rock type
153-920B-														
1W-1, 55–57	6	0.55	4487	*	2.632	2.600	2.684	0.032	3.124	1.228	100	*	*	SH
1W-2, 24–26	1C	1.29	4726	*	2.671	2.639	2.725	0.032	3.125	1.210	95	*	*	SH
1W-2, 95–97	6	2.00	4753	*	2.739	2.718	2.775	0.021	2.075	0.780	98	*	*	SH
1W-3, 46–48	4	2.94	4472	*	2.695	2.670	2.736	0.025	2.429	0.930	90	*	*	SH
2R-1, 17–19	2	14.17	4654	*	2.697	2.674	2.737	0.024	2.326	0.889	95	12.10	12.96	SH
3R-2, 36–38	4	25.36	3947	*	2.637	2.577	2.739	0.063	5.940	2.356	100	*	*	SL
3R-2, 98–100	10	25.98	3652	*	2.583	2.506	2.708	0.081	7.463	3.044	80	12.81	16.17	SL
4R-1, 60–62	7	33.80	4623	*	2.709	2.691	2.740	0.018	1.784	0.678	88	11.51	11.52	SH
5R-1, 52–54	9	43.22	4451	*	2.670	2.644	2.712	0.026	2.515	0.972	90	*	*	SH
5R-2, 60–62	10	44.74	4378	*	2.706	2.685	2.741	0.021	2.053	0.782	(98)*	*	*	SH
5R-3, 61–63	5	46.23	4410	*	2.653	2.618	2.712	0.036	3.478	1.358	98	*	*	SL
5R-3, 99–101	6	46.61	4502	*	2.641	2.598	2.711	0.044	4.185	1.647	95	12.26	15.52	SL
6R-3, 20–22	2	55.05	4727	*	2.727	2.705	2.766	0.023	2.220	0.839	85	11.00	12.72	SH
6R-3, 23–25	2	55.08	4945	110.1	2.706	2.688	2.736	0.018	1.774	0.675	90	*	*	SH
6R-3, 57–59	7	55.42	4717	*	2.851	2.830	2.887	0.020	1.975	0.713	90	*	*	SH
7R-2, 42–44	4	62.84	4447	*	2.633	2.580	2.723	0.056	5.263	2.085	80	11.97	12.82	SH
8R-2, 24–26	2	71.92	4182	117.6	2.610	2.553	2.704	0.059	5.585	2.236	(95)*	*	*	SH
8R-2, 70–72	6	72.38	4276	*	2.646	2.601	2.721	0.046	4.424	1.739	91	12.51	14.85	SH
8R-2, 73–75	6	72.41	4375	*	2.659	2.618	2.728	0.042	4.050	1.582	96	*	*	SH
8R-3, 69–71	7	73.71	4246	*	2.640	2.599	2.707	0.041	3.974	1.563	96	*	*	SH
8R-3, 115–117	11	74.17	*	*	2.662	2.621	2.732	0.042	4.074	1.589	90	12.75	14.71	SH
8R-3, 118–120	11	74.20	*	*	2.651	2.563	2.803	0.094	8.567	3.416	92	*	*	SH
8R-4, 11–13	2	74.48	4249	181.2	2.640	2.600	2.705	0.040	3.880	1.526	85	*	*	SH
8R-5, 62–64	5	76.36	*	*	2.652	2.608	2.723	0.044	4.214	1.651	(80)*	*	*	SH
9R-1, 41–43	3	80.11	4231	250.7	2.667	2.616	2.753	0.052	4.955	1.936	(96)*	*	*	SH
9R-2, 36–38	3	81.52	4039	*	2.641	2.580	2.744	0.064	6.003	2.379	90	*	*	SH
9R-2, 39–41	3	81.55	3746	81.7	2.614	2.554	2.714	0.062	5.878	2.352	85	12.79	13.52	SH
9R-2, 84–86	4C	82.00	4759	*	2.645	2.606	2.710	0.040	3.853	1.512	98	12.77	13.20	SH
9R-2, 87–89	4C	82.03	*	*	2.645	2.607	2.707	0.039	3.708	1.454	90	*	*	SH
9R-4, 10–12	2	84.22	5132	118.9	2.860	2.827	2.920	0.033	3.159	1.142	(20–100)*	*	*	MD/D
10R-1, 20–22	2A	89.30	4102	101.4	2.631	2.567	2.738	0.067	6.247	2.488	97	12.23	15.74	SH
10R-2, 2–4	1A	90.48	4072	95.3	2.629	2.574	2.721	0.057	5.420	2.153	98	*	*	SH
10R-2, 70–72	3	91.16	4410	84.8	2.665	2.626	2.732	0.040	3.887	1.513	(98)*	*	*	SH
10R-3, 120–122	8	93.07	4681	106.5	2.750	2.706	2.828	0.040	4.213	1.620	95	*	*	SH
10R-4, 64–66	3	93.95	3741	119.6	2.638	2.579	2.737	0.061	5.792	2.296	95	*	*	SH
10R-5, 13–15	1	94.87	3778	*	2.638	2.574	2.747	0.067	6.272	2.490	87	13.82	13.08	SH
11R-1, 70–72	8C	99.20	4979	128.2	2.722	2.704	2.753	0.018	1.776	0.671	95	*	*	SH
11R-1, 119–121	14	99.69	4520	74.7	2.731	2.711	2.765	0.020	1.965	0.741	80	11.25	12.58	SH
11R-2, 10–12	1	100.06	4359	58.4	2.718	2.677	2.790	0.042	4.040	1.543	95	*	*	SH
12R-1, 51–53	2	108.21	4604	49.1	2.751	2.715	2.816	0.037	3.581	1.348	90	*	*	SH
12R-1, 100–102	3	108.70	4296	17.7	2.638	2.589	2.719	0.050	4.790	1.891	(90)*	*	*	SH
12R-2, 50–52	4	109.65	4717	73.3	2.708	2.676	2.762	0.032	3.104	1.186	85	*	*	SH
12R-3, 80–82	8	111.45	*	*	2.638	2.583	2.730	0.057	5.391	2.133	95	*	*	SH
12R-4, 80–82	4	112.52	4577	60.3	2.656	2.617	2.721	0.040	3.824	1.494	(95)*	*	*	SH
12R-5, 10–12	1A	113.10	4334	21.9	2.654	2.603	2.740	0.053	5.015	1.970	72	11.86	12.92	SH
12R-6, 16–18	1	114.52	4378	101.4	2.659	2.620	2.724	0.040	3.829	1.494	95	*	*	SH
13R-1, 60–62	2D	117.80	4312	49.2	2.685	2.635	2.770	0.051	4.865	1.887	85	12.60	14.65	SL
13R-1, 94–96	2F	118.14	3929	27.1	2.636	2.575	2.740	0.064	6.042	2.399	80	*	*	SL
13R-2, 80–82	7	119.37	4337	28.0	2.585	2.547	2.647	0.039	3.780	1.518	75	*	*	SH
13R-3, 36–38	1A	120.25	4332	19.9	2.727	2.653	2.861	0.078	7.260	2.797	80	*	*	SH
13R-4, 23–25	3	121.51	5764	233.6	3.052	3.050	3.056	0.002	0.179	0.060	(30–40)*	*	*	GA/GG

Notes: * = not measured in this sample (nearby value). LOI and $H_2O + CO_2$ results do not correspond exactly with sample intervals identified here. SH = serpentinized harzburgite, SL = serpentinized lherzolite, MD/D = metadiorite/diabase, GA/GG = gneissic amphibolite with gneissic gabbro.

particularly high values associated with the pyroxene-rich serpentinized harzburgite of Unit 2 and particularly low porosity associated with the gneissic gabbro of Unit 7. An isolated positive porosity spike at 74 mbsf in the serpentinized harzburgite at the base of Unit 3 is probably spurious as it is not associated with any trends in other physical properties measurements. Bulk density (right curve) generally varies inversely with porosity, as does velocity. These behavioral trends are typical of this crystalline rock.

Thermal conductivity (Fig. 95) varies considerably with depth. Some variation is likely due to differences in rock thickness and boundary conditions at the rock-needle interface. The lowest value measured was a from a diabase sample from Unit 4 and correctly reflects the lower conductivity of this material. Variations in thermal conductivities measured in rocks recovered above 45 mbsf appear to roughly correspond with variations in other physical properties determinations and seem reasonable. However, low values measured in serpentinized harzburgite from 52 m and 114 mbsf do not appear to correlate with any trends that might be inferred from the combined measurements.

Estimates of alteration from visual core descriptions are shown in Figure 95 (see also "Metamorphic Petrology," this chapter). Alteration of the serpentinized harzburgite is somewhat variable but generally high, whereas alteration of the diabase (Unit 4; 84 m) and gabbro (Unit 7; 122 m) is minor.

Hole 920D

Samples from rock recovered from coring at Hole 920D are predominantly serpentinized harzburgite and lesser dunite, with some altered diabase and gabbro (Table 11). Bulk densities for these rocks range from 2.58 to 3.04 g/cm^3 with a median value of 2.66 g/cm^3. Porosity ranges from 1.18% to 10.35% with a median value of 3.96%. V_p measurements ranged from 3903 to 5214 m/s with a median value of 4394 m/s. Thermal-conductivity measurements ranged from 2.28 to 3.96 W/m°C with a median value of 3.024 W/m°C.

Resistivity, velocity, porosity, density, and thermal-conductivity measurements for Hole 920D are shown as a function of depth in Figure 96. Also shown are bars representing core recovery and units

Table 11. Index properties, horizontal compressional-wave velocities (V_p), resistivities, and water contents of crystalline rocks recovered from Hole 920D.

Core, section, interval (cm)	Piece	Depth (mbsf)	V_p (m/s)	Resistivity (Ωm)	Wet-bulk density (g/cm³)	Dry-bulk density (g/cm³)	Grain density (g/cm³)	Void ratio	Porosity (%)	Water content (%)	Alteration estimate (%)	LOI (%)	$H_2O + CO_2$ (%)	Rock type
153-920D-														
2R-1, 21–23	4	8.21	4620	228.7	2.699	2.681	2.729	0.018	1.781	0.679	95	11.67	11.45	SH
2R-1, 116–118	13	9.16	5214	14.0	3.041	3.029	3.065	0.012	1.177	0.397	84	*	*	SH
3R-2, 49–51	4	19.49	4296	3.7	2.642	2.605	2.704	0.038	3.677	1.443	98	*	*	SH
4R-1, 22–24	5	27.52	4317	18.3	2.614	2.557	2.709	0.059	5.597	2.237	96	*	*	SH
4R-2, 17–19	3	28.77	4157	78.2	2.638	2.597	2.704	0.041	3.950	1.554	94	*	*	SH
4R-3, 35–37	5	30.19	4475	30.1	2.643	2.616	2.688	0.028	2.702	1.056	98	11.01	11.89	SH
5R-1, 56–58	8	37.46	4461	137.1	2.699	2.672	2.745	0.027	2.659	1.017	97	*	*	SH
5R-2, 33–35	1A	38.24	4322	21.6	2.640	2.594	2.718	0.048	4.557	1.796	99	12.35	12.49	PSH
5R-3, 127–129	13	40.54	4253	39.6	2.594	2.528	2.701	0.068	6.398	2.586	100	12.07	12.51	PSH
5R-4, 93–95	7	41.66	4113	50.1	2.657	2.617	2.724	0.041	3.906	1.526	85	*	*	PSH
6R-1, 53–55	6B	47.03	4493	94.7	2.655	2.609	2.731	0.047	4.445	1.741	83	*	*	SH
6R-2, 48–50	9A	48.3	4736	182.3	2.674	2.654	2.706	0.019	1.903	0.733	98	12.5	11.45	SH
6R-3, 54–56	7	49.6	4452	41.8	2.647	2.616	2.697	0.031	3.003	1.174	83	*	*	SH
7R-2, 22–24	2B	57.89	4773	148.9	2.878	2.833	2.964	0.046	4.427	1.598	(89)*	*	*	MMG
8R-1, 141–143	16	67.31	4608	64.8	2.651	2.618	2.704	0.033	3.182	1.242	97	12.09	13.42	SH
8R-2, 43–45	3	67.77	4418	113.1	2.672	2.640	2.726	0.033	3.157	1.222	90	*	*	SH
8R-3, 74–76	9	69.54	4732	112.3	2.757	2.691	2.877	0.069	6.478	2.461	2	*	*	PD
9R-2, 52–54	4A	77.37	4904	77.9	2.810	2.770	2.883	0.041	3.917	1.446	(0)*	*	*	MPD
10R-1, 54–56	7B	78.64	4363	95.0	2.673	2.567	2.863	0.115	10.347	4.121	(10)*	*	*	D
10R-2, 134–136	7	80.83	4029	117.6	2.655	2.601	2.745	0.055	5.224	2.053	93	*	*	SH
10R-3, 77–79	9A	81.73	4201	261.4	2.648	2.608	2.715	0.041	3.956	1.550	93	11.9	11.56	SH
10R-4, 80–82	7	83.24	4641	67.6	2.709	2.693	2.737	0.016	1.597	0.606	89	*	*	SH
11R-1, 27–29	4	85.57	3938	59.7	2.665	2.606	2.765	0.061	5.748	2.255	93	*	*	SD
11R-1, 125–127	13	86.55	4394	113.8	2.637	2.600	2.697	0.037	3.611	1.420	(96)*	*	*	SH
11R-2, 66–68	4	87.38	4449	89.8	2.657	2.620	2.720	0.038	3.702	1.444	98	12.26	13.3	SH
11R-3, 22–24	1	88.14	3943	56.2	2.633	2.593	2.700	0.041	3.954	1.559	100	12.42	12.84	SH
12R-1, 104–106	5	96.04	4276	100.5	2.679	2.662	2.707	0.017	1.657	0.636	98	*	*	SH
12R-2, 122–124	11	97.67	4302	93.8	2.652	2.605	2.730	0.048	4.576	1.796	87	12.44	13.2	SH
12R-3, 86–88	4	98.59	4314	189.4	2.681	2.649	2.734	0.032	3.080	1.188	76	*	*	SH
12R-4, 54–56	2	99.57	4096	21.3	2.678	2.622	2.772	0.057	5.403	2.106	(91)*	*	*	SH
12R-5, 23–25	3	100.8	3903	133.7	2.583	2.521	2.685	0.065	6.095	2.471	100	12.76	12.55	SH
13R-2, 84–86	3	106.3	4488	102.3	2.759	2.725	2.820	0.035	3.380	1.268	73	*	*	SH
13R-3, 126–128	19	108.2	4816	148.7	2.644	2.607	2.706	0.038	3.688	1.446	94	*	*	SH
13R-4, 41–43	6	108.7	4912	45.6	2.728	2.694	2.788	0.035	3.352	1.272	77	*	*	SH
14R-1, 58–60	5B	114.9	4004	44.0	2.624	2.569	2.716	0.058	5.439	2.165	62	*	*	SH
14R-3, 82–84	3	117.9	4413	446.8	2.768	2.742	2.815	0.027	2.597	0.968	62	10.36	11.08	SH
14R-3, 85–87	3	117.9	4380	101.4	2.782	2.753	2.832	0.028	2.756	1.023	69	*	*	SH
14R-4, 137–139	8	119.9	4449	47.5	2.658	2.604	2.749	0.056	5.259	2.064	77	*	*	SH
14R-5, 69–71	5	120.6	3955	587.4	2.614	2.543	2.733	0.075	6.938	2.788	(12–90)*	*	*	SH
15R-1, 80–82	4C	124.7	4096	123.4	2.656	2.600	2.751	0.058	5.475	2.152	55	*	*	SH
15R-2, 92–94	3	126	4159	37.2	2.655	2.608	2.735	0.049	4.645	1.821	94	12.34	12.63	SH
15R-3, 48–50	3	127	4525	58.8	2.709	2.673	2.770	0.036	3.494	1.336	95.5	11.91	10.87	SH
16R-1, 98–100	5C	134.4	4102	42.3	2.686	2.638	2.767	0.049	4.669	1.809	76	11.23	11.39	SH
16R-3, 5–7	1A	136	4339	22.2	2.666	2.616	2.749	0.051	4.840	1.891	73	*	*	SH
16R-4, 82–84	1C	137.8	3919	53.8	2.590	2.523	2.701	0.071	6.600	2.674	82	*	*	SH
16R-5, 80–82	4A	138.9	4661	65.3	2.651	2.610	2.718	0.041	3.982	1.560	93	*	*	SH
16R-7, 54–56	6	141.5	4394	74.6	2.677	2.642	2.737	0.036	3.460	1.338	97	12.16	12.91	SH
17R-3, 37–39	1C	145.7	4222	37.5	2.640	2.594	2.715	0.047	4.449	1.753	97	12.17	12.3	SH
18R-1, 123–125	14	153.8	4617	17.7	2.665	2.640	2.707	0.025	2.469	0.956	92	*	*	SH
18R-3, 75–77	4	156.1	4821	68.3	2.686	2.623	2.796	0.066	6.209	2.420	93	12.1	12.4	SD
18R-4, 12–14	1	156.9	4828	8.9	2.676	2.651	2.718	0.025	2.443	0.942	85	*	*	SD
19R-1, 18–20	3A	162.5	4662	10.7	2.626	2.598	2.671	0.028	2.765	1.088	99	*	*	SD
19R-2, 13–15	1	163.8	4323	17.5	2.678	2.632	2.757	0.047	4.514	1.732	78	11.86	11.69	SD
20R-1, 106–108	13	173	4065	34.5	2.648	2.595	2.738	0.055	5.203	2.049	83	12.3	12.98	RG
20R-2, 24–26	1B	173.3	4036	23.4	2.689	2.636	2.780	0.055	5.197	2.015	90	11.83	12.68	SH
20R-4, 38–40	3A	175.9	4454	24.7	2.675	2.628	2.753	0.048	4.553	1.771	96	12.02	12.04	SH
21R-1, 93–95	1	182.4	4448	47.7	2.681	2.625	2.778	0.058	5.510	2.146	100	*	*	SH
21R-2, 40–42	1C	183.2	4312	25.9	2.713	2.668	2.790	0.045	4.349	1.666	92	12.21	11.18	SH
21R-2, 86–88	1D	183.6	4257	41.8	2.834	2.809	2.879	0.025	2.430	0.884	72	*	*	SH
21R-2, 97–99	4	183.7	4817	382.9	2.645	2.596	2.728	0.051	4.869	1.918	(72)*	*	*	SH
22R-4, 50–52	1B	193.9	4623	36.5	2.778	2.745	2.838	0.034	3.280	1.222	73	9.62	8.78	SH
22R-5, 104–106	6B	195.7	4915	45.2	2.676	2.646	2.725	0.030	2.898	1.119	86	11.99	11.97	SH
22R-7, 111–113	8	198.4	4048	72.0	2.686	2.638	2.767	0.049	4.629	1.793	68	*	*	SLG

Notes: * = not measured in this sample (nearby value). LOI and $H_2O + CO_2$ results do not exactly correspond with sample intervals identified here. SH = serpentinized harzburgite, PSH = pyroxene-rich serpentinized harburgite, MMG = meta-microgabbro, PD = porphyritic diabase, D = diabase, MPD = moderately phyric diabase, SD = serpentinized dunite, RG = rodingitized gabbro, SLG = serpentinized lherzolite with gabbro vein.

identified from considerations of primary mineralogy and texture (see also "Igneous Petrology," this chapter). Resistivity measurements generally fell in the 10–103 Ωm range (Fig. 96), with notably low values of 3–11 Ωm associated with the serpentinized harzburgite of Unit 1. Compressional-wave velocities (Fig. 96) are highest in the somewhat less serpentinized harzburgite occurring near 9 mbsf in Unit 1. Resistivity and velocity fluctuate considerably down the core in similar patterns that are less striking than those observed in the lower section of Hole 920B.

Porosity variations show no particular trend with depth (Fig. 96), except that the lowest porosity is observed near the top (10 m) and the local highs occur at about 79 m and 156 mbsf. The former occurs within diabase of Unit 6, whereas the latter occurs within serpentinized harzburgite of Unit 13. Density variations also show no particular trend with depth (Fig. 96). The highest density material occurs at 10 mbsf in the core, and density and porosity appear generally to vary inversely, as do velocity and porosity.

Thermal conductivity also fluctuates considerably downcore (Fig. 96). An isolated low occurring at 58 m represents a measurement from meta-microgabbro of Unit 4; a series of thermal conductivity lows observed from 69 to 79 mbsf correspond to measurements in diabase of Unit 6. Another isolated low at 99 mbsf corresponds to a measure-

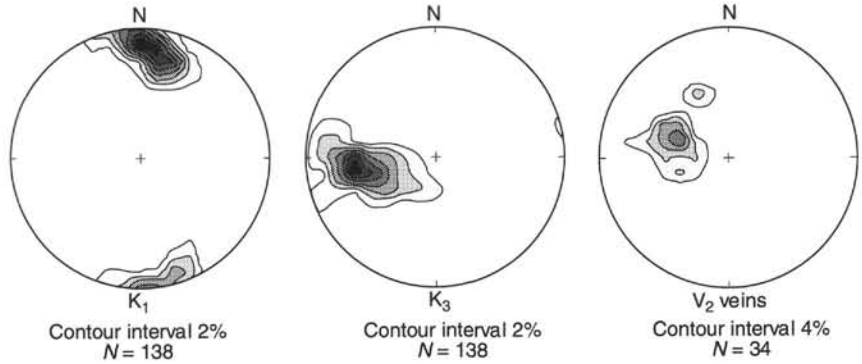

Figure 92. Lower hemisphere contour plots of magnetic fabric and vein orientation data (poles to V2 vein set) after azimuthal reorientation of characteristic remanent declination to 360°. The minimum (K_3) and maximum (K_1) axes of the susceptibility ellipsoid are directed approximately west and north, respectively. The magnetic foliation is approximately parallel to the composite deformation fabric in the serpentinite.

Table 12. Thermal-conductivity data for samples from Hole 920B.

Core, section, interval (cm)	Piece	Depth (mbsf)	Thermal conductivity (W/m°C)	Rock type	Alteration (%)
153-920B-					
1W-3, 54–69	5	3.02	3.126	SH	95
2R-1, 39–54	4	14.39	3.019	SH	94
3R-1, 121–133	9A	24.71	2.803	SH	90
3R-2, 27–39	4A	25.27	2.685	SH	98
4R-1, 31–44	5	33.51	2.930	SH	98
5R-3, 95–111	6	46.57	3.030	SH	98
6R-1, 31–46	2B	52.21	2.221	SH	95
7R-2, 1–13	1A	62.43	2.670	SH	88
8R-3, 32–47	5	73.34	2.870	SH	(95)*
9R-2, 14–28	3A	81.30	3.339	SH	90
9R-3, 65–80	10	83.30	2.089	PD	100
10R-1, 30–45	2B	89.40	2.911	SH	98
11R-1, 51–66	9B	99.01	3.144	SH	(95)*
12R-6, 27–42	2	114.60	2.442	SH	98
13R-1, 110–124	3*	118.30	3.150	SL	90

Notes: * = not measured in this sample (nearby value). SH = serpentinized harzburgite, PD = porphyritic diabase, SL = serpentinized lherzolite.

Table 13. Thermal-conductivity data for samples from Hole 920D.

Core, section, interval (cm)	Piece	Depth (mbsf)	Thermal conductivity (W/m°C)	Rock type	Alteration (%)
153-920D-					
2R-1, 115–132	13	9.15	3.239	SH	84
3R-1, 29–43	3B	17.79	3.208	SH	95
4R-2, 36–51	6A	28.96	2.632	SH	92
5R-3, 114–132	13	40.41	3.277	PYX SH	98
6R-1, 53–70	6B	47.03	3.398	SH	83
7R-1, 123–139	17	57.43	3.024	SH	78
7R-2, 23–36	2B	57.90	1.881	MMG	(89)*
8R-1, 130–144	16	67.20	3.012	SH	(86)*
8R-3, 74–90	9	69.54	2.384	PD	*
9R-1, 48–72	4A	76.08	2.166	PD	*
9R-2, 48–72	4A	77.33	2.106	MPD	*
10R-1, 41–53	7A	78.51	2.125	D	*
11R-1, 124–141	13	86.54	3.068	SH	(96)*
11R-2, 25–38	6	86.97	3.292	SH	100
12R-3, 74–92	4	98.47	3.208	SH	76
12R-3, 108–129	6	98.81	1.921	POXGN	29
13R-2, 126–142	7	106.75	3.055	OXMG/PYX	29
13R-3, 30–45	6	107.23	2.898	SH	87
14R-1, 21–34	4	114.51	2.932	SH	62
14R-4, 125–141	8	119.74	3.118	SH	76
15R-1, 1–21	1	123.91	2.280	SH	55
15R-6, 13–28	1	130.48	2.701	SH	99
16R-1, 90–103	2	134.30	2.784	SH	73
16R-7, 46–63	5C	141.45	3.097	SH	(86)*
17R-4, 92–109	6	147.58	3.017	SH	93
18R-1, 110–132	14	153.70	3.956	SH	92
19R-1, 38–56	5	162.68	2.601	SH	97
20R-4, 19–35	2	175.73	2.990	SH	81
21R-2, 86–103	4	183.61	3.216	SH	*
22R-3, 50–67	1B	193.23	2.723	SH	58

Notes: * = not measured this sample (nearby value). SH = serpentinized harzburgite, PYX SH = pyroxene-rich serpentinized harzburgite, MMG = meta-microgabbro, D = diabase, MPD = moderately phyric diabase, POXGN = pegmatitic oxide gabbronorite, OXMG/PYX = oxide metagabbro-pyroxenite.

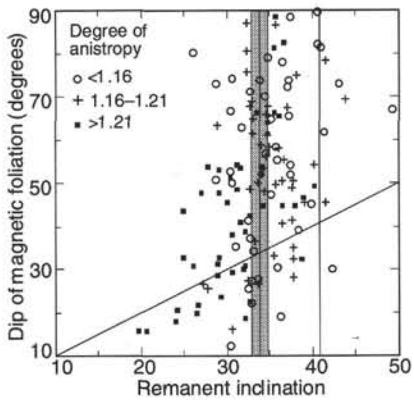

Figure 93. Anisotropy of magnetic susceptibility (AMS) and remanent inclination data for Site 920 discrete samples. The magnetic foliation is the plane containing the maximum (K_1) and intermediate (K_2) AMS axes. The mean remanent inclination for the data is 33.7° (vertical line with associated error limit as gray band) and the geocentric axial dipole inclination is 41°. If anisotropy entirely controlled the remanent inclination the data would follow the diagonal line where the remanent inclination lies within the plane of the magnetic foliation.

ment from pegmatitic oxide gabbronorite of Unit 10. The local low observed at 124 mbsf corresponds to a measurement in comparatively unaltered (55%) serpentinized harzburgite of Unit 13. The singular high at 154 mbsf in serpentinized harzburgite of Unit 13 is not correlated to any change in lithology or degree of alteration.

Alteration estimates from visual core descriptions are shown in Figure 96 (see also "Metamorphic Petrology," this chapter). Alteration is moderately high to high to about 68 mbsf, then drops to very low values in the diabase of Unit 6. Lower degrees of alteration occur in the serpentinized harzburgite at 124 mbsf in Unit 13, as discussed above. Slightly lesser (72%–73%) degrees of alteration occur in serpentinized harzburgite at 183.5–195 mbsf in Unit 13 and correspond with local increases in V_p and a relative decrease in thermal conductivity.

GRAPE Assessment

Variations in density with depth were determined by GRAPE and analysis of discrete minicore samples from Holes 920B and 920D. Results from Hole 920D are shown in Figure 97. As was the case for Hole 920B, GRAPE densities are systematically low although the major trends recorded by the discrete sample analysis remain. Spurious GRAPE determinations generally correspond with ends of core pieces or gaps between pieces (Fig. 97). However, in sections with relatively good recovery it appears that the GRAPE may be providing greater resolution in density variations with depth where the core is characterized by relatively continuous and long (>15 cm) piece lengths (e.g.,

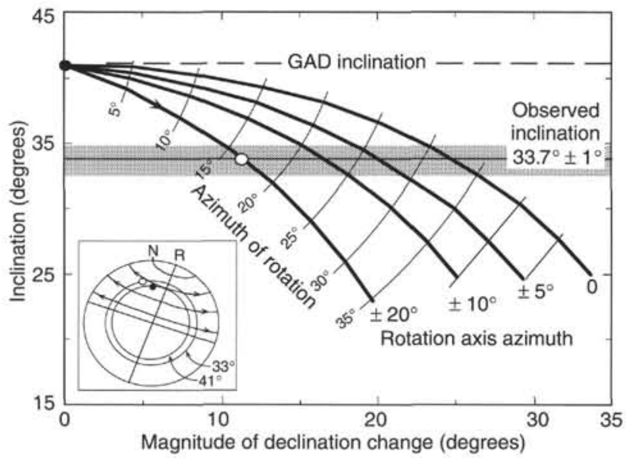

Figure 94. Hypothetical rotation paths based on paleomagnetic inclination data from Site 920. Paths (heavy lines) are shown for horizontal rotation axes oriented between ±20° with respect to north (i.e., 340°–020°). The amount of rotation is indicated by the thinner lines crossing these paths. Only positive rotations are shown for northeasterly rotation axes and only negative rotations for northwesterly rotation axes. Positive (negative) rotations are CW (CCW) when looking in the direction of the rotation axis. For example, a 17° CW rotation about a horizontal rotation axis with azimuth 020° will rotate an initial remanence direction of 360°, 41° (filled circle) to 348°, 33° (open circle). Inset: Lower hemisphere stereoplot shows rotation paths about a horizontal axis with azimuth (R) bearing 020°. Equal inclination lines are shown for 41° (the presumed original inclination) and 33° (the observed mean inclination).

112–121 m, 192–196 m). This suggests that this approach could be useful in future hard rock legs if measurements from the GRAPE apparatus can be appropriately calibrated and volume corrected.

Comparative Analysis of Measured Physical Properties

The uppermost oceanic crust at this location is largely serpentinized peridotite interpreted as altered upper mantle material emplaced by extensional tectonics at a slow spreading mid-ocean ridge. It is characterized by relatively high thermal conductivity and low compressional-wave velocity (measured along the horizontal axis at ambient conditions). Thermal conductivities of serpentinized harzburgite samples from Hole 920B show a mean value of 2.86 W/m°C; those measured at Hole 920D show a mean value of 3.03 W/m°C. These values are somewhat higher than those reported elsewhere for serpentinite and serpentinized harzburgite exposed near slow spreading mid-ocean ridges (mean values 2.29–2.71, for Hole 670A; Detrick, Honnorez, Bryan, Juteau, et al., 1988). Fluctuations in conductivity appear to mostly reflect variations in rock lithology and extent of alteration, although unexplained variations are observed as well.

Compressional wave velocities (V_p) of about 3600 m/s to 5800 m/s measured at this site are within the range generally associated with seismic Layer 2 of upper oceanic crust. The near surface is characterized by a relative velocity high, with velocity minima occurring at about 25 mbsf (Unit 2 of Hole 920B; Unit 1 of Hole 920D). The remainder of Hole 920B continues along this trend, with another local velocity high at the top of Unit 3, a general decreasing trend with another local high within the diabase Unit 4 (Fig. 97). Beneath Unit 4, velocity, density, and resistivity fluctuate harmoniously and inversely with porosity in a general decreasing trend truncated by the occurrence of high-velocity gneissic metagabbro at the top of Unit 7.

By contrast, the local velocity low at 25 mbsf in Unit 1 of Hole 920D is underlain by variable but modest increases in velocity with depth to about 78 m, where velocity drops considerably with the change in lithology from diabase to serpentinized harzburgite at the contact between Units 6 and 7. Velocities remain relatively low with several highs evident in the oxide-rich metagabbro of Unit 12, then begin a variable but generally increasing trend with depth to the base of Unit 13. Thus, velocity variations with depth appear to be cyclic within both holes of this site, although the patterns of cyclicity vary between locations.

V_p measurements from this site are generally well-behaved, displaying an increase with increasing density and decreasing porosity in the rock (Fig. 98). The scatter in the velocity-porosity and velocity-density relationships at Site 920 does not appear to reflect varying degrees of alteration from sample to sample as the fresher samples show as much variation as the more altered ones. Scatter in observations could reflect the effect of seismic anisotropy associated with lineated crystalline fabric in our single orientation (horizontal) V_p measurements.

Resistivity measurements at Site 920 are shown in relation to rock porosity in Figure 99. The data from each location are coded according to the rock lithology and degree of alteration. Data from less altered serpentinized harzburgite sampled from Hole 920B form a subparallel trend in a log-log plot (Fig. 99), which could indicate a preferred mechanism of conduction in these rocks (e.g., Broglia and Moos, 1988; Pezard, 1990; Pezard et al., 1991). However, results from Hole 920D show no such relationship, perhaps indicating that highly conductive bound water or highly conductive minerals lining porosity dominate the electrical properties of these rocks.

REFERENCES*

Bideau, D., Hébert, R., Hekinian, R., and Cannat, M., 1991. Metamorphism of deep-seated rocks from the Garret Ultrafast Transform (East Pacific Rise near 13°25'S). *J. Geophys. Res.*, 96:10079–10099.

Bonatti, E., Peyve, A., Kepezhinskas, P., Kurentsova, N., Seyler, M., Skolotnev, S., and Udintsev, E., 1992. Upper mantle heterogeneity below the Mid-Atlantic Ridge, 0°–15°N. *J. Geophys. Res.*, 97:4461–4476.

Broglia, C., and Moos, D., 1988. *In-situ* structure and properties of 110-MA crust from geophysical logs in DSDP Hole 418A. *In* Salisbury, M.H., Scott, J.H., et al., *Proc. ODP, Sci. Results,* 102: College Station, TX (Ocean Drilling Program), 29–47.

Brown, J.R., and Karson, J.A., 1988. Variations in axial processes on the Mid-Atlantic Ridge: the median valley of the MARK area. *Mar. Geophys. Res.,* 10:109–138.

Bryan, W.F., Humphris, S., Thompson, G., and Casey, J.F., 1994. Comparative volcanology of small eruptive centers in the MARK area. *J. Geophys. Res.,* 99:3013–3029.

Cannat, M., Juteau, T., and Berger, E., 1990. Petrostructural analysis of the Leg 109 serpentinized peridotites. *In* Detrick, R., Honnorez, J., Bryan, W.B., Juteau, T., et al., *Proc. ODP, Sci. Results,* 106/109: College Station, TX (Ocean Drilling Program), 47–57.

Christensen, N.I., 1982. Seismic velocities. *In* Carmichael, R.S. (Ed.), *Handbook of Physical Properties of Rocks:* Boca Raton, FL (CRC Press), 2:1–228.

Detrick, R., Honnorez, J., Bryan, W.B., Juteau, T., et al., 1988. *Proc. ODP, Init. Repts.,* 106/109: College Station, TX (Ocean Drilling Program).

Dick, H.J.B., 1989. Abyssal peridotites, very slow spreading ridges and ocean ridge magmatism. *In* Saunders, A.D., and Norry, M.J. (Eds.), *Magmatism in the Ocean Basins.* Geol. Soc. Spec. Publ. London, 42:71–105.

Di Donato, G., Joron, J.L., Treuil, M., and Loubet, M., 1990. Geochemistry of zero-age N-MORB from Hole 648B, ODP Legs 106–109, M.A.R., 22°N. *In* Detrick, R., Honnorez, J., Bryan, W.B., Juteau, T., et al., *Proc. ODP, Sci. Results,* 106/109: College Station, TX (Ocean Drilling Program), 57–65.

Gillis, K.M., Mével, C., Allan, J.F., et al., 1993. *Proc. ODP, Init. Repts.,* 147: College Station, TX (Ocean Drilling Program).

Hamano, Y., Bina, M.M., and Krammer, K., 1990. Paleomagnetism of the serpentinized peridotite from ODP Hole 670A. *In* Detrick, R., Honnorez, J., Bryan, W.B., Juteau, T., et al., *Proc. ODP, Sci. Results,* 106/109: College Station, TX (Ocean Drilling Program), 257–262.

*Abbreviations for names of organizations and publications in ODP reference lists follow the style given in *Chemical Abstracts Service Source Index* (published by American Chemical Society).

Hamlyn, P.R., and Bonatti, E., 1981. Petrology of mantle derived ultramafics from the Owen fracture zone, northwest Indian Ocean: implications for the nature of the oceanic upper mantle. *Earth Planet. Sci. Lett.*, 48:965–979.

Hébert, R., Adamson, A.C., and Komor, S.C., 1990. Metamorphic petrology of ODP Leg 109, Hole 670A serpentinized peridotites: serpentinization processes at a slow spreading ridge environment. *In* Detrick, R., Honnorez, J., Bryan, W.B., Juteau, T., et al. *Proc. ODP, Sci. Results,* 106/109: College Station, TX (Ocean Drilling Program), 103–115.

Honnorez, J., and Kirst, P., 1975. Petrology of rodingites from the equatorial Mid-Atlantic fracture zones and their geotectonic significance. *Contrib. Mineral. Petrol.,* 49:233–257.

Humphris, S.E., Bryan, W.B., Thompson, G., and Autio, L.K., 1990. Morphology, geochemistry, and evolution of Serocki Volcano. *In* Detrick, R., Honnorez, J., Bryan, W.B., Juteau, T., et al., *Proc. ODP, Sci. Results,* 106/109: College Station, TX (Ocean Drilling Program), 67–84.

Juteau, T., Berger, E., and Cannat, M., 1990. Serpentinized, residual mantle peridotites from the MAR median valley, ODP Hole 670A (21°10′N, 45°2′W, Leg 109): primary mineralogy and geothermometry. *In* Detrick, R., Honnorez, J., Bryan, W.B., Juteau, T., et al., *Proc. ODP, Sci. Results,* 106/109: College Station, TX (Ocean Drilling Program), 27-45.

Karson, J.A., Thompson, G., Humphris, S.E., Edmond, J.M., Bryan, W.B., Brown, J.R., Winters, A.T., Pockalny, R.A., Casey, J.F., Campbell, A.C., Klinkhammer, G., Palmer, M.R., Kinzler, R.J., and Sulanowska, M.M., 1987. Along-axis variations in seafloor spreading in the MARK area. *Nature,* 328:681–685.

Kelley, D.S., Gillis, K.M., and Thompson, G., 1993. Fluid evolution in submarine magma-hydrothermal systems at the Mid-Atlantic Ridge. *J. Geophys. Res.,* 98:19579–19596.

Kelley, D.S., and McDuff, R.E., 1993. Carbon-bearing fluids in the oceanic crust. *Eos,* 74: 654.

Kirby, S.H., 1983. Rheology of the lithosphere. *Rev. Geophys.,* 21:1458–1487.

Kirschvink, J.L., 1980. The least-squares line and plane and analysis of palaeomagnetic data. *Geophys. J. R. Astron. Soc.,* 62:699–718.

Kolstedt, D.L., 1992. Structure, rheology and permeability of partially molten rocks at low melt fractions. In Morgan, J.P., Blackman, D.K., and Sinton, J.M. (Eds.), *Mantle Flow and Melt Generation at Mid-Ocean Ridges.* Am. Geophys. Union, Geophys. Monogr., 71:103-121.

Komor, S.C., Elthon, D.E., and Casey, J.F., 1985. Serpentinization of cumulate ultramafic rocks from the North Arm Mountain massif of the Bay of Islands ophiolite. *Geochim. Cosmochim. Acta,* 49:2331–2338.

Komor, S.C., Grove, T.L., and Hébert, R., 1990. Abyssal peridotites from ODP Hole 670A (21°10′N, 45°02′W): residues of mantle melting exposed by non-constructive axial divergence. *In* Detrick, R., Honnorez, J., Bryan, W.B., Juteau, T., et al., *Proc. ODP, Sci. Results,* 106/109: College Station, TX (Ocean Drilling Program), 85–101.

MacDonald, W.D., and Ellwood, B.B., 1988. Magnetic fabric of peridotite with intersecting petrofabric surfaces, Tinaquillo, Venezuela. *Phys. Earth. Planet. Inter.,* 51:301–312.

McFadden, P.L., and Reid, A.B., 1982. Analysis of paleomagnetic inclination data. *Geophys. J. R. Astron. Soc.,* 69:307–319.

Mével, C., Cannat, M., Gente, P., Marion, E., Auzende, J.-M., and Karson, J.A., 1991. Emplacement of deep crustal and mantle rocks on the west median valley wall of the MARK area (MAR 23°N). *Tectonophysics,* 190:31–53.

Michael, P., and Bonatti, E., 1985. Peridotite composition from the North Atlantic: regional and tectonic variations and implications for partial melting. *Earth Planet. Sci. Lett.,* 73:91–104.

Miyashiro, A., Shido, F., and Ewing, M., 1969. Composition and origin of serpentinites from the Mid-Atlantic Ridge, 24° and 30°N. *Contrib. Mineral. Petrol.,* 32:38–52.

Mottl, M.J., and Holland, H.D., 1978. Chemical exchange during hydrothermal alteration of basalt by seawater. I. Experimental results for major and minor components of seawater. *Geochim. Cosmochim. Acta,* 42:1103–1115.

Pearce, J.A., 1987. An expert system for the tectonic characterization of ancient volcanic rocks. *J. Volcanol. Geotherm. Res.,* 32:51–65.

Pezard, P., 1990. Electrical properties of mid-ocean ridge basalt and implications for the structure of the upper oceanic crust in Hole 504B. *J. Geophys. Res.,* 95:9237–9264.

Pezard, P.A., Howard, J.J., and Goldberg, D., 1991. Electrical conduction in oceanic gabbros, Hole 735B, Southwest Indian Ridge. *In* Von Herzen, R.P., Robinson, P.T., et al., *Proc. ODP, Sci. Results,* 118: College Station, TX (Ocean Drilling Program), 323–332.

Shipboard Scientific Party, 1993. Explanatory notes. *In* Gillis, K., Mével, C., Allan, J., et al., *Proc. ODP, Init. Repts.,* 147: College Station, TX (Ocean Drilling Program), 15–42.

Spear, F.S., 1981. An experimental study of hornblende stability and compositional variability in amphibolite. *Am. J. Sci.,* 281:697–734.

Stacey, F., and Banerjee, S.K., 1974. *The Physical Principles of Rock Magnetism:* Amsterdam (Elsevier).

Vanko, D.A., and Stakes, D.S., 1991. Fluids in oceanic layer 3: evidence from veined rocks, Hole 735B, Southwest Indian Ridge. *In* Von Herzen, R.P., Robinson, P.T., et al., *Proc. ODP, Sci. Results,* 118: College Station, TX (Ocean Drilling Program), 181–218.

Ms 153IR-102

NOTE: For all sites drilled, core-description forms ("barrel sheets"), and core photographs can be found in Section 3, beginning on page 277. Thin-section data are given in Section 4, beginning on page 665. The CD-ROM (back pocket, this volume) contains the complete set of spreadsheets with piece-by-piece data for all structural features identified and measured. A set of summary spreadsheets that are linked to the igneous and metamorphic spreadsheets are also contained on the CD-ROM. Keys, summary tables, checklists, and thin-section summaries and notes are also archived. Compressed versions of the figures created for this volume, compatible with Macintosh computers, are located in the directories labeled REPT92X in the "Structure" directory. Scanned TIFF images of all the SVCD drawings are archived in the "STRCDRAW" file. Apparent dip data and true strike and dip data for all measurable features are contained in the "STR_DIP" subdirectory. This directory also contains the LinesToPlane documentation and program that converts the apparent dip data to true strike and dip in an archived form. GRAPE, MST, and index properties are also reported on the CD-ROM.

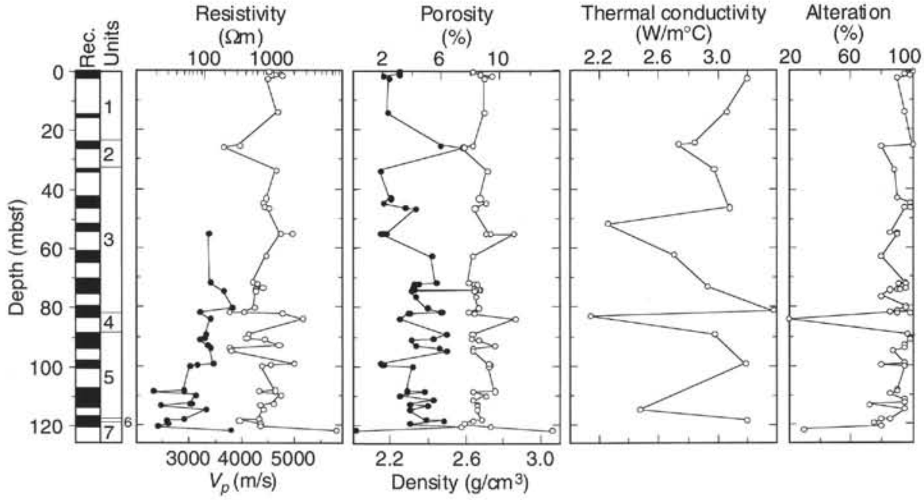

Figure 95. Physical property determinations as functions of depth for Hole 920B. Circles represent sample locations. First panel from left: left curve is resistivity (filled circles), right curve is compressional-wave velocity (open circles). Compressional-wave velocity measured in horizontal direction at ambient temperature and atmospheric pressure. Second panel: left curve is porosity (filled circles), right curve is density (open circles). Alteration estimates from visual core descriptions.

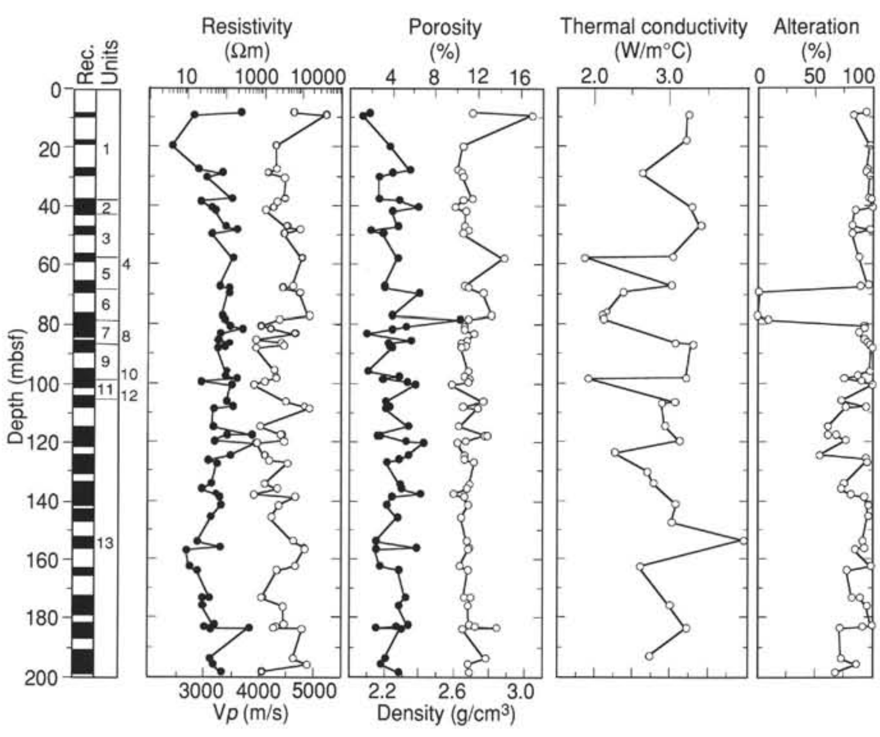

Figure 96. Physical property determinations, column indicating core recovery, and unit identification as functions of depth for Hole 920D. Circles represent sample locations. First panel from left: left curve is resistivity (filled circles), right curve is compressional-wave velocity (open circles). Compressional-wave velocity measured in horizontal direction at ambient temperature and atmospheric pressure. Second panel: left curve is porosity (open circles), right curve is density (filled circles). Alteration estimates from visual core descriptions.

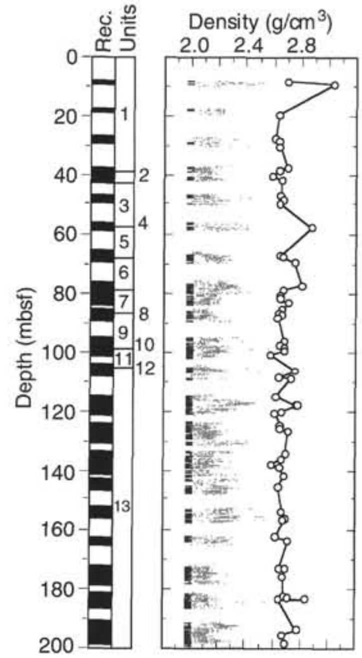

Figure 97. Core recovery, unit identification, and density data for Hole 920D. Bars aligned below 2.0 g/cm^3 show locations of piece lengths greater than 15 cm, scattered dots are GRAPE determinations, and connected open dots represent bulk density measurements from discrete samples.

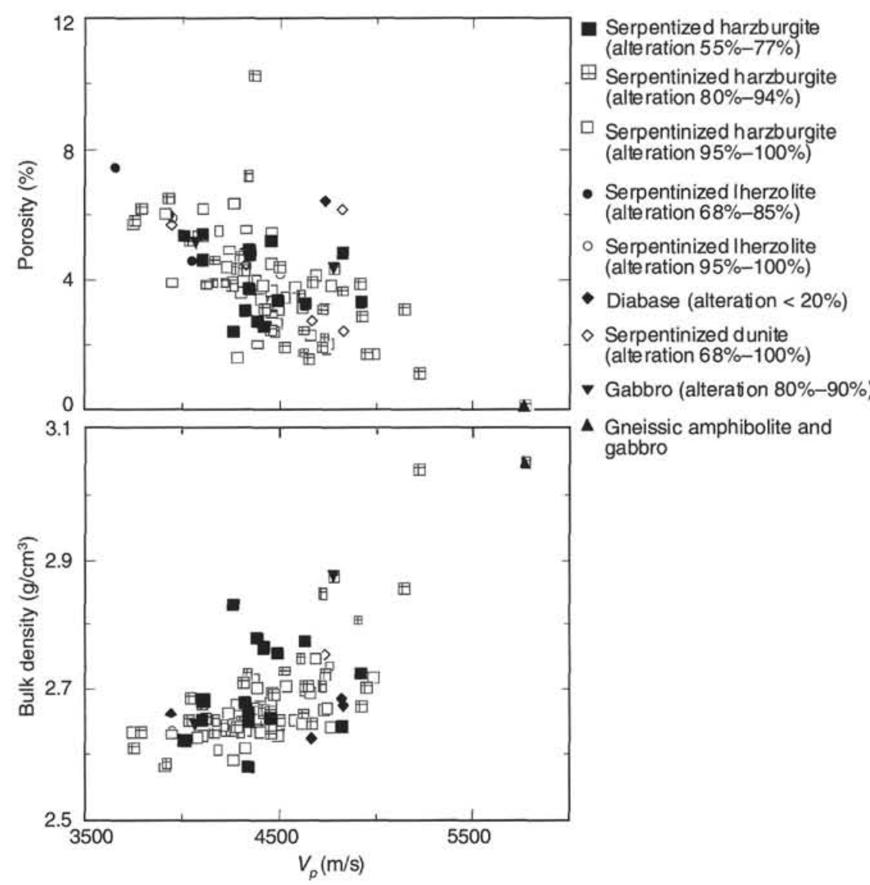

Figure 98. Velocity-porosity and velocity-density relationships for rocks recovered at Site 920. Rock types used are listed in Table 10.

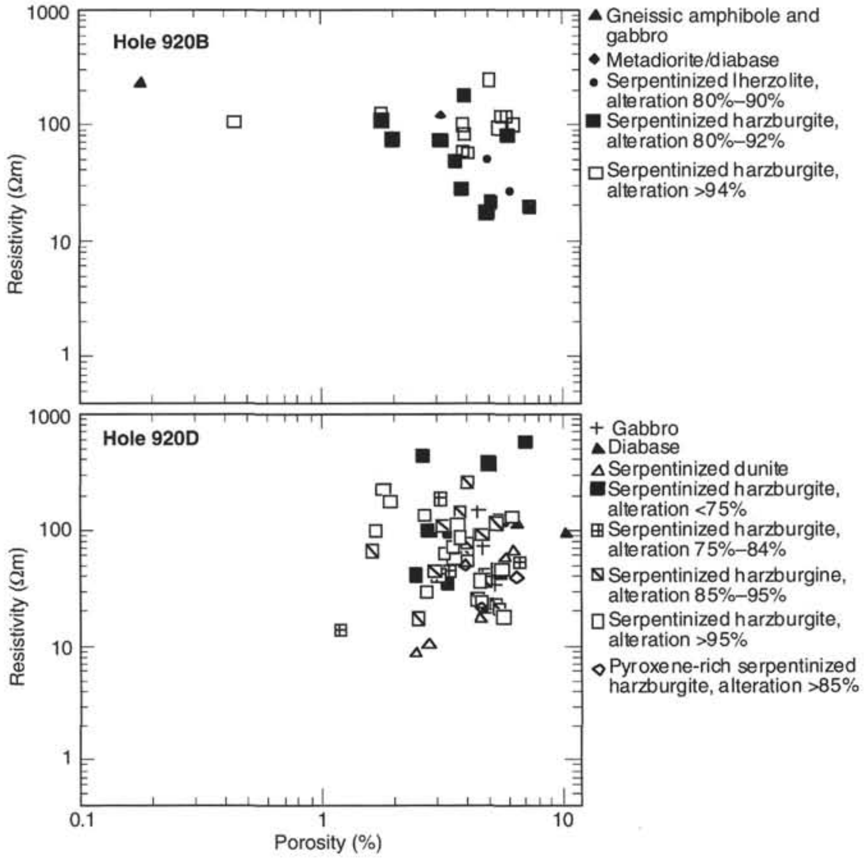

Figure 99. Resistivity-porosity relationships for rocks recovered at Holes 920B and 920D. Rock types used are listed in Table 10.